1983

SURFACE FLASHOVER STUDIES AND ELECTRIC FIELD COMPUTATIONS TO OPTIMIZE THE DESIGN OF CONDUCTOR-SOLID INSULATOR GEOMETRY IN VACUUM.

ARUNACHALAM SIVATHANU. PILLAI
University of Windsor

Recommended Citation

PILLAI, ARUNACHALAM SIVATHANU., "SURFACE FLASHOVER STUDIES AND ELECTRIC FIELD COMPUTATIONS TO OPTIMIZE THE DESIGN OF CONDUCTOR-SOLID INSULATOR GEOMETRY IN VACUUM." (1983). *Electronic Theses and Dissertations.* Paper 3676.

CANADIAN THESES ON MICROFICHE

I.S.B.N.

THESES CANADIENNES SUR MICROFICHE

National Library of Canada
Collections Development Branch

Canadian Theses on
Microfiche Service

Ottawa, Canada
K1A 0N4

Bibliothèque nationale du Canada
Direction du développement des collections

Service des thèses canadiennes
sur microfiche

NOTICE

The quality of this microfiche is heavily dependent upon the quality of the original thesis submitted for microfilming. Every effort has been made to ensure the highest quality of reproduction possible.

If pages are missing, contact the university which granted the degree.

Some pages may have indistinct print especially if the original pages were typed with a poor typewriter ribbon or if the university sent us a poor photocopy.

Previously copyrighted materials (journal articles, published tests, etc.) are not filmed.

Reproduction in full or in part of this film is governed by the Canadian Copyright Act, R.S.C. 1970, c. C-30. Please read the authorization forms which accompany this thesis.

THIS DISSERTATION
HAS BEEN MICROFILMED
EXACTLY AS RECEIVED

AVIS

La qualité de cette microfiche dépend grandement de la qualité de la thèse soumise au microfilmage. Nous avons tout fait pour assurer une qualité supérieure de reproduction.

S'il manque des pages, veuillez communiquer avec l'université qui a conféré le grade.

La qualité d'impression de certaines pages peut laisser à désirer, surtout si les pages originales ont été dactylographiées à l'aide d'un ruban usé ou si l'université nous a fait parvenir une photocopie de mauvaise qualité.

Les documents qui font déjà l'objet d'un droit d'auteur (articles de revue, examens publiés, etc.) ne sont pas microfilmés.

La reproduction, même partielle, de ce microfilm est soumise à la Loi canadienne sur le droit d'auteur, SRC 1970, c. C-30. Veuillez prendre connaissance des formules d'autorisation qui accompagnent cette thèse.

LA THÈSE A ÉTÉ
MICROFILMÉE TELLE QUE
NOUS L'AVONS REÇUE

NL-339 (r. 82/08)

Canada

SURFACE FLASHOVER STUDIES AND ELECTRIC FIELD COMPUTATIONS TO OPTIMIZE THE DESIGN OF CONDUCTOR-SOLID INSULATOR GEOMETRY IN VACUUM

by

Arunachalam Sivathanu Pillai

A Dissertation
submitted to the Faculty of Graduate Studies and
Research through the Department of Electrical
Engineering in Partial Fulfillment of the
requirements for the degree of
Doctor of Philosophy at
The University of Windsor

Windsor, Ontario, Canada

1983

ABSTRACT

The surface flashover strength of cylindrical and conical solid insulators has been investigated in ultra-high vacuum ($<10^{-8}$ Torr) using DC, AC (60 Hz) and lightning impulse and a combination of a DC and impulse and a DC and AC. In general the DC and the impulse flashover voltages for a fixed length of the insulator are almost the same (within ±5%) and the AC flashover voltage is lower than the DC and the impulse. The combined DC ± 1.2/50 μs impulse flash-over voltage of cylindrical and conical solid insulators in vacuum is influenced by the applied DC pre-stress. A DC pre-stress causes an increase in the subsequent flashover values of the AC superimposed on DC. In general the flashover voltage of solid insulators are independent of the pressure in the range 10^{-8} to 6×10^{-3} Torr. The effects of ultra-violet (UV) light on the electrical performance of solid insulator in vacuum has been studied. The UV irradiation on solid insulator-vacuum interface degrades the electrical performance of the insulator.

A method for calculating the DC surface flashover voltage of cylindrical insulators based on the assumption that the discharge occurs in a layer of desorbed gases from the insulator surface has been proposed. The effect of surface charge accumulation on the field distribution has been studied by assuming different patterns of surface charge distributions. The results showed that for a heterocharge accumulation the electric field is enhanced at both the cathode and the anode electrode junctions and for a homocharge accumulation the field enhancement is on the surface of the insulator away from the electrode junctions. In the case of a positive charge accumulation throughout the surface of the solid insulator, an enhancement in the field is found at the cathode and a reduction in the field value at the anode.

The electric field distribution along the solid insulator-vacuum interface is computed and analyzed for a cylindrical insulator with metal inserts, cylindrical insulator placed in recessed electrodes, cylindrical insulator with convex curved edges, cylindrical insulator with concave curved edges and cylindrical insulator with metal inserts and placed in recessed electrodes. The electrode-insulator geometry which gives the best performance has been suggested.

I dedicate this work to my parents

ACKNOWLEDGEMENTS

I would like to express my sincere thanks to my supervisor, Dr. Reuben Hackam, Professor of Electrical Engineering, for his supervision, valuable guidance, suggestions and advice throughout this project and preparation of this dissertation.

I wish to thank Dr. G. R. Govinda Raju and Dr. A. Watson of Electrical Engineering Department and Dr. Van Wijngaarden of Physics Department for their valuable discussions on part of this project. I wish to thank Prof. P. H. Alexander for helpful discussions related to field computations.

Thanks are also due to Mr. D. K. Liebsch and other staffs of Central Research, Mr. Alan Thibert and Mr. J. M. Novosad of Electrical Engineering and Mr. G. A. Vazsonyi of Engineering Materials for their valuable technical assistance and Mrs. A. Zeleney for her excellent typing of this dissertation. I also thank the Natural Sciences and Engineering Research Council of Canada for providing funds for this project.

Finally, I want to express my deep appreciation to my wife, Prema, for her patience and moral support and our parents for their good wishes and kindness throughout my doctoral program.

TABLE OF CONTENTS

LIST OF SYMBOLS

V	applied positive voltage to the top electrode
L	largest gap separation between the electrodes
R_1	radius or width of the solid insulator (R_1=R)
ε_1	relative dielectric constant of the vacuum ($\varepsilon_1 = 1.0$)
ε_2	relative dielectric constant of the solid insulator (ε_r)
ε_o	permittivity of the free space (8.854×10^{-14} F cm^{-1})
E_{av}	average applied electric field ($E_{av} = V/L$)
E_{11}	electric field parallel to the surface of the insulator ($E_{av} = E_{11}$ for cylindrical insulator)
$E_{\perp}$	electric field normal to the surface of the insulator
M_{cr}	Critical desorbed amount of gas density
A_o	electron emission energy in eV
A_1	electron impact energy in eV
δ	secondary electron emission rate
β	field enhancement factor
θ	angle between the conical insulator surface and the applied field (cone angle)
γ	angle between the concave curved solid insulator and the normal to the electrode at the contact point
α	angle between the convex curved solid insulator and the electrode surface
r	radius of convex curved edge
σ_s	surface charge density (C cm^{-2})

P_{ij}	potential coefficient of the contour point at the location i due to the influence of the charge located at the position j
F_{ij}	field coefficient which is the contribution of the charge j to the normal component of the field vector at a given contour point i
Q_j	value of the ring charge at the location j
λ_j	value of the infinite line charge per unit length at the location j
E_t	computed tangential field
E_n	computed normal field
E'_t	normalized tangential field ($E'_t = E_t/E_{av}$)
E'_n	normalized normal field ($E'_n = E_n/E_{av}$)
E'_{t_1}	normalized tangential field in the vacuum side of the solid insulator-vacuum boundary
E'_{t_2}	normalized tangential field in the solid dielectric side of the solid insulator-vacuum boundary
E'_{n_1}	normalized normal field at the solid insulator-vacuum boundary in the vacuum side
E'_{n_2}	normalized normal field at the solid insulator-vacuum boundary in the dielectric side
$E'_{t_{1c}}$	normalized tangential field value at the cathode junction (vacuum side)
$E'_{n_{1c}}$	normalized normal field value at the cathode junction (vacuum side)
$E'_{t_{1a}}$	normalized tangential field value at the anode junction (vacuum side)
$E'_{n_{1a}}$	normalized normal field value at the anode junction (vacuum side)
$E'_{t_{1m}}$	maximum normalized tangential field value on the solid insulator-vacuum interface (vacuum side)

$E'_{n_{1m}}$	maximum normalized normal field value on the solid insulator-vacuum interface (vacuum side)
ϕ	computed potential
ϕ'	normalized potential ($\phi' = \phi/V$)
z	axial distance from the bottom electrode
E'_{z_1}	normalized axial field in the vacuum side
E'_{z_2}	normalized axial field inside the solid dielectric
UV	ultra-violet

LIST OF FIGURES

LIST OF TABLES

LIST OF APPENDICES

CHAPTER I

INTRODUCTION

The study of the mechanisms responsible for the failure of the electrical insulation of vacuum gaps bridged by a solid insulator is of considerable interest for practical applications. It is well known that the withstand voltage of the gap containing a solid insulator is considerably lower than that of an identical vacuum gap without the solid insulator or the volume strength of the solid insulator [1-14]. Development of modern devices such as high voltage vacuum switches, particle accelerators and separators, X-ray equipment, cryogenic power transmission cables and electrostatic generators for operation in outer space employ vacuum for insulation. The high voltage vacuum devices necessitates either constructing the vacuum chamber itself of an insulating material or insulating the high-voltage conductor as it passes through the wall of a metallic vacuum chamber. Quite often the insulator surface flashover can be the limiting factor in the operation of vacuum insulated equipment. An improvement in the withstand voltage capability of the solid insulators in vacuum could lead to a fair reduction in the size of many high voltage devices.

In the design of high voltage systems such as megavolt accelerator tubes, voltage grading is used to provide a uniform electric field throughout the surface of the insulator used to support the high voltage electrodes [15]. The voltage-graded surface is achieved by dividing the insulating length into multiple insulator rings separated by metallic potential rings. These metallic rings divide the insulator surface into segments and keep a uniform voltage difference between them. It has been experimentally found that this type of design helps to reduce the total length of the high voltage support and also to improve the surface flashover strength of the solid dielectric [15]. In X-ray tube designs a number of optimum-angle conical insulator tubes are stacked together with metal spacers between them to construct the tube envelope [10]. This type of arrangement overcomes the difficulty associated with falling breakdown strength with increasing tube wall length. The principle of dividing the insulator structure into a series of electrically independent, high gradient, low-voltage segments is important in vacuum applications [10,15]. For this reason the surface flashover studies of short cylindrical and conical solid insulators in vacuum are considered to be very useful.

In vacuum, the study of the effect of the contact between the solid insulator and the electrodes is important in order to improve the withstand voltage of solid insulators. Kofoid investigated the phenomena arising at the solid insulator-electrode-vacuum triple junction in some detail [4,5]. He postulated that the large lowering of the breakdown strength of solid insulators in vacuum is due to the production of negative particles by the field emission process at or near the cathode junction. The field at the electrode-dielectric junction can be reduced by a large factor by a suitable end-cap design [4]. Higher flashover values have been observed for a solid insulator with a metal insert and for those placed in a recessed electrode [5,16,17]. The field computation studies show that the field at the triple junction is reduced in the case of the insulator with a metal insert [16,18] or placed in a recessed electrode [18].

In practice the electric field at the cathode triple junction is further enhanced due to geometrical edge effects [19], asperities on the electrodes [20,21], charge accumulation on the insulator surface [6-7, 22-26] and small voids between the cathode and the solid insulator [4,27]. Gleichauf [2] stated that the secondary electron emission from the insulator surface would alter the field distribution in a manner that would influence the breakdown voltage. Experimental measurements [22,23] and computational results with assumed hetero surface charge distributions [26] showed that the local field of both the electrode junctions showed considerable enhancement over the applied field and the enhancement depends on the insulator material and the end-cap design.

The present investigation by the author is aimed to explain a number of experimentally observed results relating to the flashover of solid insulators in vacuum. Experimental, theoretical and numerical computational studies have been carried out in order to obtain more information on the surface flashover phenomena of solid insulators in vacuum. The major aspects of the present investigation are:

1. Pre-breakdown and breakdown of cylindrical and conical solid insulators in vacuum using DC, AC and 1.2/50 μs impulse voltage [28,29,30].
2. Effect of DC prestress on the combined DC and 1.2/50 μs impulse or DC and AC flashover voltage [28,29].
3. Effect of the solid insulator diameter, the electrode material, the pressure, and the number of solid spacers placed in series on the flashover voltage. The effect of ultra-violet irradiation at the solid insulator-vacuum interface on the insulator performance has also been studied.
4. A method has been proposed to calculate the surface flashover voltage of solid insulators in vacuum. This method is based on the assumption that the discharge

occurs in a layer of desorbed gases from the insulator surface [30].

5. Electric field modification of the solid insulator-vacuum interface arising from surface charges on the insulator is calculated by assuming different surface charge distributions. Both heterocharge and homocharge accumulation on the insulator surface are considered [26,31,32].
6. Electric field distributions are computed and analyzed for different solid insulator-electrode geometries to optimize the solid insulator flashover performance. The geometry which gives the best performance has been suggested [18, 19,33].

CHAPTER II

EXPERIMENTAL TECHNIQUES AND PROCEDURE

2.1 Solid Insulators and Electrodes

Most of the solid insulator spacers used in the present investigation are of cylindrical or conical shape. Macor ® machinable glass ceramic supplied by Corning Glass is extensively used for the study. The electrical and thermal properties of the Macor glass ceramic at 25°C are as follows:

Dielectric constant (ϵ_2) = 5.8 (f = 10 kHz)
Dielectric strength E (D.C.) = 3000 Volt/mil.
Loss Tangent (tan δ) = 0.003 (f = 10 kHz)
Volume resistivity = 10^{14} Ω - cm.

The coefficient of linear thermal expansion of the Macor glass ceramic from 25° to 400°C is 94 x 10^{-7}/°C. The maximum usable temperature without a change occurring in the crystal structure is 1000°C. The investigation shows that the material has good electrical properties in vacuum. Other solid insulator materials used for the present investigation are quartz ($\epsilon_2 = 3.8$), Pyrex ® glass ($\epsilon_2 = 4.6$), plexiglass (Polymethylmethacrylate, $\epsilon_2 = 3.2$), Teflon (PTFE, Polytetrafluoroethylene, $\epsilon_2 = 2.2$) and sapphire ($\epsilon_2 = 12.0$). In general

---

® Registered Trademark

the dielectric properties of the insulator vary in accordance with the particular chemical composition used and the techniques employed in the manufacturing process [34].

Insulators of different diameters and lengths have been used in order to find the effect of the insulator diameter and the length on the flashover performance. Quartz, pyrex glass and sapphire insulator materials are obtained as well polished samples to the required thickness and diameters and used as supplied. Other materials are cut to the required size from the stock in standard sizes of rods and are machined and polished using 600 grit sand paper. The insulators are arranged to make a butt joint with both electrodes.

The flat electrodes are made of stainless steel type 304 and are rounded at the edges to give a uniform electric field in the region of the spacers. The electrodes diameter used are either 22 or 15 mm. The electrodes are machined and first polished by using 600 grit sand paper and finally polished to a mirror finish by using 1 μm aluminium powder suspended in water solution 1:10. Copper and aluminium flat electrodes and stainless steel recessed electrodes have also been used to study the effect on the insulator performance. Before installation in the vacuum system, the electrodes and the solid insulator spacers are thoroughly degreased with the aid of an ultrasonic vibrator, using a detergent solution followed by acetone and distilled water. The solid insulators are housed in three breakdown chambers connected to an all-metal bakeable vacuum system.

2.2 Breakdown Chamber

The investigations are carried out in a stainless steel chamber fitted with a high voltage bushing and a sapphire view port (Fig. 2.1). The useful light transmission range of the sapphire view port (Huntington® VPS-100) is from 0.25 to 5.5 microns. Three breakdown chambers with the sapphire view-port are simultaneously employed. The high voltage bushing is made of pyrex glass and is capable of withstanding a working voltage over 100 kV. A linear motion drive made of stainless steel bellows and welded to a stainless steel flange is used to hold the lower electrode. An aligning adapter [35] made of 304 stainless steel is used for the accurate alignment of the lower electrode. The high voltage electrode (upper electrode) is connected to the bushing through a tungsten rod. The stainless steel breakdown chambers are electrically isolated from the rest of the system. The design and the procedure for the accurate alignment of the electrodes are similar to that reported previously by Hackam and Salman [35,36].

2.3 Vacuum System

The bakeable vacuum system used is shown in Fig. 2.1 Stainless steel is used for tubings and flanges, and OFHC®

copper gasket for compression seals. Metal-sealed bakeable right-angle valves are used to seal the vacuum system. Pumping is achieved by means of a bakeable-diode ion pump preceded by a sorption pump (Fig. 2.1). A brief description of the pumping system and vacuum measurement is given here.

2.3.1 Sorption Pump

A sorption pump is used as the roughing pump to obtain the base pressure for the ion pump. The sorption pump is especially suitable for ion-pumped systems in which cleanliness and elimination of vibration are prime considerations. Liquid nitrogen (-196°C) is used as a coolant to cool the surface of the sorption pump. In this cooling state the synthetic zeolite molecular sieve type 5A (a porous material) absorbs the gas molecules and creates a local region of low pressure. The overall pressure of the system is reduced due to absorption. The sorption pump can be disconnected from the vacuum system by closing the right angle valve V_3 (Fig. 2.1). When the sorption pump saturates, it is heated up to about 200°C to reactivate the molecular sieve absorbent. When doing this the right angle valve connected to the vacuum system is closed and a rotary pump (pumping speed 1.7 ℓ/sec) is used to evacuate the sorption pump down to 5×10^{-3} Torr. The pressure obtained using the sorption pump is down to 5×10^{-6} torr. The pumping speed of the sorption pump is respectively for water vapour

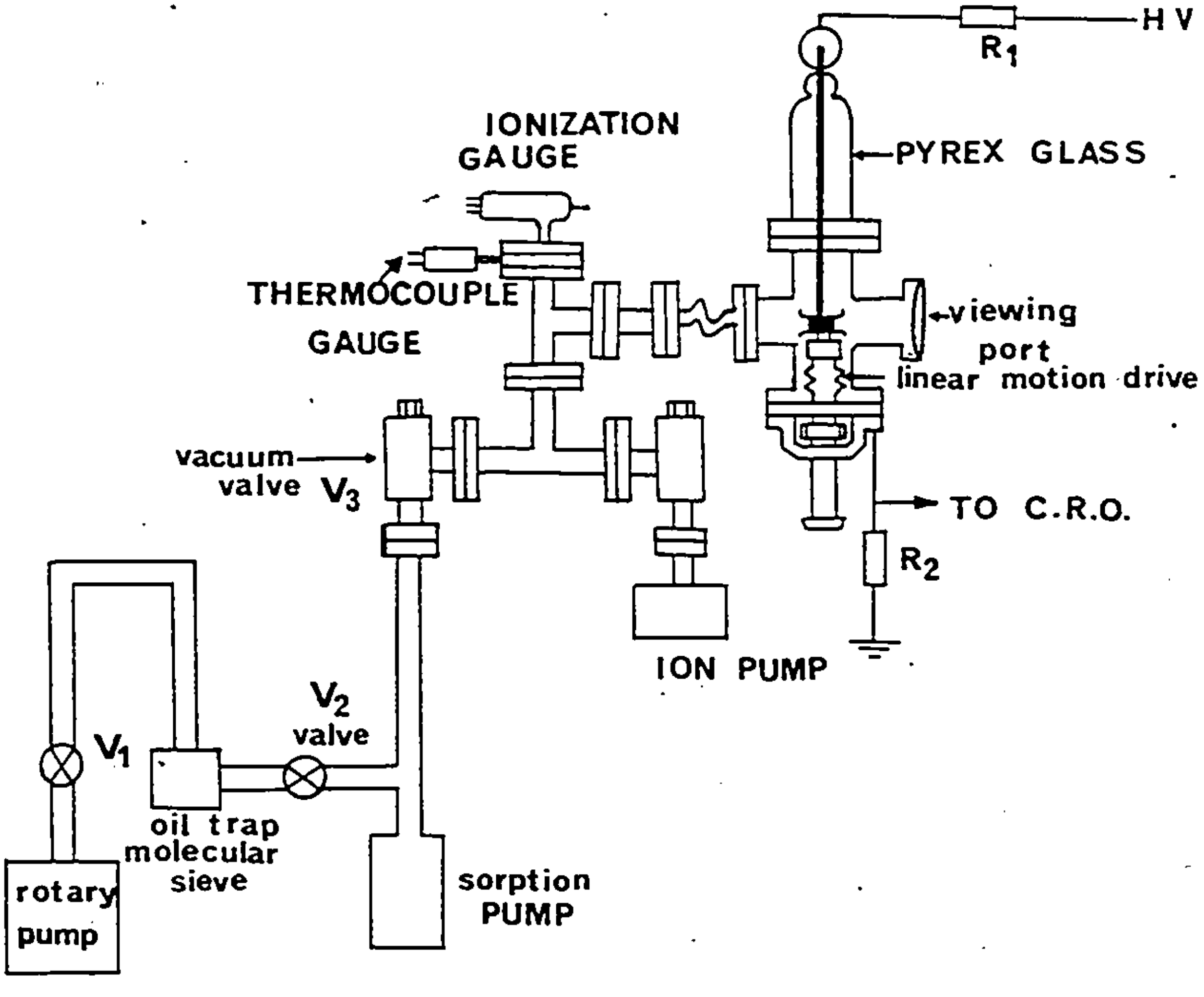

Fig. 2.1. Layout of the vacuum system with one of the three breakdown chambers.

500 l/sec, nitrogen 43 l/sec and hydrogen 100 l/sec.

2.3.2 Ion Pump

A Varian 8 l/sec Vac Ion® pump is used to maintain the background pressure throughout the experiments by continuously pumping the gases released at the onset of the flashover. A roughing pressure below to 10^{-4} Torr is required to start the pump. The residual pressure of the vacuum system obtained using the diode ion pump is less than 10^{-8} torr ($<10^{-6}$ Pa). The pump body is made of 304 stainless steel and the magnet used is made of ferrite. The pump operates by ionizing the gas in a magnetically confined cold cathode discharge. The pumping speed varies with pressure and with different gases. Figure 2.2 illustrates the pumping speed vs. pressure. The pumping speeds for common gases relative to that for air are:
Air 100%, nitrogen 100%, water vapour 100%, argon 24% and helium 30%.

2.3.3 Vacuum Measurement

The ion pump is connected to a control unit by a coaxial high-voltage cable. The pressure at the pump inlet flange over the range of 10^{-4} to 10^{-8} Torr can be read directly on the pressure scale of the control unit. Since the pressure within the ion pump is proportional to the current drawn by the pump, the pressure can be determined from the pressure vs. current graph as shown in Fig. 2.3. The accuracy obtained

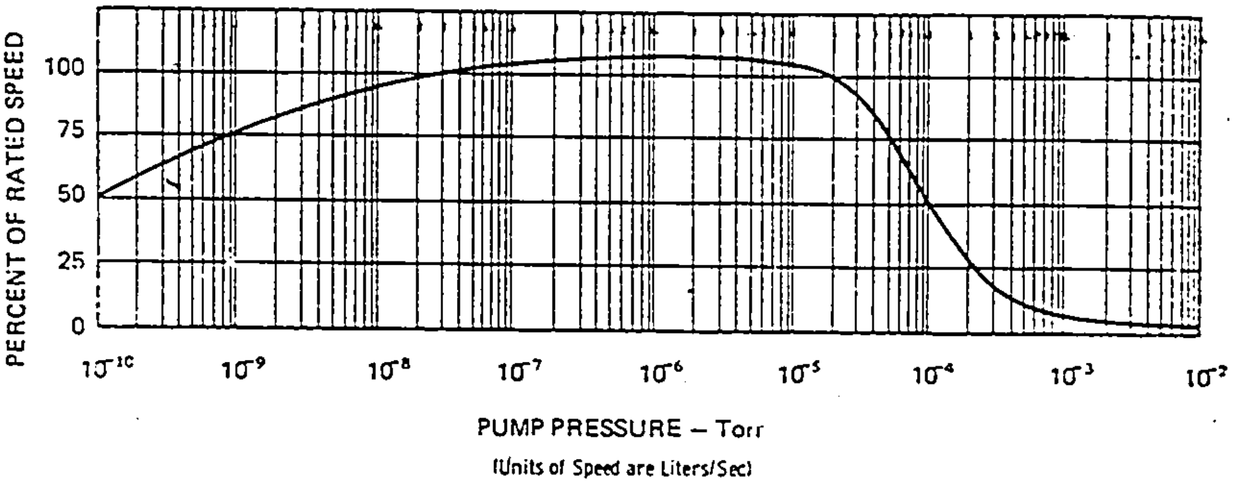

Fig. 2.2. Pumping Speed vs. Pressure (Varian VacIon® Pump).

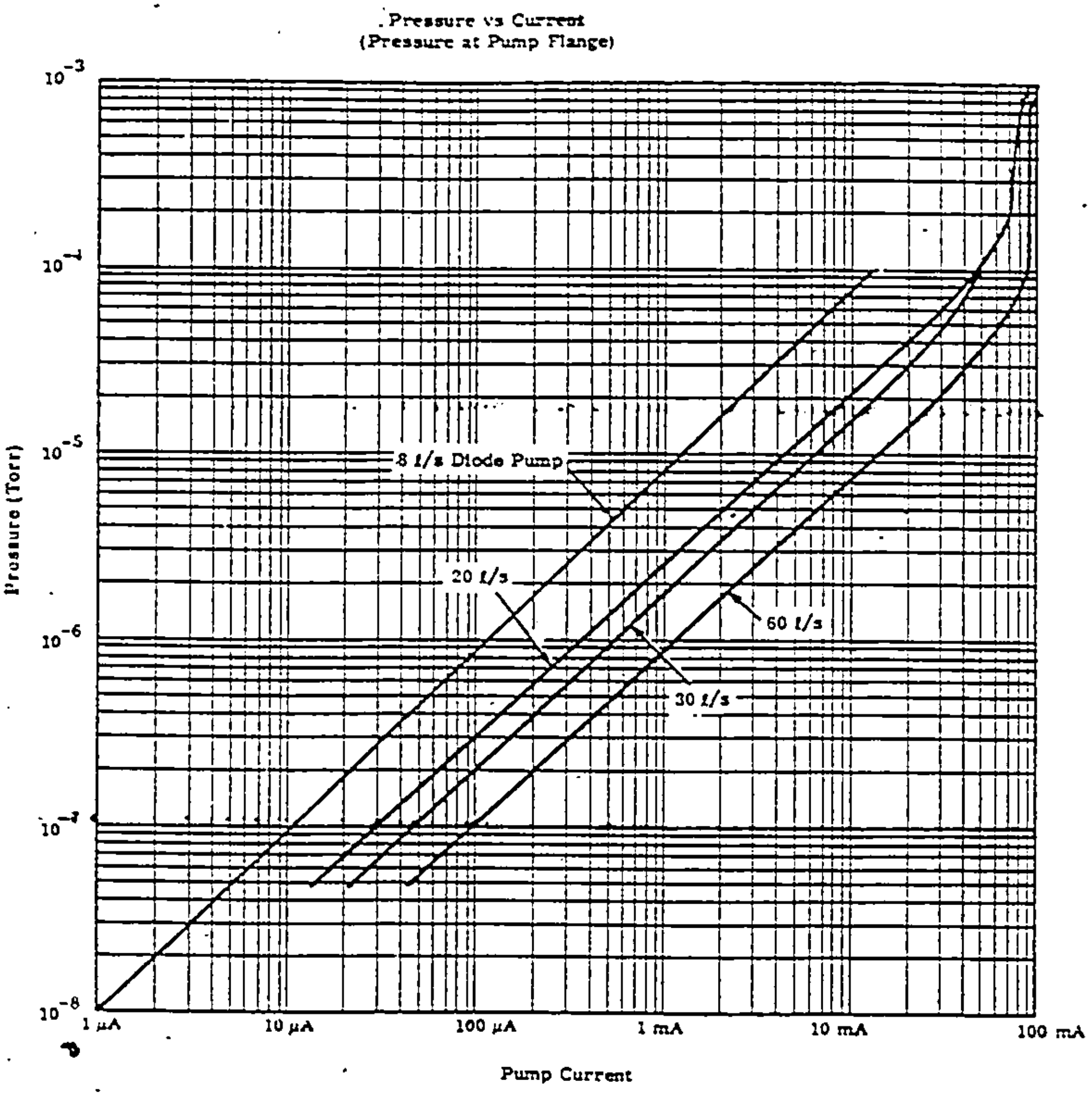

Fig. 2.3. Pressure vs. Varian VacIon pump current.

is comparable to that of an ionization gauge. The ion pump system is automatically protected against pressure rises above 5×10^{-4} Torr when the pump is left unattended. If such a rise should occur, the control unit will be turned off by a pressure relay after a few seconds delay.

A Honeywell Electronic graphic recorder is used for monitoring the vacuum system performance and to record the pressure rise during the flashover. The graph recorder input impedance is 2.5 MΩ in the 100 μV range. The accuracy of the recorder is ± 0.25% or 1 μV, whichever is higher. The recorder is connected to the control unit recorder output (0-100 mV range), which indicates the pressure continuously. The input impedance of any recorder used to monitor the control unit pressure output should be higher than 500 kΩ in order to prevent overloading and to ensure the specified accuracy of the control unit meter and the recorder circuits. The millivolt output vs. pressure graph is given in Fig. 2.4.

A bakeable (up to 250°C) thermocouple vacuum gauge (Huntington ® TCT 531W) is used to measure the pressure up to 10^{-3} Torr. A hot cathode ionization gauge of Bayard-Alpert type (Huntington ® series) with a burnout-resistant thoria-coated iridium filament is used to measure the pressure in the range 10^{-3} to 10^{-10} Torr. The complete system including the breakdown chambers containing the solid insulator is baked at about 200°C. The residual pressure on the vacuum system is less than 10^{-8} Torr.

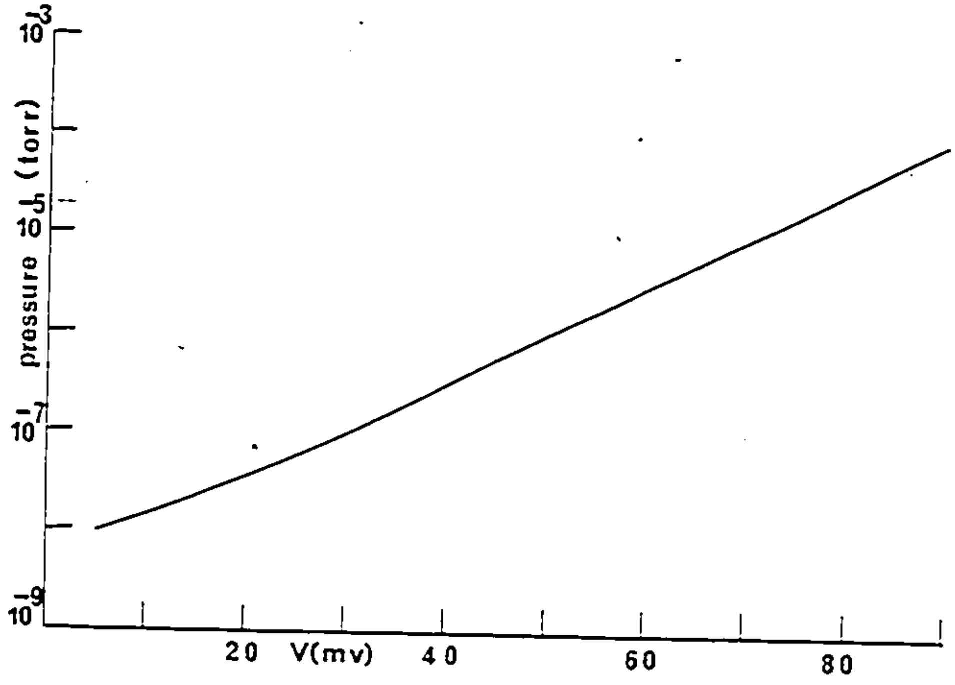

Fig. 2.4. Pressure vs. millivolt output.

2.4 Electric Circuit Arrangement and Flashover Measurement

Two Brandenburg generators capable of 100 kV DC (Type MR. 100 / R, Model 908 R) and one 30 kV DC Brandenburg generator (Alpha Series II) are used to supply the DC voltage. The power supply is set to cut-off as soon as the current value reaches 1 mA. The DC power supply unit is capable of polarity reversal and is continuously variable in the range 0 - 100 kV. The power supply is stable (< 0.5% variation) against 10% variation of the main voltage and has a maximum ripple of less than 0.15% at the full load current of 1 mA at 100 kV. The applied DC voltage to the insulator gap is measured via a resistive potential divider (Fig. 2.7) made of high stability carbon resistors (10^9 Ω ± 1 %) using a digital voltmeter (reading accuracy ± 0.05 %) connected across the low voltage section of the divider (10^4 Ω ± 1 %). The alternating voltage is obtained from a single phase transformer (8 kVA) continuously variable in the range 0 - 50 kV (RMS, frequency 60 Hz). The standard lightning impulse of 1.2 / 50 μS is obtained from a single stage impulse generator (Fig. 2.5) capable of 75 kV with 75 J of stored energy. The output wave form is shown in Fig. 2.6. The AC and impulse voltages are measured via a capacitive potential divider (10^{-9}F ± 0.1 %) using a calibrated oscilloscope connected across the low voltage arm of the divider (4.92 μF ± 0.1%). A Tektronix 549 storage oscilloscope with 1A1 dual trace plug-in unit

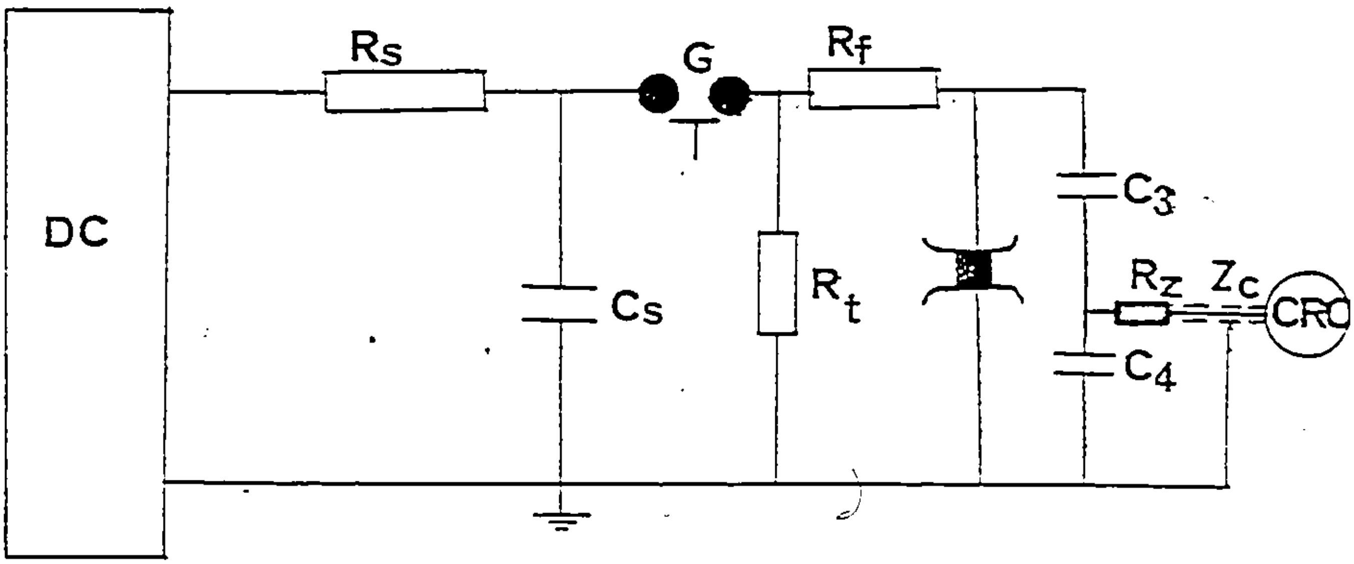

Fig. 2.5. Circuit arrangement of single stage impulse generator. DC - charging unit, 100 kV DC generator; R_s - charging resistance, 10 MΩ; C_s - impulse generator capacitance, 0.015 μF; R_f, 180 Ω; R_t, 5.6 kΩ; C_3/C_4 capacitance divider, C_3 = 1 nF; C_4 = 4.92 μF; R_z = Z_c = 58Ω cable impedance. G-Spark Gap. The capacitor C_s is charged via the charging resistance R_s to the required direct voltage and then discharged by triggering of the spark Gap G.

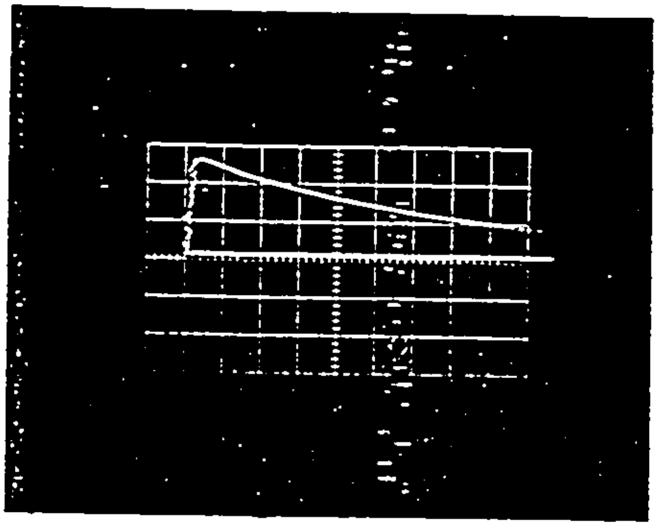

(a) 1.2/50 μs impulse wave. Horizontal scale 10 μs/div.; vertical scale 2V/div. (1 volt = 4.92 kV).

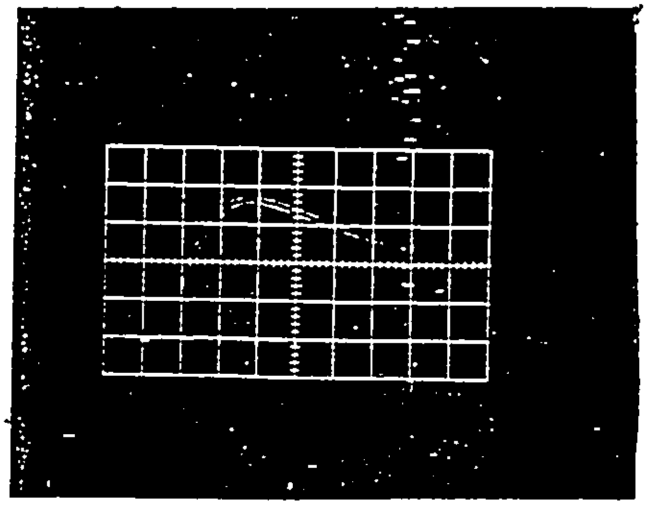

(b) 50/200 μs impulse wave. Horizontal scale 20 μs/div.; vertical scale 2V/div. (1 volt = 4.92 kV).

Fig. 2.6. Output waveform of the single stage impulse generator. (Waveform is measured across the low voltage arm of the capacitive divider).

is used. The oscilloscopes and the digital voltmeter are protected by connecting zener diodes and a spark gap (75 volt) across it. The prebreakdown current flowing across the surface of the solid insulator is measured when DC voltage is applied to the gap by monitoring the voltage drop across a resistance R_5 (100 kΩ) in series with the gap. Prebreakdown AC conduction currents are monitored after cancellation of the capacitive currents. For DC flashover measurements R_3 = 12 kΩ; C_2 and R_4 are removed. For AC flashover measurements R_4 = 12 kΩ; R_1, R_2, R_3, C_1 and C_2 are removed.

The electric circuit for applying a DC pre-stress to the solid insulator and then measuring the DC + AC flashover is shown in Fig. 2.7. A pre-determined DC voltage stress is first applied to the gap and then a DC (same or opposite polarity), AC by itself (after removal of the pre-stress) and an AC voltage superimposed on to the DC pre-stress voltage are gradually increased until a breakdown of the gap is observed. The flashover voltage is defined as the maximum voltage that the gap withstands just before it collapses to a very low level. When a combination of a DC and AC voltage

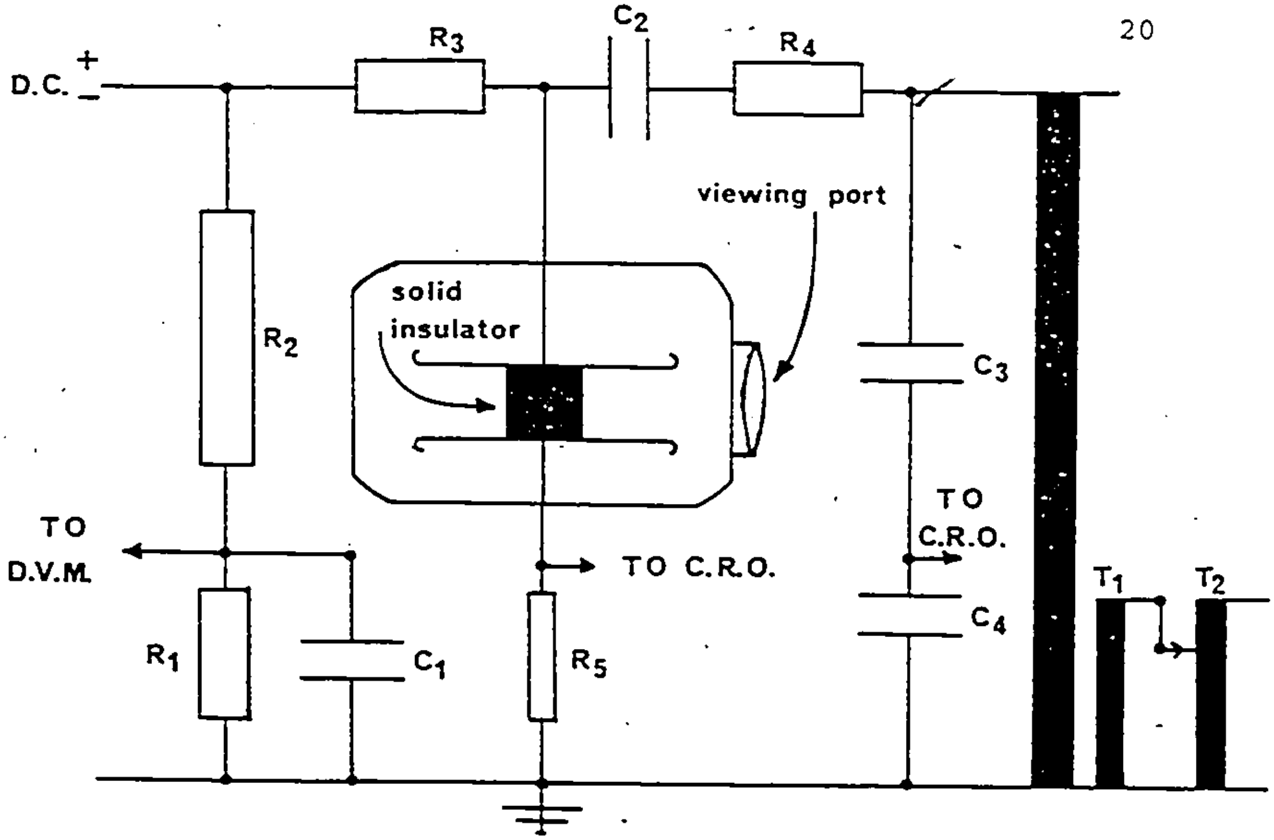

Fig. 2.7 Electrical circuit arrangement for applying DC, AC, DC + AC and DC + Impulse. T_1, HV transformer; T_2, autotransformer; $R_1 = 10$ kΩ; $R_2 = 10^9$ Ω; $R_3 = 1$ MΩ; $R_4 = 3$ kΩ; $R_5 = 100$ kΩ; $C_1 = 10$ nF; $C_2 = 5$ nF; $C_3 = 1$ nF; $C_4 = 4.92$ μF. For DC measurements $R_3 = 12$ kΩ; C_2 and R_4 are removed. For AC measurements $R_4 = 12$ kΩ; R_1, R_2, R_3, C_1 and C_2 are removed. Chamber capacitance is about 6 pF.

is used the flashover voltage is the total sum of the DC (which is also the pre-stress level) and the peak of the AC voltages. For combined DC + Impulse flashover studies, an impulse generator is used in the place of T_1 and T_2, and R_4 is removed. In this case the flashover voltage is the total sum of the DC and the peak of the impulse voltage. The onset of the breakdown is determined by one of three methods: 1) the onset of light emission from the gap which is monitored through a viewing port. 2) A sudden large rise in the gap pressure, and 3) the collapse of the voltage across the insulating gap. All three methods gave essentially identical results.

2.5 Experimental Procedure

The vacuum system is pumped from atmospheric pressure to 5×10^{-3} Torr using the 1.7 ℓ/s rotary pump for two hours. Then valves V_1 and V_2 (Fig. 2.1) are closed. The sorption pump is employed as the roughing pump to obtain the base pressure for the ion pump. Liquid nitrogen is used as a coolant to cool the sorption pump. The system pressure obtained after 2-3 hours of sorption pumping is about 5×10^{-6} Torr. Occasionally the sorption pump saturates and it is necessary to close the vacuum value V_3, remove the liquid nitrogen, start the rotary pump again and open V_1 and V_2. The sorption pump sieve is heated up to about 200°C by means of a hot-air blower for about 20 minutes. The evacuation procedure is again repeated after the sorption pump has cooled down to room temperature.

The vacuum system and the breakdown chamber containing the solid insulators have been baked at a temperature from 100°C (plexiglass) to 200°C (glass ceramic, Teflon, sapphire, Pyrex glass and quartz) by using a 2.5 kW heater and is continuously evacuated with the sorption pump. The temperature at different locations of the baked system is measured using alumel-chromel (40 μV/°C) thermocouples. A temperature controller (ETHER, 'Digi') is used for control. After 8 hours of baking at an elevated temperature (100-200°C) the system is cooled down to the room temperature. The pressure obtained is 5×10^{-6}Torr. The $8\ \ell/s$ diode ion pump is next switched on and the vacuum valve V_3 is closed. After 12 hours of pumping with the ion pump, the system pressure obtained is 10^{-7} to 5×10^{-8} Torr. The vacuum system is again thoroughly degassed at the elevated temperature (100-200°C) for two days. The residual gas pressure obtained after coo~~ling~~ the system to room temperature (~ 27 ° C) is less than 10^{-8} torr. The surface flashover is measured at ~ 27° C and the background pressure of less than 10^{-8} torr is maintained throughout the experiments by the continuous pumping with the ion pump.

For pre-breakdown current measurement, great care is taken not to spark the gap and the first breakdown is therefore estimated. The pre-breakdown current is measured using a digital voltmeter (DVM) connected across the current measuring resistance R_5 in Fig. 2.7 and also using a storage oscilloscope (Tektronix 549). As the applied voltage is gradually increased from zero the current starts to flow at a particular voltage which depends on the thickness of the insulator. In general, for insulators of small thickness (<2 mm), the pre-breakdown current is initially steady at a fixed voltage and starts to fluctuate over a large range as the applied voltage is increased. The measurement of pre-breakdown DC and AC current is discussed in Chapter 3. For flashover measurements, each new specimen is conditioned by applying a direct or alternating voltage for a period of 5 to 10 minutes at 75 percent of the anticipated flashover voltage. After this the voltage is raised in 1 kV increments until the occurrence of flashover. The flashover voltage is defined as the maximum voltage that the gap withstands just before it collapses to a very low level. Usually after 3-5 flashovers the surface flashover reached a constant value (within ± 5 %) fluctuation) and the subsequent 5 flashover values are determined and the average value is taken as the flashover value of the specimen. The DC, AC and impulse flashover voltages are measured as discussed in Section 2.4.

CHAPTER III

SURFACE FLASHOVER OF SOLID INSULATORS IN VACUUM

3.1. Pre-Breakdown Phenomena

When the voltage applied across an insulator is gradually increased from zero in a vacuum several events occur. The possible events are the emission of electrons from the cathode triple junction, flow of pre-breakdown current which can be either in a steady or pulsed form and the accumulation of charge on the insulator surface [1-9]. Measurements of currents in the region below the breakdown voltage are important for proper understanding of the flashover mechanisms of solid insulators in vacuum. It also helps to know the origin of the charged particles which are essential for the initiation of a breakdown.

Gleichauf [1] measured pre-breakdown current in the case of a 22.8 mm thickness quartz insulator placed between copper electrodes in vacuum ($\approx 10^{-5}$ Torr) by detecting X-ray quanta with a Geiger Muller counter placed outside the vacuum chamber. He observed two current components of the pre-discharge, the stationary component and the micro discharge [1]. His studies showed no critical pre-breakdown current. For comparison of the pre-breakdown measurement results with the field emission, Gleichauf [1] calculated the maximum field at the cathode using a Fowler-Nordheim (FN) plot. His calculations showed that the maximum field at the cathode was 435 times the average applied field between the electrodes.

Boersch et al [7] reported that when the voltage across an insulator between two electrodes was increased, surface discharges occurred before the breakdown of the insulator. They found that low current discharges involving light phenomena occurred below the flashover voltage and at a fixed voltage the frequency decreased with time. These current discharges were termed as micro-discharges. In addition to the current discharges, they observed a very slowly fluctuating or sometimes steady current below the breakdown voltage. Brainard and Jenson [37] have also reported emission current measurement in the case of an alumina ceramic cylindrical insulator using DC voltage. The FN plot of the data obtained indicated that the field enhancement factor at the cathode was 900 when the voltage applied to the 1.2 cm gap distance was above 50 kV.

The pre-discharge phenomena of solid insulators in vacuum preceding an AC surface flashover has been reported [38-41]. Hanna et al [39] studied the pre-discharge phenomena dependence on the insulator height. The pre-discharge measurements obtained by the authors [39] in the case of 2 mm thickness TFE (Teflon) appeared to be following the Fowler-

Nordheim law. The calculated field intensification β is much higher with insulator when compared with the β obtained in vacuum without the insulator. Lee et al. [40] reported that the measured pre-discharge AC current for 30, 45 and 60° plexiglass frustra followed the Fowler-Nordheim behaviour. They also reported that the pre-discharge current for a cylindrical insulator did not follow F-N behaviour.

In the present study the pre-breakdown behaviour of cylindrical and conical insulators has been investigated. The Fowler-Nordheim behaviour of 1 mm thickness Macor glass ceramic and 1.96 mm quartz show a stepwise decrease of field intensification. For insulators of greater thickness (>2 mm) the pre-breakdown current does not follow FN behaviour. The fluctuation in the pre-breakdown current is much higher with increasing thickness of the insulator above 2 mm.

3.1.1 Pre-breakdown DC Current (Cylindrical Insulator)

Figure 3.1 (curve a), Fig. 3.2 (curve a) and Fig. 3.3 show the pre-breakdown current flowing across the surface of a glass-ceramic and quartz as a function of the applied voltage without a pre-stress. Typically for glass-ceramic, the current is 5×10^{-10} A at an applied voltage of about 60% of the first DC breakdown voltage (i.e., 12 kV). Great care is taken not to spark the gap at this stage of the experiment and the first flashover voltage is therefore estimated. For the glass-ceramic (1 mm) and quartz (1.96 mm) insulators the pre-breakdown current is generally steady at low applied voltage. For the quartz insulator which has a longer length (3.5 mm) the pre-breakdown current is initially steady at a fixed applied voltage (e.g., 0.5 nA at 35 kV; Fig. 3.2, curve a). As the voltage is increased, however, the pre-breakdown current starts to fluctuate over a large range. Typically for quartz (3.5 mm) the current varies from 8 to 11 nA at a fixed applied voltage of 42 kV (Fig. 3.2, curve a). In all insulator materials used the current increases rapidly with increasing voltage after the applied voltage exceeds a threshold level of about 70-90% of the first breakdown level (e.g., 17 kV for 1 mm glass-ceramic, Fig. 3.1). As the applied voltage approaches the breakdown level pre-discharge pulses are found to flow in the gap. The frequency of appearance of the pre-discharge pulses decreases rapidly the longer the voltage is applied to the specimen. Typically at 17 kV (1 mm glass-ceramic) the interval between the pulses lies within the range 5-10s. After some time (5-10 minutes) the gap is conditioned and the pre-discharge pulses completely disappear at the same applied voltage. The amplitude of the pre-breakdown pulses increases with increasing voltage. Typically for glass-ceramic (1 mm), the amplitude increases from 20 to 25 μA with increasing applied voltage from 17 to 18 kV. It

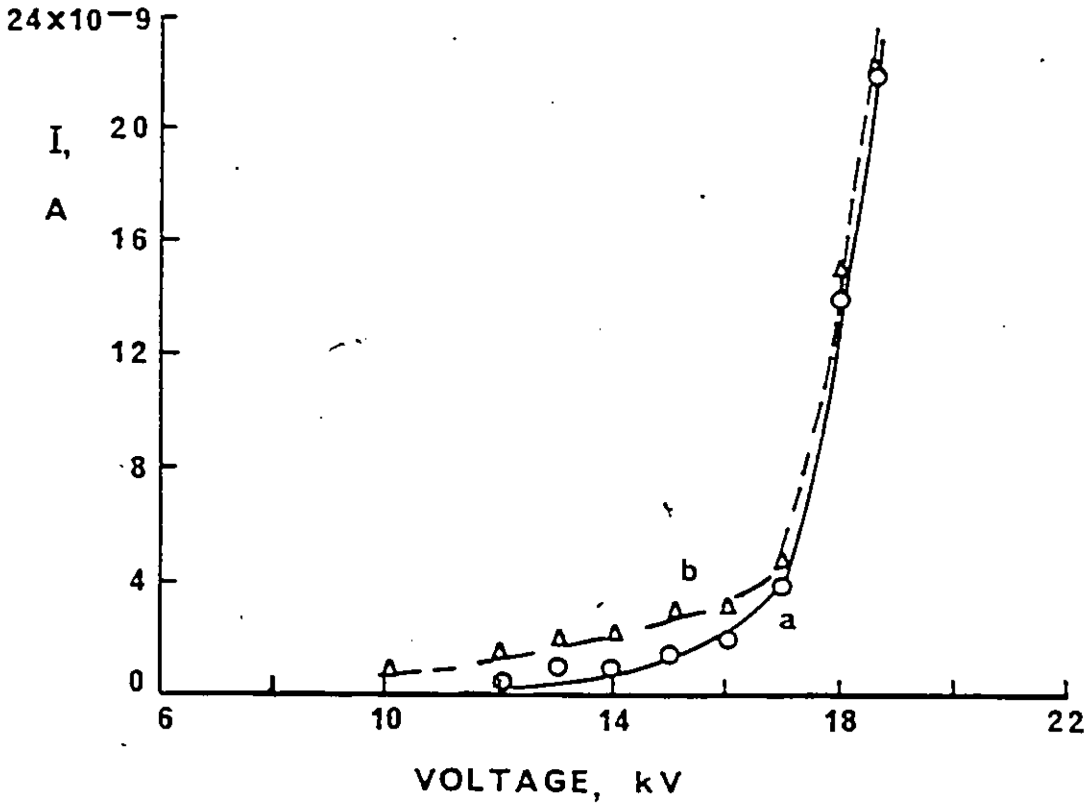

Fig. 3.1. DC Prebreakdown current vs. DC applied voltage in 1 mm thick Macor glass-ceramic. Curve a: no pre-stress applied; curve b: 13 kV opposing pre-stress applied for 300s and then removed. First flashover voltage = 19 kV.

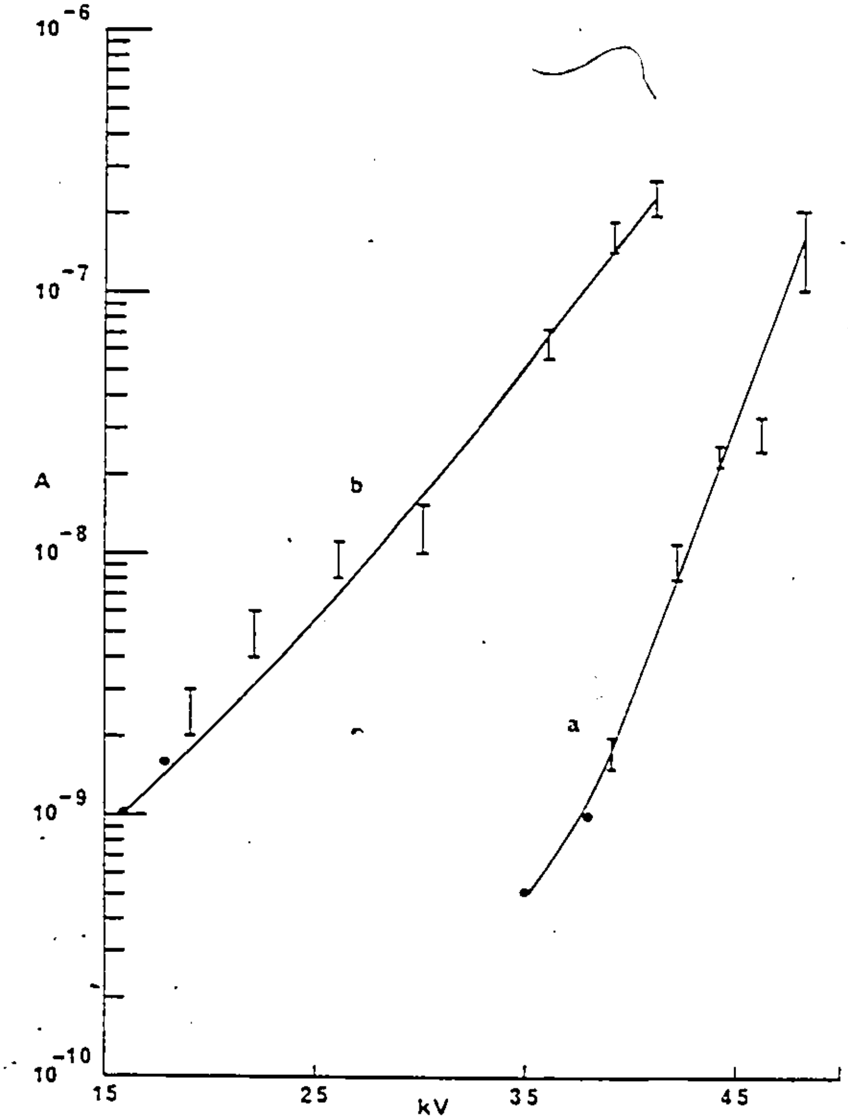

Fig. 3.2. DC prebreakdown current vs. DC applied voltage in 3.5 mm thick Quartz. Curve a: no pre-stress applied; curve b: 32 kV opposing pre-stress applied for 300s and then removed. First flashover Voltage = 48 kV. Bar(I) represent fluctuations in measurement.

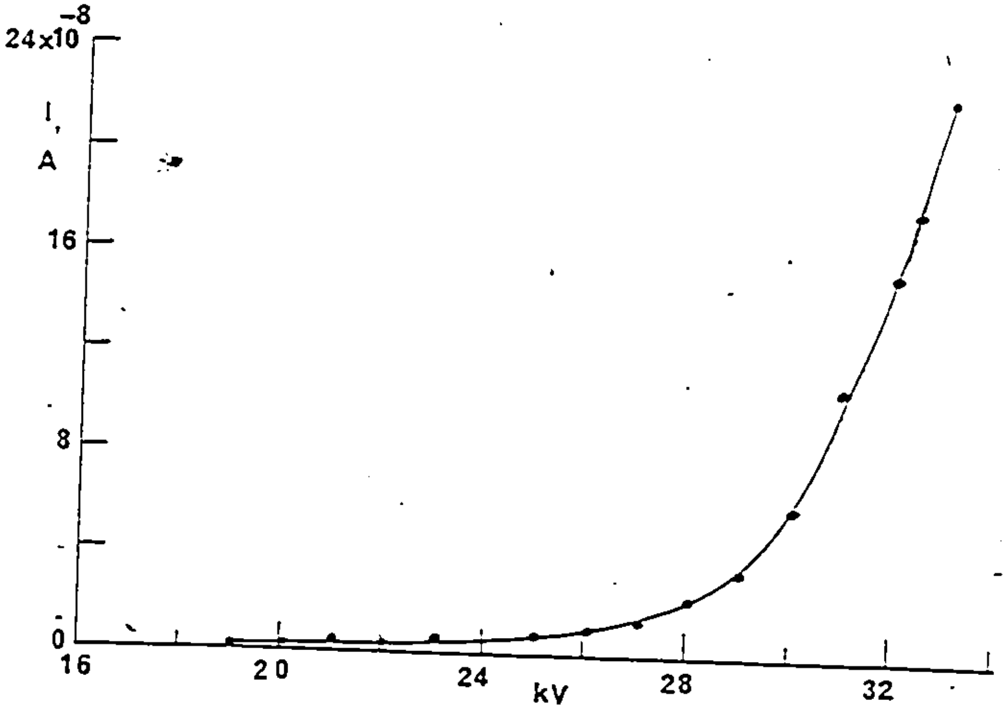

Fig. 3.3. DC Prebreakdown current vs. DC applied voltage in 1.96 mm thick Quartz.

is found that a gas desorption is associated with the onset of the pre-breakdown current across the surface of the solid insulator. Typically in glass-ceramic when a current of (13-15) nA is flowing in the gap at 18 kV a slight increase in the pressure from $< 10^{-8}$ Torr to $(3-4) \times 10^{-8}$ Torr is observed. In the current range (26-50) nA the pressure increases to $(3-4) \times 10^{-7}$ Torr. The current drops quickly to (7-8) nA and the gas pressure decreases to its original value ($<10^{-8}$) Torr by the continuous pumping of the ion pump. Just before the onset of the flashover the current in the gap containing glass-ceramic fluctuates continuously between 22 to 35 nA. At the onset of the flashover the pressure increases to about $(9-10) \times 10^{-7}$ Torr. Generally similar increases, to those found in the present work, in the amplitude of the pre-breakdown pulses and gas pressures with increasing applied voltage were reported by Borovik and Batrakov [3] in plexiglass, glass, quartz and other materials. These results give an indication of the mechanism responsible for the flashover whereby the current grows in the desorbed gases [24,30]. Both the pre-breakdown current and desorbed gases are simultaneously observed in the present work. In general the presence of gases near the insulator surface during the breakdown process of solid insulators in vacuum had been suggested by several authors [24,30,42-47].

It should be mentioned that the ionic conduction through the bulk of the insulator is not thought to be an important contribution to the total current at room temperature. Furthermore, it was noted by Sillars [48] that when the electrodes are not coated with the solid dielectric, such as in the present case, the ions may accumulate without being discharged into the electrodes due to lack of intimate contacts with the solid dielectric.

Figures 3.1 (curve b) and 3.2 (curve b) show the DC pre-breakdown current as a function of DC applied voltage after the removal of an opposing pre-stress which has been applied for 300s at a level of about 66% of the first breakdown voltage. It will be observed that larger currents flow at the same applied voltage when an opposing pre-stress has been applied to the gap. The reason for the higher current flowing in the gap after applying an opposing pre-stress is attributed to the increased fields at both the cathode and the anode junctions from the residual charges accumulated on the surface of the solid insulator. The measured pre-breakdown current in the case of glass-ceramic (1 mm) and quartz (1.96 mm) is analyzed using a Fowler-Nordheim [49] plot and discussed in section 3.1.2.

3.1.2 Analysis of Pre-breakdown Current

The current flowing in the vacuum gap with the solid insulator in the region before breakdown is analyzed using the Fowler-Nordheim theory of field emission [49] as in the case of an ordinary vacuum gap without the solid insulator [36,38]. The F-N equation is

$$\frac{I}{V^2} = \frac{1.54 \times 10^{-6}\ A\beta^2}{\phi\ d^2 t^2(y)} \exp\left\{\frac{-6.83\times10^7\ \phi^{3/2}\ d v(y)}{V\beta}\right\} \tag{3.1}$$

where I is the current in A, V is the applied voltage in the gap in V, A is the effective emitting area of the protrusions in cm^2, ϕ is the work function of the emitting surface which is assumed to be 4.4 eV in the case of stainless steel electrode and d is the electrode separation in cm. t(y) and v(y) are slowly varying functions of the enhanced electric field. β is the field enhancement factor. In the case of a vacuum gap without the insulator, the field enhancement β is due only to the roughness of the electrode surface. A semi-logarithmic plot of IV^{-2} against V^{-1} should give a straight line whose slope is given by

$$K = -6.83 \times 10^7\ \phi^{3/2}\ ds(y)/\beta \tag{3.2}$$

where $s(y) = v(y) - \frac{1}{2} y v'(y)$. v' is the first derivative of v. The value of s(y) can be assumed as unity since it has a fairly constant value close to unity within a few percent [references cited in ref. 38].

Figures 3.4 and 3.5 show the Fowler-Nordeheim plot of the measured pre-breakdown current in the case of 1 mm thickness Macor glass ceramic and 1.96 mm thickness quartz

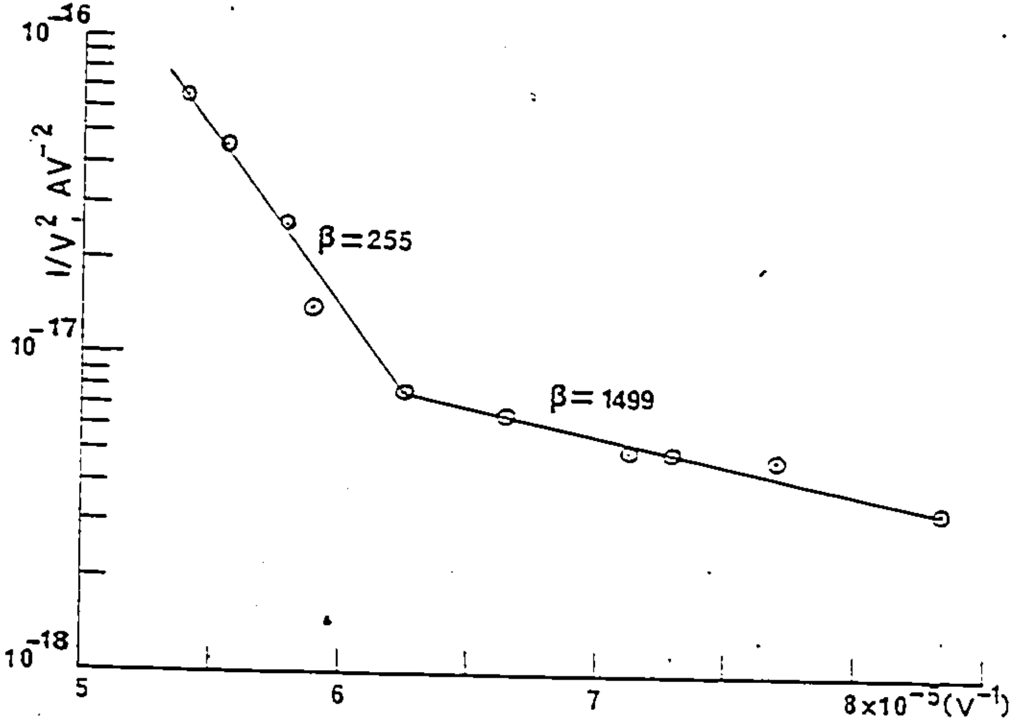

Fig. 3.4. IV^{-2} vs. V^{-1} (FN plot) for 1 mm thick Macor glass-ceramic. Stainless steel electrode.

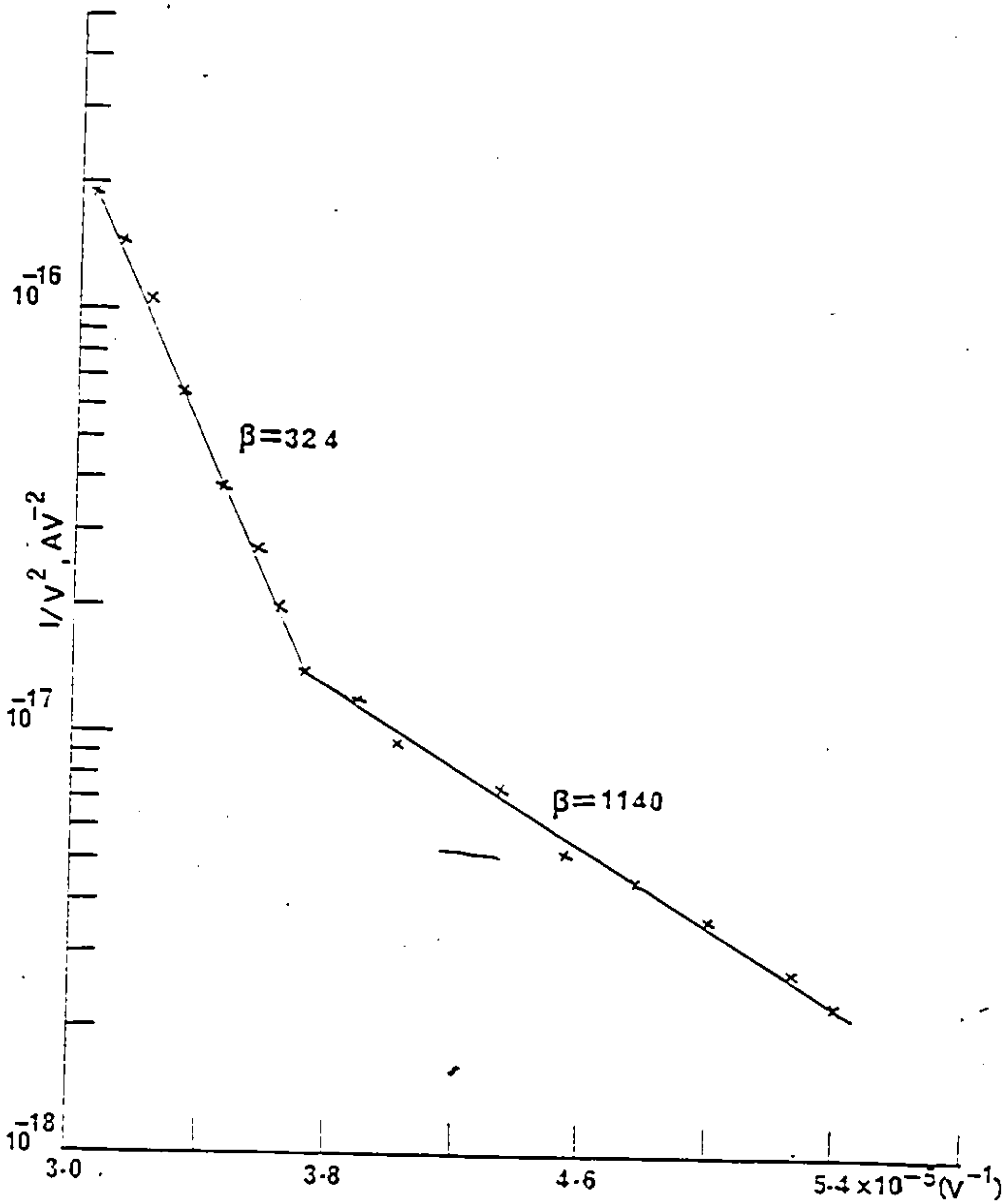

Fig. 3.5. IV^{-2} vs. V^{-1} (FN plot) for 1.96 mm thick Quartz. Stainless steel electrode.

glass respectively. The maximum field at the cathode can be written as

$$E_{max} \text{ at cathode} = (\beta_1 \beta_2) \frac{V}{d} \qquad (3.3)$$

where V is the applied voltage to the solid insulator and d is the electrode separation. In the case of cylindrical insulators, the insulator thickness is equal to the electrode separation. The factor β_1 mainly determines the influence of the solid insulator and β_2 takes into account the roughness of the cathode electrode surface [1].

As can be seen from Figures 3.4 and 3.5, the FN plot with solid insulators show a step decrease of the β ($\beta = \beta_1 \beta_2$) in the low V^{-1} region (higher values of V). The value of $\beta_1 \beta_2$ calculated from Fig. 3.4 in the case of 1 mm glass ceramic is 255. If we assume that this field enhancement is the product of the dielectric constant ε_2 (5.8 for glass-ceramic) and the roughness of the cathode surface, then $\beta_1 = 5.8$ and $\beta_2 = 44$. In general the field enhancement of electrodes in an ordinary vacuum gap without the solid insulator is in the range 100 - 400 [36,38] and much depends on the electrode material, electrode separation and surface finish. The obtained β value indicates that the cathode field junction is not enhanced by ε_2 times.

The obtained β value in the case of 1.96 mm thickness quartz is 324. If we assume $\beta_1 = 3.8$, the dielectric constant of quartz glass, β_2 is about 85 which is higher than the β_2 value obtained in the case of 1 mm glass ceramic (β_2 = 44). The calculated β values show that the field enhancement factor is lower at the high voltage region even though the current value is higher. This indicates that the increase in the pre-breakdown current is not proportional to the applied voltage. The results also suggest that the pre-breakdown currents observed are not to be totally due to field emission currents.

3.1.3 Pre-breakdown AC Current (Cylindrical Insulator)

The AC pre-breakdown current is measured after cancellation of the capacitive current using standard bridge techniques [50] as shown in Fig. 3.6. The gap capacitance with the insulator and the pre-breakdown current measuring resistance (R_c) forms the two arms of the bridge. The high voltage capacitor (C_1) and the variable resistor (R_2) with the parallel variable capacitor (C_2) forms the remaining two arms of the bridge (Fig. 3.6). The voltage across the two resistors are connected to the differential amplifier of the CRO to determine the balance of the bridge. The conduction component of the AC current flowing across the solid insulator surface is higher than the DC current at the same applied voltage. Typically for glass-ceramic (1 mm thick) an AC peak peak current of 1.95 μA is obtained at 13 kV (peak AC without pre-stress) compared to 1 nA for

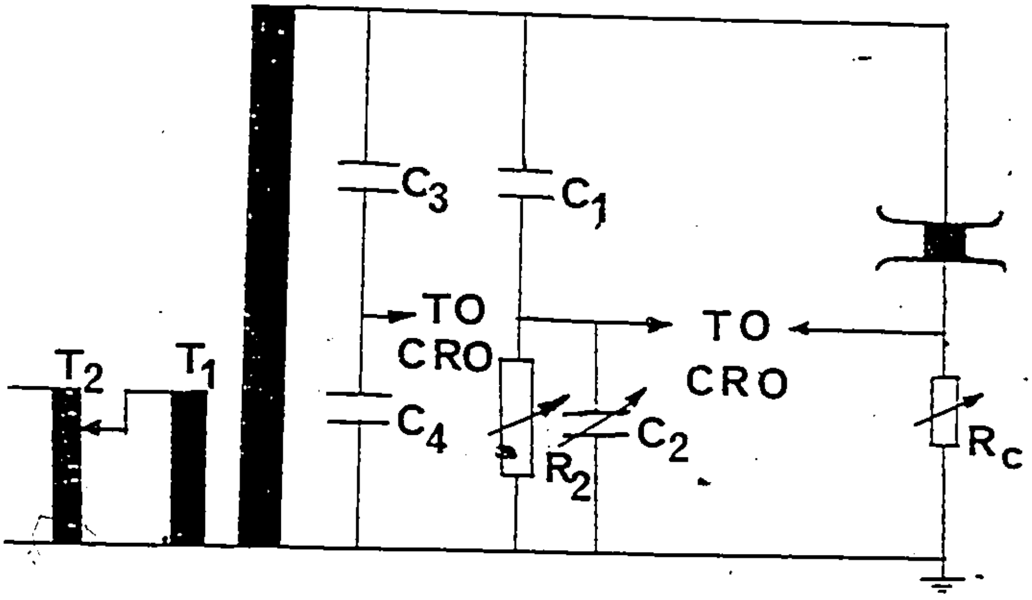

Fig. 3.6. Bridge network with measuring circuit for AC prebreakdown current measurement. T_1, HV transformer; T_2, autotransformer; C_3 = 1 nF; C_4 = 4.92 μF. C_1, C_2 and R_2, balancing arm, C_1 = HV capacitor, 625 PF, R_2 = variable resistor box, 10Ω - 1 MΩ, C_2 = variable capacitor, 0.01 μF - 1000 PF, R_c = current measuring resistance, 10 or 100 kΩ.

the pre-breakdown AC current starts to flow across the surface at a much lower applied voltage. The higher AC pre-breakdown current may be due to accumulation of surface charges in the preceding half cycle which effectively acts as an opposing pre-stress [28].

3.1.4 Pre-breakdown DC Current (Conical Insulator)

Figure 3.7 shows the pre-breakdown current flowing across the surface of a 2 mm thickness, conical insulator ($\theta = 45°$) as a function of the applied voltage. In Fig. 3.7, curve 1 refers to the pre-breakdown current measurement with the base of the cone at the anode (negative angle Fig. 3.8) and curve 2 corresponds to the measurement with the base of the cone at the cathode (positive angle, Fig. 3.8). The polarity of the applied voltage is reversed instead of changing the position of the conical specimen between the electrodes in order to have a positive and negative angle conical insulator. This is done in order not to alter the vacuum conditions and it assumes that the two planar stainless steel electrodes are identical. Great care is taken in fabricating the electrodes to be as closely similar in shape and surface finish as possible. The electrodes are also aligned to be parallel by producing flat surfaces at both ends of the insulator cone. The pre-breakdown currents are measured after both electrodes have been conditioned using repeated sparkings (10 times) with positive and negative DC voltages.

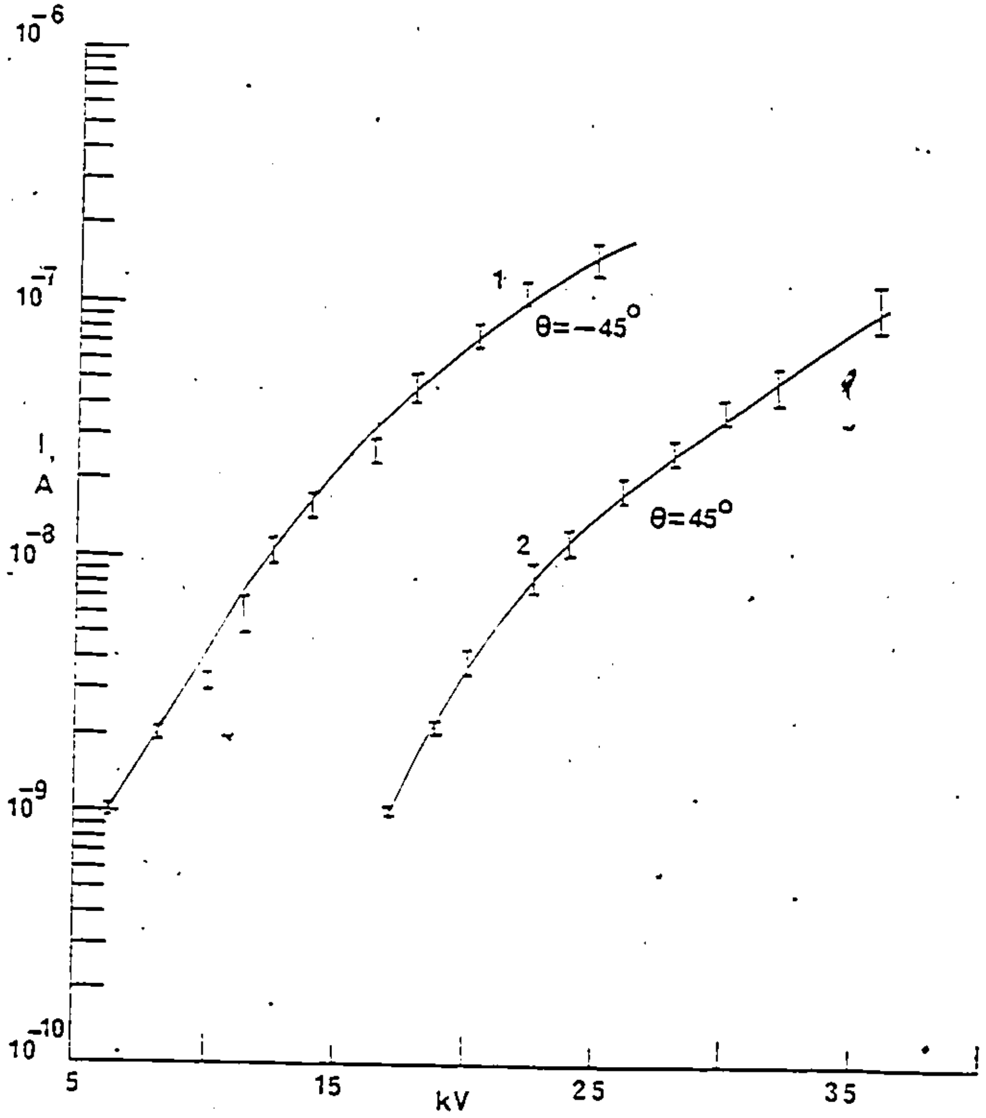

Fig. 3.7. DC prebreakdown current vs. DC applied voltage in 2 mm thick conical Macor glass-ceramic insulator. Curve 1, θ = −45°; curve 2, θ = 45°; θ = cone angle, which the insulator surface makes with the applied field.

For the negative angle insulator the pre-breakdown current starts to flow at a lower applied voltage (curve 1, Fig. 3.7). At a fixed applied voltage, the pre-breakdown current in the case of a negative angle conical insulator is much higher than that of the positive angle cone insulator. For example, when the applied voltage is 20 kV, the pre-breakdown current in the case of negative angle cone is 75 nA and the corresponding positive angle cone pre-breakdown current is 4 nA. Both in the case of positive and negative angle cones, the current starts to fluctuate over a large range as the applied voltage is increased. Moreover, in both cases the current increases rapidly with increasing voltage after the applied voltage exceeds a certain level.

3.2 Surface Flashover of Cylindrical and Conical Insulators

The surface flashover of solid insulators in vacuum depends on the shape of the insulator, the material of the insulator and the type of the applied voltage whether DC, AC or pulsed [13,51]. The pulse flashover voltage is generally higher for cone insulators than for right angle cylinders of the same thickness, and depends on the angle θ that the surface makes with the applied field as well as the voltage polarity with respect to the base of the cone [9-11].

A higher withstand voltage was generally obtained when the base of the cone was made the cathode. The pulse flashover voltage in turn depends on the width of the pulse [9-11 , 53]. From the application point of view the flashover performance of different insulator materials is important.

The surface flashover performance of cylindrical and conical insulators in ultra-high vacuum is investigated here using direct current (DC), alternating current (AC at 60 Hz), and standard lightning impulse of 1.2/50 μs. The cylindrical and conical shape insulators are shown in Fig. 3.8, where θ is defined as the angle between the cone surface and the applied field. The term positive angle is referred to the electrical connection when the narrow end of the cone is made positive and vice versa for the negative angle when the narrow end is made the cathode. The treatments of the electrode and the solid insulator are discussed in Chapter 2 (section 2.1). Standard conditioning as discussed in Chapter 2 (section 2.5) is applied before taking measurements. The DC, AC and 1.2/50 μs impulse flashover voltages after conditioning are consistent. In general at a fixed thickness of in-

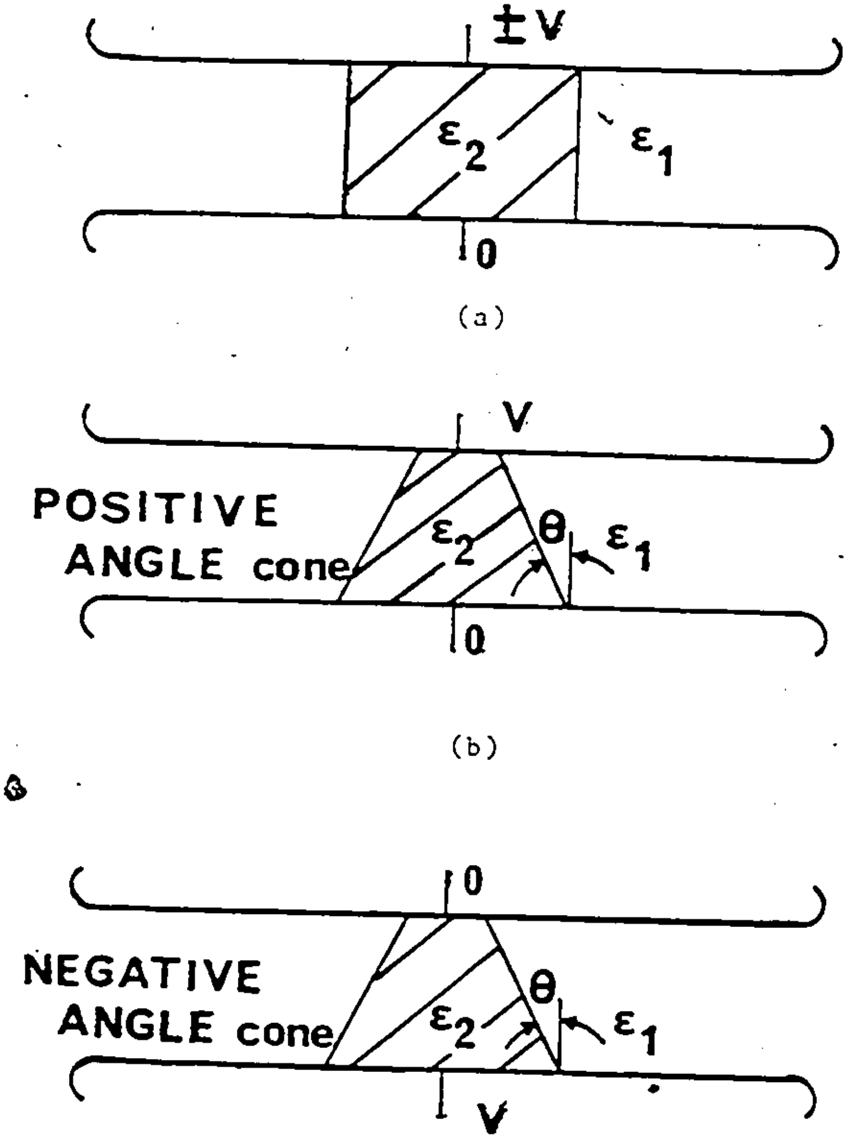

(a)

(b)

(c)

Fig. 3.8 Solid insulators and electrode arrangements. a, cylindircal insulator; b, conical insulator (positive angle); c, conical insulator (negative angle).

sulator, the DC and the impulse flashover voltages are higher than the AC (peak) flashover voltage.

3.2.1 Flashover of Cylindrical Solid Insulators

The DC, 1.2/50 μs impulse and AC (60 Hz) flashover voltages of various insulators with different thickness and diameter are given in Table 3.1. The electrode material used is made of stainless steel. As mentioned in Chapter 2, the onset of the flashover is determined by means of any one of the three methods. Flashover values are measured using DC or Impulse of both positive and negative polarities. In the case of cylindrical insulators the maximum difference between the flashover values using either one of the polarities is within ± 3%. Thus, Table 3.1 gives the DC and impulse flashover value measured using either positive or negative polarity.

The reported measurements using different dielectric constant materials of the same group showed a trend that the flashover voltage were lower in samples of higher dielectric constant [4,5,54]. Kofoid [5] measured the DC flashover voltage of different insulator materials in ceramic group. His results showed lower flashover value with higher dielectric constant. Akahane, et al. [54] ~~also~~ reported lower flashover value with higher dielectric constant in polymer insulators. This is not always the case, however, when considering insulator material belonging to different groups. As can be seen from Table 3.1 and also from the reported flashover measurements of different solid insulator materials in vacuum [12-14], that the dielectric constant of the material alone cannot explain the flashover results obtained. The field enhancement at the cathode triple junction is not entirely due to the presence of voids between the cathode and the solid insulator. If this is the case, then the flashover voltage depends only on the dielectric constant of the material. In practice the electric field at the cathode triple junction gets enhanced due to insulator edge effects [19], asperities on the cathode [20,21], and the charge accumulation on the insulator surface [22-26]. The field enhancement due to surface charge accumulation depends on the secondary electron emission characteristic of the material and not on the dielectric constant. The electron impact energy of the secondary electrons emitted from the surface of the solid insulator is different for different materials [26]. This is one possible reason for the variation in the results shown in Table 3.1.

3.2.2 Flashover Voltage Dependence on Insulator Length

The flashover voltage using DC, AC and 1.2/50 μs impulse increases with increase in length of the insulator (Table

TABLE 3.1

Flashover Voltage and Breakdown Gradient for Different Insulator Materials.
All Insulator Samples are Cylinders, Butt-jointed to the electrodes

Insulator Material	Dielectric Constant at f=1-10kHz ε_2	Thickness in mm	Diameter in mm	Flashover Voltage in kV			Flashover Field in kV/mm		
				DC	Impulse 1.2/50 μs	AC (peak)	DC	Impulse 1.2/50 μs	AC (peak)
Teflon® (Polytetra fluoro-ethylene)	2.1 - 2.2	2.00	7.00	32.0	30.2	25.6	16.00	15.10	12.80
		4.00	7.00	43.5	41.2	34.0	10.87	10.30	8.50
Plexiglass (Polymethyl methacrylate)	3.2	4.00	7.00	48.0	49.0	39.5	12.00	12.25	9.88
Quartz	3.8	1.96	9.30	40.0	38.0	29.0	20.40	19.38	14.80
		3.48	9.30	54.5	53.0	44.8	15.66	15.22	12.87
		3.50	11.80	53.0	50.2	43.5	15.14	14.34	12.42
Pyrex® glass	4.6	4.00	6.35	46.0	44.4	39.5	11.50	11.10	9.88
Macor® glass Ceramic	5.8	0.50	7.00	15.8	14.2	10.4	31.60	28.40	20.80
		1.00	~7.00	22.5	20.2	17.0	22.50	20.20	17.00
		1.50	7.00	29.0	26.2	24.0	19.33	17.47	16.00
		2.00	7.00	33.2	32.4	28.5	16.60	16.20	14.25
		3.00	7.00	45.0	43.5	35.5	15.00	14.50	11.83
		4.00	7.00	50.5	50.0	41.0	12.62	12.50	10.25
		6.00	7.00	64.8	64.4	53.0	10.76	10.73	8.83
		8.00	7.00	73.0	72.5	61.0	9.12	9.06	7.62
Sapphire	12.0	3.10	12.55	28.0	26.0	22.5	9.03	8.38	7.26

® Registered Trade Mark

3.1). The flashover voltage however does not increase in a linear manner with length of the insulator and also depends on the type of applied voltage. In Fig. 3.9 the DC, AC and impulse flashover voltage of Macor glass ceramic insulator is plotted against the length of the insulator. The rate of increase of flashover voltage with increasing the specimen length is almost the same for DC and impulse but is lower for AC voltages.

3.2.3 Flashover of Conical Insulators

The conical insulators used for the investigation are made of Macor-glass ceramic ($\varepsilon_2 = 5.8$). Specimens having $\theta = 5°$, 15°, 30°, 45° and 55° and a fixed thickness of 2 mm have been used. Flashover voltages are measured using DC, AC and 1.2/50 μs lightning impulse for cones having θ in the range -55° to 55°. The polarity of the applied voltage is reversed instead of changing the position of the conical specimen between the electrodes. The measured flashover voltages are shown in Fig. 3.10. It will be observed that the DC and impulse flashover are at about the same level throughout the range of θ used. Both the DC and the impulse flashover voltages, exhibit the dependence on the positive value of θ previously observed. Typically when θ is 45° the DC flashover at 42.2 kV is about 27% higher than that of 33.2 kV at θ = 0. The AC flashover does not exhibit a dependence on θ and similarly the dependence on θ is absent

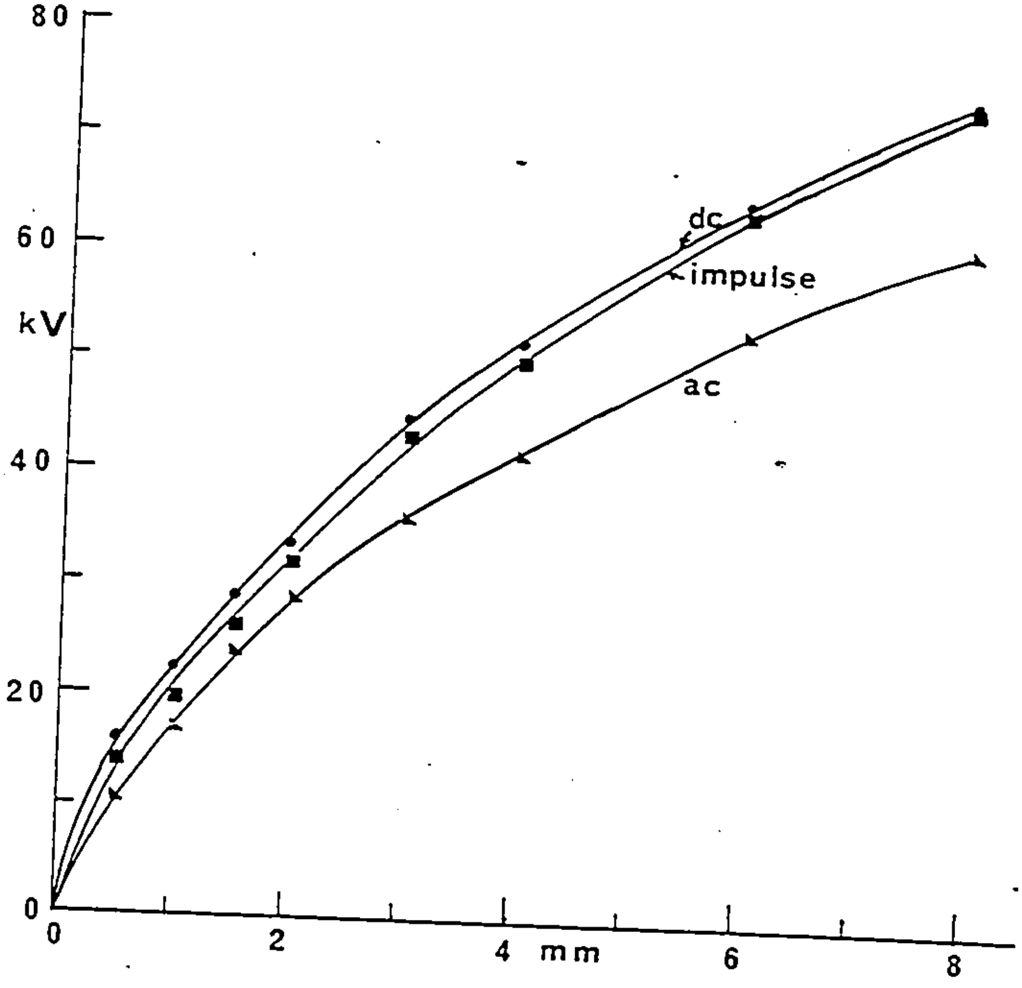

Fig. 3.9. Flashover voltage of Macor glass- ceramic as a function of length (thickness) of the insulator (mm). ● DC; ■ 1.2/50 μs lightning impulse; ▲ AC.

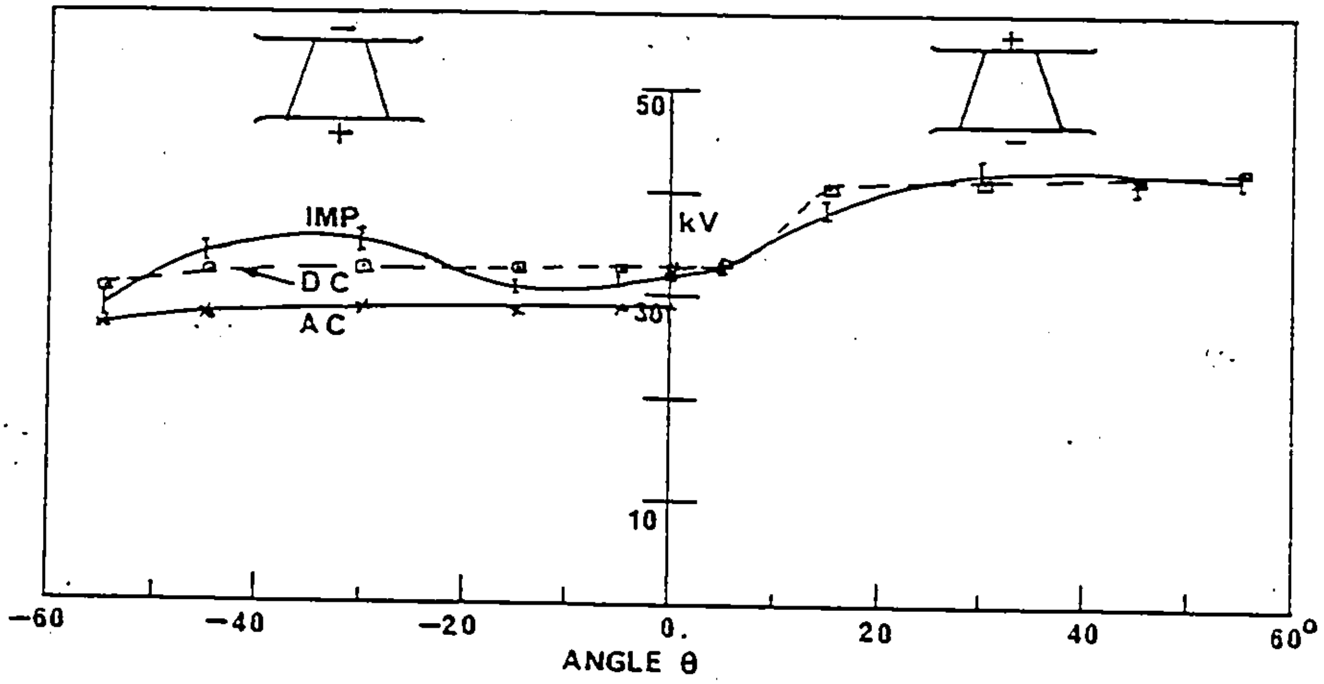

Fig. 3.10. Flashover voltage of 2 mm thick Macor glass-ceramic conical insulator as a function of angle θ. x AC (60 Hz); ⊡, DC; I, 1.2/50 μs lightning impulse.

for DC flashover when θ is negative. The AC (peak) flashover is lower than the corresponding DC and impulse values at a fixed value of θ.

When θ is positive the electric field at the cathode, which is the base of the cone, is lower than when θ is negative [29]. The lower field should lead to a higher withstand voltage as generally observed in Fig. 3.10 for DC and impulse in agreement with previous studies in cone insulators [9-11]. The lower AC flashover is attributed to the effect of the preceding half cycle which acts as an opposing pre-stress [28]. The modification to the electric field from the charge residing on the surface of the solid insulator must also be taken into account. Boersch _et al._ [7] measured the surface charge density for negative values of θ and found that the charge density decreased linearly with increasing the absolute value of |−θ|. Qualitatively, this may explain the absence of large reduction in the DC flashover voltage when θ is changed from 0 to −55°. The surface charge density was reported to decrease with increasing the negative value of θ and becomes negative at θ <−31.5° [7]. Therefore, the lower charge density on the surface of the insulator results in a lower enhancement in the field [26] say compared to when θ = 0. It is possible that the total combined enhancements in the field due to the conical geometry and to the accumulation of surface charges may be comparable in both cases.

3.3 Effect of Electrode Material and Pressure on Flashover

3.3.1 Effect of Electrode Material

The electrodes used for this study are made from 304 stainless steel, aluminium and copper. All the electrodes are 15 mm in diameter and great care is taken in fabricating the electrodes to be as closely similar in shape and surface finish as possible. It must be mentioned that the surface finish on the electrodes affected the surface flashover voltage of solid insulators when long pulses were used [11]. The solid insulator used is 2 mm thickness, 7 mm diameter Macor glass ceramic and butt-jointed to the electrode. All the electrodes and the insulator samples are treated in the same manner as discussed previously (Chapter 2). The average DC, AC and 1.2/50 μs impulse flashover voltage of glass-ceramic using the three different electrodes are given in Table 3.2.

The results obtained (Table 3.2) show that under the same experimental conditions, the electrode materials have no appreciable effect on the flashover performance of the insulator. The difference in the measured flashover value of three different samples of same dimension glass ceramic is smaller than ± 5%. Gleichauf [2] also reported that there is no appreciable difference in the breakdown voltage for

TABLE 3.2

Effect of Electrode Material on the Flashover Voltage of 2 mm Thickness, 7 mm diameter Macor Glass-ceramic Insulator, Diameter of the electrodes Used = 15 mm.

Electrode Material	Average Flashover Voltage (kV)		
	DC	Impulse (1.2/50 µs)	AC (peak)
Stainless Steel	33.2	32.2	29.0
Aluminium	31.5	30.8	28.5
Copper	31.8	30.6	28.2

when the pressure was increased from 10^{-6} to 10^{-4} Torr and the breakdown value increased sharply after 10^{-4} Torr and reached a maximum value when the pressure was about 5×10^{-4} Torr. The breakdown voltage started to decrease rapidly with increase in pressure after 5×10^{-4} Torr [61]. Smith [10] studied the breakdown over conical insulators under pulse conditions in a poor vacuum (10^{-4} - 10^{-1} Torr). He found that the 30 ns pulse breakdown voltage of 2.5 cm long perspex cone insulator ($\theta = 25°$) was independent of gas pressure in the region 2×10^{-4} to 3×10^{-2} Torr. When the pressure was raised above 0.03 Torr, the breakdown voltage began to decrease. He noted the same effect for the perspex insulator of 5 and 10 cm long ($\theta = 25°$).

In the present study the dependence of the flashover voltage on pressure has been investigated for Macor glass-ceramic, quartz and Teflon insulators using DC, AC and 1.2/50 μs impulse voltage. The results show that the variation of the ambient pressure in the range 10^{-8} - 6×10^{-3} Torr appears to have little or no effect on the flashover voltage of the insulators studied. Figures 3.11, 3.12 and 3.13 show the measured flashover value as a function of pressure for quartz (curve 1), Teflon (curve 2) and Macor glass-ceramic (curve 3) using DC (Fig. 3.11), Impulse (Fig. 3.12) and AC (Fig. 3.13) respectively. As can be seen from Figs. 3.11, 3.12 and 3.13 the flashover voltage is independent

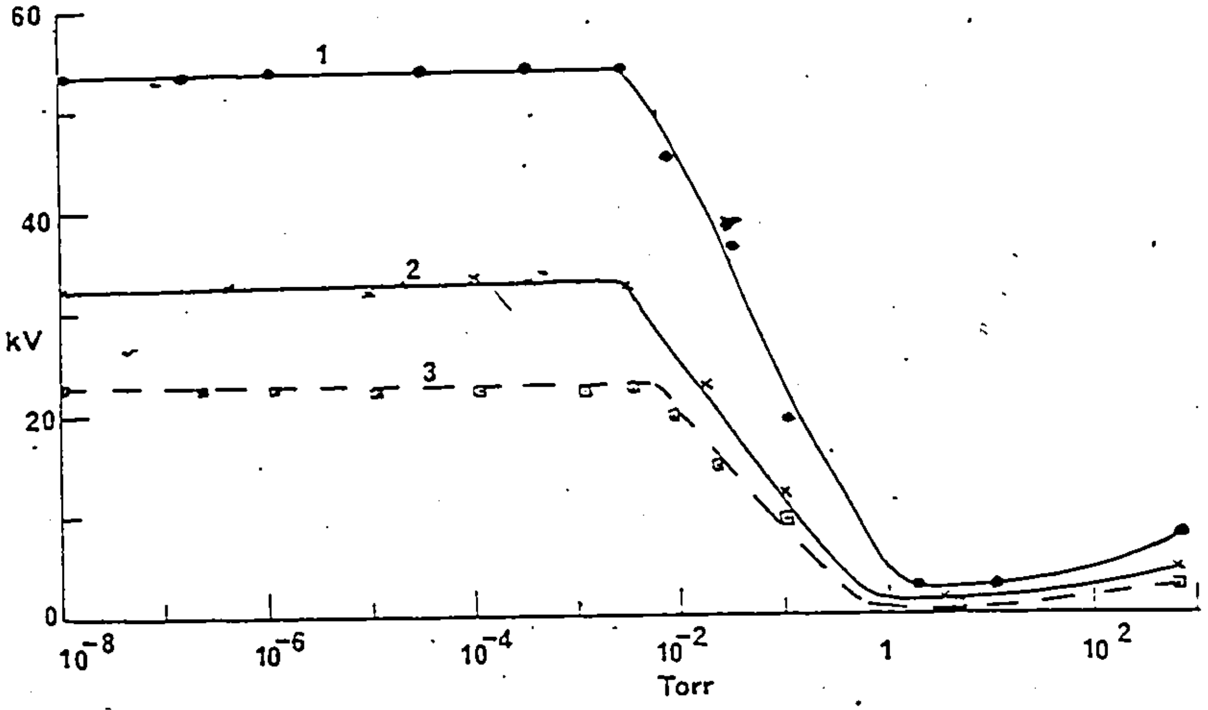

Fig. 3.11. Effect of pressure variation on the DC flashover of cylindrical insulators. Curve 1, Quartz, thickness 3.5 mm, diameter 11.8 mm; curve 2, Teflon, thickness 2.0 mm, diameter 7.0 mm; curve 3, Macor glass-ceramic, thickness 1.0 mm, diameter 7.0 mm. Electrode material: Stainless Steel.

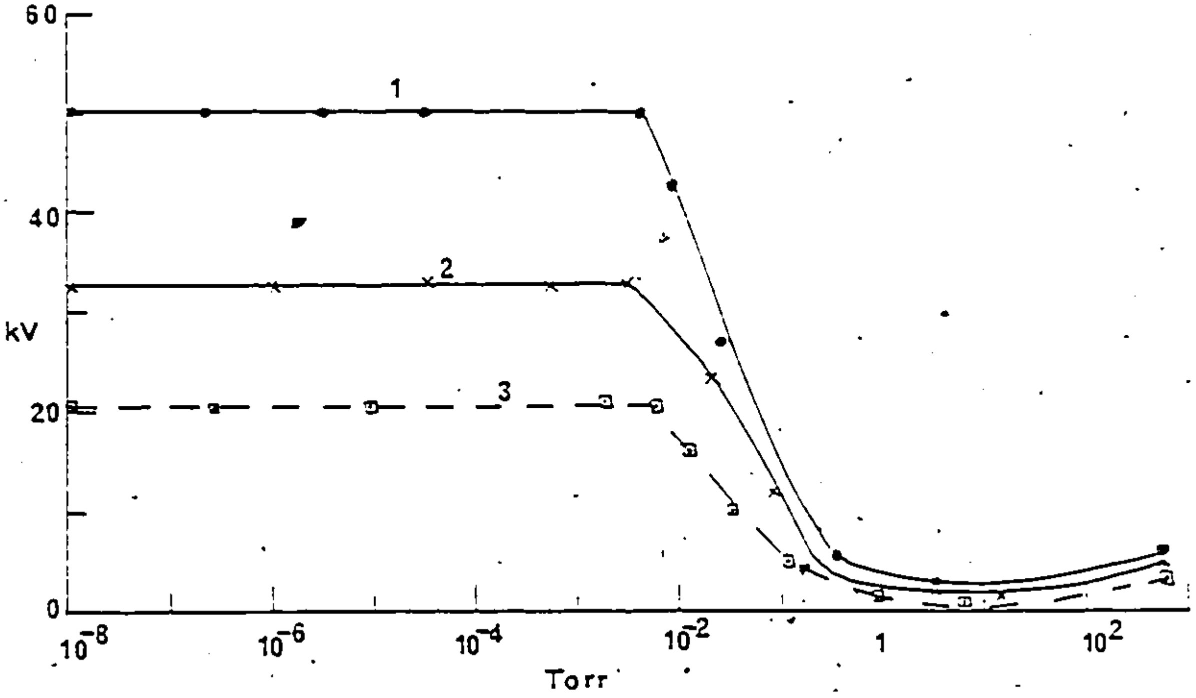

Fig. 3.12. Effect of pressure variation on the 1.2/50 μs impulse flashover of cylindrical insulators. Curve 1, Quartz, thickness 3.5 mm, diameter 11.8 mm; curve 2, Teflon, thickness 2.0 mm, diameter 7.0 mm; curve 3, Macor glass-ceramic, thickness 1.0 mm, diameter 7.0 mm. Electrode Material: Stainless Steel.

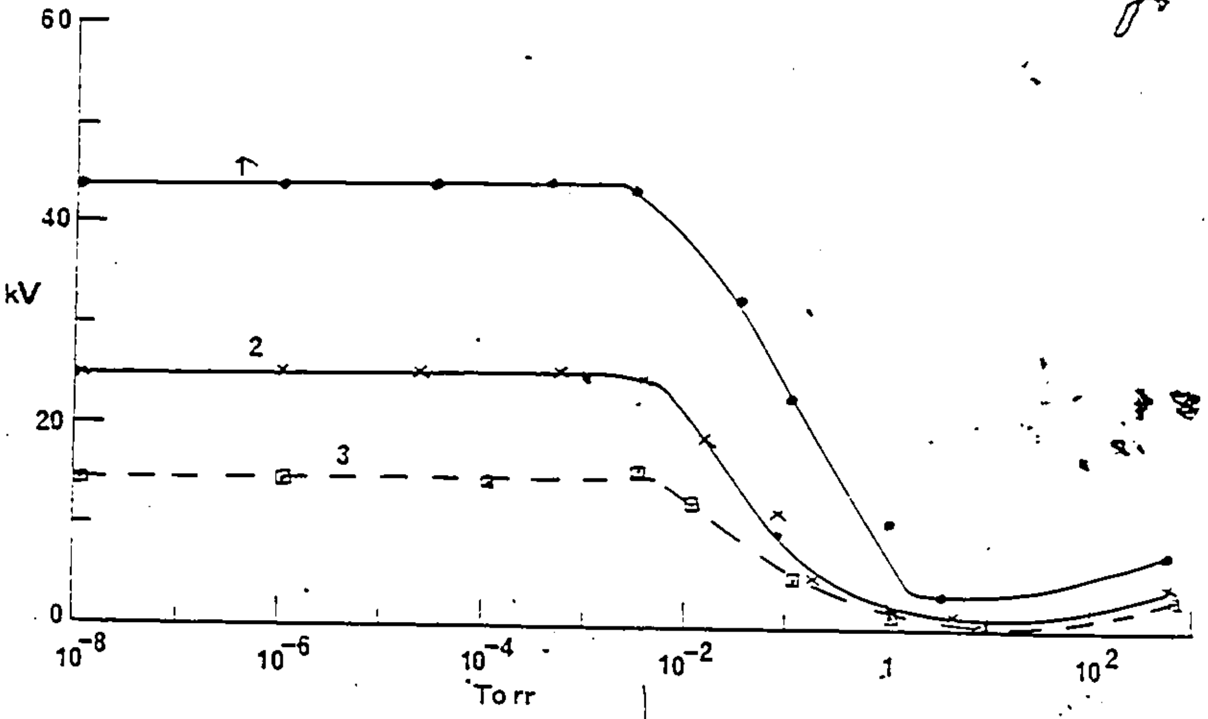

Fig. 3.13. Effect of pressure variation on the AC (60 Hz) flashover of cylindrical insulators. Curve 1, Quartz, thickness 3.5 mm, diameter 11.8 mm; curve 2, Teflon, thickness 2.0 mm, diameter 7.0 mm; curve 3, Macor glass-ceramic, thickness 1.0 mm, diameter 7.0 mm. Electrode Material: Stainless Steel.

of pressure in the range 10^{-8} - 6 x 10^{-3} Torr in all cases. When the pressure is raised above 6 x 10^{-3} Torr the flashover voltage starts to decrease rapidly. Fig. 3.14 shows the DC, Impulse and AC flashover voltage as a function of pressure in the case of $\theta = -45°$, 2 mm thickness, glass-ceramic conical insulator. In this case also, the flashover voltage is independent of pressure in the range 10^{-8} - 6 x 10^{-3} Torr.

3.4 Effect of Solid Insulator Diameter and Number of Insulators Placed in Series on Insulator Flashover

3.4.1 Effect of Solid Insulator Diameter

In ordinary vacuum gaps it has been reported that increasing the electrode area reduces the withstand voltage of the gap. Denholm *et al*. [62] showed that when the electrode area 20 cm^2 can hold 40 kV across a 1 mm gap but the electrode area of 1000 cm^2 can only hold 20 kV in stainless steel electrode.

The flashover voltage of solid insulators in vacuum is a non linear function of length of the insulator [11,13, 30]. The total surface area and the surface length appear to be related to this non linear variation of flashover voltage [11]. It is not clear, however, which one is the more dominant for this observation. An investigation has been carried out by keeping the thickness of the insulator constant and varying the diameter of the insulator. By this

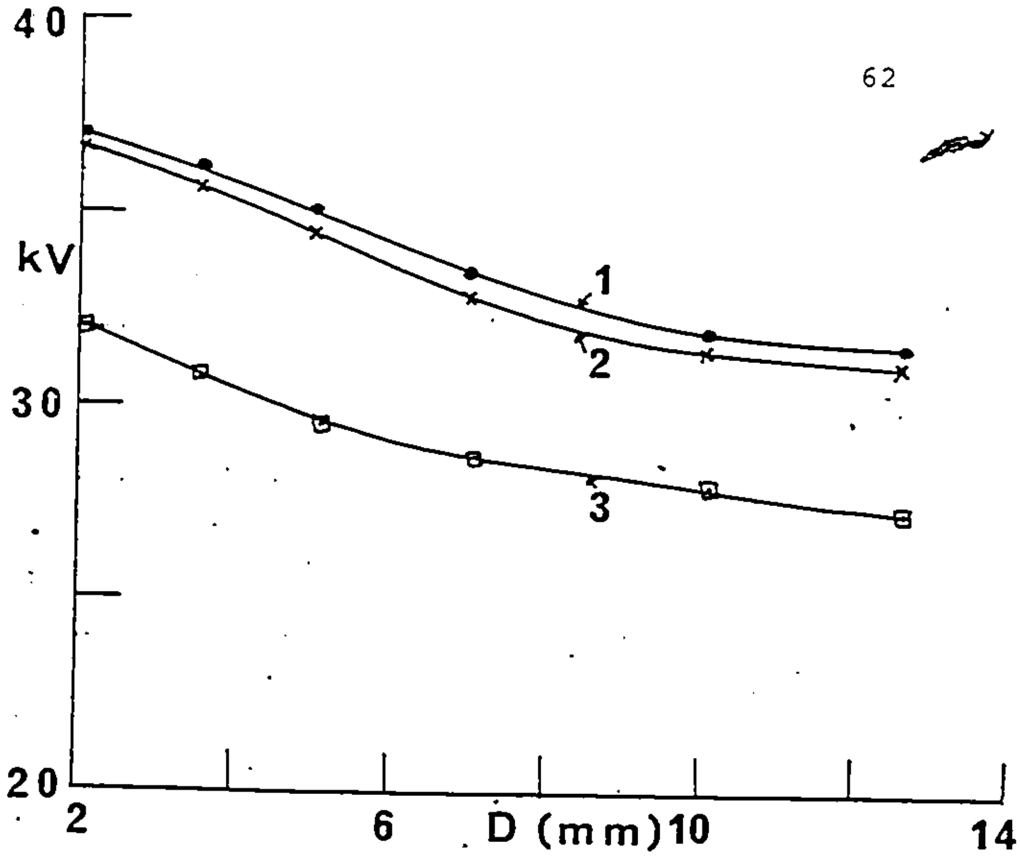

Fig. 3.15. Dependence of flashover voltage on the diameter of the cylindrical solid insulator. Insulator: Macor glass-ceramic. Electrode: stainless steel. Curve 1, DC; curve 2, impulse; curve 3, AC (60Hz).

method the contact area of the insulator with the electrode surface and the total insulator surface area in the vacuum is changed. Figure 3.15 shows the DC, AC and Impulse flashover voltage of 2 mm thickness glass-ceramic for 2, 3.5, 5, 7.0, 10.0 and 12.7 mm diameter. The contact area with the electrode is 3.14 mm^2 (diameter, D = 2 mm), 9.62 mm^2 (D = 3.5 mm), 19.63 mm^2 (D = 5.0 mm), 34.48 mm^2 (D = 7.0 mm), 78.54 mm^2 (D = 10.0 mm) and 126.68 mm^2 (D = 12.7 mm) respectively. As can be seen, there is a reduction in flashover value when the diameter of the insulator is increased. For example the DC flashover voltage for d = 2 mm is 37 kV which is about 17.5% higher when compared to the DC flashover voltage (31.5 kV) when d = 12.7 mm.

3.4.2 Effect of Number of Series Insulators on Flashover

Effect of number of insulators connected in parallel on the flashover of the vacuum system has been reported [63]. In this case, the flashover across one of the insulators is equivalent to the breakdown of the whole insulation system. Juchniewicz et al [63] reported a very distinct decrease in the breakdown voltage with increase in the number of parallel insulators. Accelerator and X-ray tubes are usually constructed with solid insulator envelope divided into a large number of

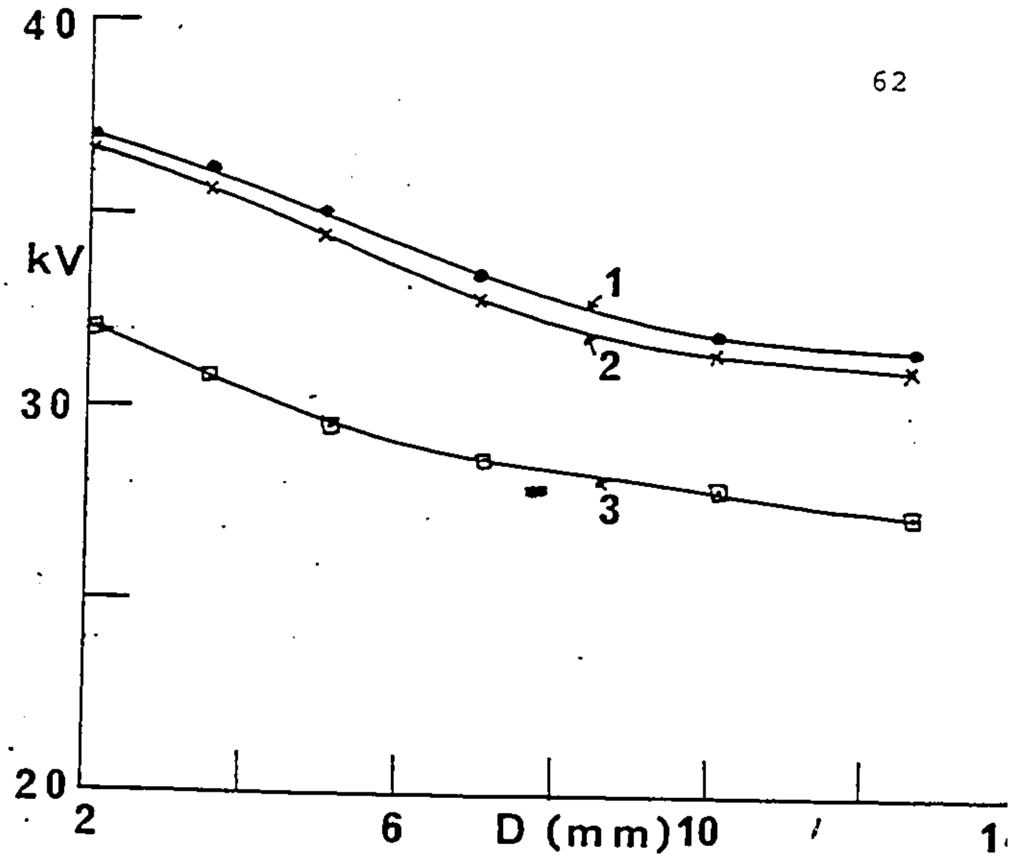

Fig. 3.15. Dependence of flashover voltage on the diameter of the cylindrical solid insulator. Insulator: Macor glass-ceramic. Electrode: stainless steel. Curve 1, DC; curve 2, impulse; curve 3, AC (60Hz).

insulating sections separated by metal grading electrodes. This kind of design is chosen to provide a uniform voltage distribution along the tube envelope and to improve the withstand capability [6,10]. In the present study a number of 2 mm thickness and 7 mm diameter Macor glass-ceramic insulator samples are bonded together using ECCOSHIELD ® ES conductive coating to make 4 mm, 6 mm and 8 mm stack . Ecchoshield is a highly conductive coating of a fine silver based lacquer adhesion to metal, plastics and ceramics. When applied to a non-conductor, the surface resistivity is substantially less than 1 Ω · cm/cm. These coatings divide the insulator length into segments. The DC, impulse and AC flashover obtained using the stacked insulator for 4 mm, 6 mm and 8 mm length is given in Table 3.3. The flashover voltage obtained is compared with the voltage measured as a single unit without voltage grading. As can be seen from Table 3.3 the DC, AC and 1.2/50 μs flashover voltage with a number of insulators connected in series is higher when compared with the same length at flashover voltage. For example, the DC, 1.2/50 μs impulse and AC flashover voltage of 6 mm thickness glass-ceramic stack is 67.3, 68.8 and 59.2kV respectively which is about 4%, 7% and 12% higher when compared to the respective flashover voltage of a 6 mm thickness Macor glass-ceramic insulator.

TABLE 3.3

Effect of Number of Solid Insulators Placed in Series on DC, 1.2/50 μs Impulse and AC Flashover Voltage. Material: Macor Glass-ceramic (each piece 2 mm Thickness, 7 mm Diameter).

Number of Insulators in Series	Insulator Stack Length L in mm	Flashover Voltage (kV)			Flashover Voltage (kV) of the Same Length Insulator		
		DC	Impulse	AC	DC	Impulse	AC
1	2.0	33.2	32.4	28.5	33.2	32.4	28.5
2	4.0	56.0	57.6	48.0	50.5	50.0	41.0
3	6.0	67.3	68.8	59.2	64.8	64.4	53.0
4	8.0	78.0	a	68.4	73.0	72.5	61.0

[a] Beyond the capacity of the impulse generator output 75 kV.

3.5 Effect of Ultra-violet Irradiation on the Solid Insulator-vacuum Interface

It has been reported that high density plasmas result in the production of large quantities of vacuum ultra violet photons in the several electron volt (ev) range [64]. In general the effect of ultra-violet light is expected to be positive charging of the insulator surface by means of photoemission. In addition the UV light incident on the vacuum-solid insulator could lead to gas evolution and surface heating which can severely affect the performance of the insulator [64,65]. Enloe _et_ _al_. [64], studied the role of soft radiation in causing flashover at the vacuum-solid dielectric interface. Their results indicate that a very modest ultraviolet photon fluence can cause the breakdown of an insulator which was capable of supporting 50 kV/cm, DC, even when the DC field stress was 20 kV/cm. Kondratov _et_ _al_. [65] studied the influence of a charge on the process of a breakdown in a system of electrodes and insulators in a sharply non-uniform field. They used a mica insulator plate with a thickness of 50 μm and the plate was irradiated by an ion beam directed perpendicular to the plate. They reported that the presence of a charge accumulated on the surface leads to a considerable (≈50%) decrease of the impulse strength of the insulator plate. Jackson _et_ _al_. [66] studied the 5 μs pulse flashover potential of various organic insulators (Lexan, Lucite, Delrin and Blue

Nylon) both before and after they have been exposed to X-ray irradiation. The results showed that the pulsed flashover potentials improved in all the samples except Blue Nylon after the samples have been irradiated. They attributed this to the lowering by irradiation of the secondary electron emission coefficient enough to reduce the chances of an electron build up and subsequent avalanche along the surface.

In the present study the DC, AC and 1.2/50 μs impulse flashover strength of different solid insulators are measured with the ultra-violet irradiation on the solid dielectric-vacuum interface as well as without the UV-irradiation. The UV range of the ultra-violet lamp used is 200-280 nm with peak at 254 nm (Model No. R25, Ultra-Violet Product Inc.). The intensity of the UV light falling on the insulator surface is measured by using a Black-Ray ultra-violet meter (Model J-225) in a similar experimental arrangement with the sapphire window. The total UV intensity expected to fall on the insulator surface is 350 μw/cm^2. The sapphire view port fitted to the breakdown chamber, provides an interface between the UV source and the solid insulator housed in the vacuum breakdown chamber. The useful transmission range of the sapphire view port is from 250 to 5500 nanometers. The UV light is arranged at a distance of 7 cm away from the solid insulator.

The change in the pressure of the vacuum system is monitored by using the Honeywell Electronic recorder. Figure

3.16 shows the change in pressure variation when the UV light is switched on in the case of 2 mm Macor glass-ceramic insulator. As can be seen from Fig. 3.16, the pressure rises from 3×10^{-8} to 2×10^{-7} Torr within 1 minute (Fig. 3.16) and after this there is no increase in pressure value. The pressure returns to the original value (3×10^{-8} Torr) after the UV lamp is switched OFF. With the UV light on, there is no increase in the pre-breakdown current flow with or without voltage up to 15 kV. When the voltage applied across the insulator is increased by about 20 kV, there is a flow of pre-breakdown current. The value of the pre-breakdown current measured is higher for the same voltage when compared to the pre-breakdown current without UV light.

Fig. 3.17 shows the pressure variation during the AC flashover of 2 mm thickness, 5 mm diameter Macor glass-ceramic. Fig. 3.17,a corresponds to the condition without UV irradiation and Fig. 3.17,b with UV irradiation. The AC flashover voltage with UV irradiation is 25.5 kV which is about 13% lower when compared to the AC flashover voltage without UV irradiation (29.2 kV, Table 3.4). The pressure variation during DC, AC and Impulse flashover for 2 mm thickness, 7mm diameter Teflon is given in Fig. 3.18. The flashover voltage with and without UV irradiation is summarized in Table 3.4 for different insulators. As can be seen from Table 3.4 the flashover value has decreased considerably and the value depends on the

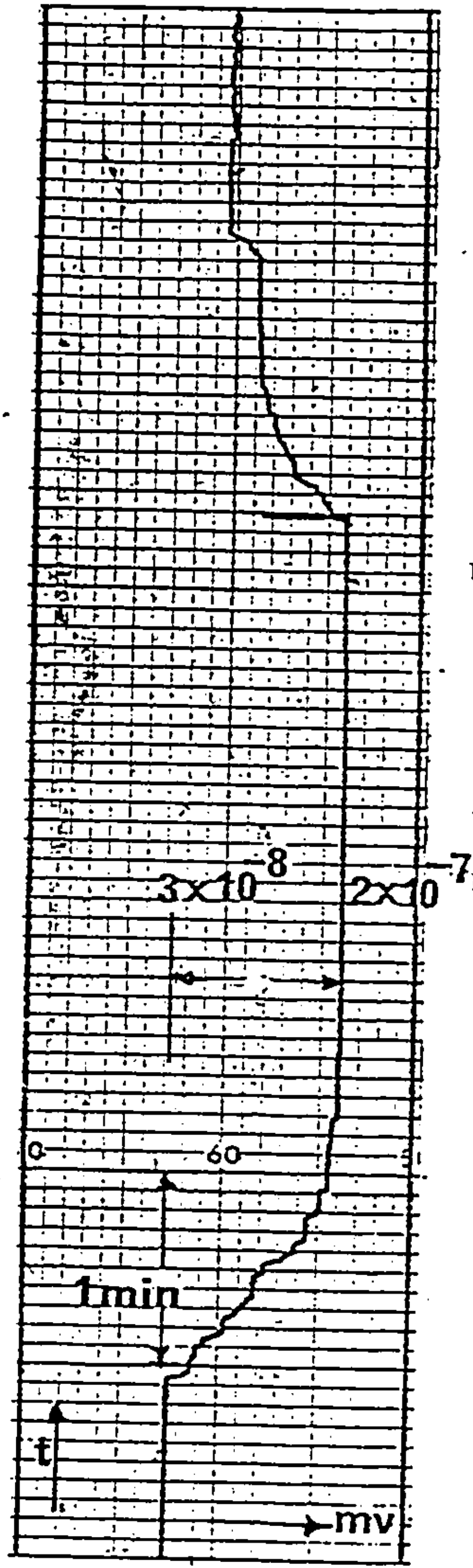

Fig. 3.16. Vacuum system pressure variation due to ultra-violet (UV) irradiation on 2 mm thickness 5 mm diameter Macor glass-ceramic insulator - vacuum interface.

Vertical scale: 1 minute/inch

Horizontal scale: 10 millivolts/inch

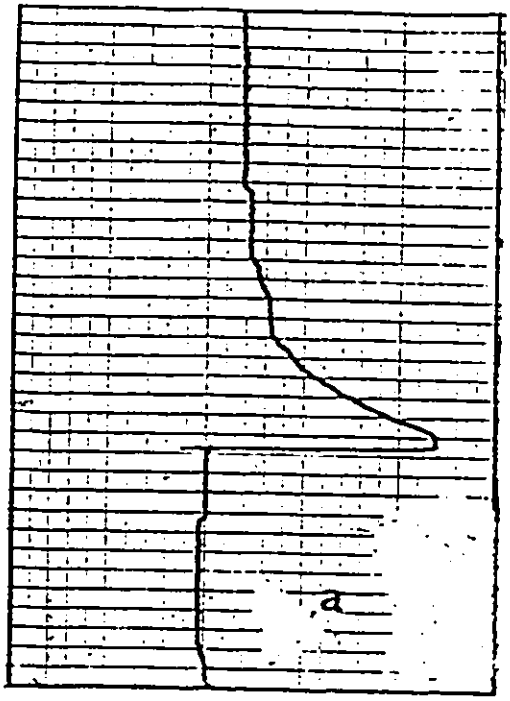

(a) without UV irradiation

Vertical scale: 1 min./inch

Horizontal scale: 10 mV/inch

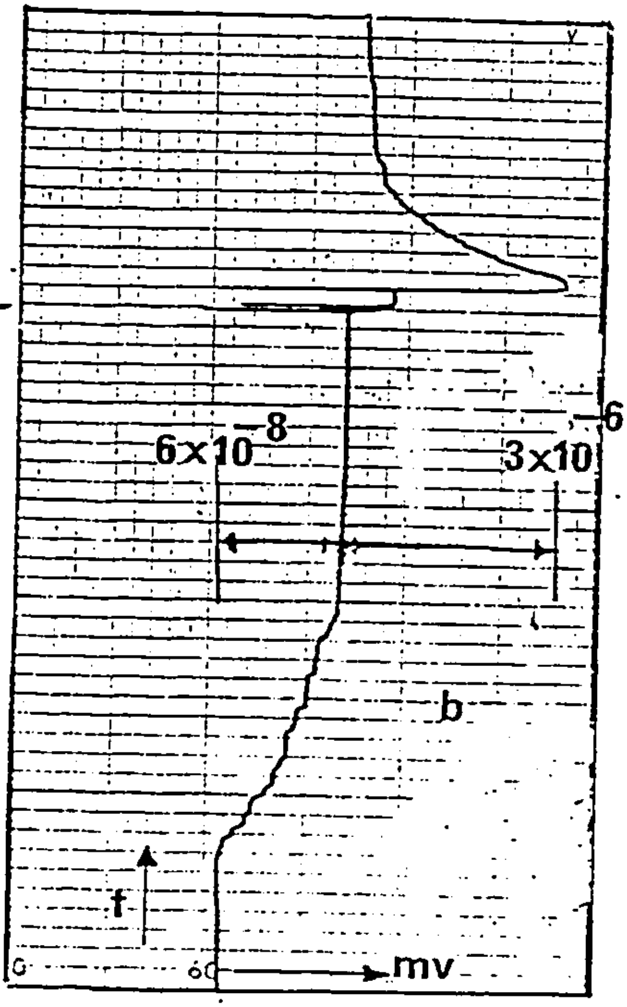

(b) with UV irradiation

Vertical scale: 1 min./inch

Horizontal scale: 10 mV/inch

Fig. 3.17. Pressure variation during AC flashover of 2 mm thickness glass-ceramic insulator.

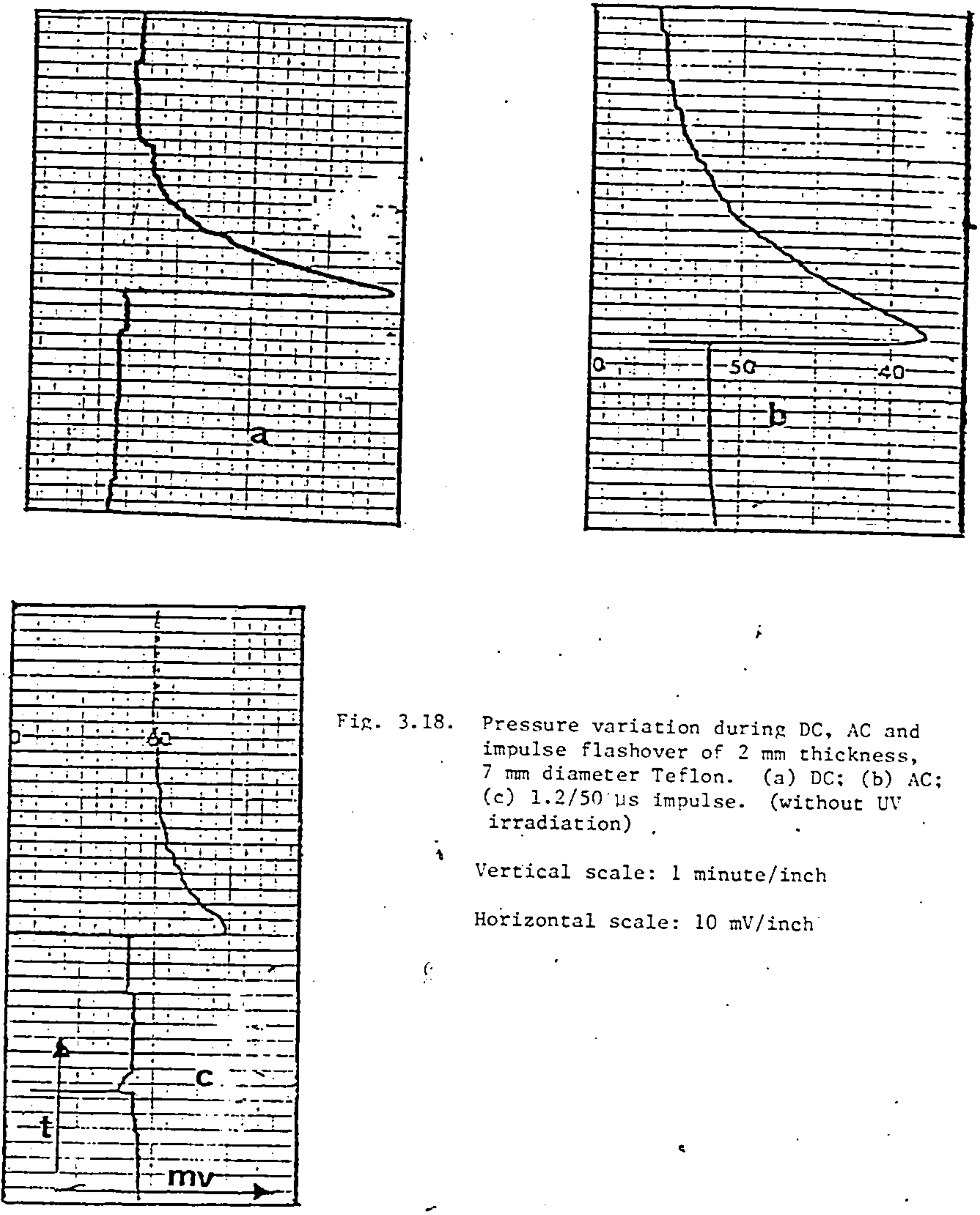

Fig. 3.18. Pressure variation during DC, AC and impulse flashover of 2 mm thickness, 7 mm diameter Teflon. (a) DC; (b) AC; (c) 1.2/50 µs impulse. (without UV irradiation)

Vertical scale: 1 minute/inch

Horizontal scale: 10 mV/inch

TABLE 3.4

Comparison of DC, 1.2/50 μs Impulse and AC Flashover Voltage of Solid Insulators With and Without UV Irradiation

Insulator Material	Thickness (mm)	Diameter (mm)	Flashover Voltage With UV Irradiation			Flashover Voltage Without UV Irradiation		
			DC	Impulse	AC	DC	Impulse	AC
Macor Glass-ceramic	2.0	5.00	28.0	26.5	25.5	35.0	34.5	29.2
Pyrex glass	4.0	6.35	44.0	43.2	39.5	46.0	44.4	39.5
Teflon	2.0	7.00	23.0	21.0	21.5	32.0	30.2	25.6
Sapphire	3.1	12.55	21.0	19.5	19.5	28.0	26.0	22.5
Macor glass-ceramic in stack (Table 3.3)	4.0	7 mm	45.5	49.8	42.5	56.0	57.6	48.0
	6.0	7 mm	56.0	60.0	52.4	67.3	68.8	59.2
	8.0	7 mm	64.5	69.5	60.5	78.0	-	68.4

insulator material. For example, the DC flashover value of 2 mm thickness glass-ceramic is decreased from 35.0 kV without UV irradiation to 28.0 kV with UV irradiation.

The experimental results show that the effect of UV light, i.e., charge accumulation on the insulator surface remains even if the UV is OFF until a flashover occurs. Moreover the electric strength of the irradiated insulator sample recovers to the original strength of the sample without irradiation after 2-4 repeated flashover of the insulator. Figure 3.19 shows the dependence of the AC flashover voltage on the number of sparkings after the UV light is switched off for 2 mm thickness Macor glass-ceramic (curve 1) and 2 mm thick Teflon (curve 2). It will be observed that the first breakdown voltage is reduced considerably compared to the final value which is attained after 4 to 5 shots. The results also show that (Table 3.4) the UV irradiation effect varies with the insulator material. For example, Pyrex glass, which has 40 eV electron impact energy, A_1, flashover voltage is less affected by the UV irradiation when compared to that of glass-ceramic having $A_1 = 25$ eV. This may be due to the variation in the value of surface charge density. The surface charge density value is lower for insulator materials having high electron impact energy [7].

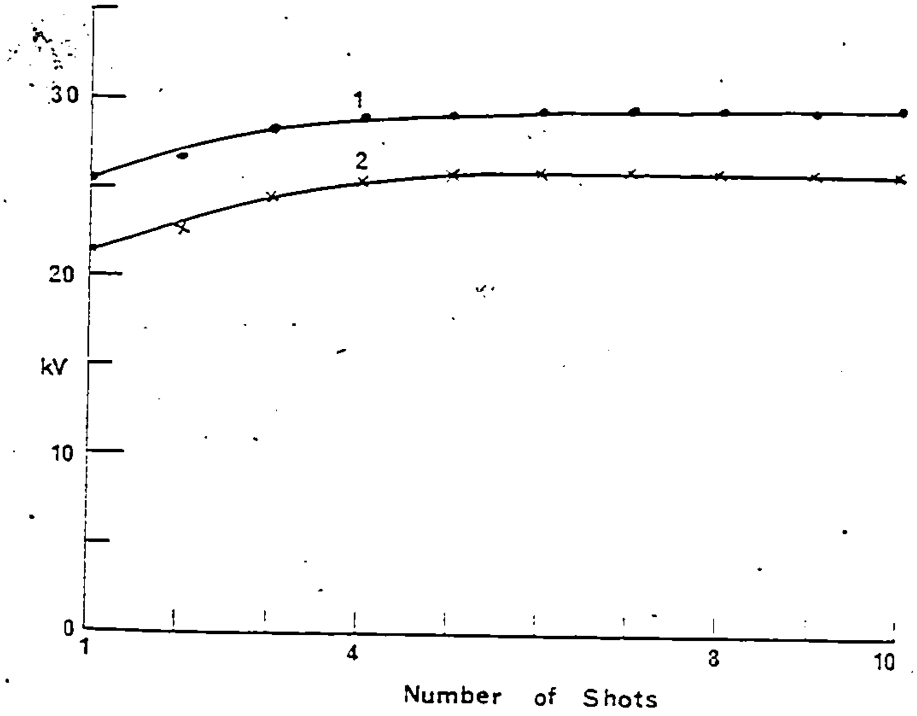

Fig. 3.19. Dependence of AC (peak) flashover voltage on number of sparkings after UV irradiation. Curve 1, Macor glass-ceramic, 2.0 mm thickness, 5 mm diameter, curve 2, Teflon, 2.0 mm thickness, 7 mm diameter.

CHAPTER IV

EFFECT OF DC PRE-STRESS ON DC, AC AND IMPULSE SURFACE FLASHOVER OF CYLINDRICAL AND CONICAL INSULATORS IN VACUUM

The surface flashover performance of cylindrical and conical insulators in vacuum is investigated using DC and AC (60Hz) following the application of a DC pre-stress and combination of DC + AC and DC + 1.2/50 μs impulse. The DC surface flashover voltage measured subsequent to applying a DC pre-stress with an opposite polarity is found to be considerably lower than the DC flashover voltage without a pre-stress. Applying a DC pre-stress with the same polarity improves only slightly the subsequent DC flashover strength. The AC flashover is unaffected by the DC pre-stress of either polarity.

The combined DC and AC flashover voltage of cylindrical and conical insulators depends on the DC pre-stress level and increases with increasing pre-stress until saturation is reached at slightly higher than the DC flashover level. In the case of the combined DC and impulse voltage, an opposing DC pre-stress causes a reduction and an aiding DC pre-stress causes an increase in the subsequent flashover voltage.

Moreover the level and the polarity of the DC pre-stress have a strong influence on the combined DC and impulse flashover voltage in cylindrical insulators and a relatively smaller influence in conical insulators.

4.1 Introduction

The study of the influence of the application of a DC pre-stress to the subsequent flashover strength of a solid insulator using DC of opposite polarity, or AC or impulse stress is useful to understand the effect of the polarity reversal of the wave present in the case of the AC voltage. The effect of application of an electrical pre-stress to the subsequent flashover or breakdown voltage of solid insulators or insulator films has been investigated by several authors [28,67,68,73,74]*. Generally the DC and the lightning impulse performance of the cylindrical insulators [67,68] were found to depend on whether or not the pre-stress was aiding or opposing the subsequent applied voltage used to measure the flashover. A space charge injection model from the electrodes was proposed [67, 68] to explain the observed effects. In the case of nano-second pulses the flashover level is influenced less by the pre-stress [73].

In the present study the DC + AC and DC + impulse flashover performance of cylindrical insulators (Teflon, Quartz, Macor glass-ceramic and Sapphire) and conical insulators

---

*Refs. 27, 68 (vacuum); 67, 73 (air); 74 (SF_6).

(Macor glass-ceramic, θ from −55° to 55°) has been investigated prior to and following the application of a DC pre-stress.

4.2 Effect of DC Pre-stress on Surface Flashover of Insulators

A pre-determined DC voltage stress is first applied to the gap (hence called pre-stress) for 300 s and either impulse (same and opposite polarity) or AC voltage is superimposed upon the pre-stress. The time of application of the pre-stress is varied in the range of up to 7200 s. As no dependence is observed on the time of application of the pre-stress, 300 s is chosen as a convenient period. The flashover voltage is defined as the maximum voltage that the gap withstands just before it collapses to a low level. When a combination of DC and AC voltages or DC and impulse voltages is used, the flashover voltage is the total sum of the DC (which is also the pre-stress level) and the peak of the impulse or the AC voltages. The flashover always occurs at the peak of the superimposed voltage.

Figure 4.1 shows the waveforms used including −DC + impulse, +DC + impulse and DC + AC. In the case of conical insulators, the positive angle and negative angle cone position is obtained by reversing the polarity of the applied voltage instead of changing the position of the conical

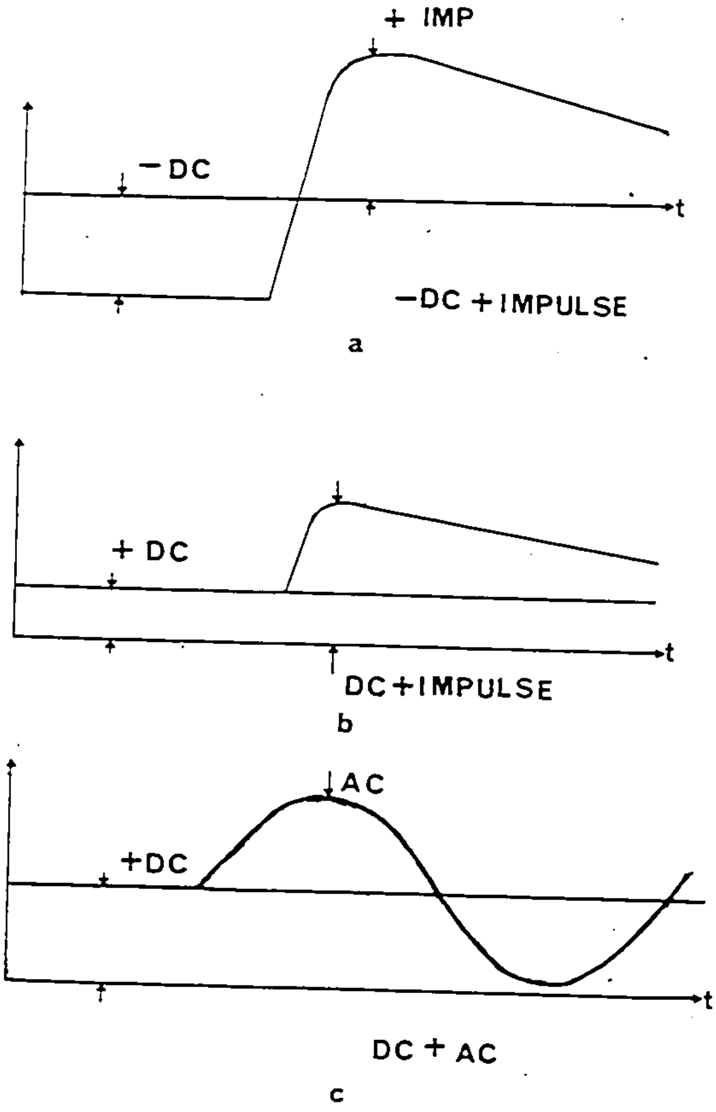

Fig. 4.1. Applied voltage waveforms. a, -DC + impulse; b, DC + impulse; c, DC + AC.

specimen between the electrodes.

4.2.1 Effect of DC Pre-Stress (opposing and Supporting) on Subsequent DC Flashover of Cylindrical Insulators

It has been generally found in the present study that a DC pre-stress of the same polarity has little effect on the subsequent final DC flashover voltage of solid insulators in vacuum. A DC pre-stress having an opposing polarity to the subsequent DC applied voltage reduces the first flashover voltage considerably.

The solid insulator is subjected to a pre-stress voltage at levels between 50 to 75% of the anticipated flashover voltage and maintained for 300 s before removal. The flashover voltage is measured 60 to 90 s after removal of the pre-stress. The pre-stress voltage polarity is chosen to be both supporting and opposing to the subsequent application of voltage to measure the flashover level. The dependence of the flashover voltage on the number of sparkings is depicted in Fig. 4.2 for an opposing pre-stress of about 60% of the conditioned flashover voltage. It will be observed that the first breakdown voltage is reduced considerably compared with the final value which is attained after 7 to 10 shots. The conditioned flashover values are higher by 24, 16, 19 and 32% over the first flashovers in quartz-silica (3.5 mm),

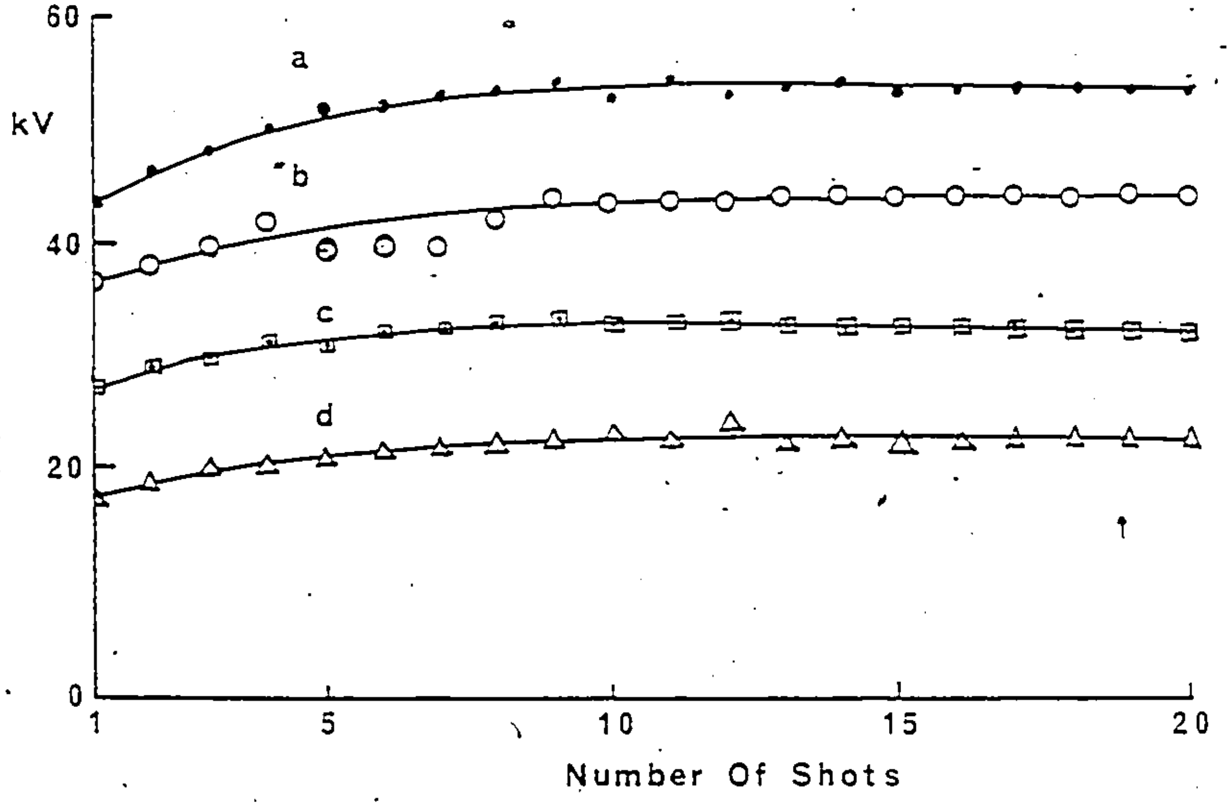

Fig. 4.2. Dependence of DC flashover voltage on number of sparkings after applying an opposing DC pre-stress. Curve a, Quartz, 32 kV pre-stress; 3.5 mm thick; curve b, Teflon 26 kV pre-stress; 4 mm thick, curve c, Teflon 19 kV pre-stress; 2 mm thick, curve d, glass-ceramic, 13 kV pre-stress, 1 mm thick. Conditions: Approximately an opposing 60% of the flashover voltage is applied for 300s and then removed. Flashover is measured 60 to 90s after removal of pre-stress.

Teflon (2 mm), Teflon (4 mm) and glass-ceramic (1.0 mm), respectively, when the pre-stress is of opposing polarity at a level of 60% of the conditioned value (Fig. 4.2). For 75% opposing pre-stress the corresponding improvements are 34, 25, 36 and 41% respectively for quartz-silica, Teflon (2 mm), Teflon (4 mm) and glass-ceramic (Table 4.1).

It is found that after applying an aiding DC pre-stress, in the range 50-75% of the conditioned flashover voltage, the subsequent conditioned flashover values are about the same as those measured without a pre-stress. However, if the conditioned specimen is left for 1-2 days without a voltage stress and then an aiding pre-stress is applied, the first DC breakdown values are usually higher by about 5-10% in all the materials studied. The conditioned flashover values remain unaltered. The effect of the pre-stress on the subsequent flashover is attributed to the creation of surface charges on the solid insulator. In the case of aiding pre-stress the polarities and the distribution of the surface charges along the length of the insulator surface are essentially the same as for the subsequent applied voltage and therefore no dependence on the pre-stress is expected.

For an opposing pre-stress, the polarities of the surface charges are expected to be different from those of the subsequent applied voltage. The charges are known to remain on the surface of the solid insulator for a considerable

TABLE 4.1

First and Conditioned Values of DC Surface Flashover Voltage After Applying an Opposing DC Pre-stress for 300 s

Opposing DC Pre-Stress	Macor glass-ceramic, 1 mm thick, 7 mm diameter		Teflon, 2 mm thick, 7 mm diameter		Teflon, 4 mm thick, 7 mm diameter		Quartz, 3.5 mm thick, 11.8 mm diameter	
(% of the Conditioned DC Flashover Value)	First Value (kV)	Final Value (kV)	First Value (kV)	Final Value (kV)	First Value (kV)	Final Value (kV)	First Value (kV)	Final Final (kV)
50	19	22.5	30	32	39.0	43.5	46	53.5
60	17	22.5	27	32	36.5	43.5	43	53.5
70	16	22.5	24	32	32.0	43.5	40	53.5

time, measured in terms of hours, after the removal of the applied voltage stress [41,69,71,72]. For the duration of 60 to 90 s which elapses between the removal of the pre-stress and the subsequent application of the voltage to measure the flashover, the charges would alter by only a negligible amount. The total surface charge remaining on the surface, it is suggested, will be increased due to the opposing pre-stress. This situation is generally similar to the case of AC in which a polarity reversal occurs. An increase in the presence of surface charge leads to higher fields at both electrode junctions assuming a heterocharge model. This leads to an increase in the pre-breakdown current and a reduction in the flashover voltage, as observed in the present work. This suggestion is supported by comparing the AC flashover voltage with the first DC flashover voltage after a large (75% of the withstand voltage) opposing pre-stress is used (Table 4.2). As can be seen from Table 4.2, about the same flashover strength is obtained for AC and DC with opposing pre-stress in glass-ceramic [17 kV (AC), 16kV (first DC)], Teflon [25.6 kV(AC), 24.0 kV (first DC)] and quartz [43.5 kV(AC), 40 kV (First DC)]. After a few flashovers, the charge magnitude and distribution will be those appropriate to the applied DC voltage and therefore the DC dielectric strength attains a steady value which is

TABLE 4.2

Comparison of AC (peak) Flashover Voltage (kV) with First DC Flashover Voltage (kV) After 75% Opposing DC Pre-stress

Material	Thickness (mm)	AC (Peak) Flashover Voltage (kV)	First DC Flashover Voltage after 75% Opposing DC Pre-stress (kV)	DC Flashover Voltage (kV)
Macor glass-ceramic	1.0	17.0	16.0	22.5
Teflon	2.0	25.6	24.0	32.0
Quartz	3.5	43.5	40.0	53.0

the conditioned value. The latter suggestion is consistent with observation of Tourriel et al. [69] who reported that the charges from the surface can be removed when the gap was sparked.

4.2.2 Effect of DC Pre-stress on subsequent AC Flashover

The application of DC pre-stress at various levels in the range 25 to 75% of the expected AC (peak) breakdown voltage, for various times in the range up to 7200 s, has negligible effect on the subsequent AC flashover voltage. This is the case when the DC pre-stress is removed for about 60 to 90 s and then the AC flashover voltage is measured.

The same results are obtained when either positive or negative DC voltages are applied in turn to one end of the solid insulator. The reason for the absence of any considerable effect after the removal of the DC pre-stress is not known at the present time. However, it is thought that as the applied AC voltage is gradually increased to the flashover level, the repeated reversal of voltage polarity combined with the higher AC pre-breakdown currents causes the surface charges to become appropriate to the applied AC field.

4.2.3 Effect of DC pre-stress on Subsequent DC + AC Flashover of Cylindrical Insulators

Figure 4.3 shows the DC + AC flashover voltage of quartz (3.5 mm thickness, 11.8 mm diameter, curve a) and Teflon (2.0 mm thickness, 7 mm diameter, curve b), Fig. 4.4 for glass-ceramic (1 mm thickness, 7 mm diameter) and Fig. 4.5, curve 3 for sapphire (3.1 mm thickness, 12.55 mm diameter) as a function of the DC pre-stress voltage. In these experiments the DC pre-stress is maintained at a constant level for 300 s and then a varying AC voltage is superimposed on the fixed DC until flashover occurs. It will be seen that the application of a pre-stress has a considerable influence on the total AC + DC flashover voltage.

The level of the combined DC and AC withstand voltage exceeds the flashover withstand voltage of the AC by a large amount. In the case of sapphire the combined value of AC + DC (34 kV) exceeds the DC flashover voltage (28) by about 20%. The flashover occurs on the AC wave portion having the same polarity as the DC stress. The bars in Figs. 4.3, 4.4 and 4.5 (curve 3) represent the effect of conditioning with repeated sparking using AC + DC at the same applied DC pre-stress. Since the total AC + DC flashover value is equal to or greater than the DC flashover voltage, the surface charges present on the insulator surface must be of the same magnitude and distribution for both cases. This suggests

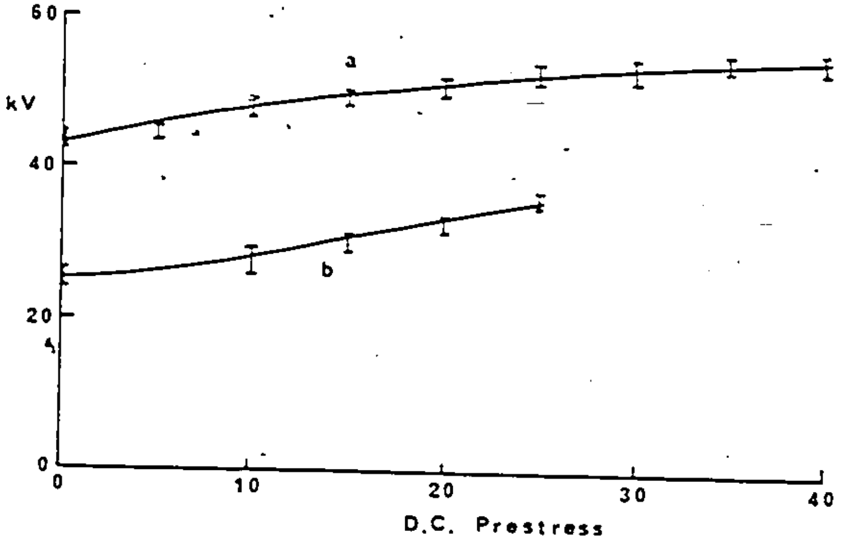

Fig. 4.3. Combined DC + AC surface flashover as a function of DC Pre-stress for 3.5 mm thick quartz silica (curve a) and 2 mm thick Teflon (curve b). Bars (I) represent conditioning effect.

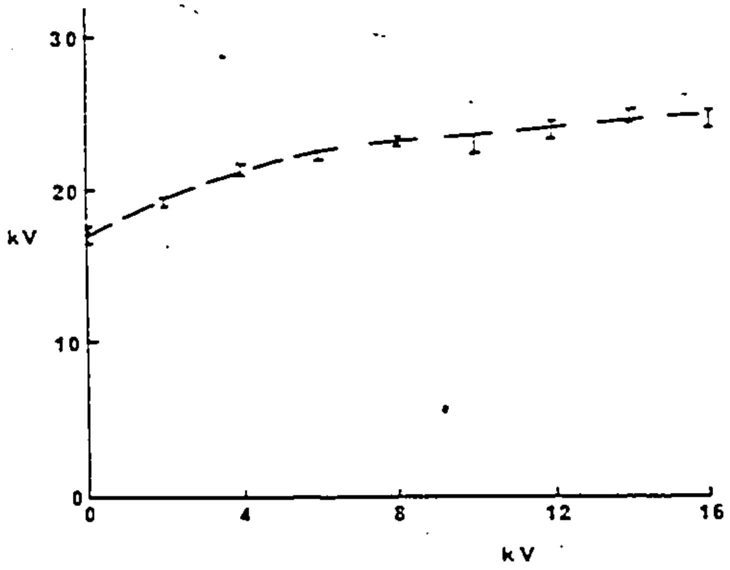

Fig. 4.4. Combined DC + AC surface flashover as a function of DC pre-stress for 1 mm thick glass-ceramic. Bars (I) represent conditioning effect.

that the steady state magnitude of the accumulated surface charges is proportional to the peak of the applied electric field. The proportionality between the surface charge density and the applied field was predicted theoretically [7] and has been demonstrated experimentally [69,70]. The electric field distribution on the surface of the solid insulator is expected to be the same in both cases leading to the same values of breakdown voltages as observed experimentally.

4.2.4 Effect of DC pre-stress on the Subsequent DC + AC Flashover Voltage of Conical Insulators

Macor glass-ceramic specimens in the shape of conical insulators having a thickness of 2 mm, a 7 mm base diameter and different θ values are used. Figure 4.5 shows the effect of applying a DC pre-stress using positive and negative polarities on the subsequent ± DC + AC flashover strength for conical insulators having $\theta = \pm 45°$ (curve 1) and $\theta = \pm 15°$ (curve 2). The pre-stress is applied for 300 s and then the AC is superimposed upon the DC pre-stress. When the DC pre-stress is positive (i.e., applied to the narrow end of the cone) and therefore $\theta = +45°$ or $+15°$ the flashover occurs in the positive cycle of the AC wave. The combined DC + AC voltage increases with increasing pre-stress until saturation is reached at the same level of DC flashover. Typically for

θ = 45°, when the pre-stress is varied from + 20 kV to + 30 kV (DC) the combined DC + AC flashover voltage is 45 kV (Fig. 4.5, curve 1), the DC breakdown for θ = 45° is 43 kV and the AC is 28.5 kV (Fig. 3.10, Chapter 3). For negative DC and therefore θ = -45°, there is also an increase in -DC + AC flashover voltage with increasing pre-stress. It should be noted that the sign convention of the angle θ follows that of the voltage polarity of the narrow end of the cone [9-11] and this has also been adopted here. The flashover value of -DC + AC (of 35 kV) reaches the DC level for θ = -45° when the applied pre-stress is in the range -16 kV to -24 kV (Fig. 4.5). For this case (i.e., θ = -45°) the DC breakdown is 33 kV and the AC is 28 kV (Fig. 3.10, Chapter 3). The DC + AC and -DC + AC flashover voltage of cones having θ = ± 15° (Fig. 4.5, curve 2) show a similar trend to that of θ = ± 45°. The flashover of ± DC + AC are measured also for θ = ± 30% and θ = ± 55° in glass-ceramic and essentially the same trend depicted in Fig. 4.5, curves 1 and 2 are found. When the DC pre-stress is negative, the flashover occurs in the negative cycle of the AC wave.

4.2.5 Effect of DC Pre-stress on Subsequent DC + Impulse Flashover of Cylindrical Insulators

Cylindrical specimens (i.e., θ = 0) made of glass-ceramic having a thickness of 1 mm and a diameter of 7 mm and a sapphire of 3.1 mm thickness and 12.55 mm in diameter are used to investigate the contributions of different materials

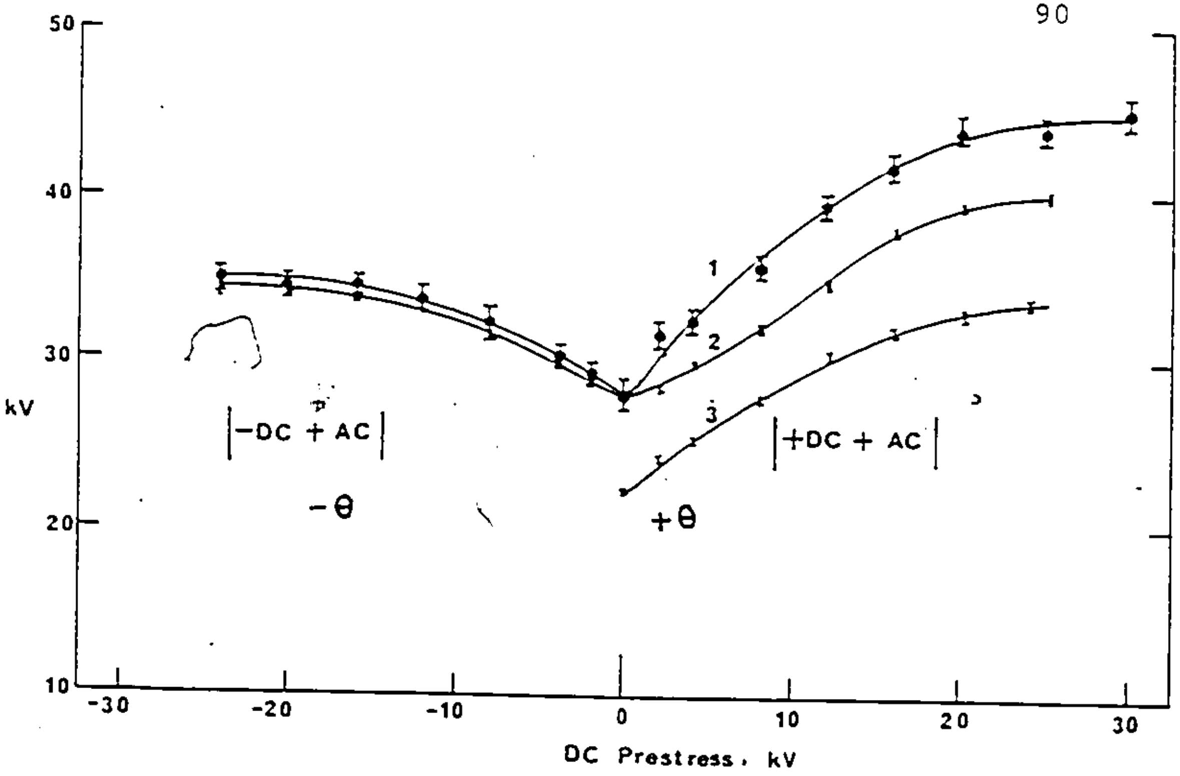

Fig. 4.5. AC superimposed on DC surface flashover of cylindrical and conical insulator as a function of DC pre-stress. Curve 1, θ = ± 45°; curve 2, θ = ± 15°; curve 3, θ = 0. Curves 1 and 2: Macor glass-ceramic, 2 mm thickness, 7 mm base diameter; curve 3, sapphire, 3.1 mm thickness, 12.55 mm diamater.

to the effect of pre-stress on the combined DC + impulse flashover.

Figure 4.6 shows the effect of applying an opposing DC pre-stress and Fig. 4.7 of an aiding DC pre-stress to the subsequent application of a 1.2/50 µs impulse superimposed on the pre-stress voltage to a sapphire specimen. The impulse flashover level is at 26 kV when a DC pre-stress is not applied to the solid insulator (Figs. 4.6 and 4.7). The bars shown in Figs. 4.5 to 4.10 represent the effect of conditioning the samples after applying the pre-stress as well as giving a measure of the reproducibility of the flashover voltage when 10 shots are used at each pre-stress level. It will be observed from Fig. 4.6 that an opposing pre-stress causes a reduction in the flashover values of either -DC + impulse or DC - impulse (Fig. 4.6). The reduction in the withstand voltage depends on the opposing pre-stress level. When a large opposing pre-stress voltage of say -20 kV DC (which is about 75% of the DC breakdown level) is applied, the subsequent DC and impulse is reduced from 26 kV (at 0 pre-stress) to 17 kV; a reduction by about 35% in the original flashover strength.

Figure 4.7 shows the effect of aiding DC pre-stress on the subsequent flashover of DC + impulse and -DC - impulse in sapphire. It will be observed that the aiding pre-stress causes an increase in the flashover strength. The flashover

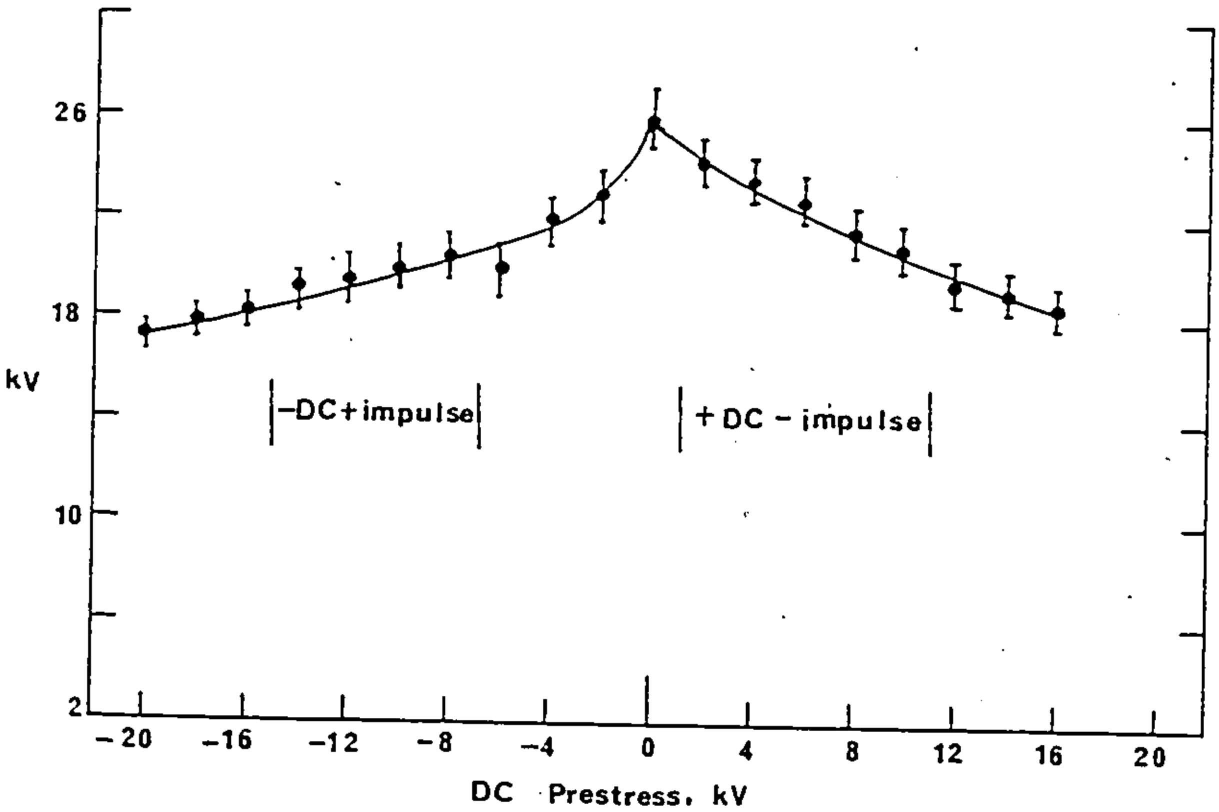

Fig. 4.6. Combined DC and 1.2/50 μs impulse flashover voltage for a cylindrical specimen of sapphire. Thickness, 3.1 mm, diameter 12.55 mm, θ = 0. DC pre-stress opposite to impulse.

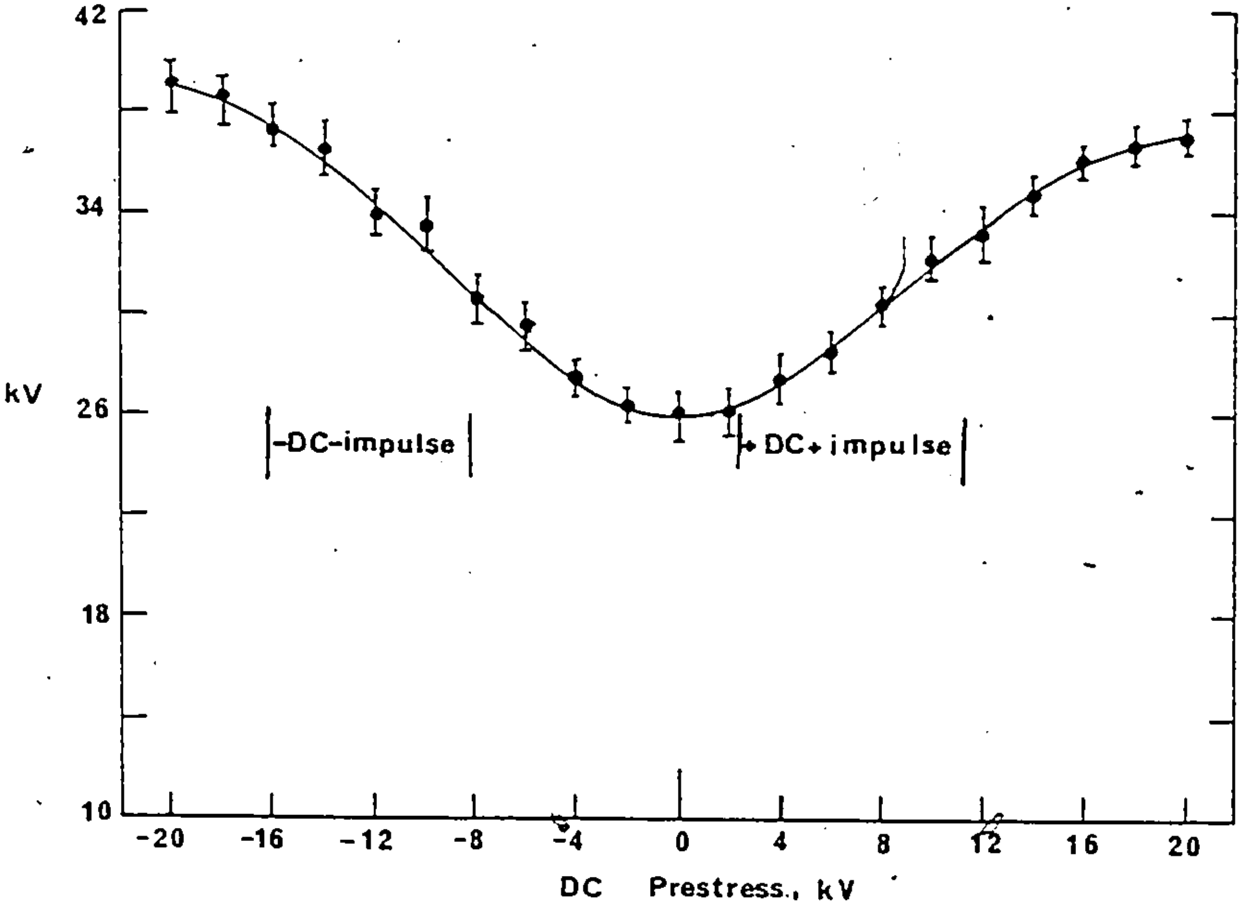

Fig. 4.7. Combined DC and 1.2/50 μs impulse flashover voltage for a cylindrical specimen of sapphire. Thickness, 3.1 mm, diameter 12.55 mm, θ = 0. DC pre-stress is aiding that of impulse.

voltage depends on the level of the pre-stress and increases with increasing the aiding pre-stree voltage. Typically, the flashover strength increases by 43% when an aiding DC voltage of about 75% of the DC breakdown voltage is used (Fig. 4.7) in the case of sapphire.

In the case of a 1 mm thick cylindrical glass-ceramic (θ = 0) the opposing pre-stress has a stronger influence then sapphire. Typically, the subsequent flashover strength of (DC - impulse) in the case of glass-ceramic decreases by 56% (Fig. 4.8) after applying an opposing DC pre-stress at a level (20 kV) of about 80% of the DC breakdown voltage. When an DC aiding pre-stress is used at the same level (80% of the DC breakdown voltage) an increase of about 22% (Fig. 4.8) is obtained in the flashover voltage of DC + impulse.

4.2.6 Effect of DC Pre-stress on Subsequent DC + Impulse Flashover Voltage of Conical Insulators

Glass-ceramic conical insulators having a thickness of 2 mm, a base of 7 mm and θ = ± 55° and θ = ± 45° were used. Fig. 4.9 shows the superimposed DC-impulse (1.2/50 μs) and -DC +

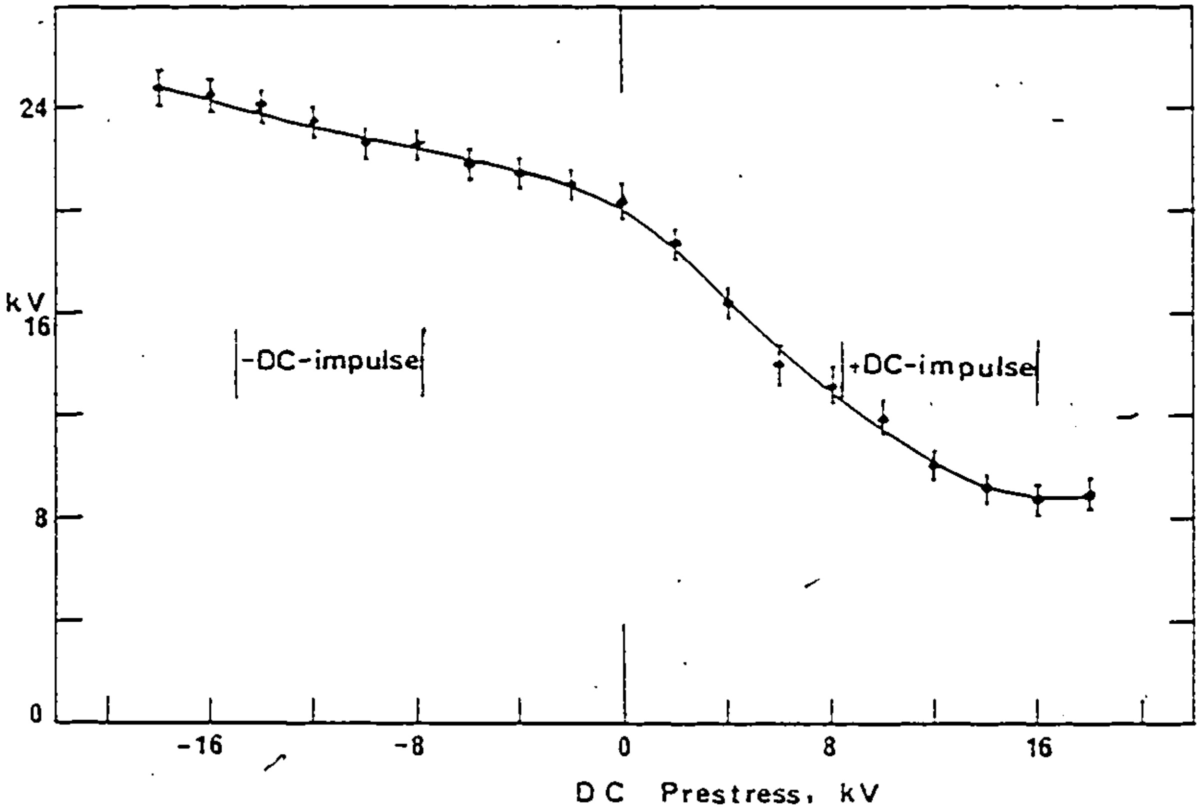

Fig. 4.8. Combined DC and 1.2/50 μs impulse flashover voltage for 1 mm thick, 7 mm diameter Macor glass-ceramic for DC pre-stress aiding and opposing impulses.

impulse flashover voltages as a function of opposing DC pre-stress for θ = 55°. It will be observed that the combined voltage decreases with increasing the opposing DC pre-stress. The flashover occurs at the peak of the impulse. Typically, for θ = 55° when an opposing DC voltage of between 12 to 20 kV is applied, the flashover decreases from 29 kV (negative impulse) to 24 kV (+DC - impulse), a reduction of about 17% (Fig. 4.9). Similarly when θ = -55°, and an opposing DC voltage of -20 kV is applied, the flashover decreases from 42 kV (positive impulse) to 35.8 kV (-DC + impulse); a reduction of about 15% (Fig. 4.9). It seems that the relative reduction in the subsequent flashover voltage is less in the case of conical insulators (Fig. 4.9) than with cylindrical insulators (Fig. 4.8) of the same material.

Figure 4.10 shows the effect of using an aiding DC pre-stress on the subsequent DC + impulse flashover voltage in a cone insulator made of glass-ceramic and having θ = ± 55°. The superimposed flashover voltages (DC + impulse) and (-DC - impulse) increase with increasing the aiding DC voltages. For θ = 55° the maximum improvement is at 13% from 42 kV positive impulse at zero pre-stress to 47.8 kV (+DC + impulse) at 24 kV DC aiding pre-stress (Fig. 4.10). Similarly for θ = -55°, the improvement is about the same at 13.8% from 29 kV (negative impulse) at zero pre-stress to 33 kV (-DC - impulse) at -24 kV DC aiding pre-stress

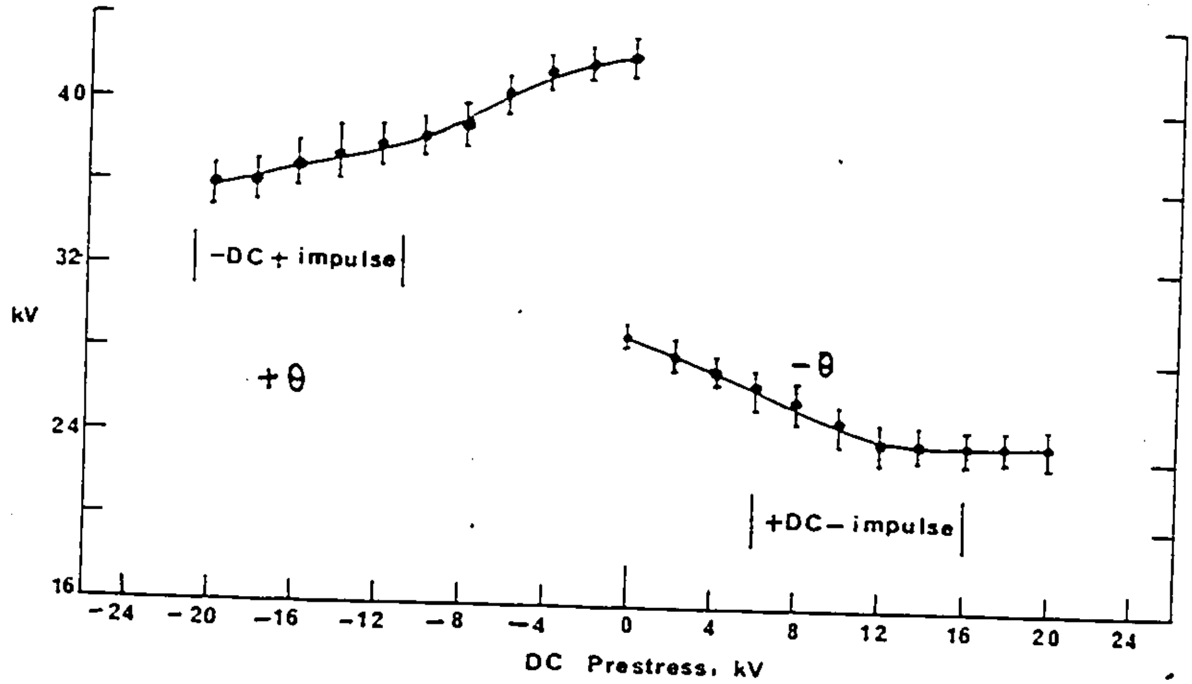

Fig. 4.9. Combined DC and 1.2/50 μs impulse flashover voltage as a function of opposing DC pre-stress for a conical insulator. θ = ± 55°. Macor glass-ceramic, 2 mm thickness, 7 mm base diameter.

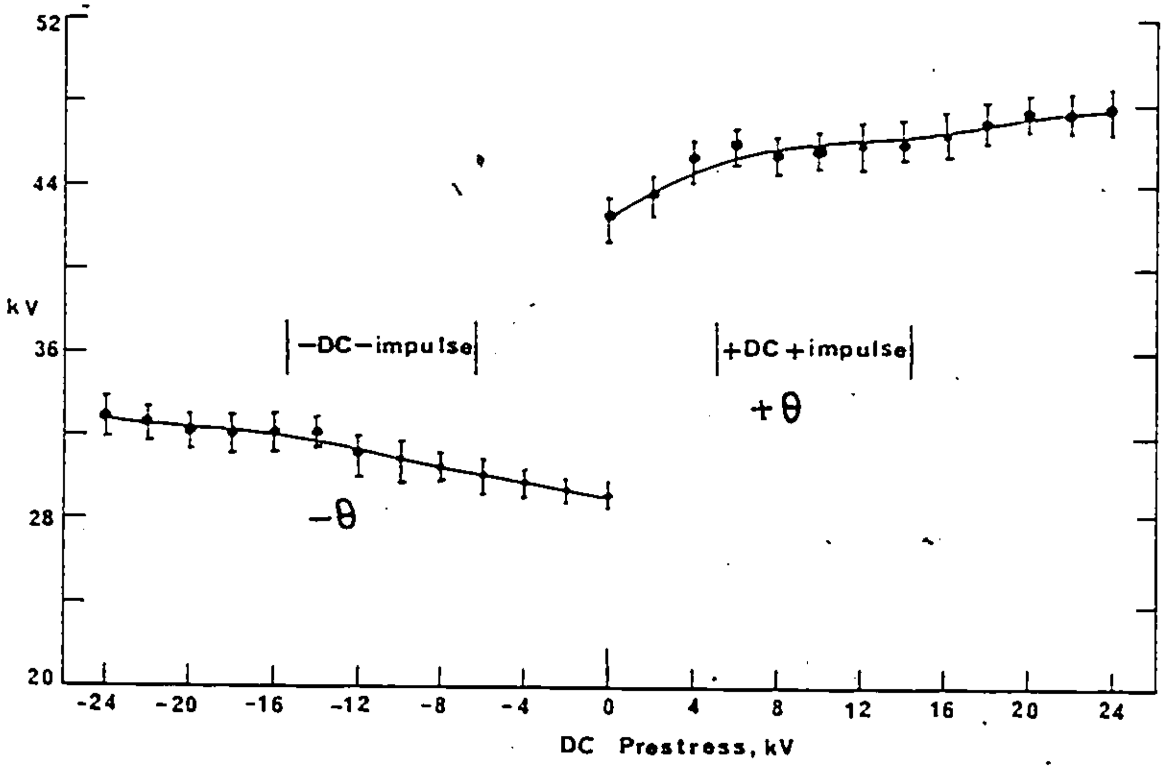

Fig. 4.10. Combined DC and 1.2/50 μs impulse flashover voltage as a function of aiding DC pre-stress for a conical insulator. θ = 55°. Macor glass-ceramic, 2 mm thickness, 7 mm base diameter.

(Fig. 4.10). Similar results are also obtained for $\theta = \pm 45°$.

4.3 Discussion

The reduction in the flashover strength of DC - impulse (and -DC + impulse) subsequent to the application of an opposing DC pre-stress is attributed to the effect of the surface charges accumulated on the solid insulator during and subsequent to the pre-stress period. Since the measured DC - impulse is lower than the impulse level by itself, the effect of the charge which is present on the surface of the solid insulator must be to modify the field in such a way as to increase it in the critical cathode triple junction. Bradwell et al [67] and Cross et al [68] attributed the observed reduction in the breakdown [67] and flashover [68] to a homocharge injection from the electrodes whereby a negative space charge is injected in the region adjacent to the cathode and a positive charge in the region close to the anode. This model enhances the field for opposing pre-stress [67]. Thus qualitatively supports the observed measurements. Kitani and Arii [73] also reported using nanosecond pulses a decrease in the (DC + impulse) breakdown of polyethylene films for opposing DC pre-stress and a slight increase for aiding pre-stress. It should be mentioned that the measurements of the electric field at triple junctions using cylindrical insulators showed intensification at both the anode and the cathode regions

[22,23]. Enhancements in the electric field at both triple junctions can only result from an accumulation of a positive surface charge near the cathode and a negative surface charge near the anode [26].

CHAPTER V

THEORETICAL ANALYSIS OF SURFACE FLASHOVER OF SOLID DIELECTRIC IN VACUUM

The surface of a solid dielectric insulator becomes electrically charged when subjected to a high voltage stress in vacuum. A method for calculating the D.C. surface flashover voltage of the insulator based on the assumption that the discharge occurs in a layer of desorbed gases from the insulator surface is proposed [30]. The electric field strength required to cause surface flashover is calculated by taking into account the secondary electron emission characteristics of the dielectric material. The dependence of the surface flashover field on the insulating material is deduced. A dependence of the flashover voltage on the insulator length to a power law of 0.5 is theoretically predicted. The calculated surface flashover voltage is compared with the previously reported measurements and good agreement is obtained.

5.1 Mechanism of Surface Breakdown

It is generally assumed that the surface of insulators in vacuum becomes positively charged when subjected to a high voltage stress [6-9,24,37]. Fryzman [6] suggested that the electrons emitted at the cathode struck the insulator surface and produced a positively charged insulator surface due to secondary electron emission. This process resulted in an enhancement in the field at the cathode-vacuum-solid insulator triple junction. The electric field at the cathode-junction is further enhanced due to geometrical effects [19], asperities on the cathode [20,21] and voids between the cathode and the insulator [4]. The various effects contribute to the electric field enhancement in the cathode junction which could initiate an insulator flashover.

Bugaev et al [47] showed that the discharge was initiated by individual electrons which might have developed in a layer of gas adsorbed on the surface of the dielectric. Avdienko and Malev [43,44] suggested that the breakdown must be preceded by a stage involving the desorption and expansion of the gas. They reported that the breakdown of solid insulator in vacuum develops in the desorbed gas cloud from the insulator surface. Flashover mechanism based on secondary electron emission from the insulator surface has also been reported [24, 75-78].

5.2 Analysis of the Charging Mechanism

The secondary electron emission rate δ from an insulator surface initially increases with increasing impinging energy of the electrons until it reaches saturation and starts to decrease at high energy. There are two energies at which $\delta = 1$ [79].

In the initial stage of charging, all the electrons striking the insulators surface are emitted from the triple junction. The impinging energy is that gained from the interelectrode field neglecting the energy of emission from the cathode. The region on the insulator surface struck by electrons yielding $\delta > 1$ becomes positively charged [6,7,70]. Near the anode the surface becomes at first slightly negatively charged. When the surface charge density of the positively charged region becomes sufficiently high, many of the secondary electrons emitted from the insulator surface will be attracted back onto the surface. The trajectory range of the electrons emitted from the insulators surface will decrease as the surface charge density increases. The energy at impact will therefore decrease. It will do so until the impact energy is equal to that corresponding to $\delta = 1$ which is the stable operating point and any deviation from it is self-correcting. This also corresponds to the electric field which is inclined at a critical angle with respect to the insulator surface [7,70].

An electron emitted from the surface with an energy A_o and having a direction normal to the insulator surface reaches height x,

$$x = \frac{A_o}{eE_\perp} \qquad (5.1)$$

where x in cm, A_o in eV and $E_\perp$ (in V cm^{-1}) is the field normal to the surface of the insulator due to the surface charge density.

The height of the electron trajectory is very small, a few micrometers, compared to the radius of the curvature of the surface of practical insulators, and therefore can be considered as a plane as far as the trajectory of the electron is concerned.

The range of trajectory is

$$y = \frac{4\ A_o E_{11}}{e E_{\perp}^{2}} \qquad (5.2)$$

where y is in cm and E_{11} (in v cm^{-1}) is the field parallel to the surface of the insulator and equal to the average applied field, E_{av}, in the case of a solid cylindrical insulator. $E_{11} = V/L$ where V is the applied voltage between the electrodes and L the gap spacing. Taking into account the cosine law distribution in the direction of emission, the average value of the impact energy A_i becomes [7]

$$A_i = A_o \left[1 + 2 \left[\frac{E_{11}}{E_{\perp}} \right]^2 \right]. \qquad (5.3)$$

When the steady state of charging is reached at unity yield, the impinging energy is A_1. The reported surface charge density measurements suggest that the stability of the surface charge occurs corresponding to the lower of the two energies A_1, at which the emission yield is unity. The relationship between the field E_{11} and the field $E_{\perp}$ is [7]

$$E_{11} = E_{\perp} \left[\frac{1}{2} \left[\frac{A_1}{A_o} - 1 \right] \right]^{1/2} \qquad (5.4)$$

By assuming the insulator surface as a plane, the field normal to the surface of the insulator resulting from the surface charge can be written as [7]:

$$E_{\perp} = \sigma_{+}/2\varepsilon_{o} \qquad (5.5)$$

where ε_o is the permittivity of the free space (8.85×10^{-14} F/cm) and σ_+ is the charge density in C/cm^2.

The critical angle θ, for which the surface charge is at an equilibrium is given by tanθ. The value of tan θ is determined by using the Equation 5.6.

$$\tan\theta = \frac{E_{\perp}}{E_{11}} = \left[2\, A_{o}/(A_{1} - A_{o}) \right]^{1/2} \qquad (5.6)$$

In general, the secondary emission parameters A_o and A_1 for solid insulators are a few eV and a few tens of eV, respectively. Using the data available on the secondary electron emission yield from insulators [79] the value of θ obtained from equation (5.6) is found to vary from about 10° to 35°. The expression for positive surface charge density σ_+ can be written in terms of the interelectrode field E_{11}

$$\sigma_{+} = 2\, \varepsilon_{o}\, E_{11} \tan\theta \qquad (5.7)$$

The current carried by the secondary emission avalanche depends on the density of negative space charge σ_- and the drift velocity of electrons in the avalanche. The density of the electrons space charge in the emitted secondary electron avalanche cannot exceed the surface charge σ_+ in magnitude without causing electrons to be repelled from the insulator. When the electrons drift towards the anode, the value of σ_- diminishes but at the same time the positive surface charge at the insulator-cathode junction enhances the field at the cathode triple junction. The increased field emission maintains σ_- equal to σ_+[24]. Hence in the analysis it is assumed that σ_- is equal to σ_+. The surface current carried by the secondary emission avalanche per cm can be written as

$$I_{11} = \sigma_- v_e \tag{5.8}$$

where I_{11} is the current per unit length of the insulator surface (A cm^{-1}). The random velocity v_e is used as an approximation for the drift velocity of an electron accelerated to the energy A_1.

$$v_e = (2 A_1 \times 10^4/m_e)^{1/2}, \text{ cm sec}^{-1} \tag{5.9}$$

where m_e is the electron mass in kg and A_1 is the electron impact energy in joule.

From the above relation, the drift velocity of an electron in the avalanche having an energey A_1 eV is

$$v_e = 5.94 \times 10^7 A_1^{1/2}. \qquad (5.10)$$

The surface current expression becomes

$$I_{11} = \sigma_1 \times 5.94 \times 10^7 \times \sqrt{A_1}, \text{ A cm}^{-1} \qquad (5.11)$$

The electrons are returned to the insulator after travelling an average distance of $s = A_1/E_{11}$. The value of s is of the order of $(10^{-4} - 10^{-3}$ cm), when σ_+ is at a saturated steady state. The current density perpendicular to the insulator surface can be obtained as

$$J_\perp = \frac{\sigma_- v_e E_{11}}{A_1}, \text{ A/cm}^2 \qquad (5.12)$$

The desorption rate from the insulator surface depends on $J_\perp$.

5.3 Electron Impact Gas Desorption and Discharge Formation

When electrons impinge on the surface of a solid insulator, the particles released depending on their energy, include neutral molecules, atoms, excited neutrals, positive and negative ions. The ratio of neutrals evolved is very much higher than other particles. In most cases the electron-impact desorption cross-sections are smaller than the corresponding ionization cross-section in the gas phase. Electron impact cross-sections vary with electron energy in a similar fashion to gas-phase ionization cross-sections. The average desorption cross-section is assumed to be 10^{-16} cm^2 [80] as the major components of the desorbed gases are carbon monoxide and hydrogen.

The electron impact desorption probability can be found from experiments on prebreakdown currents by measuring the outgassing rates of gases [80,81]. It is assumed that the prebreakdown current is due to secondary emitted electrons hopping across the surface of a fully charged insulator. For Co, H_2, N_2, H_2O and other molecules which are known to be adhered to the surface, the number of molecules per cm^2 on the surface of dielectric may be taken as the order 10^{16} - 10^{17} cm^{-2} [47,82]. In order to estimate the desorption probability, the results found in a study of the gas evolution from insulators subjected to an electric field in the direction parallel to the surface is considered [81]. The rate of gas evolution depends on the insulating material as well as the desorption probability. A value of outgassing rate of the order of (2-5) x 10^{-7} liter Torr/sec. for different insulating materials (Plexiglass, Teflon, Vinyl, Ceramic) has been reported [81]. The desorption probability corresponding to this outgassing rate, is in the range 5-15 molecules per impinging electron calculated from pre-breakdown currents of (2-6) x 10^{-7}A observed in our experiments. A desorption probability of a few molecules per electron is consistent with the product of an electron impact desorption cross-section of a small multiple of 10^{-16} cm^2 [80,83] and the number of molecules per cm^2 on the surface of 10^{16} - 10^{17} [47,82].

The rate of electron impact gas desorption, J_d, depends on the electron current density $J_\perp$ (A cm^{-2}), the desorption cross-section Q_d (cm^2) and the surface charge density σ_d (molecules/cm^2). The expression for J_d is

$$J_d = \frac{\sigma_d Q_d J_\perp}{e} \text{, molecules/cm}^2 \text{ sec} \tag{5.13}$$

In general the desorbed particle rate is written as

$$J_d = \frac{\gamma\ J_\perp}{e} \tag{5.14}$$

where γ is the desorption probability equal to $\sigma_d Q_d$ molecule/electron.

The electron impact desorption probability of gases from a clean and well outgassed insulator surface can be found by observing the pressure changes in the system housing it during electron bombardment of the sample [83]. The variation in the desorption rate for a particular insulator depends among other things on the sample temperature, the electron impact energy and the electron current density. The desorbed gases from the insulator materials like Teflon (polytetrafluoroethylene), plexiglass (polymethyl methacrylate), ceramic, and alumina (Al_2O_3) contain a higher percentage of hydrogen and water vapour particularly in the case of an unbaked vacuum systems. In a well baked system we assume that the desorbed gas consists of 30-80% CO. In order to find the density of desorbed gas, the velocity, v_o, at which a desorbed neutral leaves the insulator surface must be known. However, only a few data are available on the value of v_o. The average velocity of the gas molecules may be assumed of the order of 1.5 - 2.0 x 10^5 cm sec^{-1} [44, 79,84]. The density of the desorbed molecules, N_d, can be estimated from the value of v_o and the gas desorption rate

$$N_d = \frac{\gamma J_\perp}{e\, v_o} \text{ molecules/cm}^3 \qquad (5.15)$$

The amount of the desorbed gas molecules M per cm^2 from the insulator surface due to a predischarge field current is given by the product of N_d and length of the insulator, ℓ

$$M = \frac{\gamma J_\perp}{e\, v_o} \times \ell \text{ molecules/cm}^2 \qquad (5.16)$$

5.4 Flashover Breakdown Criteria

The electrical field is enhanced at the cathode end of the insulator due to the effect of positive charge accumulation and consequently the electron emission current from the cathode increases. Increasing the applied electric field leads to a rise of the field emission current and consequently, the amount of the desorbed gas increases. The total ionization increases rapidly with increase of the desorbed gas. When the prebreakdown current is low, the gas desorption is also low. In this case, the condition for a self-sustained discharge can only be satisfied at a very high field. There is obviously some critical current, I_{cr}, and a corresponding critical desorbed amount of gas density, M_{cr}, at which the necessary electron density required for breakdown is reached [85].

The breakdown field can be calculated from the value of M_{cr} corresponding to I_{cr}.

From Eqs. [5.5, 5.6, 5.12 and 5.16] and assigning $M = M_{cr}$ the critical value at the onset of the surface flashover, the expression for the field E_{11} required to cause flashover can be written as

$$E_{11} = \left[\frac{M_{cr} \, A_1 \, v_o \, e}{2 \, \varepsilon_o \, \ell \, \gamma \, v_e \, \tan\theta} \right]^{1/2} , \text{ V/cm} \qquad (5.17)$$

Eq. (5.17) indicates the dependence of E_{11} on the secondary electron impact energy, desorption probability and the length of the insulator. It also gives a correct description of the decrease in the dielectric strength of the surface with increasing insulator length.

The breakdown voltage can also be calculated by using Eq. (5.17). The breakdown voltage is almost independent of the electrode material and strongly dependent on the insulator material [2,13]. The breakdown voltage, V_B, is

$$V_B = E_{11}\,\ell = \left[\frac{M_{cr}\,A_1 v_o\,e\,\ell}{2\,\varepsilon_o\,\gamma\,v_e\,\tan\theta}\right]^{1/2}, \text{ volts} \qquad (5.18)$$

Eq. (5.18) shows that the flashover voltage across a solid insulator held between two planar parallel electrodes increases in a non-linear form with increasing length of the insulator. The reported results of References [2,14,86] are plotted in Fig. 5.1 for various insulating materials where it can be seen that a dependence of the flashover voltage on length of the insulator to a power law of $\ell^{0.5}$ is suggested. The predicted dependence of the flashover voltage given by Eq. (5.18) on insulator length is close to that observed experimentally (Fig. 5.1).

5.5 Analysis of the Behaviour of Insulators

The study of flashover in ultra high vacuum of cylindrical insulators made of ceramic and quartz having lengths of up to 8 mm shows that a typical pressure variation in the range $(0.8 - 8.0) \times 10^{-6}$ Torr per 1 litre of system volume is observed at the onset of surface flashover. The gas released from the insulator surface is initially confined to a small cylindrical volume $\pi r^2 \ell$, where r is the radius and ℓ the length of the cylinder, respectively. An estimate

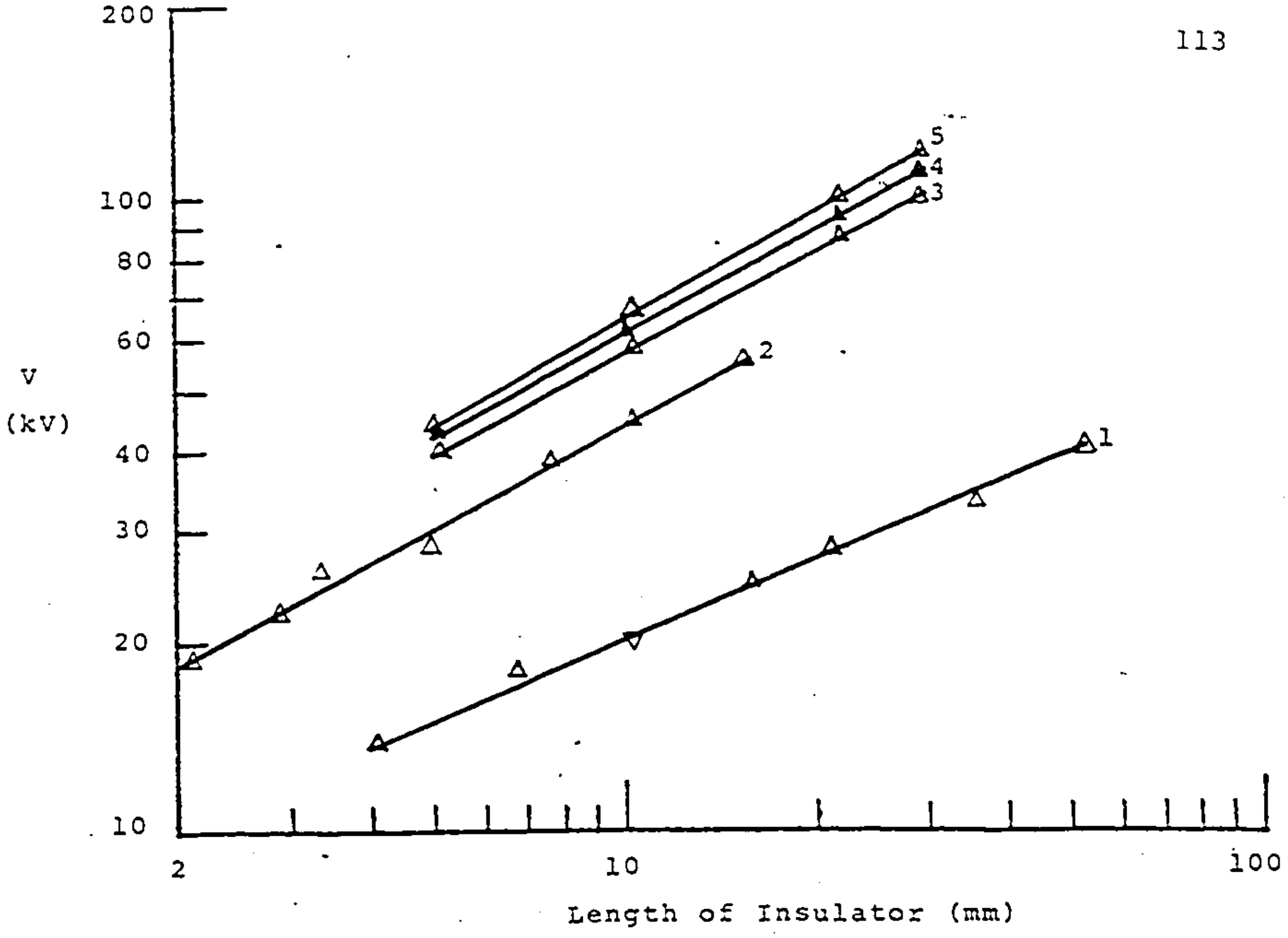

Fig. 5.1. Flashover voltage as a function of insulator length for different materials. 1, Pyrex [2]; 2. alumina ceramic [86]; 3. polyethylene [14]; 4. Teflon [14]; 5. plexiglass [14].

of $r = 10^{-3} - 10^{-1}$ mm appears to be reasonable for our conditions [3,44]. The corresponding gas density times length of the insulator $N_{cr} \ell = M_{cr}$ in the released gas at the onset of the flashover is in the range $(1.4 - 3.2) \times 10^{18}$ molecules cm^{-2}. This is in reasonable agreement with the values of $(2-5) \times 10^{18}$ molecules cm^{-2} reported by Avidenko and Malev [44] for insulators having lengths in the range 0.1 - 10 cm.

The field strength and the breakdown voltage required to cause flashover of various insulators can be calculated by using the physical data available in the literature. Fig. 5.2 shows the dependence of the average electric field strength on the desorption efficiency for plexiglass which has an impact energy of $A_1 = 25$ eV. It is seen that the required electric field strength to cause surface flashover decreases with increasing desorption efficiency. This is because as the desorption efficiency increases, the ionization rate also increases. Hence, the field strength required to get a critical desorbed gas density is reduced in value.

The field strength required to cause a surface flashover in a given insulating material depends on the impact energy A_1. Fig. 5.3 shows the dependence of the flashover field strength on the impact energy at a constant desorption efficiency. It can be seen that the field strength increases

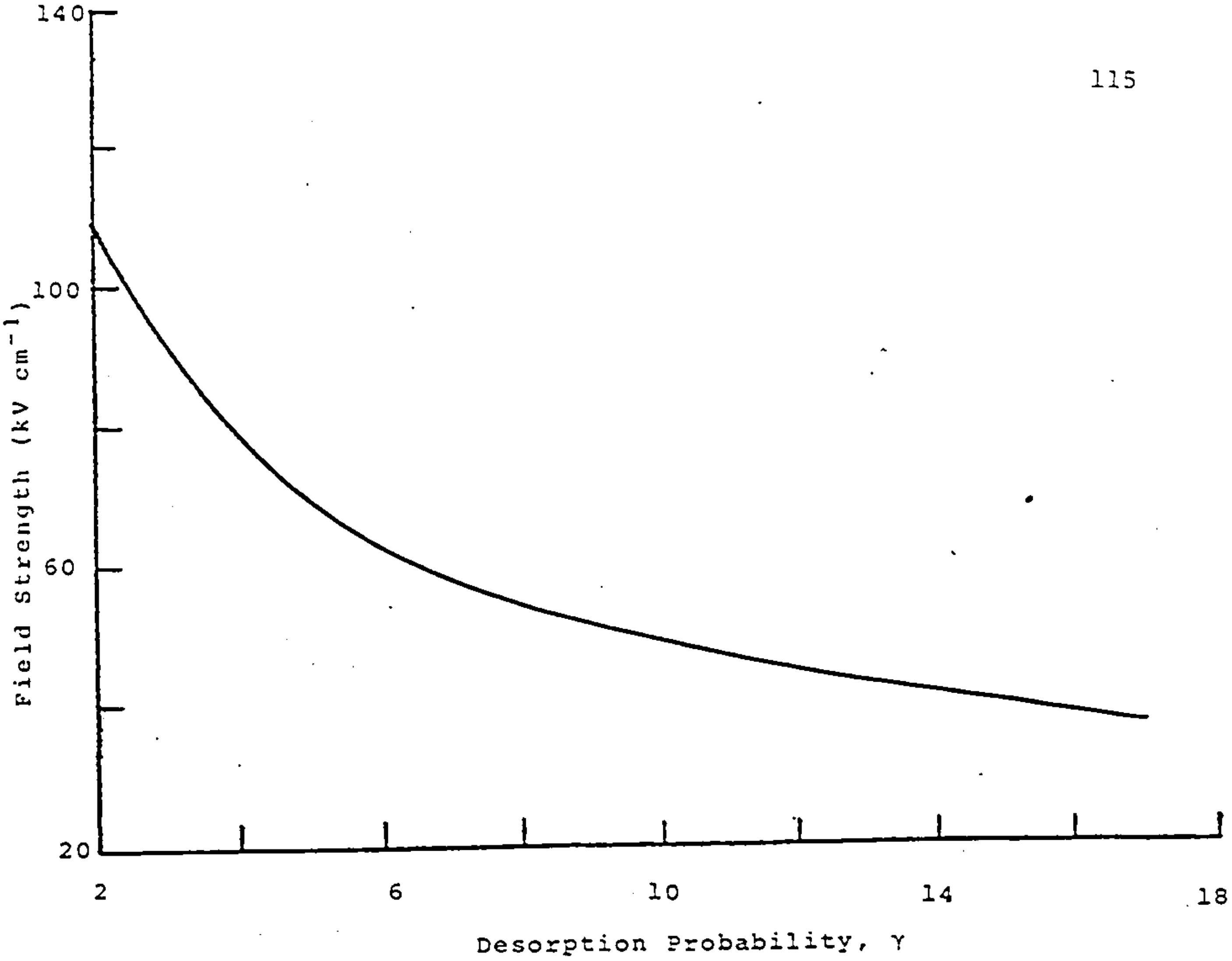

Fig. 5.2. Calculated field strength as a function of desorption probability for Plexiglass. Impact energy A_1 = 25 eV and M_{cr} = 1.4 x 10^{18} cm^{-2}.

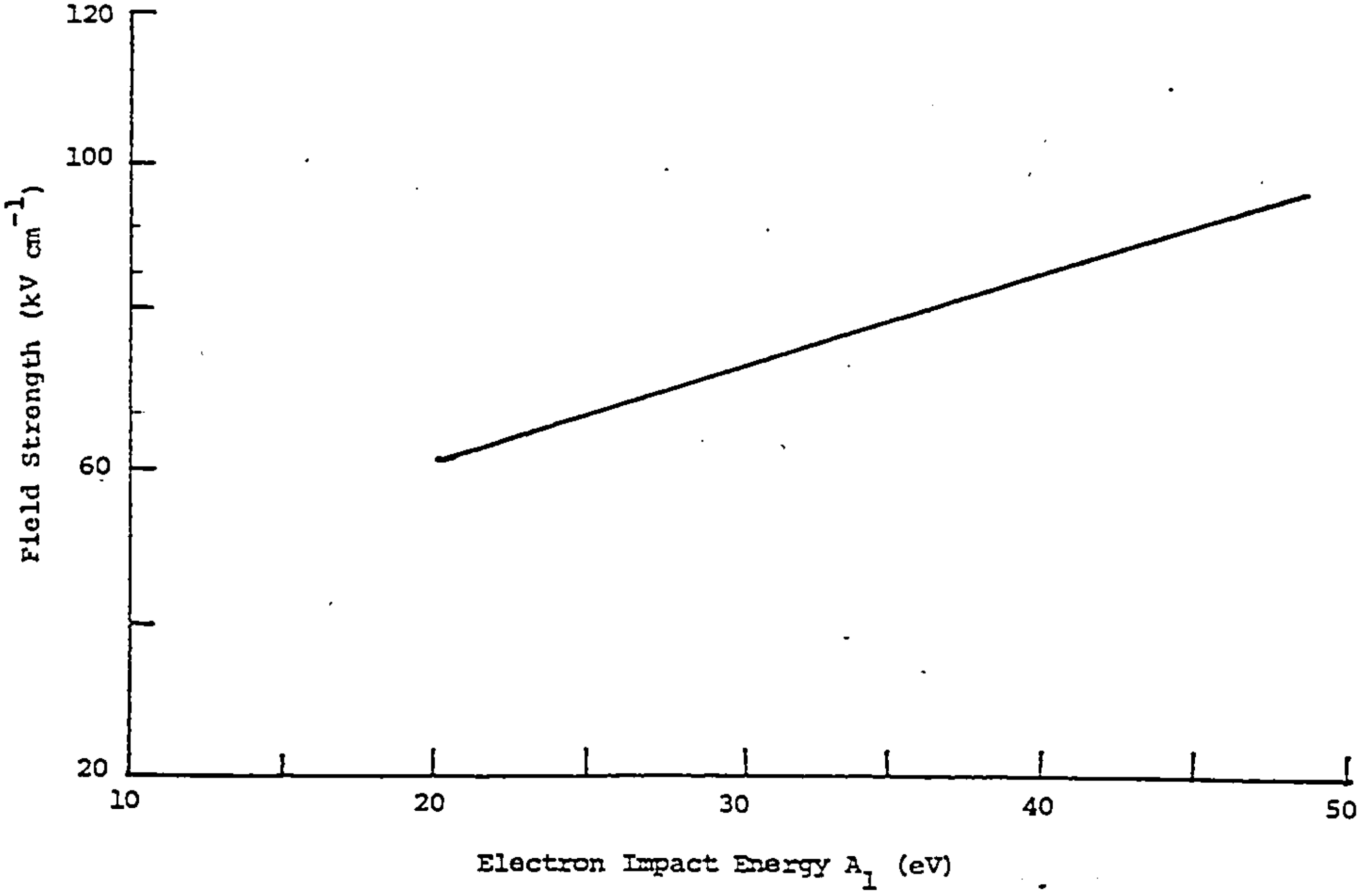

Fig. 5.3. Calculated field strength as a function of electron impact energy. γ = 5 molecule/electron, $M_{cr} = 1.4 \times 10^{18}$ cm^{-2}.

linearly with the impact energy A_1. The higher the value of impact energy, the higher the electric field necessary to cause surface flashover.

The calculated breakdown voltage at various desorption efficiencies for different length of plexiglass is given in Fig. 5.4. It shows the non-linear dependence of the breakdown voltage on insulator length. The variation in the breakdown voltage for different value of probable critical desorption concentration, M_{cr}, (1.4, 2.0, 3.5×10^{18} molecule cm^{-2}) is shown in Fig. 5.5. If a higher value is assumed for the critical desorption concentration, the estimated value of the breakdown voltage increases as can be seen from Fig. 5.5. The calculated breakdown voltage of alumina ceramic, quartz, plexiglas and pyrex glass using Eq. (5.18) as a function of insulator length is shown in Fig. 5.6. The measured values for alumina ceramic [86] in the range 2 mm - 12 mm length and plexiglas [14] in the range 5 mm - 20 mm are shown in Fig. 5.6 for comparison with the present calculation of the flashover voltage. There is good agreement between the measured and predicted values. In the case of quartz [3] the reported flashover voltage at 22 mm length is 82 kV. The calculated value for quartz having an impact energy of 30 eV at 22 mm is 87 kV. The measured values for quartz at 1.96 mm, and 3.5 mm from our laboratories is 40 kV and 54.5 kV respectively.

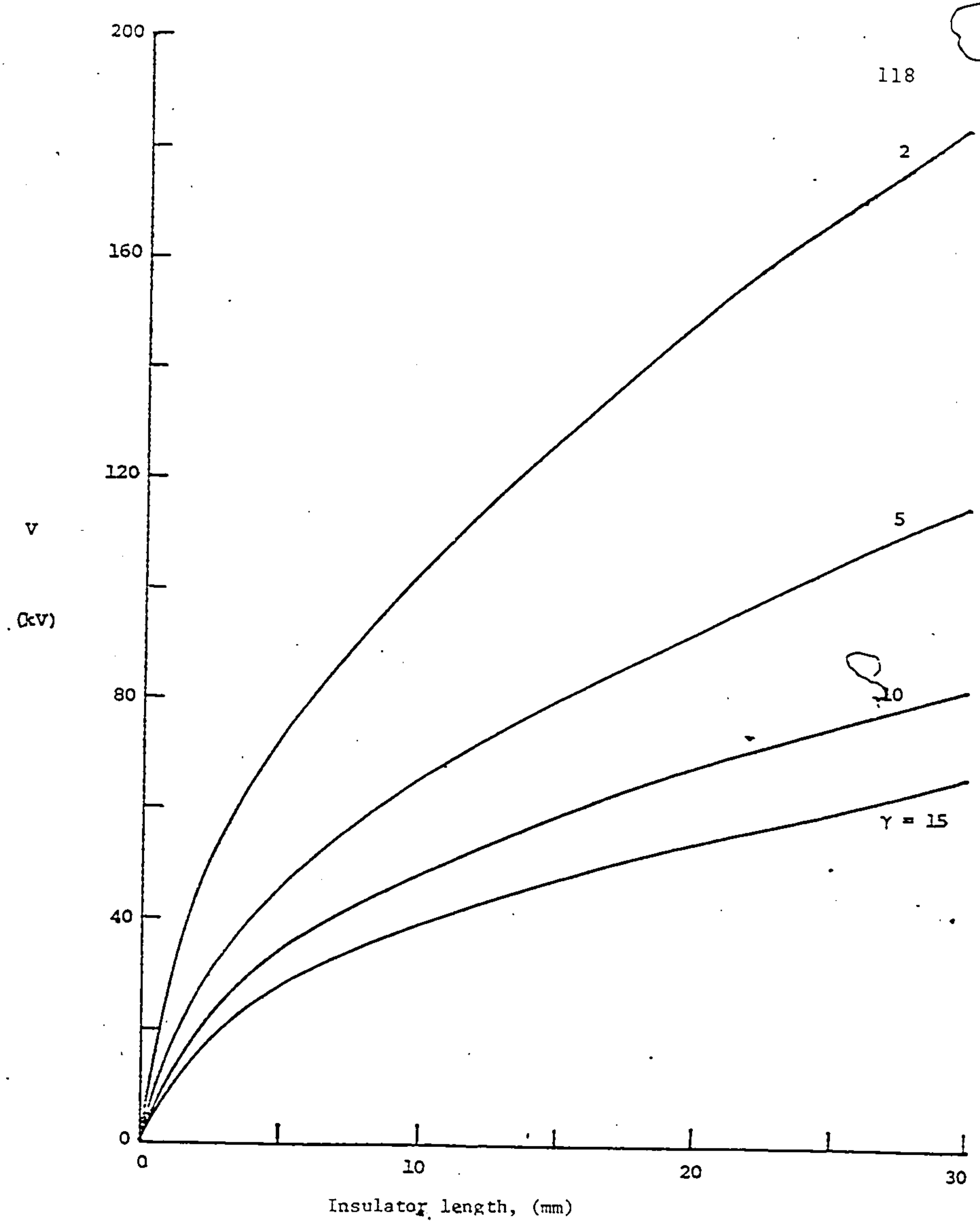

Fig. 5.4. Calculated surface flashover voltage as a function of insulator length for plexiglass for different desorption probability values of γ. $M_{cr} = 1.4 \times 10^{18}$ cm^{-2}.

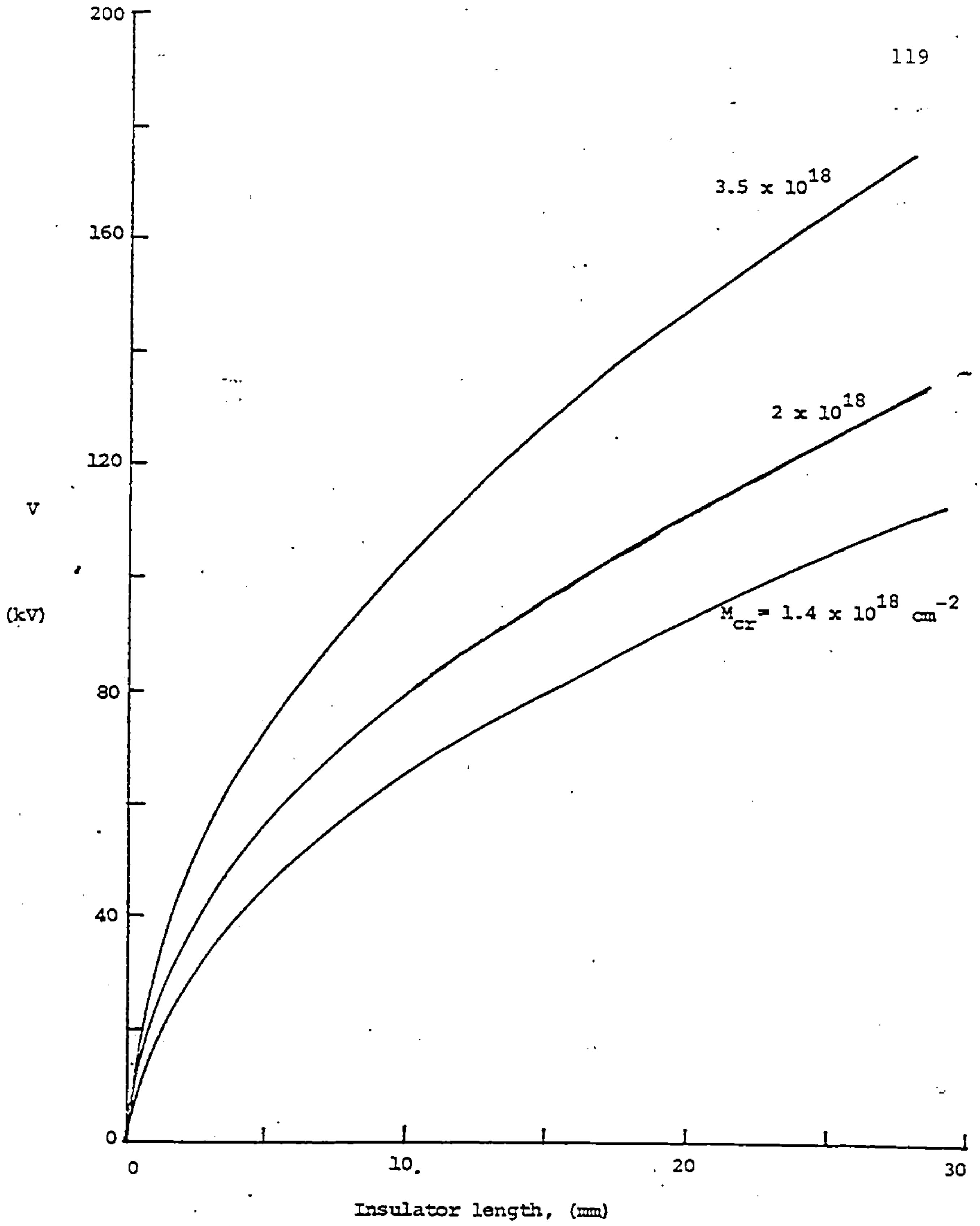

Fig. 5.5. Calculated flashover voltage as a function of insulator length for different values of M_{cr}. $\gamma = 5$; $A_1 = 25$ eV (for Plexiglass).

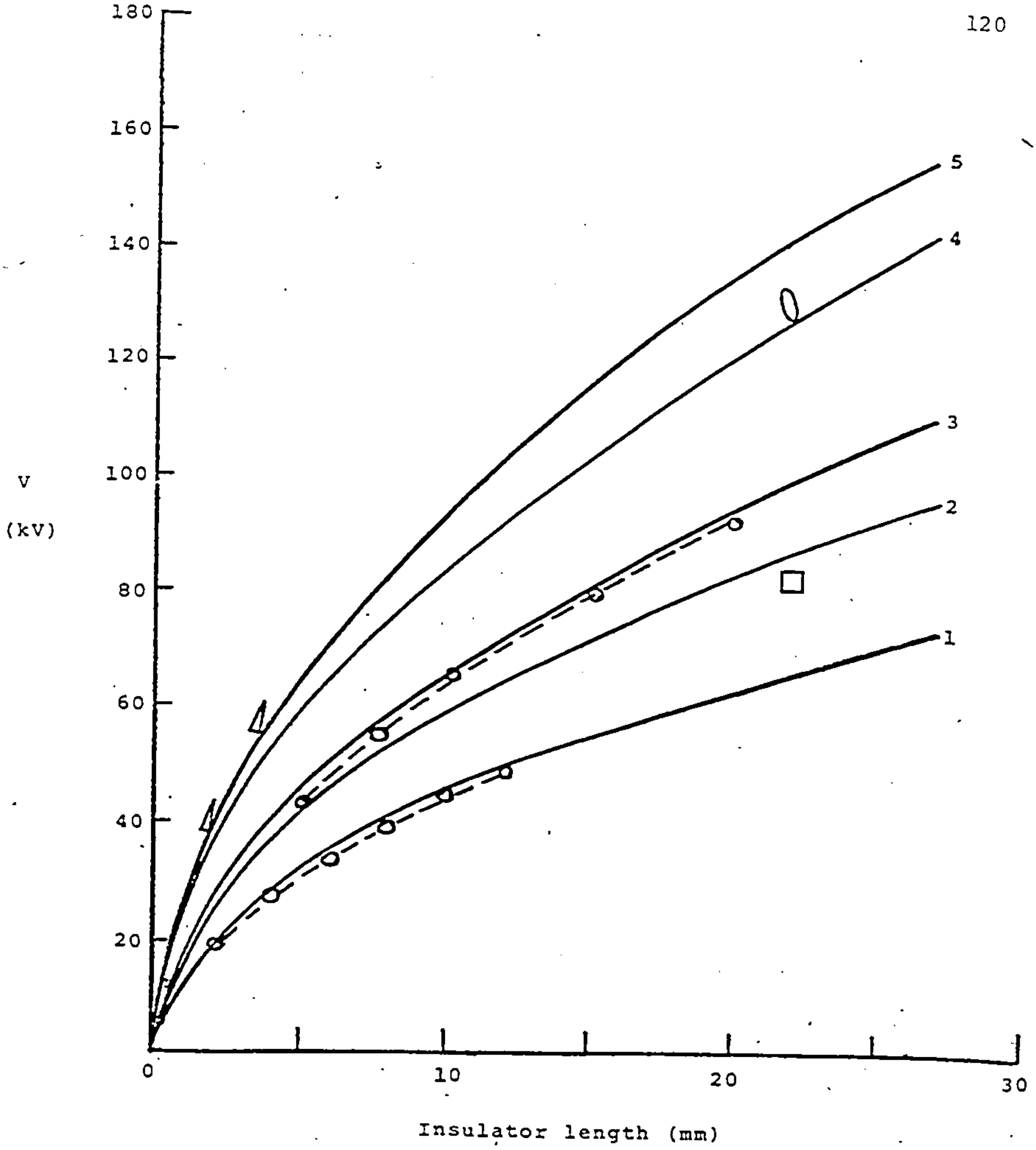

Fig. 5.6. Comparison of calculated and measured surface flashover voltage for different insulating materials as a function of insulator length. ($M_{cr} = 1.4 \times 10^{18}$ cm^{-2}). Curve 1, alumina ceramic [86] $\gamma = 8$, $A_1 = 20$ eV); curve 2, Quartz ($\gamma = 8$, $A_1 = 30$ eV); curve 3, Plexiglass [14] ($\gamma = 5$, $A_1 = 25$ eV); curve 4, Pyrex glass ($\gamma = 5$, $A_1 = 40$ eV); curve 5, Quartz ($\gamma = 5$, $A_1 = 50$ eV). (——) calculated; (- -) measured 3 ; □ Quartz (Measured) [3]; ⬯ Glass (Measured) [3]; ▲ Quartz (measured, present work).

This is in agreement with the predicted value of quartz having an impact energy of $A_1 = 50$ eV. It should be noted that a desorption probability in the range $\gamma = 4 - 8$ molecules/electron seems to be a reasonable value. In general, the surface flashover voltage is higher for insulating materials having higher electron impact energy.

CHAPTER VI

ELECTRIC FIELD COMPUTATION OF DIFFERENT SHAPES OF SOLID INSULATORS

6.1 Introduction

The electric fields calculation requires the solution of Laplace's and Poisson's equations with boundary conditions satisfied. The solution to the above equations can be obtained either by analytical or numerical methods. The analytical solution is very difficult or may be impossible for complex physical systems. Hence, in engineering applications the numerical methods are extensively used for the computation of electrostatic fields. The available numerical methods are generally based on difference techniques or integral concepts. The difference technique is based on employing Laplace's and Poisson's equations in the space where the field is to be calculated. This is carried out by dividing the whole space into small meshes. In the integral concept method, the computation of electric fields is to integrate Laplace's or Poisson's equation either by using discrete charges or by dividing the electrode surface into subsections of charges. The concept of discrete charges is used in the charge simulation method [87]. The charge simulation technique is proved to be successful in the case of three-dimensional field problems [87,88], multi-dielectric (vacuum and solid dielectric) arrangements [87,89,90] and to space charge problems. This chapter describes the application of charge simulation technique to the numerical computations of fields in vacuum-solid dielectric system.

6.2 Computation of Field in Two-Dielectric Arrangement Using Charge Simulation Technique

The charge simulation technique is based on the simulation of the actual field with a field formed by a finite number of fictitious charges, the values of which are determined from the boundary conditions at the contour points [87]. The method involves the selection of a set of charges suitable for modelling the systems of electrodes and the solid insulator. The type of charge systems commonly used are the point-charge which is due to its spherically symmetrical field behavior suits spherically shaped surfaces; the ring charge (toroidal line charge) which can be applied to modelling axially symmetric components and the line charge which is appropriate to cylindrical configurations that includes the region with translational symmetry. As shown in Fig. 6.1 a solid dielectric cylinder mounted between uniform electrodes in vacuum is chosen to explain the method. Since the arrangement considered has a rotational symmetry, the charge simulation is carried out by employing ring charges to model the electrodes and the solid dielectric boundaries. The arrangement of charge locations (x) and contour points (o) used are also given in Fig. 6.1.

The charge distribution at the electrodes is simulated by the ring charges located inside the electrodes. Each electrode has $n_e/2$ ring charges where n_e is the total number of ring charges used for both electrodes. The charge distribution at the solid dielectric-vacuum interface is simulated by $2\ n_d$ ring charges located at either side of the interface of the solid dielectric, as shown in Fig. 6.1. In order to determine the magnitude of the charges, the contour points are chosen both on the surface of the electrodes and the solid dielectric boundary.

The charges inside the electrodes are valid for the calculation of potentials and field strengths inside the solid dielectric and in the vacuum media. The charges in the vacuum side are valid for the solid dielectric and the charges placed on the solid dielectric side of the interface are valid for calculating the potential and field values in the vacuum side.

The potential of the countour points at the top electrode on the solid dielectric side must be equal to the applied potential V and at the bottom electrode equal

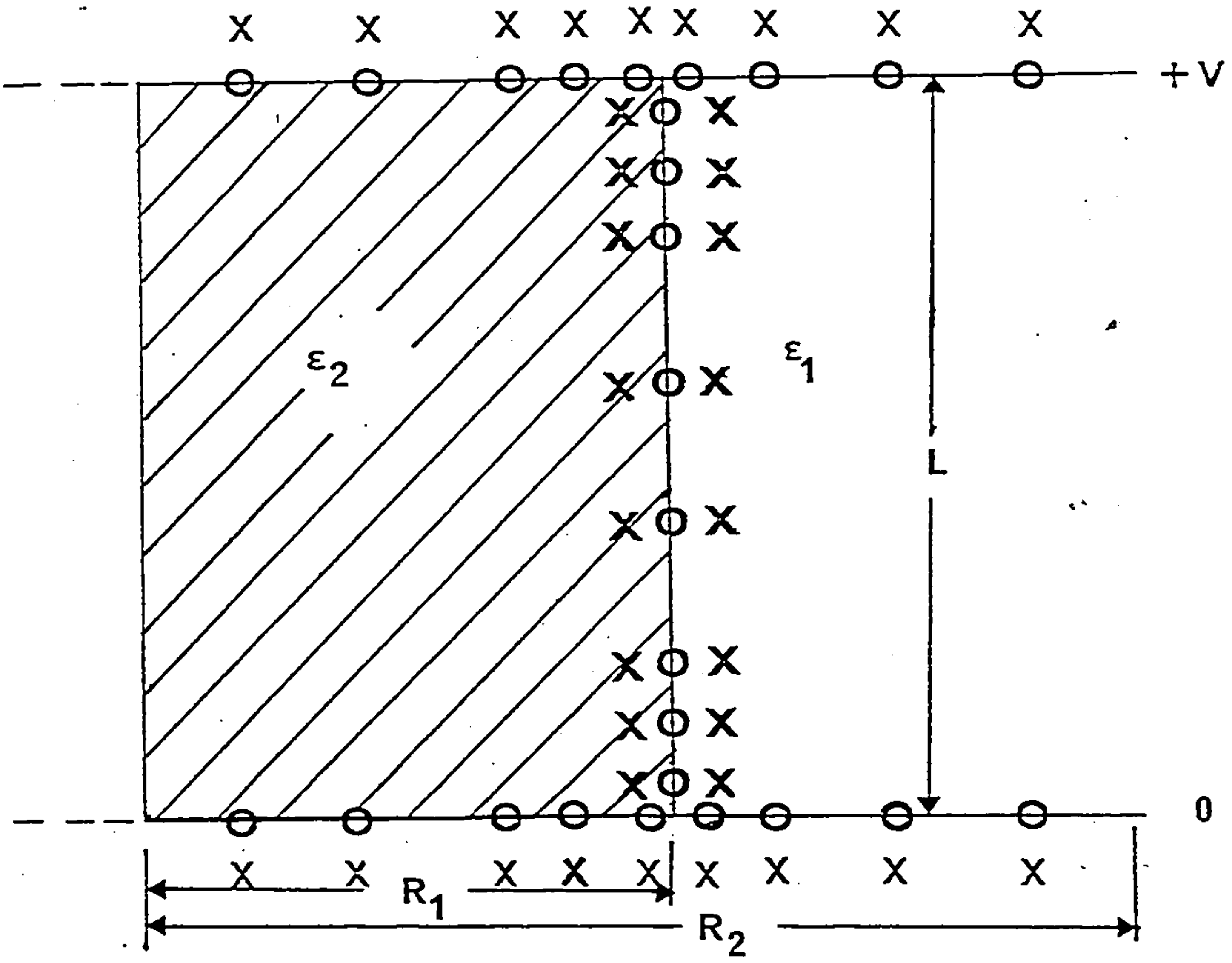

Fig. 6.1. Distribution of ring charges and contour points in electrode-cylindrical solid insulator system. O, contour point; x, ring charge location; R_1, radius of solid insulator rod; R_2, radius of the disc electrode; L, length of the solid insulator rod. ε_1, relative dielectric constant of vacuum ($\varepsilon_1 = 1$); ε_2, relative dielectric constant of solid insulator. V, applied positive voltage to the top electrode and zero to the bottom electrode.

to zero. The equation at the top electrode, for example, is

$$\sum_{j=1}^{n_e} P_{ij} Q_j + \sum_{j=n_e+1}^{n_e+n_d} P_{ij} Q_j = V \qquad (6.1)$$

In the case of the grounded electrode, Eq. (6.1) is equated to 0.

On the side of the vacuum the potential of the contour points at the electrode must also be V′ and 0 at the top and bottom electrodes, respectively. For the top electrode the equation is

$$\sum_{j=1}^{n_e} P_{ij} Q_j + \sum_{j=n_e+n_d+1}^{n_e+2n_d} P_{ij} Q_j = V \qquad (6.2)$$

In the case of the grounded electrode, Eq (6.2) is equated to 0.

The potential of the contour points of the solid dielectric-vacuum interface is unknown but it must be the same whether it is calculated from the region of vacuum or from the solid dielectric.

$$\sum_{j=n_e+1}^{n_e+n_d} P_{ij} Q_j = \sum_{j=n_e+n_d+1}^{n_e+2n_d} P_{ij} Q_j \qquad (6.3)$$

In Equations 6.1, 6.2 and 6.3, P_{ij} is the potential coefficient of the contour point at location i due to the influence of the charge located at position j and Q_j is the value of the ring charge at location j.

At the contour points on the solid dielectric-vacuum boundary the normal component of the flux densities are continuous [87,89]. Let D_{n1} be the normal component of the flux density in the vacuum side and D_{n2} be the normal component in the solid dielectric side. The normal flux densities are continuous across the interface between the solid insulator-vacuum boundary. When electric charge is not residing on the surface

$$D_{n1} = D_{n2}$$

Hence
$$\varepsilon_0 \, \varepsilon_1 \; E_{n1} = \varepsilon_0 \, \varepsilon_2 \, E_{n2} \tag{6.4}$$

where E_{n1} and E_{n2} are the normal components of the electric field in vacuum (region 1) and the solid dielectric (region 2), respectively, ε_1 and ε_2 are the relative dielectric constants of vacuum (ε_1=1) and the solid insulator, respectively and ε_0 is the permittivity of free space ($\varepsilon_0 = 8.85 \times 10^{-14}$ F cm^{-1}). Hence at the contour points on the dielectric boundary, the normal field strength in the vacuum must be ε_2 times greater than in the dielectric, that is

$$\varepsilon_2 \left[\sum_{j=1}^{n_e} F_{ij} Q_j + \sum_{j=n_e+1}^{n_e+n_d} F_{ij} Q_j \right]$$

$$= \sum_{j=1}^{n_e} F_{ij} Qj + \sum_{j=n_e+n_d+1}^{n_e+2n_d} F_{ij} Q_j \qquad (6.5)$$

where the field coefficient F_{ij} is the contribution of the charge j to the normal component of the field vector at the given contour point i on the dielectric boundary. The potential (P_{ij}) and field (F_{ij}) coefficients at a point (r,z) is given in the Appendix I.

The number of equations (n_e+2n_d) are equal to the number of the unknown ring charges. From these equations the magnitude of each charge Q_j can be obtained.

The accuracy of the charge simulation technique largely depends on the positioning of the charges and the corresponding contour points. The accuracy of the calculations is increased with increasing the number of charges, but beyond a certain optimum number of charges, the increase in the number of charges assumed has little effect on the accuracy of the computed electric field [89]. In general the accuracy of the computed electric fields is improved by increasing the density of the contour points in the region of interest. A practical criterion is obtained by the definition of an assignment factor [87], defined as the ratio of the distance between two successive contour points and the distance between a contour point and the corresponding charge location. Experience shows that [18, 19, 91] the assignment factor should be kept between 0.8 - 1.8 to obtain reliable computation results.

The following criteria are used to evaluate the accuracy of the solution: 1. The potential of the electrode surface at locations other than at the contour points is calculated from the charges modelling the system. A measure of the accuracy of the simulation is the "potential error" (defined as the difference between the known electrode potential and the computed potential at the electrode surface) at various check points on the surface of the electrode between the contour points [87]. The potential error should be less than 1% in the vicinity of the electrode in order that a similarly small error value is obtained in the field strength. 2. The potential discrepancy (defined as the difference in the solutions for the potential at the solid dielectric-vacuum boundary evaluated on both sides of the interface) should be small (<1%) [92]. It should be noted that the accuracy of the charge simulation of the geometry has a practical limit arising from the manufacturing tolerances of the conducting electrodes and the determination of the relative dielectric constant of the solid insulator.

6.3 Application to a Solid Insulator Block with Convex Curved Edges

Figure 6.2 shows a cross-section of an infinite solid insulator block with convex edges sandwiched between two discs of metal electrodes in vacuum (or in a gas, $\varepsilon_1 = 1$). The solid insulator has a rounded edge of radius r at both electrode junctions. The insulator has planar symmetry as in the case of a rectangular or prism shaped insulator. The field at the solid insulator-vacuum-electrode junctions is enhanced due to geometrical effects such as rounded edge of the solid insulator at the junction because the solid insulator may not meet the electrode surface at 90°. The field near the triple junctions is of considerable interest in the design of insulator for high voltage applications. The field enhancement at the triple junction has been analyzed using charge simulation method by assuming different solid insulator-electrode configurations that can arise in multi-dielectric arrangements. Infinite line charges are used.

Figure 6.3 shows the angle of contact α between the solid insulator and the planar electrode which may vary in the range 0 - 90°. The location on the curved surface of the solid insulator is determined by the angle θ which is defined as the angle between the line OP connecting the origin x_o, y_o to the contact point P of the solid boundary of the solid insulator. The dependence of the field is studied for varying contact angle α between the solid insulator and the electrode in the range 0 - 90°, for a varying ratio r/L of the radius of curvature r of the

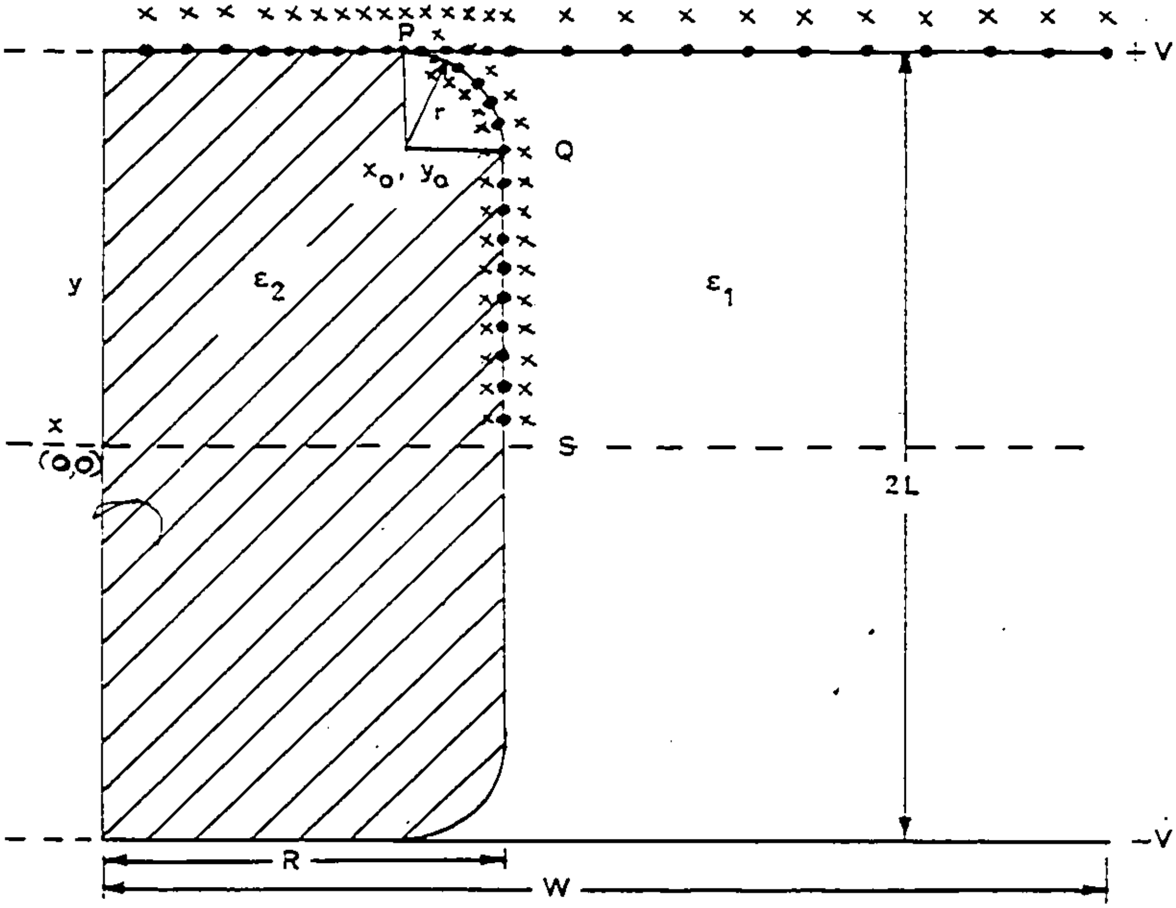

Fig. 6.2. Distribution of infinite line charges in the electrode-solid insulator block system. • contour point; x, infinite line charge; r, radius of circle of curved edge; R, width of solid insulator block; W, width of electrode; 2L, length of solid insulator block. Applied voltage to the top electrode = V; applied voltage to the bottom electrode = -V. Number of contour points; electrode, 20; curved section PQ of solid insulator = 20; linear section QS of solid insulator = 18.

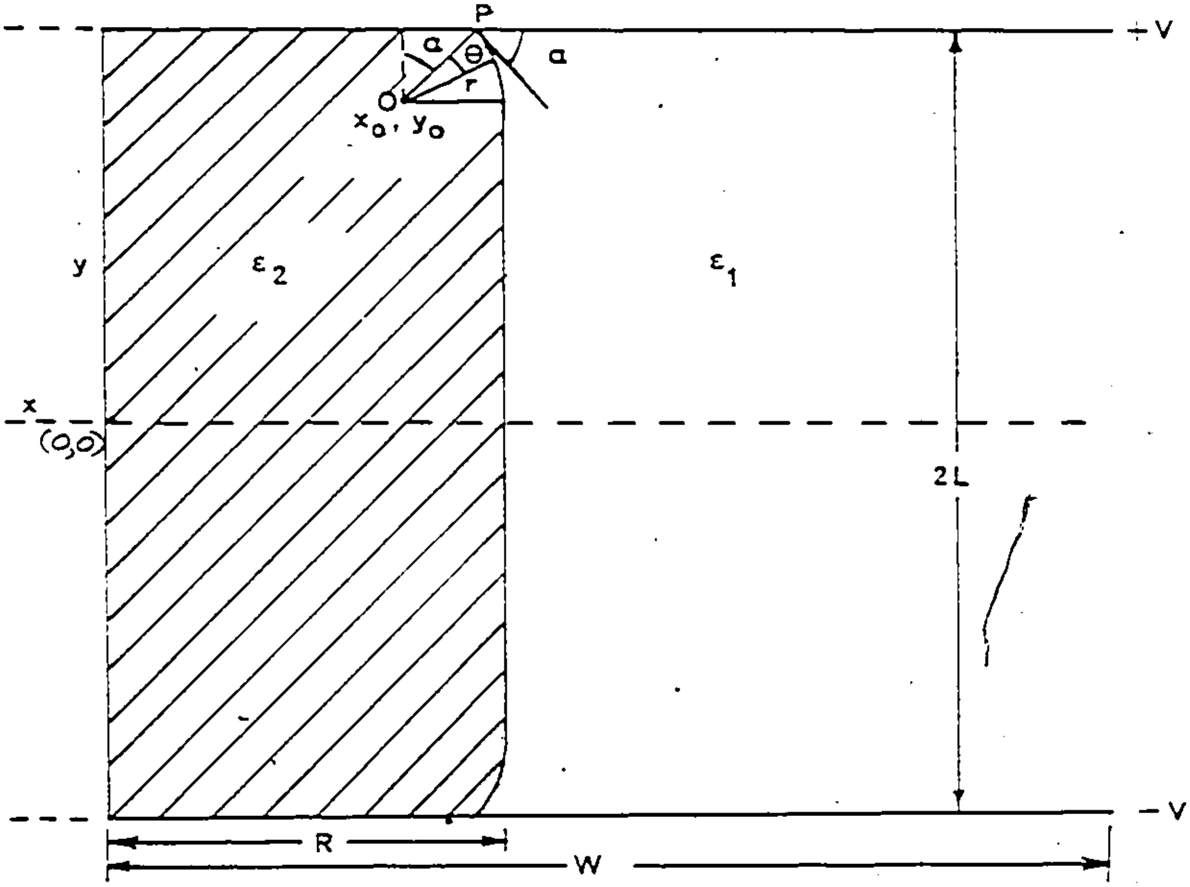

Fig. 6.3. Schematic diagram of the vacuum gap (ε_1) bridged by a solid insulator (ε_2). α, angle between insulator and electrode surface; r, radius of curved edge; P, contact point of solid insulator with the electrode.

rounded edge of the solid insulator at the junction to the length of the solid insulator L (Fig. 6.3) and the material of the solid insulator

6.3.1 Computation of Electric Field in Two Dimensional Arrangement

A set of n-points selected on a surface at a potential V and n charges inside the electrode leads to a system of n-linear equations for the n-infinite line charges in the form

$$V_i = \sum_{j=1}^{n} P_{ij} \lambda_j, \quad i = 1, 2, \ldots, n \qquad (6.6)$$

where P_{ij} is the potential coefficient at the i-th contour point due to line charges of infinite length at the position j, V_i the voltage at the i-th contour point and λ_j is the charge per unit length. The potential coefficients of infinite line charges are defined by [87,93]

$$P_{ij} = \frac{1}{2\pi\varepsilon_o\varepsilon_2} \ln \left[\sqrt{(y_i+y_j)^2 + (x_i-x_j)^2} \Big/ \sqrt{(y_i-y_j)^2 + (x_i-x_j)^2} \right] \qquad (6.7)$$

where x_i, y_i and x_j, y_j are the coordinates of the contour point and the charge location, respectively in the two-dimensional system, ε_o is the dielectric constant of vacuum $= 8.85 \times 10^{-12}$ F/m and ε_2 is the relative dielectric constant of the solid insulator. Since the arrangement is symmetrical about the x and y axes only one quarter of the system needs to be analyzed. The potential coefficient is computed as the combined effects of charges from both sides of the axis symmetry. The field components E_x and E_y are calculated from

$$E_x = \frac{1}{2\pi\varepsilon_o\varepsilon_2} \sum_{j=1}^{n} \lambda_j \left[\frac{x_i - x_j}{(y_i-y_j)^2 + (x_i-x_j)^2} - \frac{x_i - x_j}{(y_i+y_j)^2 + (x_i-x_j)^2} \right] \quad (6.8)$$

$$E_y = \frac{1}{2\pi\varepsilon_o\varepsilon_2} \sum_{j=1}^{n} \lambda_j \left[\frac{y_i - y_j}{(y_i-y_j)^2 + (x_i-x_j)^2} - \frac{y_i + y_j}{(y_i+y_j)^2 + (x_i-x_j)^2} \right] \quad (6.9)$$

the origin of the cartesian coordinates is conveniently chosen at the centre of the solid insulator block which is also at the centre of the insulating vacuum-solid block gap.

6.3.2 Normal and Tangential Fields Calculations

The normal E_n and the tangential E_t fields are calculated assuming the curved portion of the solid insulator is a quadrant of a circle having a radius r with respect to the origin (x_o, y_o) as shown in Fig. 6.2.

$$\bar{E} = E_x \, \bar{a}_x + E_y \, \bar{a}_y \quad (6.10)$$

where $\bar{a}_x$ and $\bar{a}_y$ are unit vectors in the directions of x and y, respectively.

The normal field

$$E_n = |\,\bar{a}_r \cdot \bar{E}\,| = \frac{E_x(x_1 - x_0) + E_y(y_1 - y_0)}{\sqrt{(x_1 - x_0)^2 + (y_1 - y_0)^2}} \qquad (6.11)$$

the tangential field

$$E_t = |\,\bar{a}_r \times \hat{E}\,| = \frac{E_y(x_1 - x_0) - E_x(y_1 - y_0)}{\sqrt{(x_1 - x_0)^2 + (y_1 - y_0)^2}} \qquad (6.12)$$

where $\bar{a}_r$ is a unit vector in the direction of r (Fig. 6.3).

$$\bar{a}_r = \frac{\bar{r}}{|r|} = \frac{(x_1 - x_0)\bar{a}_x + (y_1 - y_0)\bar{a}_y}{\sqrt{(x_1 - x_0)^2 + (y_1 - y_0)^2}} \qquad (6.13)$$

The computed results of the fields are presented in a normalized format. The average field in the gap is $E_{av} = V/L$. +V and -V are the applied voltages to the anode and cathode, respectively and 2L is the length of the insulator forming also the gap distance between the electrodes.

$$E_n' = E_n/E_{av} = E_n\ L/V \qquad (6.14)$$

$$E_t' = E_t/E_{av} = E_t\ L/V \qquad (6.15)$$

where E_n' and E_t' are normalized normal and tangential field components, respectively. E_x' and E_y' are similarly defined as the normalized components of the field E_x and E_y. In the interior region of the solid insulator and outside it (i.e., in the vacuum) we define $E'_x = E'_n$ and $E'_t = E'_y$. It should be noted that along the non-curved portion of the boundary, $E'_n = E'_x$ and $E'_t = E'_y$.

6.4 Solid Insulator-Electrode Junction Field Calculation (Contact angle $\alpha = 0$).

For $\alpha = 0$ the electrode surface is tangential to the solid insulator at the line of contact P (Fig. 6.2). In order to assume zero contact angle, the rounded edge of the solid insulator is assumed to be of a circular shape of radius r. The charge simulation is carried out by employing 20 infinite line charges to model the electrode and 76 infinite line charges to model the solid dielectric boundary. The potential and field strengths along the curved surface are calculated at an interval of 1.5°. The quality of the solution is evaluated by computing the potential error, the potential discrepancy and the tangential electric field discrepancy as specified in Section 6.2.

The maximum potential error was found to be about 0.78% near the central axis (Fig. 6.2). The maximum potential discrepancy is 0.01% near the contact region with the electrodes and less than 0.01% in the rest of the solid insulator boundary. The maximum discrepancy in the tangential field is found to be 2.5% near the contact region with the electrodes in the material having the highest dielectric constant of $\varepsilon_2 = 12000$. For materials having a dielectric constant in the range $\varepsilon_2 = 2.1 - 10$ the maximum tangential discrepancy is about 2% in the contact region with the electrode. The tangential field discrepancy is less than 1% in the rest of the solid insulator boundary. For the cases of solid insulator materials having a very high dielectric constant ($\varepsilon_2 > 30$), the difference between the normal flux density ($\varepsilon_1 E_{n_1}$) values obtained using charges inside the solid dielectric and from using the charges on the vacuum side to calculate $\varepsilon_2 E_{n_2}$ on the curved boundary other than the contour points is found to be higher at 10 to 20% for ε_2 in the range 650 - 12,000. However, these are special cases involving very high relative dielectric constants which tend to enhance the difference between the two normal fields. The tangential fields are affected much less. The fields are computed for various insulating materials including Teflon ($\varepsilon_2 = 2.1$), quartz ($\varepsilon_2 = 3.8$), Pyrex glass ($\varepsilon_2 = 5.0$), Macor glass ceramic ($\varepsilon_2 = 5.8$), porcelain-zircon ($\varepsilon_2 = 10.0$), titanium dioxide ($\varepsilon_2 = 20\text{-}100$), Hevea compound ($\varepsilon_2 = 36$), Tempradex ($\varepsilon_2 = 650$), Faradex ($\varepsilon_2 = 4500$) and barium titanate ($\varepsilon_2 = 12000$) [94].

6.4.1 Effect of Convex Curved Edges on Field Distribution ($\alpha = 0$, $\varepsilon_2 = 3.8$)

The effects of the convex curved edge surface on the field distribution at the solid insulator-vacuum interface, inside the solid insulator and in the vacuum are investigated. Fig. 6.4 shows the computed normalized tangential and normal fields for quartz ($\varepsilon_2 = 3.8$) at a contact angle $\alpha = 0$ of the solid insulator with the electrode. The field components are calculated at the solid insulator-vacuum boundary just inside the insulator (curves a_t and a_n), away from the boundary in the interior of the solid dielectric (curves b_t and b_n; $x/W = 0.15$) and in vacuum which is away from the solid insulator (curves c_t and c_n; $x/W = 0.8$). The distance x is measured from the central axis (Fig. 6.2). It should be mentioned that the normal field component on the solid insulator-vacuum boundary on the vacuum side E'_{n_1} is ε_2 times the normal field just inside the insulator E'_{n_2}. The tangential fields on both sides of the solid insulator-vacuum boundary are equal $E'_{t_1} = E'_{t_2}$. In Fig. 6.4 the normal field component on the solid insulator boundary is given for the location inside the insulator to show the influence of the investigated parameters more pronouncedly. For Fig. 6.4 the width of the electrodes (2W) and the solid insulator block (2R) used are chosen conveniently to be 200 and 80 mm,

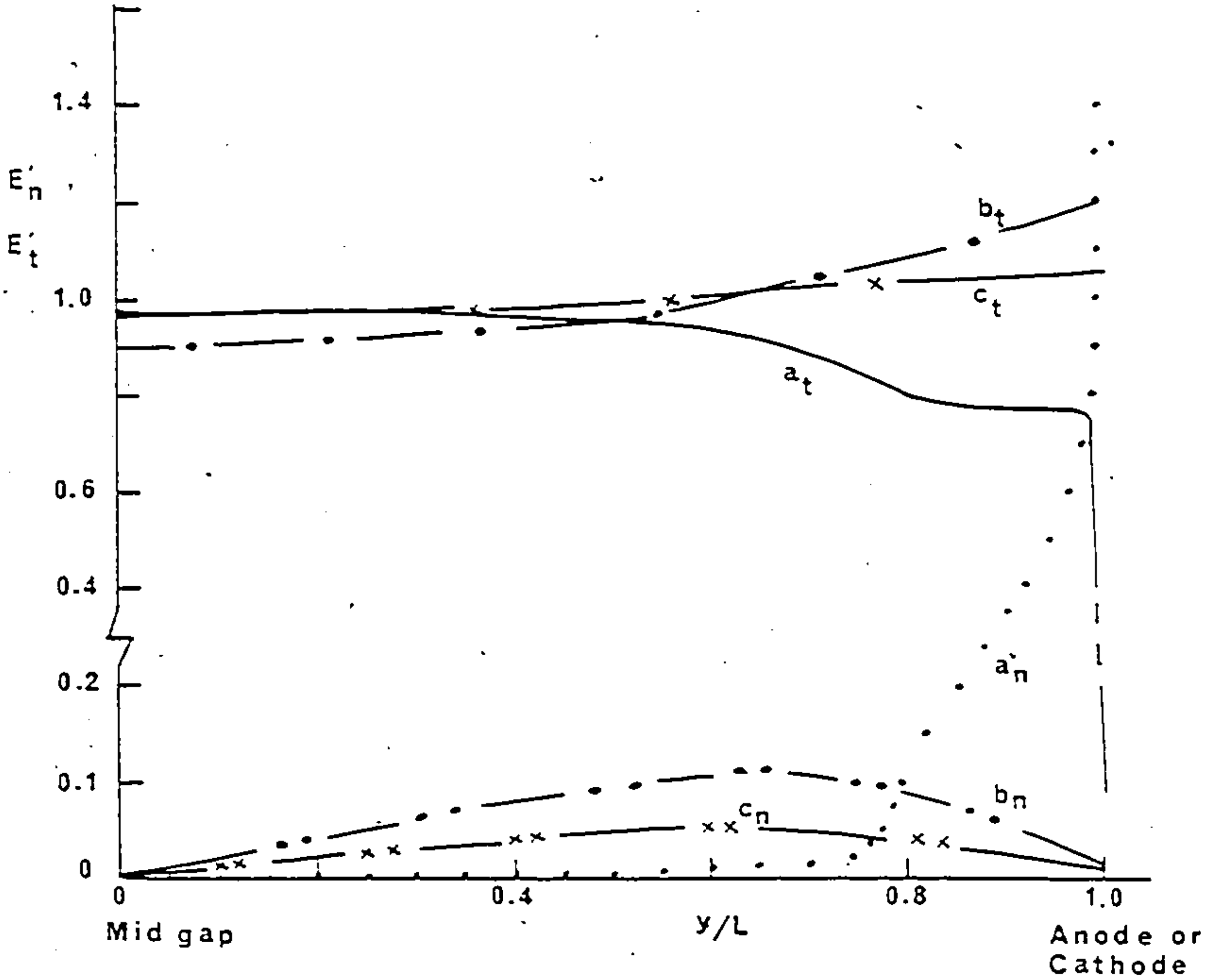

Fig. 6.4. Normalized tangential $E_t' = E_t L/V$ and normal $E_n' = E_n L/V$ field components in different regions of the gap as a function of Y/L. a_t: E_{t_2}' at solid insulator-vacuum boundary ($= E_{t_1}'$); a_n: E_{n_2}' at solid insulator-vacuum boundary on solid insulator side; b_t: $= E_{t_2}'$ at interior of solid insulator in location x/W = 0.15; b_n: $= E_{n_2}' = E_{x_2}'$ at interior of solid insulator in location x/W = 0.15; c_t: $= E_{t_1}' = E_{y_1}'$ in vacuum in location x/W = 0.8; c_n: $= E_{x_1}'$ in vacuum in location x/W = 0.8. Width of electrode = 100 mm; width of the solid insulator block = 40 mm; contact angle $\alpha = 0$; $\varepsilon_2 = 3.8$; r/L = 0.25 (r = 1 cm, L = 4 cm).

respectively. The ratio of r/L = is 0.25. The rounded edge of the solid insulator starts at $y/L = 0.75$, y is the distance measured from the mid-gap point to either the anode or the cathode. To simplify the computation for the present symmetrical block, it is sufficient to consider only a half portion of the gap. The insulator is assumed to have identical curve edges in both the anode and the cathode regions.

It will be seen from Fig. 6.4 that at the surface of the solid insulator the normal field E'_{n_2} (curve a_n) increases rapidly from 0.028 at $y/L = 0.75$ (onset of curvature on the surface of the solid insulator) to about 1.4 at $y/L = 1$ (at contact point with the electrode while the tangential field E'_2 (curve a_t) decreases from 0.856 at $y/L = 0.75$ to 0.098 at $y/L = 1$. The field E'_{t_1} on the other hand in the regions outside the insulator ($x/W = 0.8$, curve c_t) and inside the insulator E'_{t_2} ($x/W = 0.15$, curve b_t) increases steadily throughout the range of y/L. Typically at $y/L = 1$, $E'_{t_2} = 1.18$ (curve b_t) and $E'_{t_1} = 1.05$ (curve c_t) giving a slight enhancement in the field due to the presence of a curvature in the solid insulator though the locations are well away from the triple junction.

In order to obtain finer details of the normalized fields in the curved section of the solid insulator-vacuum boundary the field components E'_{t_2} and E'_{n_2} along the curved surface are shown in Fig. 6.5 as a function of the angle Θ. Θ, defined in Fig. 6.3 varies from 0 at the contact point of the solid insulator with the electrode to 90° − α the location on the solid insulator surface at the onset of the curvature and the linear section at $y/L = 0.75$. It will be observed from Fig. 6.5 that except for Porcelain ($\varepsilon_2 = 10$), E'_{n_2} initially increases with increasing θ from 0 and reaches maximum at about 3° and then decreases steadily up to $\theta = 90°$. E'_{t_2} on the other hand initially increases rapidly with increasing θ and then starts to saturate. The angle at which $E'_{t_2} = E'_{n_2}$ is termed here the cross over angle η. At $\theta > \eta$ the change in the value of E'_{t_2} along the surface is realtively small. Typical values of E'_{n_2} and E'_{t_2} say for $\varepsilon_2 = 3.8$ at $\theta = 90°$ (i.e. at $y/L = 0.75$ where the linear portion and the curved section of the solid insulator meet) are 0.028 and 0.856, respectively. At the solid insulator boundary, just away from the electrode for $y/L < 0.985$ E'_{t_2} is larger than E'_{n_2}. For $y/L < 0.75$, E'_{n_2} becomes negligibly small while E'_{t_2} is about 0.96 (Figs. 6.4 and 6.5).

6.4.2 Effect of the Relative Dielectric Constant on the Field Strength ($\alpha = 0$)

The normalized fields are calculated for the case of the contact angle $\alpha = 0$ at the curved surface of the solid insulator-vacuum boundary and for relative dielectric constants in the range $\varepsilon_2 = 2.1 - 12000$. These are presented in Figs. 6.5-6.7. Fig. 6.5 shows E'_{n_2} and E'_{t_2}, on the solid

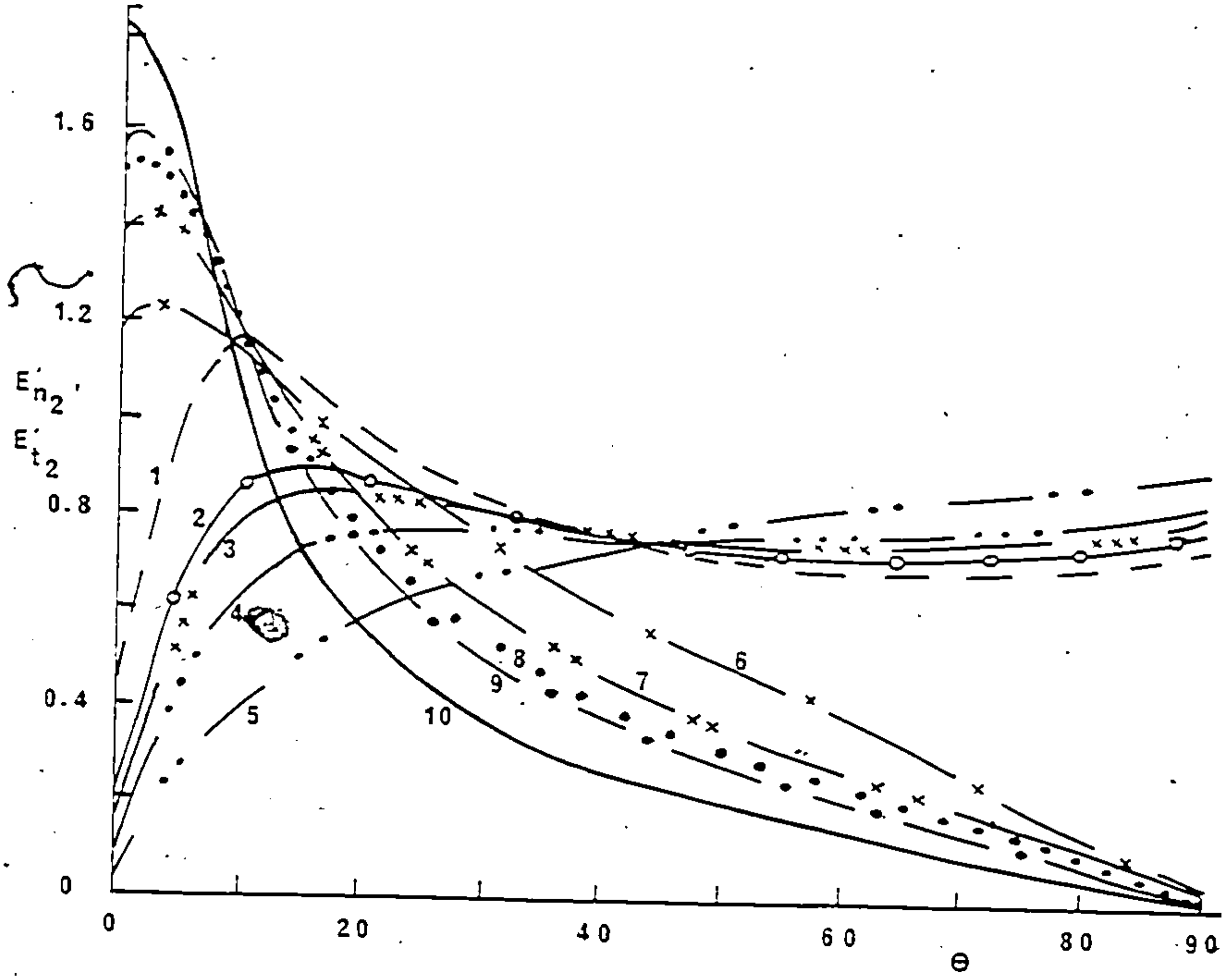

Fig. 6.5. Dependence of E'_{t_2} and E'_{n_2} on θ for different solid insulator materials at the boundary of the solid dielectric and vacuum. Contact angle $\alpha = 0$; $r/L = 0.25$ ($r = 1$ cm, $L = 4$ cm). E'_{t_2}: curves 1, 2, 3, 4 and 5; E'_{n_2}: curves 6, 7, 8, 9, and 10 (values are for the insulator side of the insulator-vacuum boundary); curves 1 and 10 ($\varepsilon_2 = 10.0$); 2 and 9 ($\varepsilon_2 = 5.8$); 3 and 8 ($\varepsilon_2 = 5.0$); 4 and 7 ($\varepsilon_2 = 3.8$); 5 and 6 ($\varepsilon_2 = 2.1$).

insulator side and Fig. 6.6, E'_{n_1} and E'_{t_1} on the vacuum side of the boundary of the solid insulator for the range ε_2 = 2.1 - 10.0. Fig. 6.7 shows E'_{n_1} and E'_{t_1} for ε_2 in the range 20 - 12000. It will be observed that particularly near the contact with the electrode the type of insulator has a strong influence on the values of E'_n and E'_t. At small values of θ (i.e. near the contact junction with the electrode) the value of the normal component of the electric field is enhanced considerably over the ambient average field. The enhancement near the contact point in E'_{n_2} varies from 23% for $\varepsilon_2 = 2.1$ to 54% for $\varepsilon_2 = 5.0$ and 82% for $\varepsilon_2 = 10.0$ (Fig. 6.5). The enhancement in the field occurs near the contact location of the solid insulator with the electrode at θ values between 0 to 3° for $\varepsilon_2 \leq 5.8$. Fig. 6.6 shows the computed values of E'_{n_1} and E'_{t_1} on the vacuum side of the solid insulator-vacuum boundary. It will be observed that large enhancements are found in the E'_{n_1} value at the electrode junction varying from $E'_{n_1} = 2.52$ ($\varepsilon_2 = 2.1$) to $E'_{n_1} = 18.2$ ($\varepsilon_2 = 10.0$) (Fig. 6.6), to $E'_{n_1} = 537$ ($\varepsilon_2 = 12000$) (Fig. 6.7) at locations close to the contact point with the electrode in the range θ = 0-2°. It can be seen from Fig. 6.7 a zig zag in the (E'_{n_1}, θ) curves is present for high values of ε_2. The zig zag first appears at $\varepsilon_2 = 38$ where it is relatively small and is more enhanced with increasing ε_2. The zig zag is at a location on the curve section of the solid insulator close to the electrode end

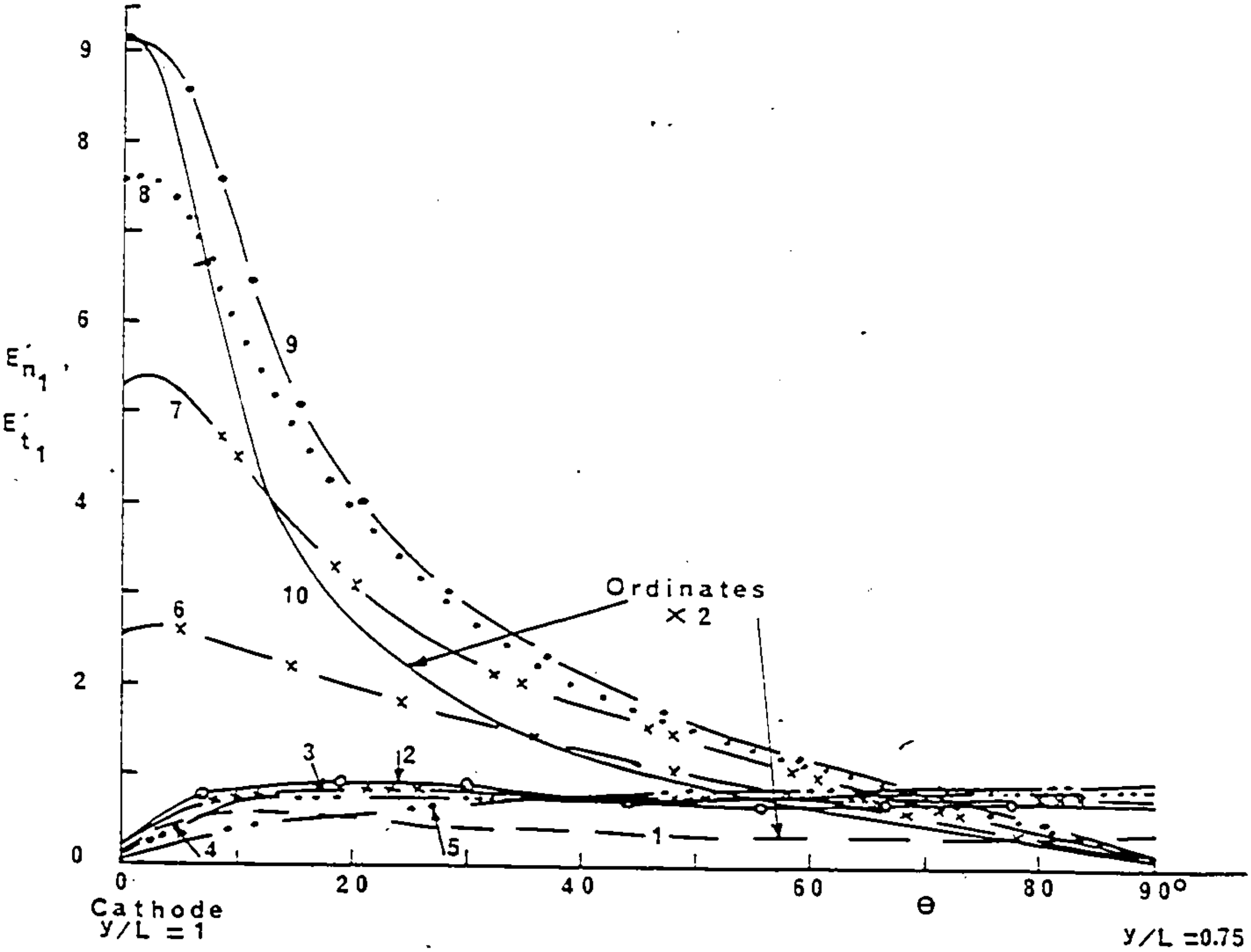

Fig. 6.6. As for Fig. 6.5 except that E'_{n_1} is shown on the vacuum side of the solid insulator-vacuum boundary.

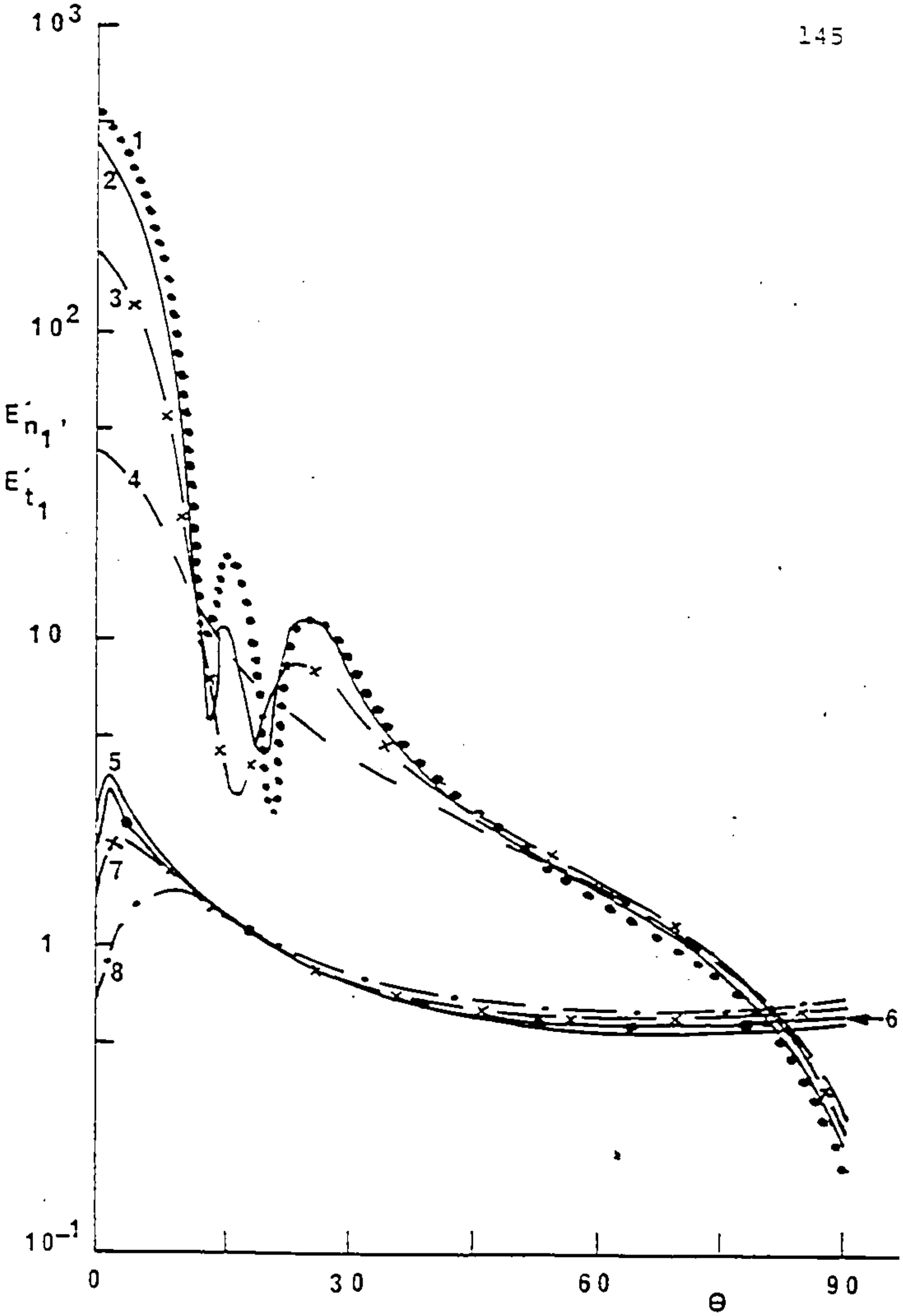

Fig. 6.7. Dependence of E'_{n_1} and E'_{t_1} on θ for different solid insulator materials. Contact angle $\alpha = 0$; $r/L = 0.25$ E'_{n_1} = curves 1, 2, 3 and 4; E'_{t_1} = curves 5, 6, 7 and 8; curves 1 and 5 ($\varepsilon_2 = 12000$); 2 and 6 ($\varepsilon_2 = 650$); 3 and 7 ($\varepsilon_2 = 100$), 4 and 8 ($\varepsilon_2 = 20$).

and occurs in the range $\theta = 12 - 28°$.

The large increase in the electric field at the electrode junction in the vacuum regime has a pronounced influence on the withstand voltage of the gap containing a solid insulator causing a reduction in the hold-off voltage of the total gap. The high value of E'_{n_1} calculated for high dielectric constants is consistent with the previously reported measurements of low withstand voltage say in barium titanate. Typically about 200V was found to be sufficient to cause a breakdown across a surface length of a 0.41 mm of barium titanate in vacuum [95-96]. Kofoid [4,5] obtained similarly low values of dielectric strengths for higher dielectric constant materials. Typically 20 kV/cm (D.C.) for $\varepsilon_2 = 6.6$ decreasing to 5.2 kV/cm (D.C.) for $\varepsilon_2 = 3800$.

The cross over angle η is seen to depend on ε_2 (Fig. 6.5) and decreases with increasing ε_2. The corresponding values for Teflon ($\varepsilon_2 = 2.1$), quartz ($\varepsilon_2 = 3.8$), and Pyrex glass ($\varepsilon_2 = 5.0$), glass ceramic ($\varepsilon_2 = 5.8$) and porcelain zircon ($\varepsilon_2 = 10.0$) are, respectively 34.5°, 22.5°, 18.5°, 15.5° and 9°. For $\varepsilon_2 > 20$ the cross over angle saturates at a value of about 9° and remains about the same up to $\varepsilon_2 = 12000$. This shows that the location on the curved section of the solid insulator at which $E'_{n_2} = E'_{t_2}$ (on the side of solid insulator of the solid dielectric-vacuum boundary) becomes closer to the electrode the higher is the relative dielectric constant of the insulator. On the boundary surface of the insulator at the ε_1 side (in the vacuum side) the cross over angle for $E'_{n_1} = E'_{t_1}$ is found to be approximately $(90°-\eta)$ as can be seen from Figs. 6.6 and 6.7 where η is the cross over angle obtained on the ε_2 side.

Table 6.1 gives the computed values for E'_n and E'_t on both sides of the boundary surface at the contact point P with the electrode for $\alpha = 0$ and for different insulator materials. It will be observed that very large enhancements occur in E'_{n_1} and E'_{t_1} in all the materials investigated at high ε_2 values at the triple junction. It will be observed from Table 6.1 that the value of E'_{n_2} starts to decrease rapidly for $\varepsilon_2 > 40$. It is readily seen that the enhancement and the decrease in the field are not proportional to the relative dielectric constant. The low values of E'_{n_2} at high ε_2 are a consequence of the continuity of the normal flux along the solid dielectric-vacuum boundary.

6.4.3 Effect of the Radius of Curvature r ($\alpha = 0$)

The influence of the radius of curvature r, of the edge of the insulator in the vicinity of the electrode on the electric field components is examined. Fig. 6.8 shows the computed E'_{t_1} and E'_{n_1} fields for the quartz insulator ($\varepsilon_2 = 3.8$) and for r/L values in the range 0.033 - 0.500. In general a decrease in both field components with increasing r/L value is observed in the range r/L = 0.033 - 0.2. A saturation

TABLE 6.1

Maximum normalized field intensities E'_{n_1}, E'_{n_2}, E'_{t_1} and E'_{t_2} at or near the contact point P of the solid insulator with the electrode (anode or cathode) at contact angle $\alpha = 0$ for different solid insulator materials. $y/L = 1$, $r/L = 0.25$

Material	ε_2 [34,94]	E'_{n_1} (on ε_1 side, i.e., vacuum)	E'_{n_2} (on ε_2 inside solid insulator)	E'_t ($E'_{t_1} = E'_{t_2}$)
Polytetra-Fluoroethylene (Teflon)	2.1	2.52	1.23	0.02
Quartz	3.8	5.31	1.40	0.10
Pyrex Glass	5.0	7.55	1.54	0.16
Glass-Ceramic	5.8	9.10	1.57	0.21
Porcelain-Zircon	10.0	18.23	1.82	0.39
Titanium dioxide	20	41.59	2.08	0.71
	30	64.46	2.15	0.97
Hevea Compound	36	75.37	2.15	1.00
Titanium Dioxide	40	85.88	2.15	1.07
	50	105.73	2.11	1.19
Rutile	100	184.75	1.85	1.55
Titanates, Ba, Sr, Ca, Mg, and Pb	200	280.75	1.40	1.90
	300	336.52	1.12	2.08
	500	398.53	0.80	2.28
	650	425.31	0.65	2.37
	1,000	461.21	0.46	2.47
	4,500	524.54	0.12	2.66
	12,000	537.62	0.045	2.70

is reached in both E'_{n_1} and E'_{t_1} for higher values of $r/L \geq 0.2$ (Fig. 6.8). A considerable enhancement in the E'_{n_1} field is observed at the electrode junction at point P. Typically for the case of $r/L = 0.05$ an enhancement of 7.9 is observed for E'_{n_1} (for $\varepsilon_2 = 3.8$) on the vacuum side of the junction. This large enhancement in the normal field is expected to result in lowering the breakdown voltage of the gap. At a fixed value of L higher E'_{n_1} and E'_{t_1} are observed with decreasing r (fig. 6.8). In Fig. 6.9 E'_{n_1} and E'_{y_1} are shown for a fixed low value of $r/L = 0.05$ and for varying values of r and L in the range r = 1.0 - 1.5 cm and L = 20-30 cm. It can be seen (Fig. 6.9) that E'_{n_1} is higher the higher the values of L and r. For high values of $r/L \geq 0.2$ there is only a negligible dependence of the field components on the variation of either r or L at a fixed value of r/L.

6.5 Solid Insulator Electrode Junction Field Calculation (Varying Contact Angle α)

In practical devices employing solid insulators for supporting conducting electrodes in vacuum (or in gaseous apparatus such as cables and switchgear) the solid insulators may not meet the electrode surface at 90° or 0°. The voltage hold-off of vacuum gaps containing solid insulators strongly depends on the shape and the geometry of contact of the solid insulator with the electrodes [8,13]. The angle between the applied uniform field and the insulator interface is believed

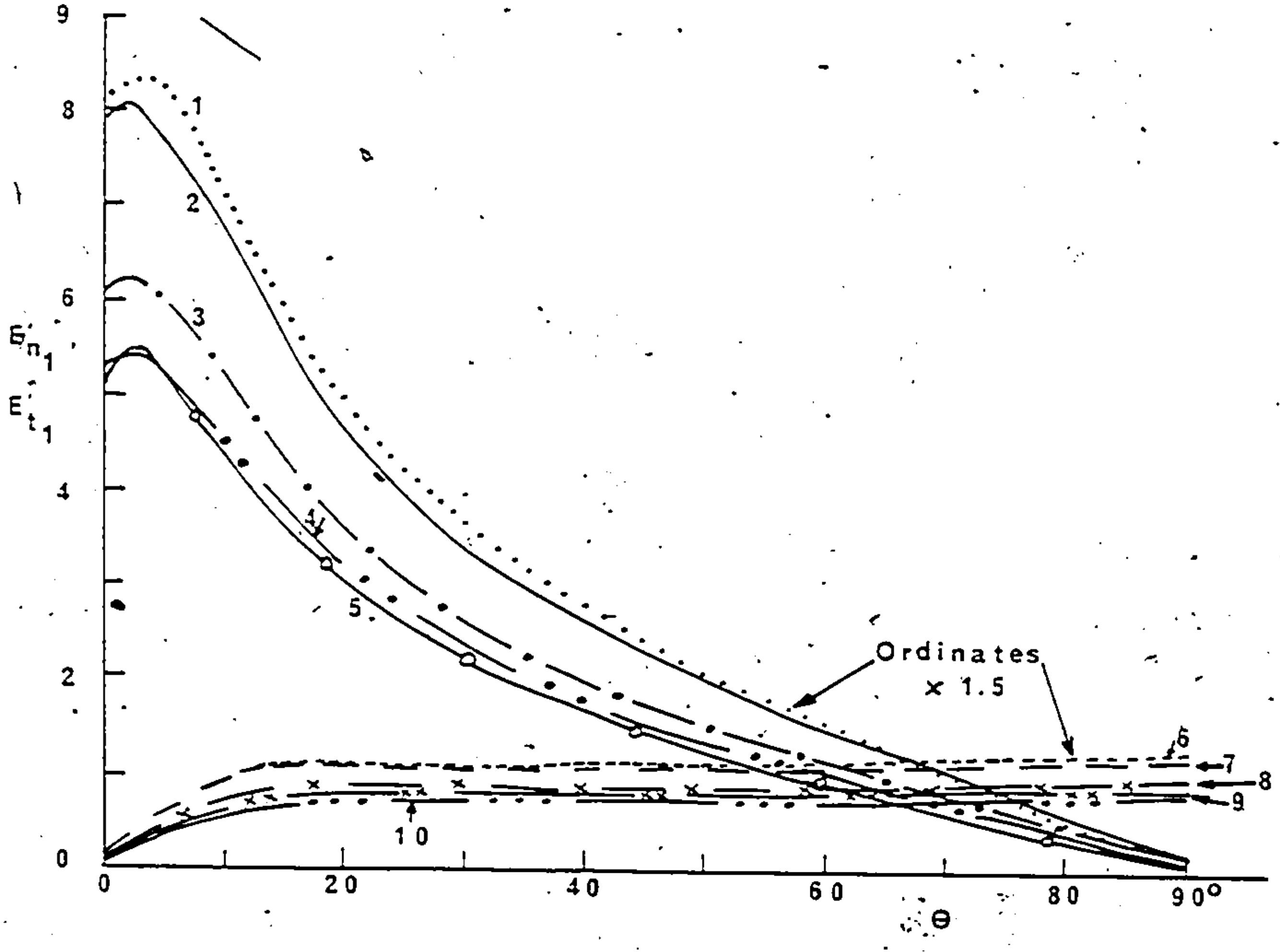

Fig. 6.8. Dependence of electric field E'_{n_1} and E'_{t_1} on θ along the curved portion of the solid insulator surface for different values of r/L. Contact angle $\alpha = 0$; $\varepsilon_2 = 3.8$; curves 1 and 6 (r = 1 cm; L = 30 cm; r/L = 0.33; ordinates are times 1.5); curves 2 and 7 (r = 0.8 cm; L = 16 cm; r/L = 0.05); curves 3 and 8 (r = 0.8 cm; L = 8 cm; r/L = 0.1); curves 4 and 9 (r = 0.8 cm; L = 4 cm; r/L = 0.2); curves 5 and 10 (r = 0.8 cm; L = 1.6 cm; r/L = 0.5).

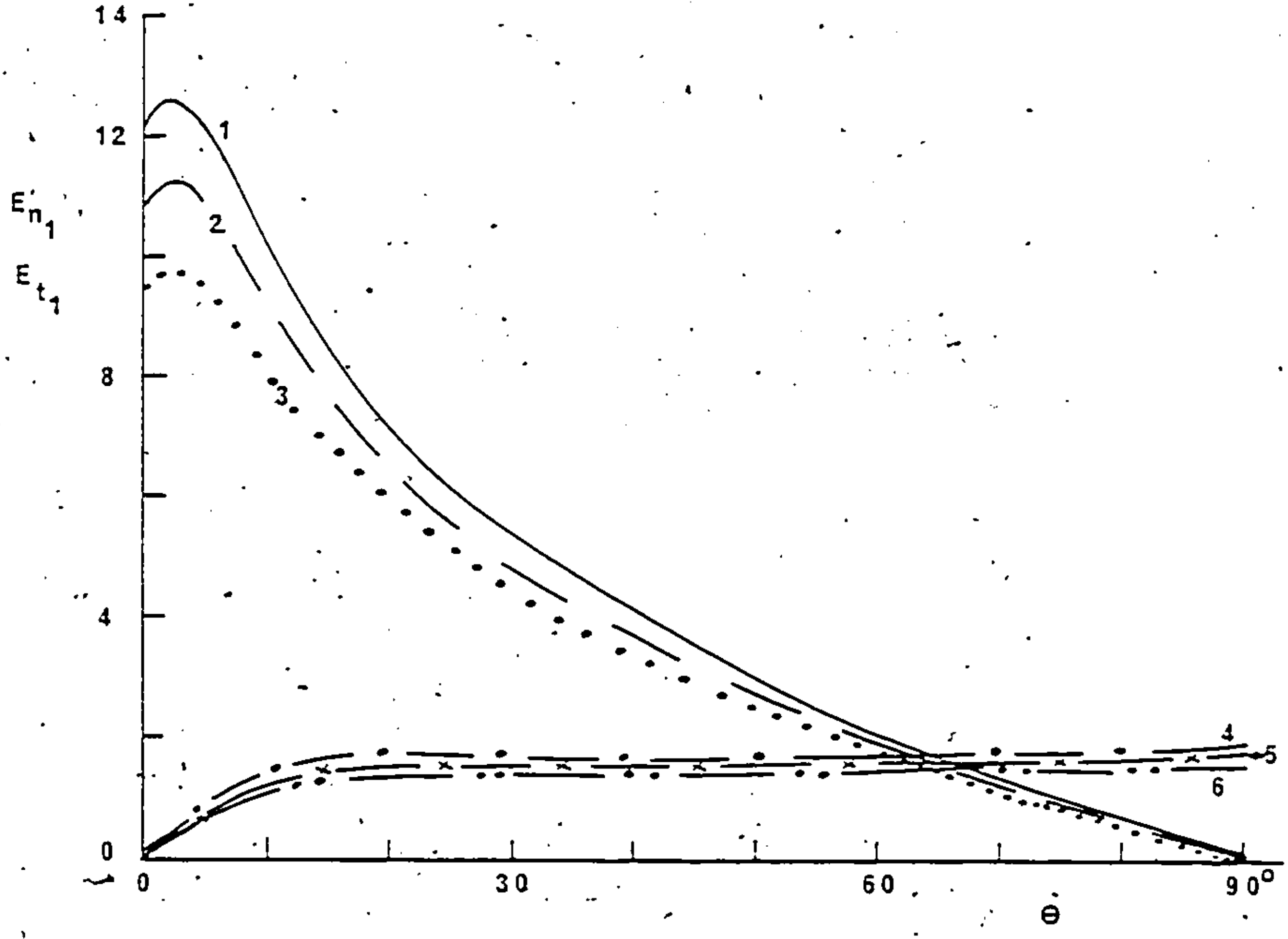

Fig. 6.9. Dependence of E'_{n_1} and E'_{t1} on θ at a fixed ratio of r/L for different values of r and L. $\alpha = 0$; $\varepsilon_2 = 3.8$; $r/L = 0.05$; E'_{n_1} = curves 1, 2 and 3; E'_{t_1} = 4, 5 and 6; curves 1 and 4 (r = 1.5 cm, L = 30 cm); curves 2 and 5 (r = 1.25 cm, L = 25 cm); curves 3 and 6 (r = 1.0 cm, L = 20 cm).

to be a fundamental parameter in the breakdown process of these gaps [13].

6.5.1 Fields at the Surface of the Solid Insulator ($\alpha = 45°$)

Fig. 6.10 shows E'_{n_2} and E'_{t_2} for a contact angle $\alpha = 45°$ along the surface of the insulator in the region of the triple junction. The field components are plotted against the angle θ. In order to cover the full curved surface of the solid insulator, θ varies from 0 at the contact with the electrode to 45° which is $90° - \alpha$. It will be observed that E'_{t_2} and E'_{n_2} increase rapidly as the region of the contact with the electrode is approached at lower values of θ. Since for all the insulator materials studied for the case of $\alpha = 45°$, $\alpha > \eta$ the values of E'_{t_2} are larger than E'_{n_2} at all locations on the curved section of the insulator surface as is observed (Fig. 6.10). Typically for $\epsilon_2 = 3.8$ (quartz) at the contact point with the electrode the values of the fields inside the insulator are $E'_{t_2} = 1.538$ and $E'_{n_2} = 0.758$. On the vacuum side at the boundary of the solid insulator and very close to the contact point $E'_{n_1} = 3.8 \times 0.758 = 2.88$. This shows that at $\alpha = 45°$ a considerable enhancement occurs in the field arising from the curved solid insulator edge. The enhanced electric field leads to an increase in the electron emission from the cathode resulting in a lower breakdown voltage of the complete gap.

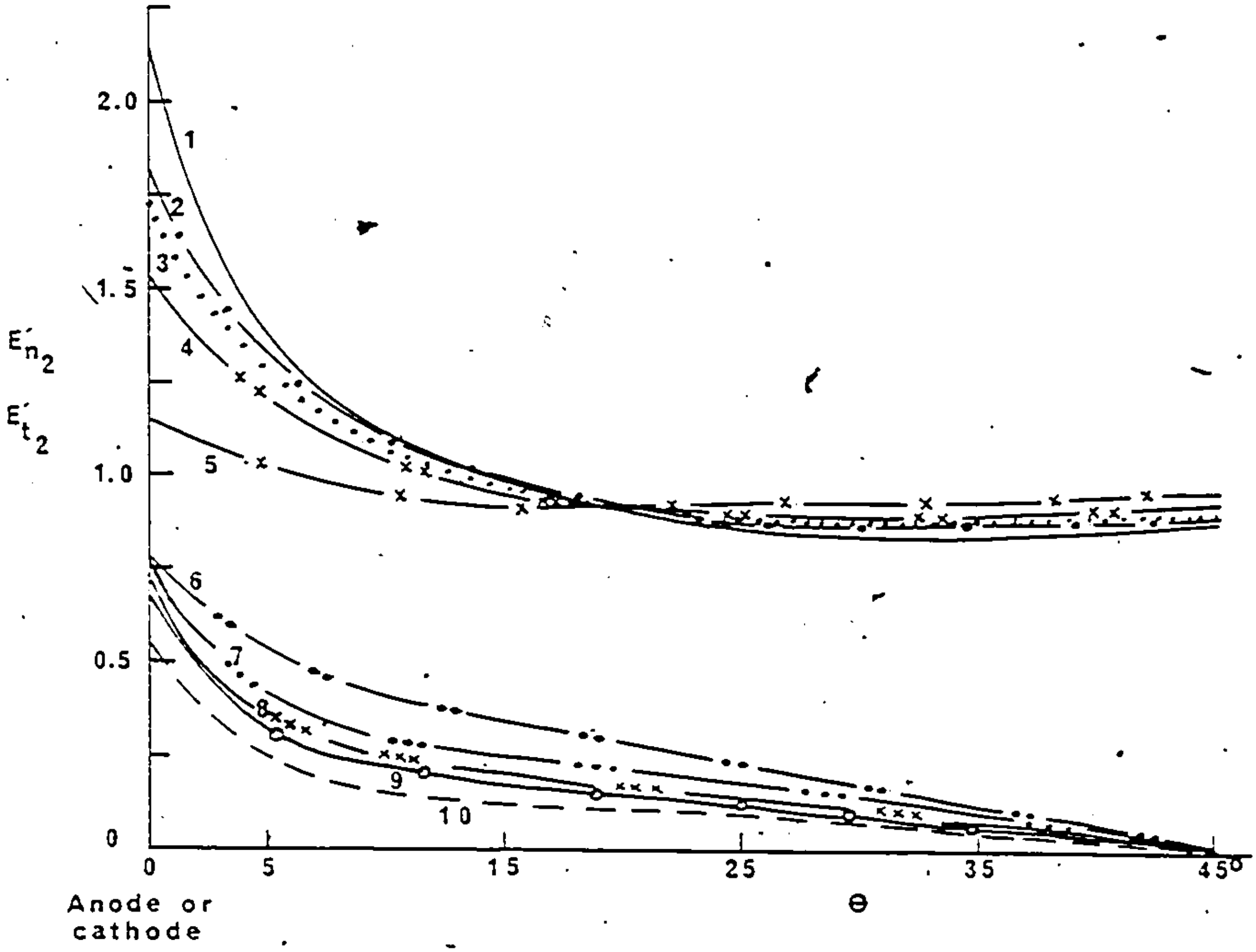

Fig. 6.10. E'_{t_2} and E'_{n_2} as a function of θ along the surface of the solid insulator at the boundary with vacuum for different solid insulator materials. α = 45° r/L = 0.35. (Curve numbers as for Fig. 6.5).

6.5.2 Field Strength Along the Solid Insulator Boundary with ε_2 as a Parameter ($\alpha = 45°$)

The normalized field values along the boundary of the solid insulator near the junction for $\varepsilon_2 = 2.1, 3.8, 5.0, 5.8$ and 10 are also shown in Fig. 6.10. The field intensities at the contact point with the electrodes are given in Table 6.2. Along the solid insulator boundary including the contact region, the tangential field strength, E'_{t_2}, is higher in the case of higher ε_2 while the value of the normal field strength E'_{n_2} is lower with increased ε_2. The normal field strength decreased rapidly away from the contact point with the electrode with increasing θ as shown in Fig. 6.10. In the case of the tangential field strength and after a relatively short distance from the electrode along the curved surface of the solid insulator ($\theta = 20°$, Fig. 6.10), the value of E'_{t_2} for the lowest dielectric constant is of the order of 10% higher than the corresponding E'_{t_2} value for the highest ε_2. Also the value of E'_{t_2} reaches a saturation for $\theta > 20°$ approximately. The values of E'_{n_1} can be readily obtained from Fig. 6.10 by multiplying E'_{n_2} by the appropriate ε_2 value.

Fig. 6.11 shows E'_{n_1} and E'_{t_1} at $\alpha = 45°$ for ε_2 in the range 20 - 12000. The values of the field components remain relatively unchanged for $\varepsilon_2 \geq 650$. At the contact point with the electrode E'_{n_1} saturates at about 10.6 and E'_{t_1} at 2.8 (for $\varepsilon_2 \geq 650$).

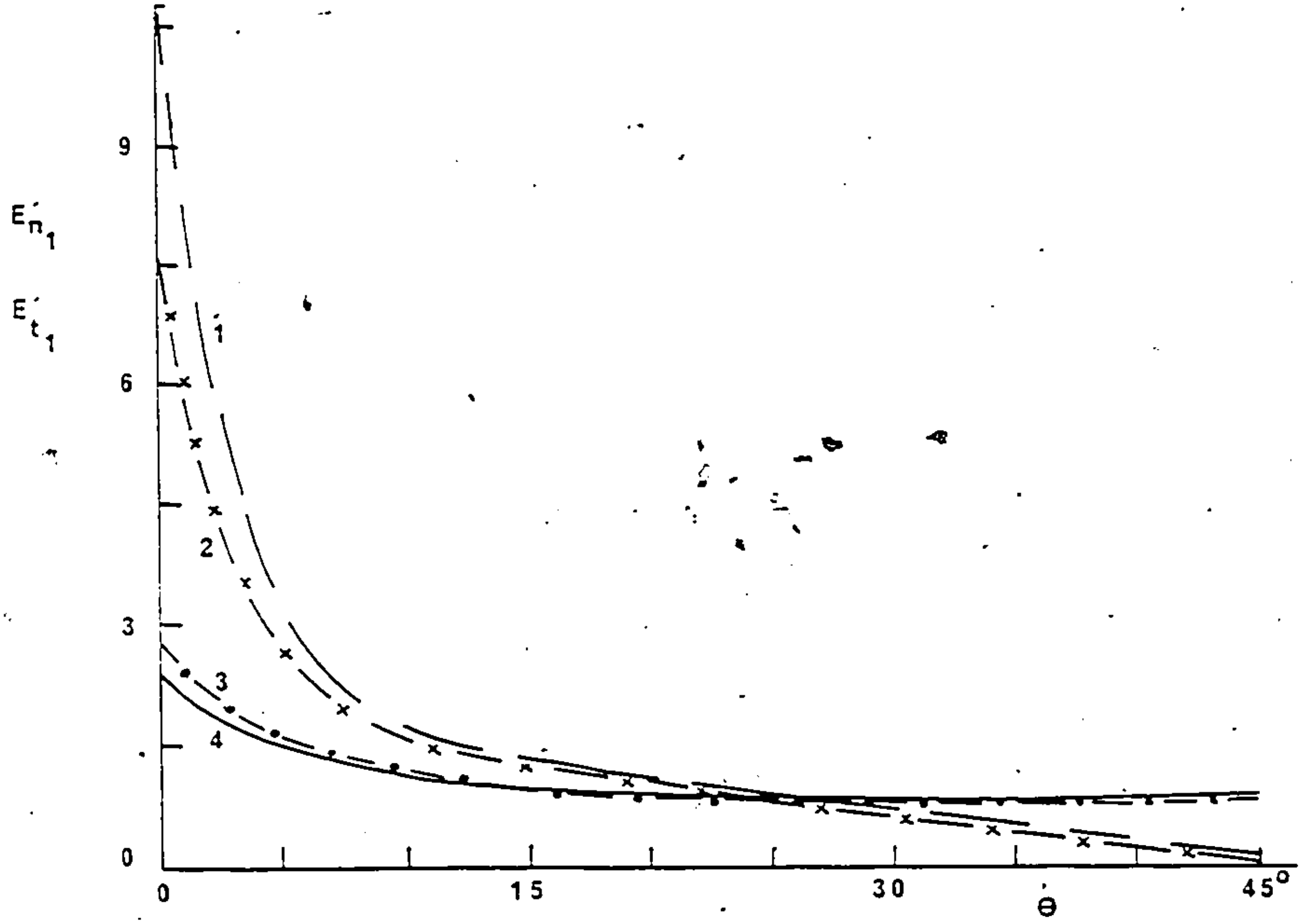

Fig. 6.11. Dependence of E'_{n_1} and E'_{t_1} on θ along the surface of the solid insulator at the boundary with vacuum for different solid insulator materials. $\alpha = 45°$; $r/L = 0.35$; E'_{n_1}: curves 1 and 2; E'_{t_1} curves 3 and 4; curves 1 and 3 (ε_2 = 650, 1000, 4500 and 12,000); curves 3 and 4 (ε_2 = 20).

TABLE 6.2

Normalized field intensities E'_{n_1}, E'_{n_2}, E'_{t_1} and E'_{t_2} at the contact point P of the solid insulator with the electrode (anode or cathode) at contact angle $\alpha = 45°$ and different solid insulator materials. $\alpha = 45°$, $y/L = 1$, $r/L = 0.35$

ε_2	E'_{n_1} (on ε_1 side in vacuum)	E'_{n_2} (on ε_2 inside solid insulator)	E'_t ($E'_{t_1} = E'_{t_2}$)
2.1	1.66	0.79	1.15
3.8	2.88	0.76	1.54
5.0	3.59	0.72	1.72
5.8	3.99	0.69	1.81
10.0	5.56	0.56	2.14
20	7.55	0.37	2.40
*70	9.50	0.14	2.70
100	9.83	0.098	2.75
250	10.30	0.04	2.81
650	10.52	0.02	2.84
1,000	10.56	0.0105	2.848
4,500	10.63	0.0026	2.857
12,000	10.65	0.0009	2.863

*Titanate dioxide

6.5.3 Effect of Contact Angle α on Field Enhancement

Figs. 6.12 and 6.13 show the normalized tangential E'_{t_1} and normal field E'_{n_1} distributions along the surface of the solid insulator for different values of contact angle α. Fig. 6.12 shows the field values along the boundary for contact angle 45° and below and Fig. 6.13 for $\alpha \geq 45°$ for a fixed solid insulator $\varepsilon_2 = 5.0$ (Pyrex glass).

The field enhancements at the contact point P (Fig. 6.3) of the solid insulator with the electrode is given in Table 6.2 for $\alpha = 45°$ and different solid dielectrics. It will be observed that a considerable enhancement in the field is found on the vacuum side of the triple junction which is higher the larger value of ε_2.

Table 6.3 gives the fields E'_{n_1}, E'_{n_2} and E'_{t_1} at the contact point P with the electrodes for different contact angle α and r/L for a fixed solid insulator ($\varepsilon_2 = 5.0$). It will be observed (Table 6.3) that E'_{n_2} is higher than E'_{t_2} (on the insulator side of the boundary) near the contact point with the electrode, when the contact angle α is lower than the cross over angle η. For example $\varepsilon_2 = 5.0$, $\eta = 18.5°$ and $E'_{n_2} = 1.867$, $E'_{t_2} = 1.537$ at $\alpha = 15°$. As α increases above η the situation reverses and E'_{t_2} becomes larger than E'_{n_2}. In the same Pyrex glass material, at $\alpha = 30°$ the normalized fields become $E'_{n_2} = 1.256$ and $E'_{t_2} = 1.81$. When $\alpha = \eta$, $E'_{n_2} = E'_{t_2}$. For $\alpha > \eta$, $E'_{t_2} > E'_{n_2}$ over the entire surface of

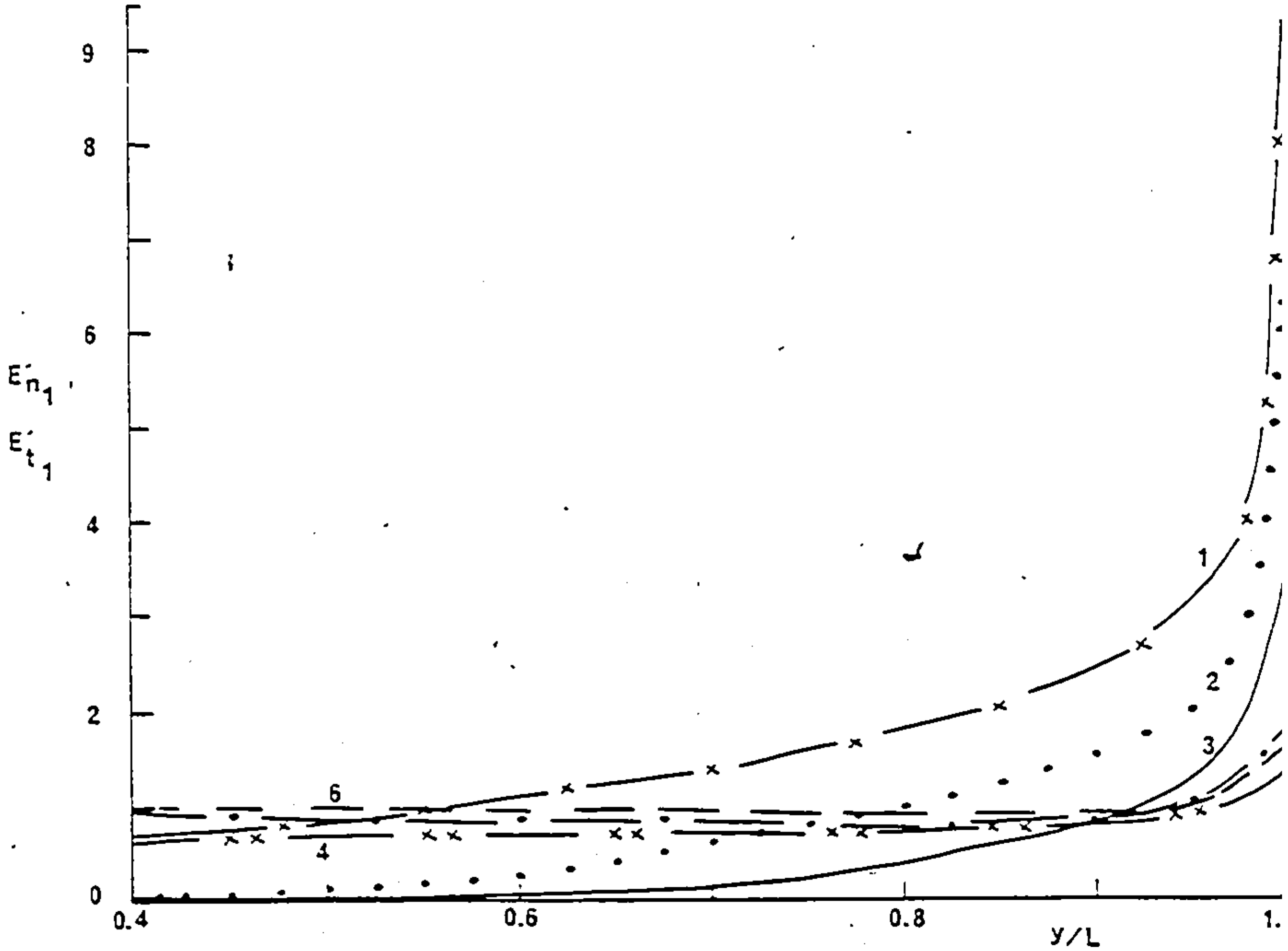

Fig. 6.12. E'_{t_1} and E'_{n_1} as a function of y/L along the surface of the solid insulator at the boundary with vacuum for different contact angles in the range $\alpha \leq 45°$. $\varepsilon_2 = 5.0$ r/L (variable - see Table 6.3); E'_{n_1}: curves 1, 2 and 3; E'_{t_1}: curves 4, 5 and 6; curves 1 and 4 ($\alpha = 15°$); 2 and 5 (30°), 3 and 6 (45°).

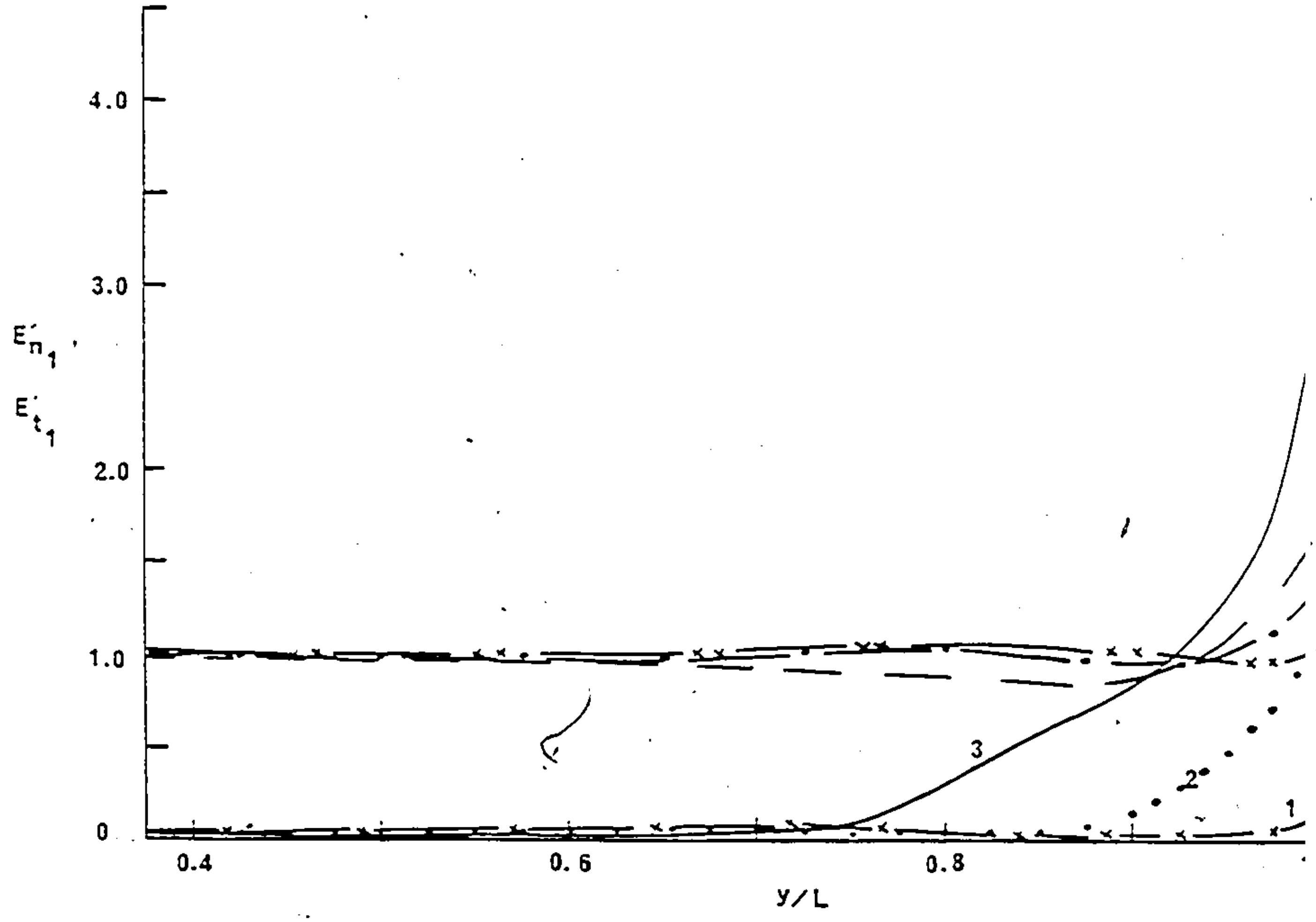

Fig. 6.13. E'_{t_1} and E'_{n_1} along the surface of the solid insulator for different contact angle in the range $\alpha \geq 45°$. $\varepsilon_2 = 5.0$ r/L (variable - see Table 6.3); E'_{n_1}: curves 1, 2 and 3; E'_{t_1} = curves 4, 5 and 6; curves 1 and 4 (α = 85°); 2 and 6 (α = 65°); 3 and 5 (α = 45°).

TABLE 6.3

Normalized field intensities E'_{n_1}, E'_{n_2}, E'_{t_1} and E'_{t_2} at the contact point P of the solid insulator with the electrode (anode or cathode) for different contact angles α. $\varepsilon_2 = 5.0$, $y/L = 1$

Contact angle of solid insulator with electrode α°	r/L	E'_{n_1} (on ε_1 side i.e., vacuum)	E'_{n_2} (on ε_2 inside solid insulator)	$E'_{t_1} = E'_{t_2}$
15°	0.97	9.34	1.87	1.54
18°	0.81	8.87	1.77	1.68
30°	0.50	6.28	1.26	1.81
45°	0.35	3.59	0.72	1.70
59°	0.29	1.84	0.37	1.49
65°	0.28	1.30	0.26	1.38
75°	0.26	0.62	0.12	1.19
85°	0.25	0.17	0.03	1.03

the solid insulator including the contact points with the electrodes (Table 6.3). Comparison of Figs. 6.12 and 6.13 shows that higher enhancement is obtained in E'_{n_1} for contact angles $\alpha < 45°$ (Fig. 6.12), at same locations on the curved section of the solid insulator in the vicinity of the elctrode (y/L $\geq$ 0.9), than for $\alpha > 45°$ (Fig. 6.13). It will be observe (Fig. 6.13) that for large values of the contact angle the tangential field E'_{t_1} remains almost constant in the region distant from the contact point with the electrodes (y/L < 0.9) while E'_{n_1} becomes negligibly small. Figs. 6.14 and 6.15 show the fields E'_{y_1} and E'_{x_1} on the vacuum side of the boundary for $\alpha \leq 45°$ and $\alpha \geq 45°$ respectively. E'_{y_1} is the electric field in the direction of the ambient applied field. Considerable field enhancement of E'_{y_1} at the contact point P of the solid insulator with the electrodes is observed. Typically for $\varepsilon_2 = 5.0$, $\alpha = 15°$ (Fig. 6.14), r/L = 0.97 (Table 6.3) E'_{y_1} at the contact point P (i.e., y/L = 1) is 9.42 and $E'_{x_1} = 0.98$ The high E'_{y_1} contributes to enhanced electron emission from the cathode and leads to a lower withstand voltage.

Fig. 6.16 shows the dependence of E'_{n_2} and E'_{t_2} at the contact point P with the electrodes on the contact angle for a typical solid insulator $\varepsilon_2 = 5.0$. At contact angles $\alpha > 18.5°$, in this material, the normal field E'_{n_2} is smaller than the tangential field. It is readily seen that for Pyrex glass an enhancement in the normalized field E'_{n_1} over the

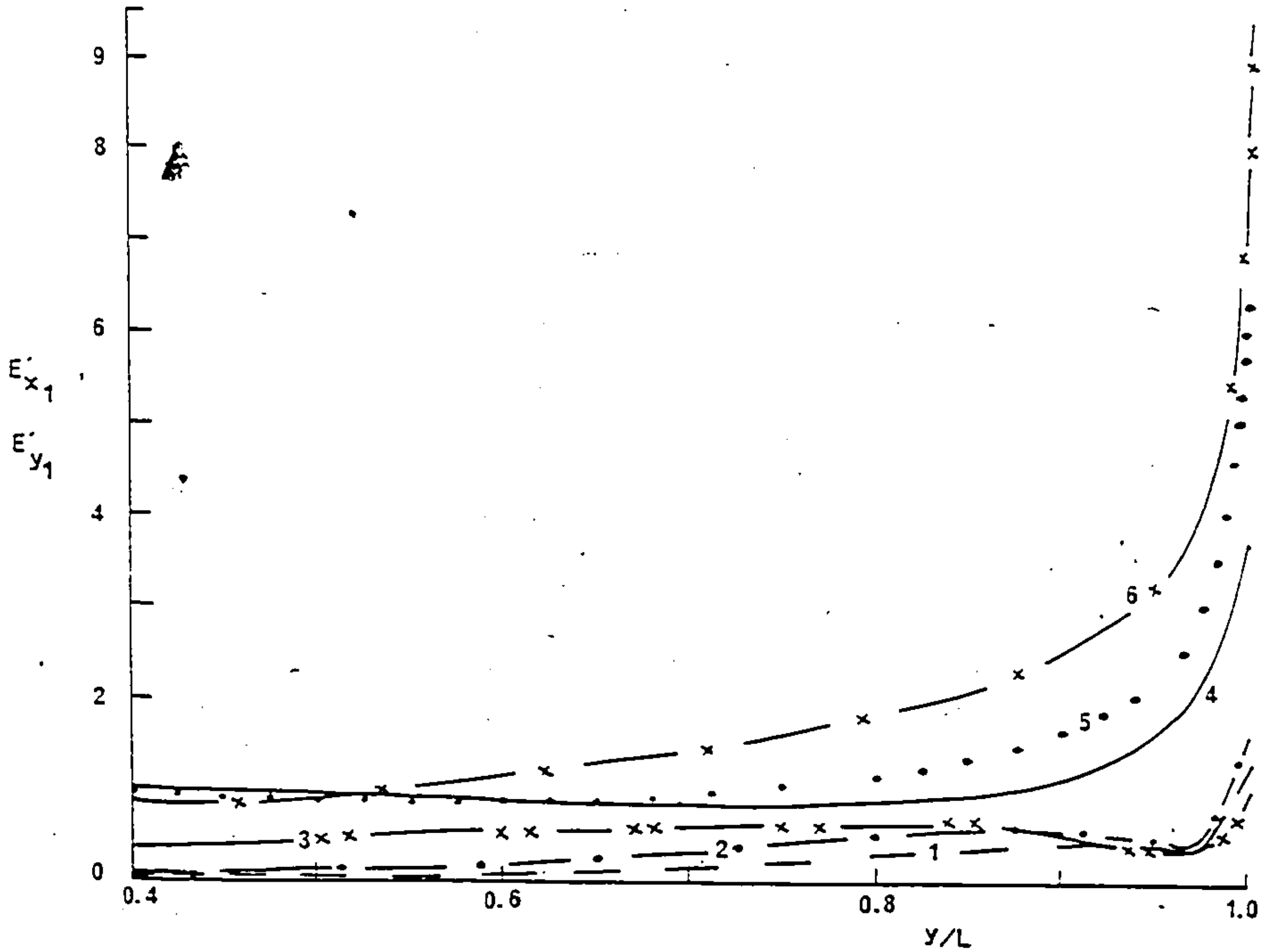

Fig. 6.14. E'_{y_1} and E'_{x_1} as a function of y/L on the vacuum side of the boundary of the solid insulator-vacuum for $\alpha \leq 45°$. $\varepsilon_2 = 5.0$; $E'_{x_1} = 1, 2, 3$; $E'_{y_1} = 4, 5, 6$. Curves 3 and 6 ($\alpha = 15°$), 2 and 5 ($\alpha = 30°$); 1 and 4 (45°).

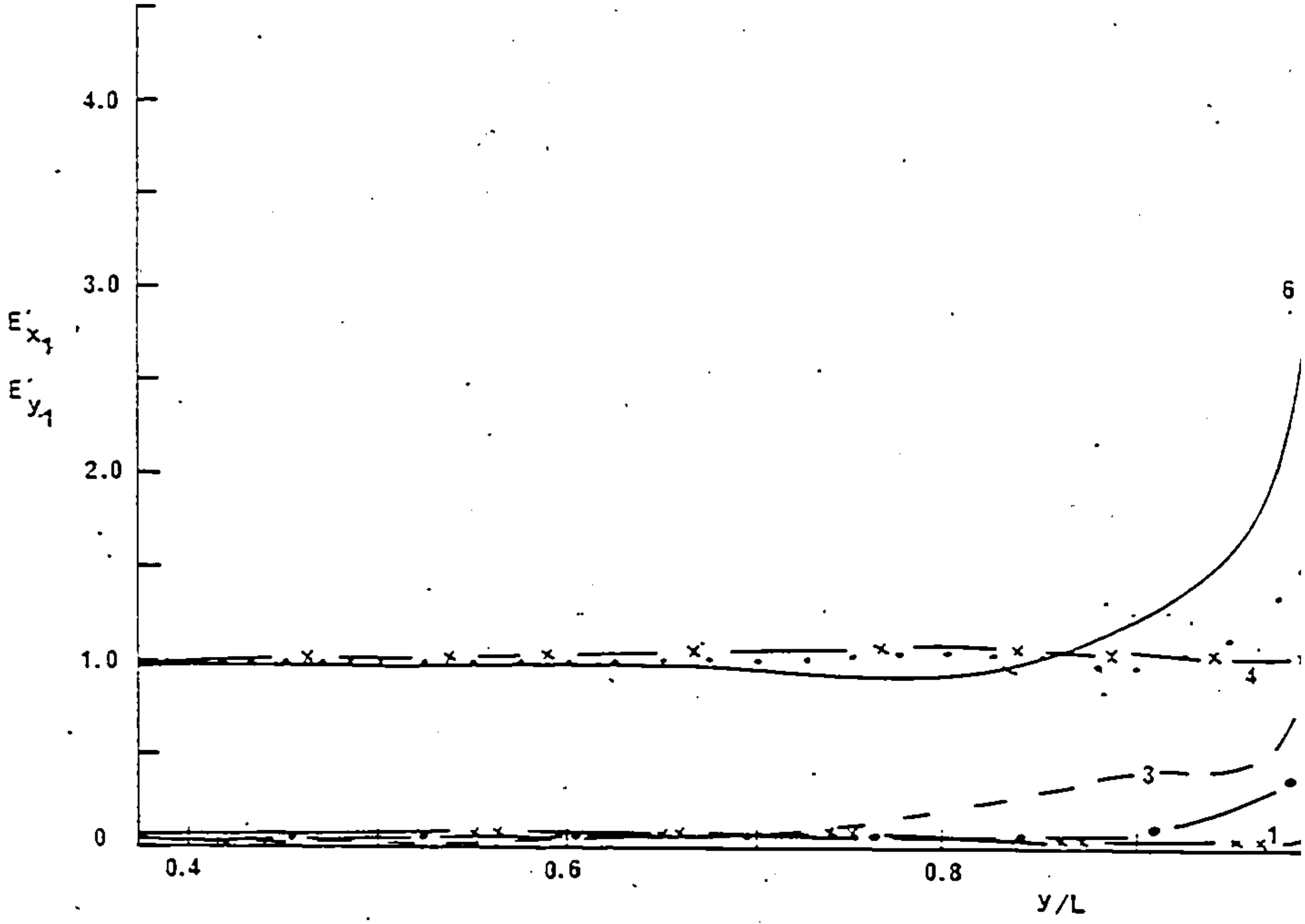

Fig. 6.15: E'_{y_1} and E'_{x_1} as a function of y/L on the vacuum side of the boundar of the solid insulator-vacuum for $\alpha \geq 45°$. $\varepsilon_2 = 5.0$; E'_{x_1} = 1, 2, E'_{y_1} = 4, 5, 6; curves 3 and 6 (α = 45°); 2 and 5 (α = 65°); 1 and 4 (α = 85°).

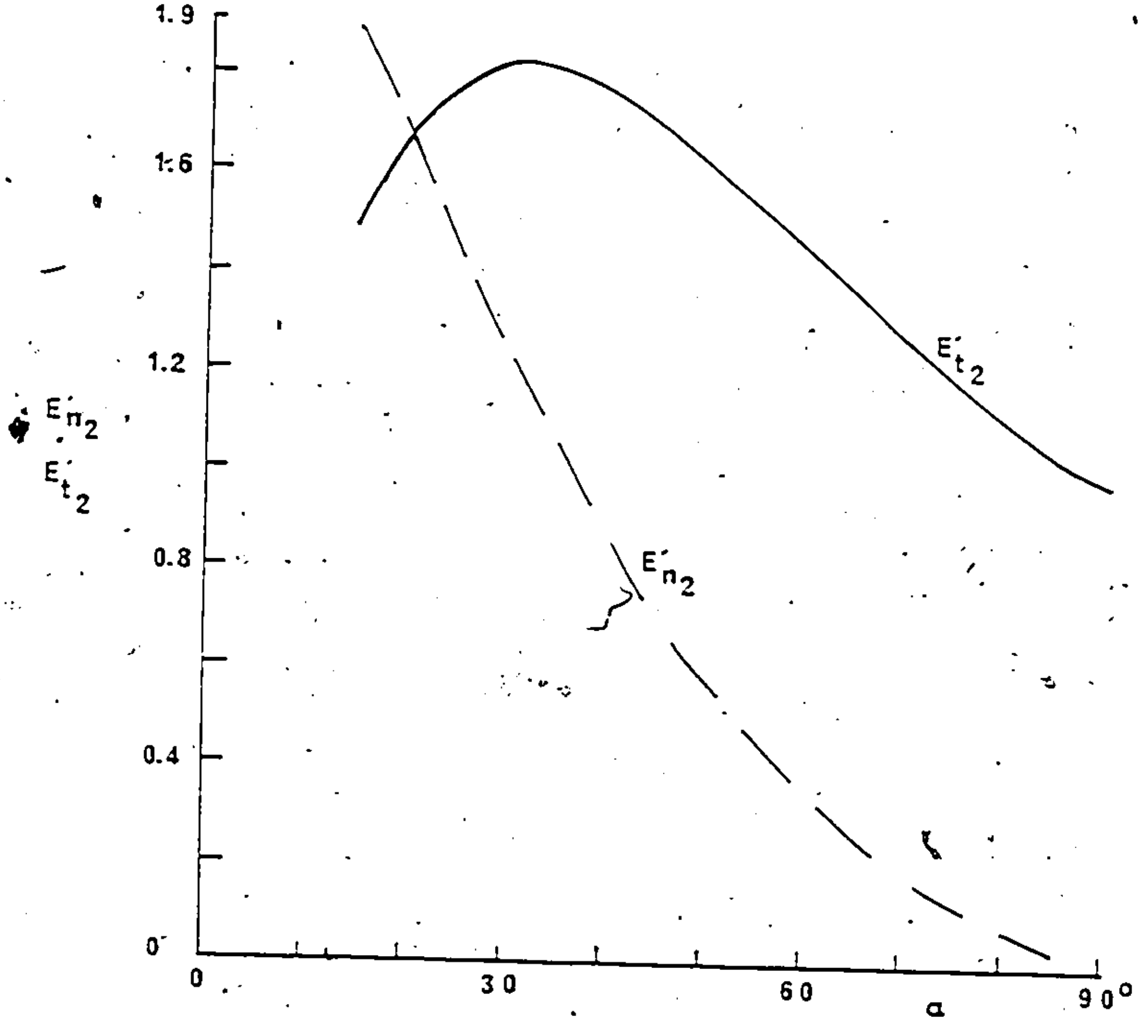

Fig. 6.16. Field distribution E'_{t_2} and E'_{n_2} at the contact point P of the solid insulator with the electrode as a function of the contact angle α. $\varepsilon_2 = 5.0$. r/L varies according to α (see Table 6.3).

ambient average applied field occurs for all contact angles $\alpha \leq 70°$ (Fig. 6.16 where $E'_{n_2} = 0.2$).

6.6 Discussion

The triple junction field enhancement at the curved solid dielectric-electrode-vacuum interfaces has been analyzed using charge simulation techniques and by assuming different solid insulator-electrode contact configurations that can arise in multi-dielectric arrangements. In the case when the solid dielectric boundary contact-angle with the electrode surface is 0°, the normal field strength is very much higher than the tangential field value in the vicinity of the contact line in addition to the line of contact itself. At point locations away from the line of contact there is a rapid change over from higher normal field values to higher tangential field values. This occurs when the point on the solid dielectric boundary is at a certain angle defined as the cross over angle η, which depends on the dielectric constant ε_2 of the insulating material. After this point on the solid dielectric surface, the value of E'_t is almost constant and of the order of 0.9 - 1.0 whereas the value of E'_{n_2} decreases rapidly and becomes very small near the linear boundary surface of the solid insulator-vacuum. The effect of the curved contact has been observed both inside and outside the solid dielectric (vacuum or gas). There is not much variation in the field enhancement due to changes in the solid dielectric boundary radius of curvature at high $r/L > 0.2$ while at low values of r/L below 0.1 the electric field strongly depends on r, L and r/L.

The effect of contact-angle of the solid insulator with the electrode on field distribution has been studied. A strong dependence of the field at the triple junction on the angle of contact has been observed. The value of E'_{t_2} is much higher than E'_{n_2} in the materials where the contact angle is above the cross over angle η. In cases where the contact angle α is less than η, the value of $E'_{n_2} > E'_{t_2}$ near the contact region then E'_{n_2} decreases rapidly as α increases. In all cases a strong dependence of the field on the relative dielectric constant has been observed at the triple junction.

6.7 Application to a Cylindrical Solid Insulator with Convex Curved Edges

In order to establish the degree of the applicability of the results obtained for the case of an infinite solid insulator block with convex curved edges to a cylindrical solid insulator with convex curved edges, some of the computation is repeated. The infinite line charges used in the case of the insulator block is replaced by ring charges to model the cylindrical solid insulator. For this purpose, Fig. 6.2 is to be considered as a cross section of a cylindrical solid insulator. The case of $\alpha = 45°$, $\varepsilon_2 = 2.1$, gap length 4 cm and $r/L = 0.35$ is re-examined. The equations for the potential coefficient P_{ij} and the field components E_r (radial) and E_z (axial) of the ring charges used are given in Appendix I.

Figure 6.17 shows the values of E'_{t_1} (curve 4) and E'_{n_1} (curve 2) when ring charges are used. When the same geometry is considered as block with no rotational symmetry the field values are computed by using infinite line charges. The results obtained are also shown in Fig. 6.17 for E'_{t_1} (curve 3) and E'_{n_1} (curve 1). It will be observed that at large values of θ (> 15°) the discrepancy between both methods are negligibly small for both E'_{t_1} (± 1.6%) and for E'_{n_1} (± 2.5%). As θ decreases and the electrode junction is approached, the difference for E'_{n_1} becomes significant. For example at the electrode junction the values of E'_{t_1} and E'_{n_1} using ring charge are respectively 1.09 and 1.24 (Fig. 6.17, curves 2 and 4 respectively at $\theta = 0$). The corresponding values for infinite line charges are 1.15 and 1.66 (Fig. 6.17, curves 3 and 1 respectively at $\theta = 0$). The observed maximum differences between the two methods is ± 2.7% for E'_{t_1} and ± 14.5% for E'_{n_1} which occur at the electrode junction.

6.8 Application to a Conical Insulator

The electric field and the potential distributions have been computed at the solid insulator-vacuum interface for conical insulators having different angle θ. Fig. 6.18 shows the arrangement of placing the fictitious charges and

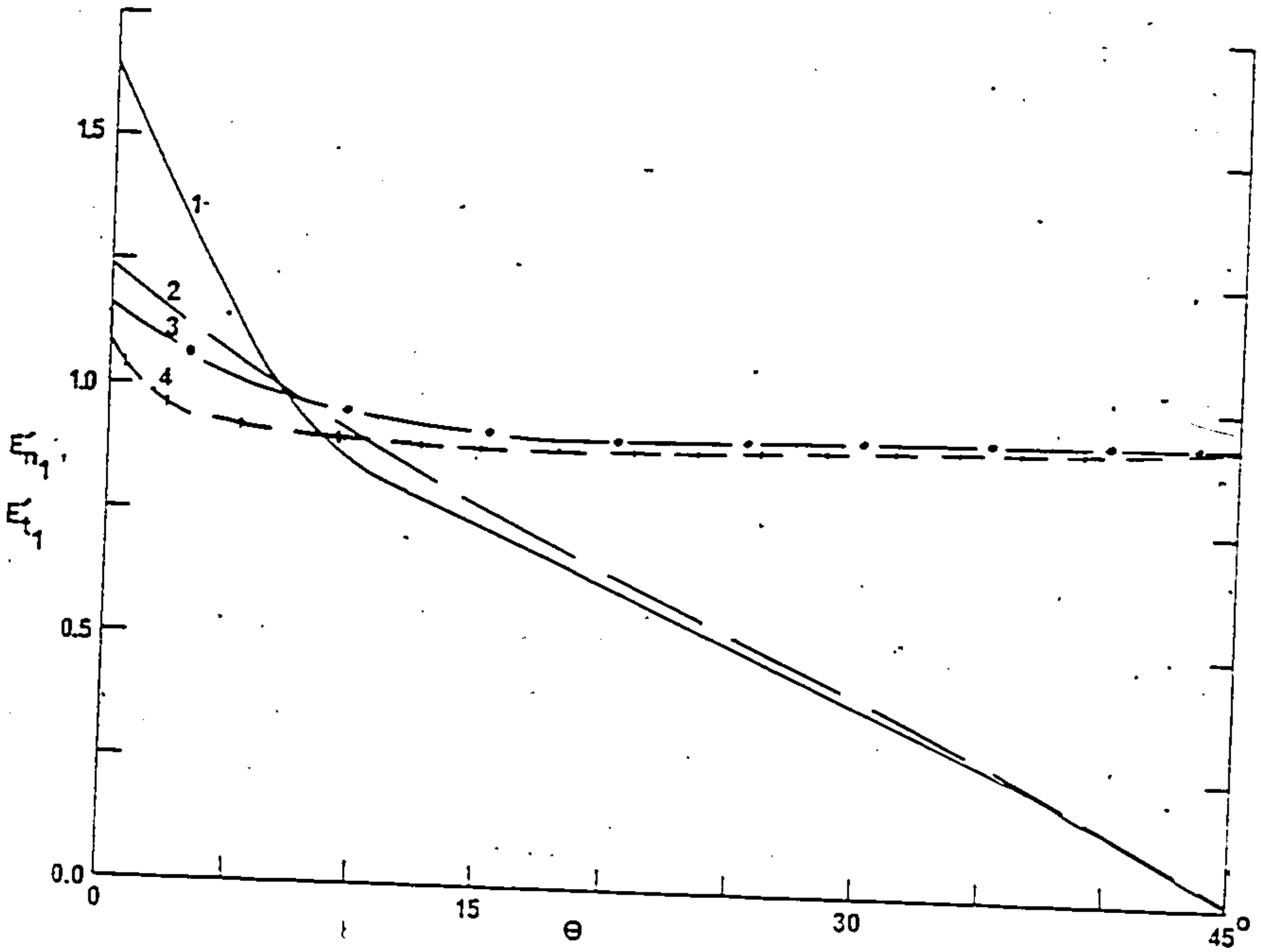

Fig. 6.17. Dependence of E'_{t_1} and E'_{n_1} on θ for Teflon ($\varepsilon_2 = 2.1$) using infinite line charges and ring charges. E'_{n_1} = curves 1 and 2; E'_{t_1} = curves 3 and 4; infinite line charges: curves 1 and 3; ring charges: curves 2 and 4; $\alpha = 45°$; $\varepsilon_2 = 2.1$; $r/L = 0.35$; $L = 4$ cm. Dimensions and location of charges are as per Fig. 6.2

the contour points on the conical insulator and the electrodes. Since the conical configuration considered here has a rotational symmetry, the charge simulation is carried out by employing ring charges to model the electrodes and the solid dielectric boundary. The number of ring charges used for the simulation is sufficiently large at 106 to yield accurate results. The computed values of the tangential field E_{t_1} to the surface and the normal field E_{n_1} on the vacuum side (region 1) of the solid insulator-vacuum interface are reported in a normalized format

$$E'_{t_1} = E_{t_1}/E_{av} = E_{t_1}\ L/V \qquad (6.16)$$

and

$$E'_{n_1} = E_{n_1}/E_{av} = E_{n_1}\ L/V \qquad (6.17)$$

where E_{av} is the average electric field between the planar electrodes. $E_{av} = V/L$ where V is the applied voltage across the solid insulator and L is the gap distance between the electrodes. Similarly the normalized potential ϕ' is defined

$$\phi' = \phi/V \qquad (6.18)$$

where ϕ is the potential at the surface of the cone insulator.

The accuracy of the solutions is evaluated by computing the potential error, the potential discrepancy and the tan-

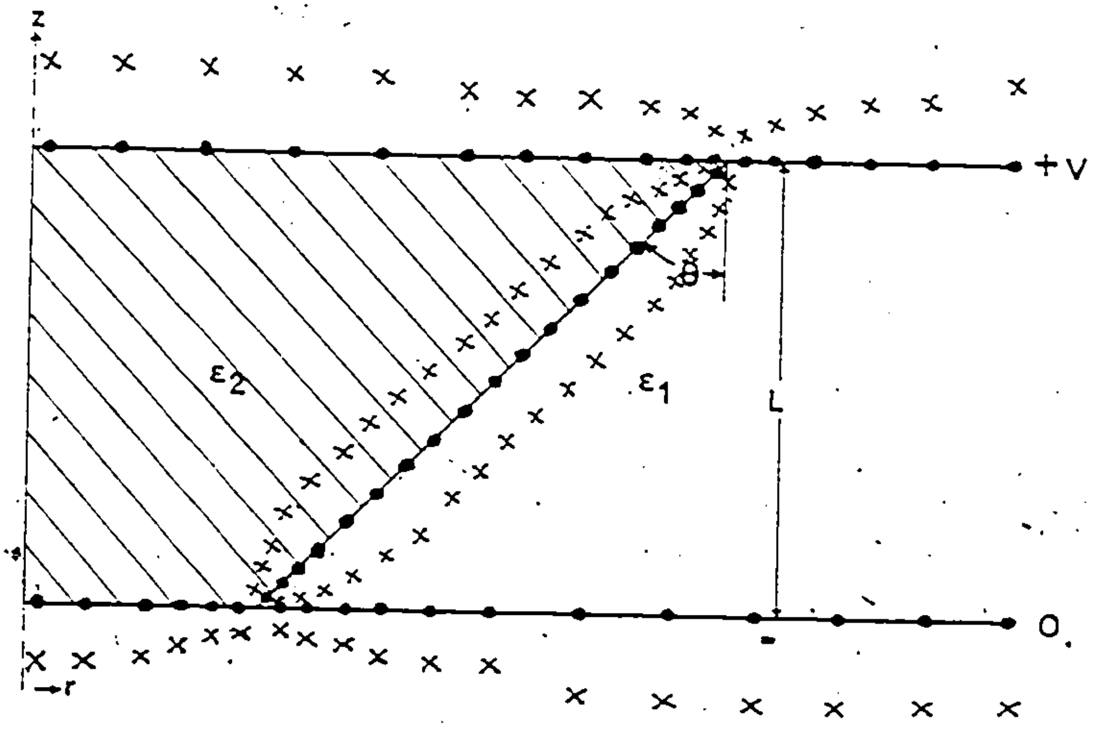

Fig. 6.18. Distribution of charges and contour points in the electrode and the conical solid insulator system. • contour points; x, ring charge location; L, distance between electrodes = 2 mm; θ = 45°; ε_2, solid insulator side (region 2), ε_1 vacuum side (region 1); V, applied voltage.

gential electric field discrepancy as specified in Section 6.2. The maximum electrode potential error is 0.08%; the maximum potential discrepancy is 0.01% near the contact region with the electrodes and less than 0.01% in the rest of the solid insulator boundary; the maximum tangential field discrepancy is 1.5% near the contact region with the electrode and less than 0.2% in the rest of the solid insulator boundary.

6.8.1 Potential Distribution Along the Cone Surface

The normalized potential distribution ϕ' along the Macor glass-ceramic cone insulator surface at the vacuum interface is shown in Fig. 6.19 as a function of Z/L. Z is the distance from the narrow end of the cone. ϕ' is calculated for different angles θ in the range 0 to 55°. It will be observed from Fig. 6.19 that the potential distribution becomes non-uniform as θ increases above 0°. The non-uniformity in ϕ' increases with increasing θ. It will be observed from Fig. 6.19 that there is a relatively larger increase in ϕ' towards the narrow end of the cone, at a fixed location of Z/L as θ increases. Typically at $Z/L = 0.125$, $\phi' = 0.125$ for $\theta = 0$ (Fig. 6.19 curve 1) and $\phi' = 0.302$ for $\theta = 45°$ (Fig. 6.19, curve 5). Near the base of the cone the relative change in ϕ' is much less at a fixed value of Z/L. For example at $Z/L = 0.875$, $\phi' = 0.875$ for $\theta = 0$ (Fig. 6.19, curve 1) and $\phi' = 0.963$ for $\theta = 45°$

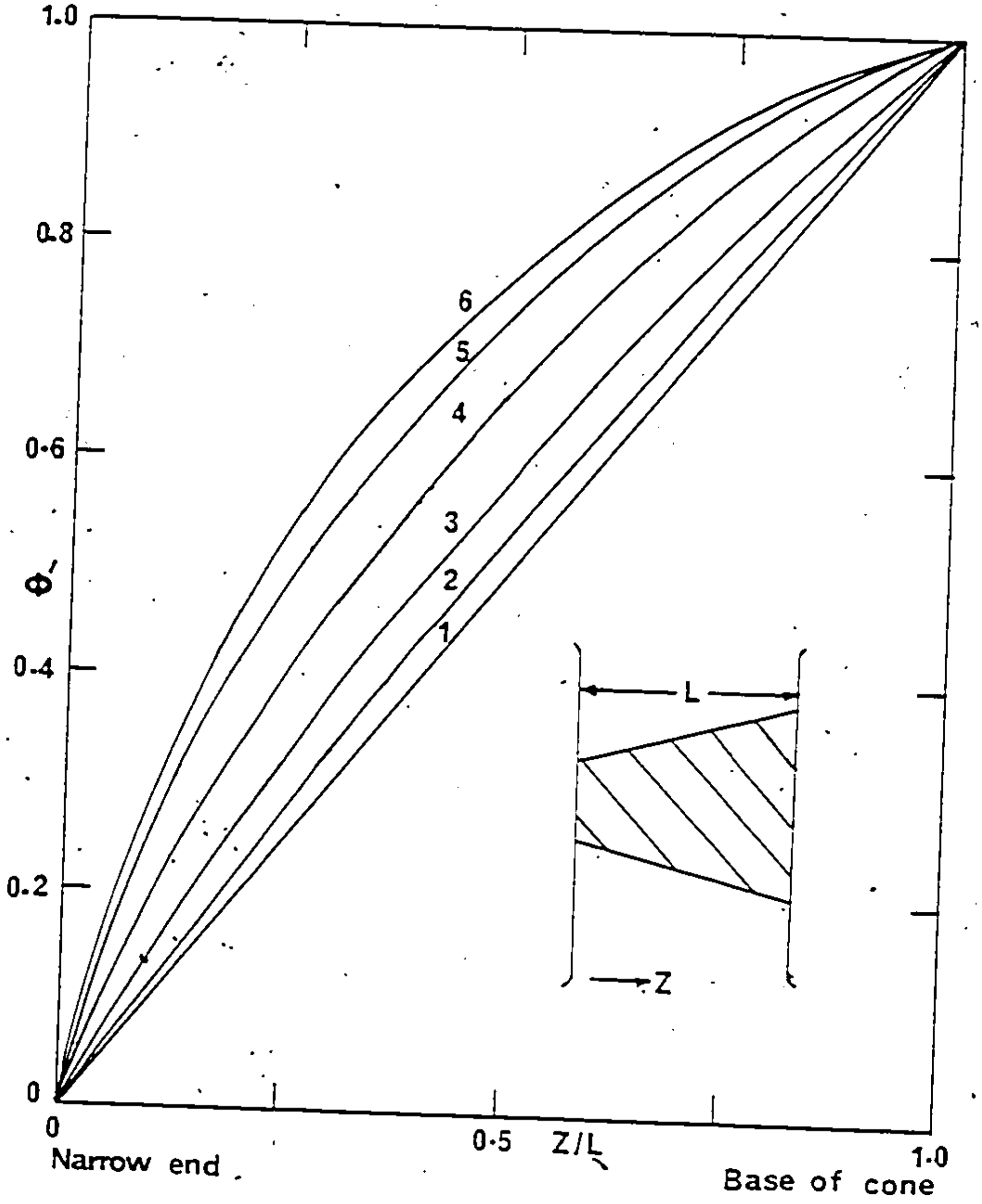

Fig. 6.19. Normalized potential ϕ' along the conical solid insulator interface (at the vacuum side) as a function of Z/L. Z is taken from the narrow end of the cone. L = 2 mm; ϵ_2 = 5.8: curve 1, θ = 0; curve 2, θ = 5°; curve 3, $\theta°$= 15 ; curve 4, θ = 30°; curve 5, θ = 45°; curve 6, θ = 55°.

(Fig. 6.19, curve 5).

6.8.2 Normalized Tangential and Normalized Normal Field Distributions

The normalized tangential [E'_{t_1}] and normalized normal [E'_{n_1}] field distributions on the solid insulator-vacuum interface are shown in Fig. 6.20 and 6.21 respectively as a function of Z/L. It will be observed from Figs. 6.20 and 6.21 that both E'_{t_1} and E'_{n_1} increase as the narrow end of the cone insulator is approached. E'_{t_1} ~~and~~ E'_{n_1} strongly depend on θ. Typically at the narrow end of the cone where $Z/L = 0$, $E'_{t_1} = 1.21$ (Fig. 6.20, curve 2) at $\theta = 5°$ and $E'_{t_1} = 2.7$ (Fig. 6.20, curve 5) at $\theta = 45°$. The corresponding values at the base of the cone where $Z/L = 1$ are $E'_{t_1} = 0.81$ (Fig. 6.20, curve 2) and $E'_{t_1} = 0.18$ (Fig. 6.20, curve 5). Hence when the base is made the cathode (positive θ) the flashover voltage is expected to be higher due to the lower electric field there compared to when the narrow end is made the cathode (negative θ). This situation has been observed both previously [9-11,97] and in the present investigation (Chapter 3), for impulse and DC applied voltages.

The normal field E'_{n_1} increases with increasing θ at both ends of the cone insulator. Typically at $Z/L = 0$, $E'_{n_1} = 0.18$ at $\theta = 5°$ (Fig. 6.21, curve 2) and $E'_{n_1} = 4.2$ at $\theta = 45°$ (Fig. 6.21, curve 5). At the base where $Z/L = 1$, $E'_{n_1} = 0.15$ at $\theta = 5°$ (Fig. 6.21, curve 2) and $E'_{n_1} = 0.45$ at $\theta = 45°$

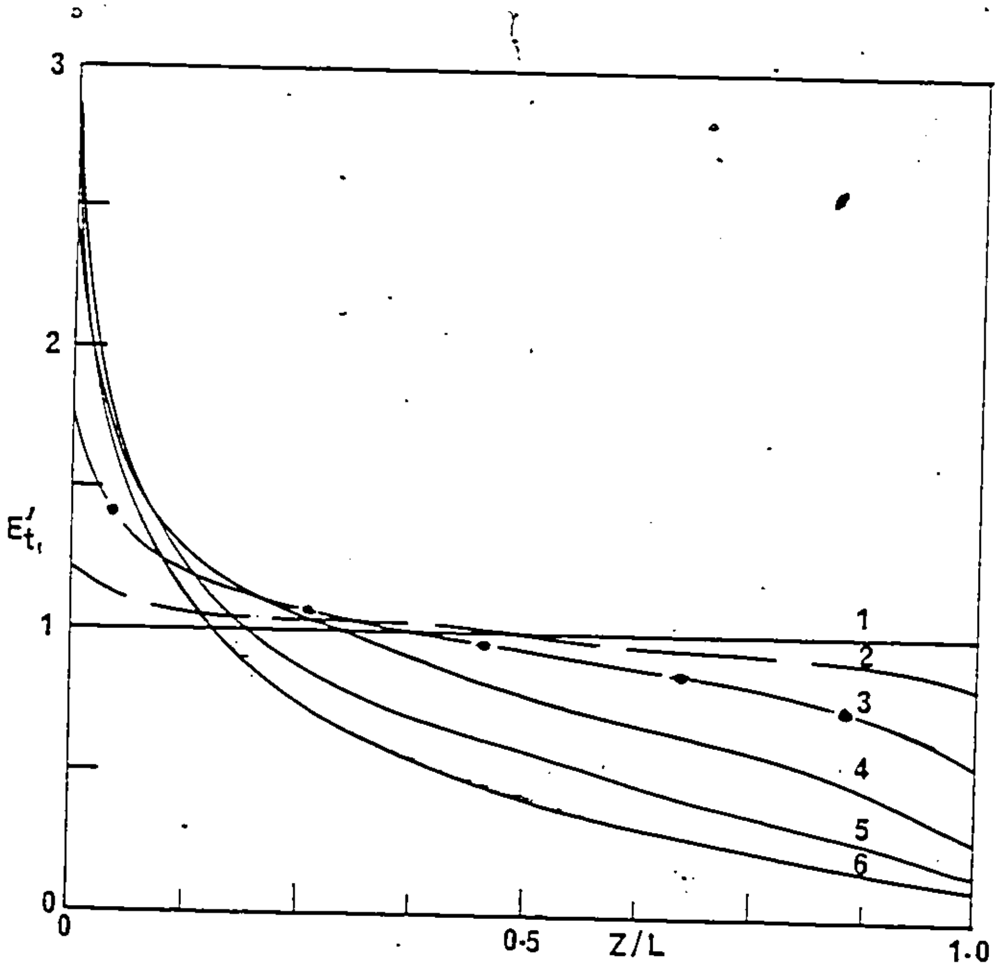

Fig. 6.20. Normalized tangential electrical field E'_{t1} at the conical solid insulator-interface (at the vacuum side) as a function of Z/L. Curve numbers as for Fig. 6.19.

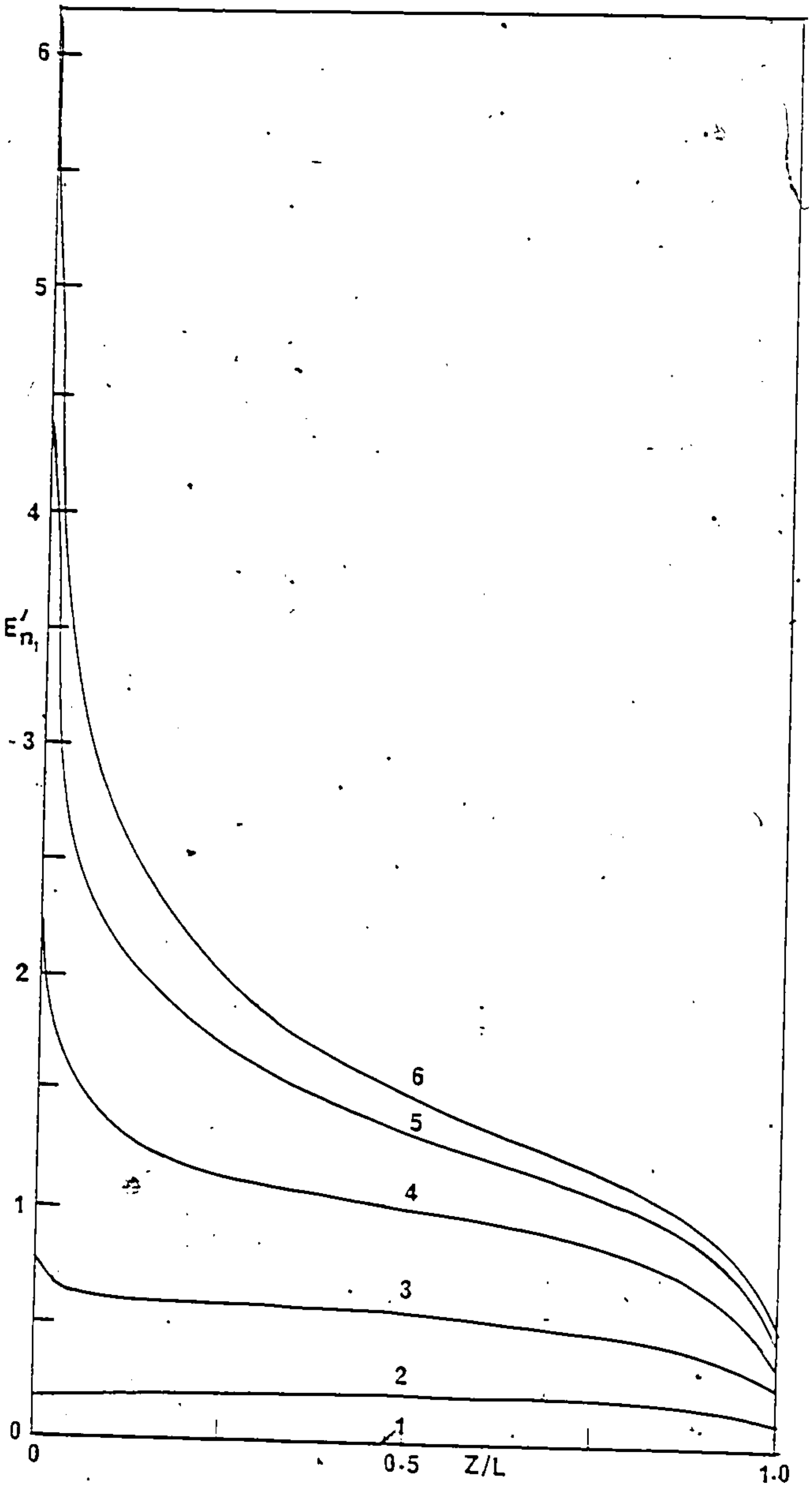

Fig. 6.21. Normalized normal electrical field E'_{n_1} at the conical solid insulator interface (at the vacuum

(Fig. 6.21, curve 4). The magnitude of the normal field is important for the production of charges on the surface of the insulator either from drift within the insulation towards the surface or from deposition on the surface from charges present in the vacuum region adjacent to the surface.

CHAPTER VII

MODIFICATION OF ELECTRIC FIELD AT THE SOLID INSULATOR-VACUUM INTERFACE ARISING FROM SURFACE CHARGES ON THE SOLID INSULATOR

The surface of a solid insulator in vacuum (and in a high gas pressure) becomes electrically charged when subjected to a high voltage stress. [7,13]. For cylindrical insulators sandwiched between two parallel plates in vacuum, the surface charge density is proportional to the applied voltage. The magnitude of the surface charge density depends on the secondary electron emission characteristic of the insulator. The fiele enhancement, contributing to a lower withstand voltage of solid insulators in vacuum, (and in compressed gases), due to the presence of surface charge is computed along the surface of the solid insulator and at the triple (electrode-solid insulator-vacuum) junction near the anode and cathode. Different patterns of surface charge density distribution have been considered in order to evaluate their effects on the field enhancement. The polarity, the magnitude and the shape of the distribution of the surface charge density has been found to have a considerable effect on the field enhancement. The observed influence of the charge distribution patterns on the electric field suggests that in order to obtain the experimentally observed field enhancement at both the cathode and anode junctions the insulator surface must possess a heterocharge accumulation (i.e., a positive charge towards the cathode and a negative charge towards the anode). For a positive charge accumulation throughout the surface of the insulator an enhancement in the field is found at the cathode and a reduction in the field value at the anode. An enhancement in the field on the surface of the insulator of location away from the electrodes is observed for a homocharge accumulation. In this case the field value is lower near both electrode junctions. The electric field and the potential distributions of the interfacial boundary between the solid insulator and vacuum is computed for different realistic surface charge distributions. The computed electric field at the triple junction for varying values of the D.C. applied field is then compared with the measured values reported in the literature. Good agreement is obtained. The effects of the magnitude of surface charge density, the applied field and the length of the solid insulator on the field enhancement at the triple junctions are also investigated. Nine different solid insulator materials having a relative permittivity in the range 2.1 - 13 and electron impact energies in the range 20 - 60 eV are examined. The field distributions at locations away from the boundary both inside the solid insulator and in the vacuum are computed with surface charge presence. The effect of the surface charge on the withstand voltage of the insulating vacuum gap bridged by a solid insulator is discussed.

7.1 Introduction

Measurements of the enhancement of the field at the triple junction due to the accumulation of a surface charge on the surface of a solid insulator has been reported in the literature [22,23]. The Monte Carlo simulation of surface charge distribution in the case of alumina (AL_2O_3) indicates that the surface has a positive charge polarity sufficiently close to the cathode region and a negative polarity towards the anode [23]. The latter simulation has been recently supported by the measurement of the distribution of the accumulated surface charge on an epoxy spacer surface in a high pressure (1 bar) sulphur hexafluoride gas where it was shown that the surface close to the cathode is positively charged and the surface near the anode is negatively charged [71]. The secondary electron emission coefficient (δ) of the solid insulator surface must be greater than unity in order to create a positive charge by the electron impact process. In the case of many practical solid insulators δ can be >1 over a wide range of electron impact energies [79,98]. Coating of the insulator surface with certain materials such as chromium oxide (Cr_2O_3) and cuprous oxide (Cu_2O) may reduce the value of δ to less than unity resulting in an improvement in the flashover voltage of insulators [23]. In the latter cases the surface near the cathode junction is negatively charged. This charge polarity in the particular location results in a decrease in the triple-junction field and therefore an increase in the withstand voltage of the insulating gap.

The variation in the computed triple junction (electrode-insulator-vacuum) field is examined by considering different patterns of surface charge distributions. An additional objective of using different charge distribution patterns is to find an optimum pattern which is subsequently used here to study the effects of the parameters of the length of the solid insulator, the applied voltage and the material of the solid insulator on the enhancement level of the electric field at the triple junction and along the surface of the solid insulator.

7.2 Method of Analysis

The charge simulation technique discussed in Chapter 6 is used to compute the electric field and the potential distribution along the solid insulator-vacuum interface and at both triple junctions, cathode and anode. The geometry is a solid dielectric cylinder, 12.5 mm in diamater and 12.5 mm in length mounted between uniform electrodes in ultrahigh vacuum. Since the arrangement considered has a rotational symmetry, the charge simulation is carried out by employing ring charges to model the electrodes and the solid dielectric boundaries. The number of ring charges used for the simulation is 92.

In the charge simulation technique, the surface polarization charge at the solid-dielectric-vacuum interface is approximated by a system of unknown charges located at both sides of the interface. The normal flux densities are continuous across the interface between the solid insulator and the vacuum boundary. When there is no surface charge present on the interface between the solid dielectric and vacuum (Eq. 6.4, Chapter 6).

$$D_{n1} = D_{n2} \tag{7.1}$$

Hence $\varepsilon_o \varepsilon_1 E_{n1} = \varepsilon_o \varepsilon_2 E_{n2}$ where E_{n1} and E_{n2} are the normal components of the electric field in the vacuum (region 1) and the solid dielectric (region 2), respectively, ε_1 and ε_2 are the relative dielectric constants of vacuum ($\varepsilon_1 = 1$) and the solid insulator (for glass-ceramic $\varepsilon_2 = 5.8$), respectively and ε_o is the permittivity of free space ($\varepsilon_1 = 8.854 \times 10^{-14}$ Fcm^{-1}). In the present case a surface charge density having a magnitude σ_s (in C cm^{-2}) is also assumed to be present on the interface between the solid dielectric and vacuum. The charge arises as a consequence of the application of the voltage stress across the cylindrical solid insulator. In this case the tangential intensities of the electric fields are also continuous as in the case of the solid insulator-vacuum boundary without surface charges. However, the normal flux density (Eq. 7.1) is modified in order that an account is taken of the presence of the surface charge. In the case of a solid insulator boundary with a surface charge density σ_s (in C cm^{-2}) present on the interface between two insulators, Eq. (7.1) becomes [99],

$$D_{n1} - D_{n2} = D_{ns} \tag{7.2}$$

$$\varepsilon_1 E_{n1} - \varepsilon_2 E_{n2} = \varepsilon_1 E_{ns} \tag{7.3}$$

and for $\varepsilon_1 = 1$

$$E_{n1} - \varepsilon_2 E_{n2} = E_{ns} \tag{7.4}$$

where

$D_{ns} = \varepsilon_0 \varepsilon_1 E_{ns}$ and E_{ns} is the normal field due to the presence of surface charge density given by Eq. (7.5). E_{ns} is directed outward away from the solid insulator when σ_s has a positive polarity and inward if σ_s is negative.

In the case of a solid insulator in vacuum, the height of the electron trajectory from the solid surface is very small, a few micrometers, compared to the radius of the curvature of the surface of practical insulators [7]. Therefore, the solid insulator surface can be considered as a plane as far as the trajectory of the electron is concerned. Hence, the normal field E_{ns} ($V\ cm^{-1}$) in the vacuum region produced due to the presence of surface charge density σ_s in the plane geometry is (Eqn. 5.5, Chapter 5).

$$E_{ns} = \sigma_s/2\varepsilon_0 \qquad (7.5)$$

The computed results of the normal field intensity, E_{n1} (in region 1 in the vacuum side of the solid insulator - vacuum interface) and the tangential field intensity E_{t_1} (in region 1) are presented in a normalized format. The average electric field in the gap is $E_{av} = V/L$ where V is the applied voltage (in V) with respect to the ground electrode at zero potential and L (in cm) is the length of the solid insulator forming also the gap distance between the electrodes.

$$E'_{n_1} = E_n/E_{av} = E_{n_1}\ L/V \qquad (7.6)$$

$$E'_{t_1} = E_t/E_{av} = E_{t_1}\ L/V \qquad (7.7)$$

where E'_{n_1} and E'_{t_1} are the normalized normal and the tangential field components to the surface of the solid insulator, respectively. The normalized normal and tangential field components at the cathode triple junction are referred to as E'_{nc} and E'_{tc} respectively. At the anode junction, E'_{na} and E'_{ta} are similarly defined. The maximum of the normalized values of the tangential and the normal fields are referred to as $E'_{t_{1m}}$ and $E'_{n_{1m}}$ respectively. Inside the solid insulator and in the vacuum regimes the normalized field also has two components in the axial (E'_z) and the radial directions (E'_r)

7.3 The Origin of Surface Charges on Solid Insulators in Vacuum

The presence of surface charges on solid insulators may explain some of the conflicting results reported in the studies of the electrical breakdown of solid insulators in vacuum and in high pressure gases. The mode of the surface charge distribution along the solid insulator surface is dependent on the secondary emission yield of the insulator surface. The charging of the solid insulator surface occurs as a result of the impinging electrons and the subsequent secondary electron emission during the conduction of the electric current prior to the breakdown of the gap. The surface charge density is directly proportional to the interelectrode field (in V cm^{-1}). The interelectrode field is the field parallel to the surface of the solid insulator and is equal to the average field E_{av} in the case of a cylindrical solid insulator. The expression for the surface charge density σ_s can be written as (Eq. 5.7, Chapt. 5):

$$\sigma_s = 2\,\varepsilon_0\,E_{av}\left[\frac{2A_0}{(A_1 - A_0)}\right]^{1/2} \qquad (7.8)$$

where A_o and A_1 are the electron emission energy and the impact energy (in eV), respectively. In general the secondary electron emission parameters A_0 and A_1 for solid insulators are a few eV and a few tens of eV [7,79,98]. In the present study the values for A_1 are obtained from Refs. 7, 79 and 98 and A_0 is assumed 4.6 to 5 eV [7].

7.4 Surface Charge Density Distributions

The field strength required to cause a surface flashover in vacuum for a given solid insulating material increases with increasing value of the impact energy [30]. The surface charge density is a linear function of the applied voltage [7,69,70]. Figure 7.1 shows the surface charge density distribution calculated from Eq. (7.8) as a function of the applied electric field for different insulating materials. Alumina ceramic, glass-ceramic, Pyrex glass, Quartz and plexiglass are considered. It can be seen from Fig. 7.1 that for the same applied field, the surface charge density varies according to the emission characteristic of the insulating material. The emission characteristics are determined by the appropriate values of A_0 and A_1. The measured surface charge density in the case of plexiglass (Fig. 7.1, curve 6) and alumina ceramic (Fig. 7.1, curve 7) along with the Monte Carlo simulation [70] of surface charge density for alumina (Fig. 6.1, curve 8) are plotted in Fig. 7.1

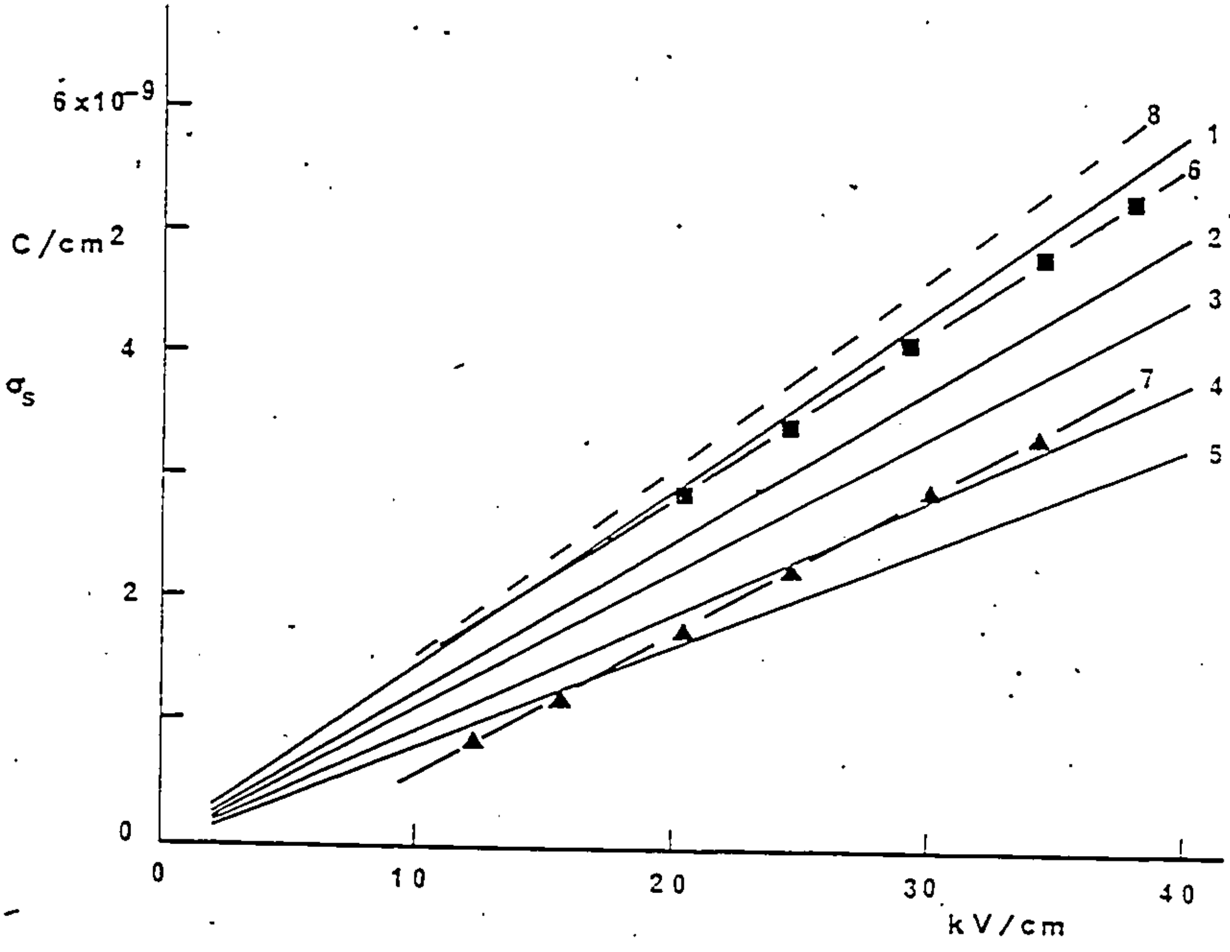

Fig. 7.1. Variation of surface charge density at the solid insulator surface with applied electric field. Curve 1, Alumina ceramic - (Al_2O_3) (Impact energy A_1 = 20 eV [79], Eqn. 7.8); 2, Glass ceramic (A_1 = 25 eV, Eqn. 7.8); 3, Plexiglass (A_1 = 30 eV, Eqn. 7.8); 4, Pyrex glass (A_1 = 40 eV, Eqn. 7.8); 5, Quartz (A_1 = 50 eV, Eqn. 7.8); 6, Plexiglass (measured) [69,70]; 7, Al_2O_3 (measured) [69,70]; 8, Al_2O_3 (Monte Carlo simulation [79]).

for comparison. It will be observed that the surface charge density derived from Eq. 7.8 increases linearly with increasing electric field in general agreement with the previously reported measurements [7,69,70].

The polarity and the distribution pattern of the accumulated charge on the surface of the solid insulator depends on the microscopic property of the surface and the material as well as the type of applied voltage and the electrical treatment to which the gap has been subjected. The electric field measurements at the triple junctions show that at both the anode and the cathode locations the fields were enhanced due to the presence of a solid insulator in vacuum [22,23]. On qualitative grounds it may be suggested that enhancements in the fields at both electrode junctions occur only when a positive charge accumulates near the cathode and a negative charge near the anode. This qualitative suggestion is confirmed on analytical and quantitative grounds in this work. The assumed value of the total positive charge accumulation near the cathode surface in the present work is higher than that of the negative charge accumulation near the anode. This assumption is reasonable and is also in general agreement with the Monte Carlo simulation of the charge density distribution by Sudarshan et al. [23] and the measurements reported by Nakanishi et al. [71]. In order to obtain a suitable pattern of charge density distribution which gives the qualitatively expected field distribution along the surface of the solid insulator many patterns of surface charge distribution are considered in the present analysis. A variety of surface charge patterns showing nine distinct distributions along the surface of the solid insulator are depicted in Figs. 7.2, 7.3 and 7.4. The patterns are identified as P_1, P_2, ..., P_9 (Figs. 7.2-7.4). In the region where the charge polarity is positive it is indicated as (+) and where it is negative (-).

The solid insulator considered in detail is Macor glass-ceramic. This insulator is widely used in a variety of engineering and other applications. In the case of glass-ceramic, it is assumed that the secondary electron emission coefficient is less than unity for normal incident primary electrons with energies less than 25 eV which is the value of A_1. The surface charge density σ_s is assumed to be 1.90×10^{-9} C cm^{-2} at an applied electric field of 16 kV cm^{-1} and electron emission energy $A_0 = 4.6$ eV. The surface charge density is distributed as a function of distance from the cathode in different patterns. In Fig. 7.2 the assumed surface charge distribution in patterns, P_1, P_2, P_3 are different, but the maximum value of σ_s is at the same value of 1.9×10^{-9} C Cm^{-2}. The minimum value of σ_s varies from -1.9×10^{-2} C cm^{-2} (Fig. 7.2, P_1 and P_2) to -0.5×10^{-9} C cm^{-2} (Fig. 7.2, P_3). The total amount of the positive charge on the surface of the insulator in the

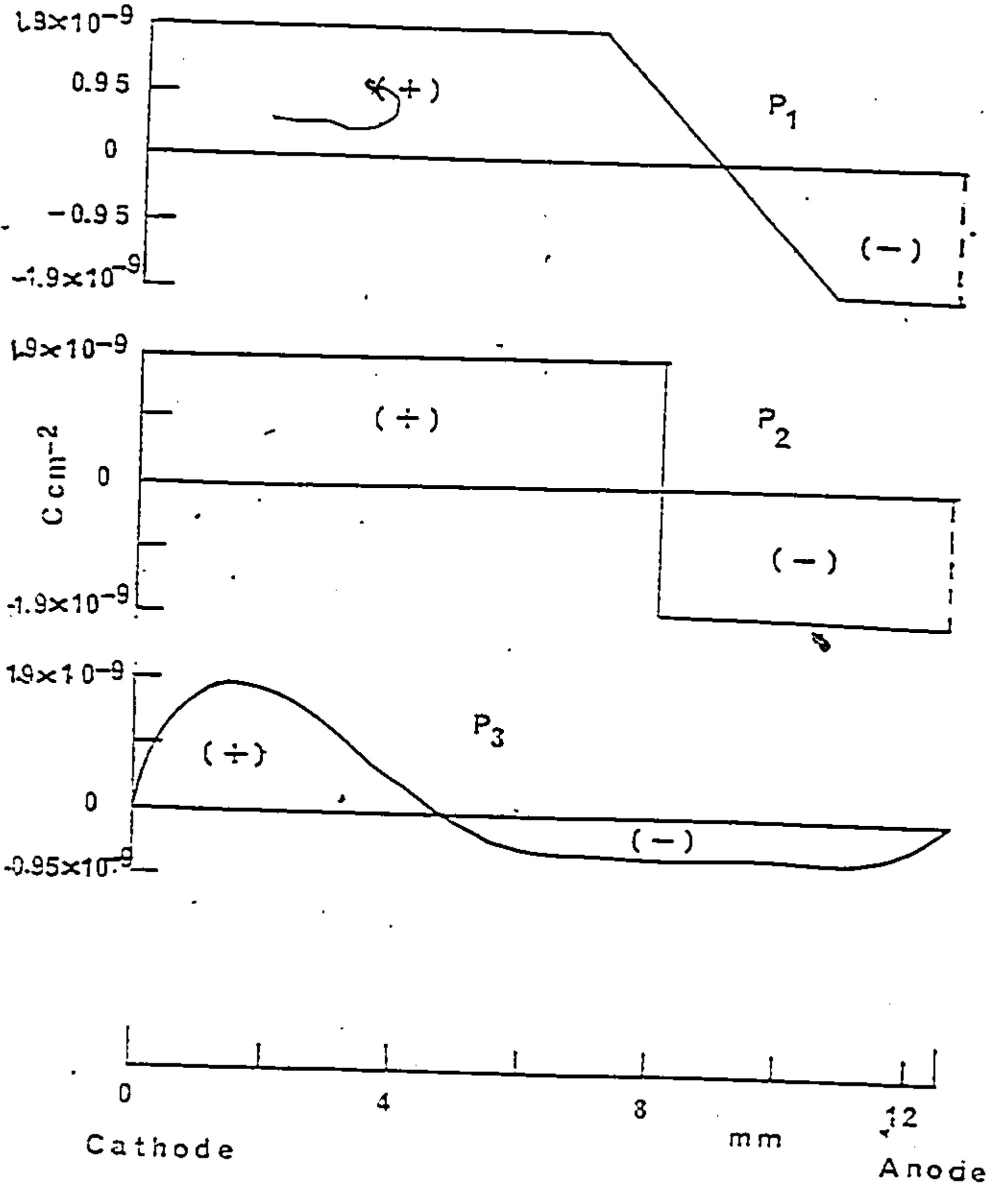

Fig. 7.2. Patterns P_1 to P_3 showing charge density distributions σ_s along the surface of the solid insulator used in the calculation of the electric field. Length of solid insulator L = 12.5 mm: (+) indicates positive charge polarity; (−) negative charge polarity.

region of the cathode is at least more than double the absolute value of the negative surface charge density in the region of the anode. In pattern P_4 (Fig. 7.3), the maximum value of σ_s towards the cathode is 3.9×10^{-9} C cm^{-2} and the charge density towards the anode is -3×10^{-9} C cm^{-2}. In Fig. 7.3, a pattern (P_5) is also shown where the positive value of the charge is at a maximum level near the cathode ($\sigma_s = 3.0 \times 10^{-9}$ C cm^{-2}) and at a minimum near the anode ($\sigma_s = 2.0 \times 10^{-9}$ C cm^{-2}). For completeness and in order to find the dependence of the electric field on a unique charge polarity (either positive or negative) but having different charge distributions along the surface of the solid insulator an additional four patterns are considered (Fig. 7.4, P_6-P_9). The assumption of one type of charge polarity may be realistic in the presence of high pressure electronegative (for example SF_6) or inert (nitrogen) gases surrounding solid insulators used as spacers in gas insulated system for high voltage power transmission. The abundance of negative ions (say in SF_6 or in air) or positive ions (in N_2) in the vicinity of the solid insulator surface may favor one or the other charge polarity depending on the type of the insulator material, the electrode geometry [71] and the energy of the impinging electrons and ions on the solid insulator surface.

In pattern 6 (Fig. 7.4), the charge density near the cathode is 1.9×10^{-9} C cm^{-2} and decreases linearly to a value

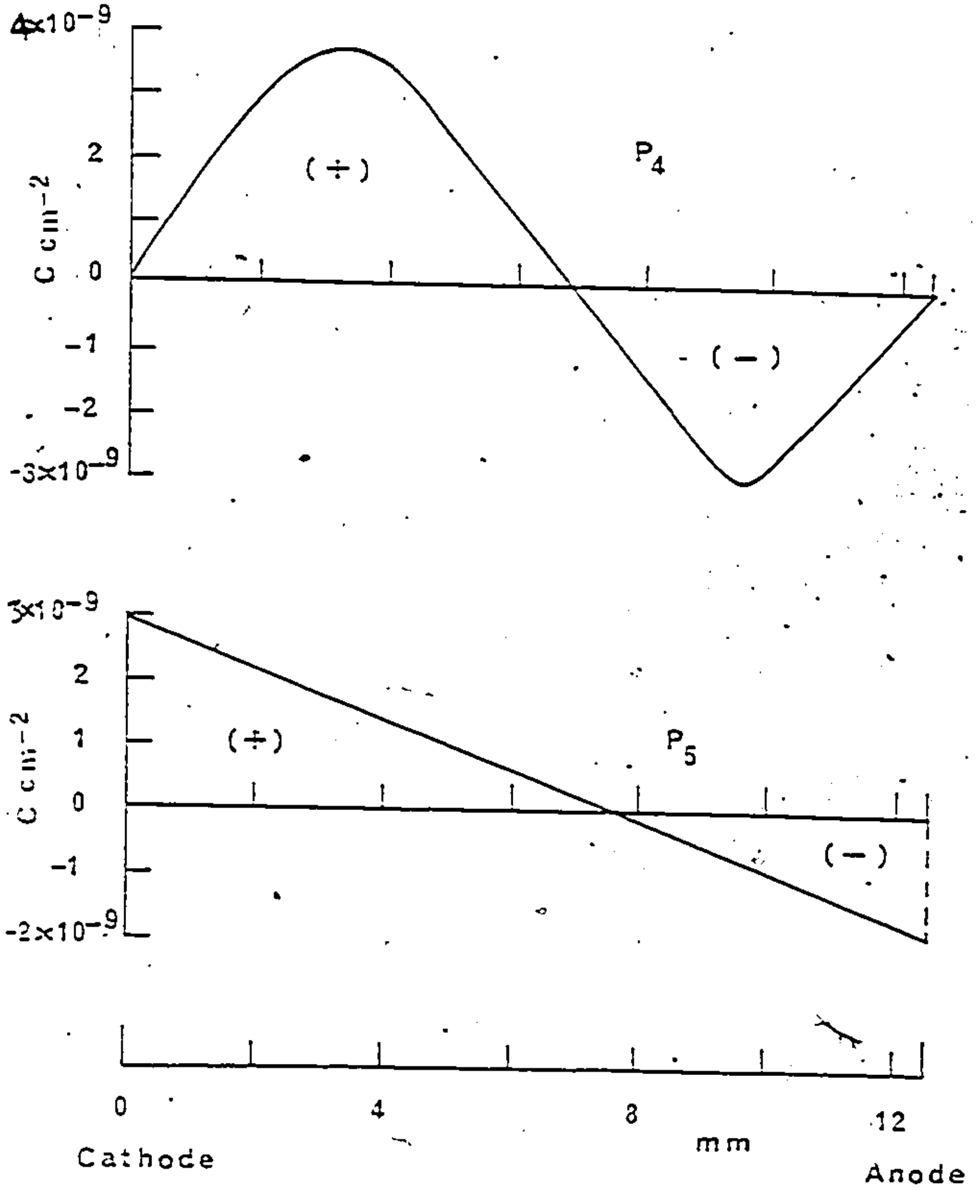

Fig. 7.3. Patterns P_4 and P_5 showing the charge distribution along the surface of the solid insulator in vacuum. Length of solid insulator and notations (+) and (-) are as for Fig. 7.2.

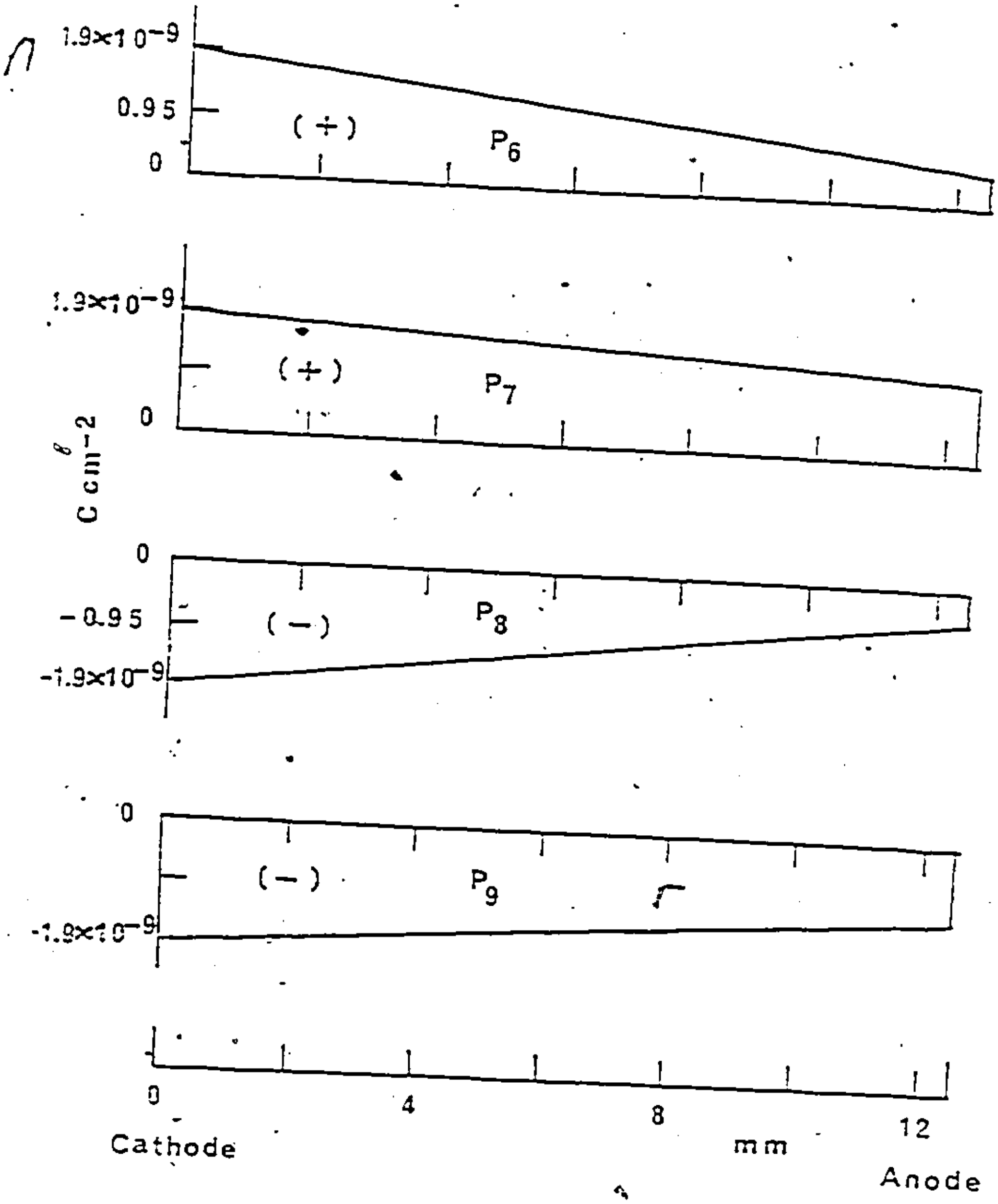

Fig. 7.4. Patterns P_6 to P_9 showing charge density distribution σ_s along the surface of a solid insulator in vacuum. Length of solid insulator and notation (+) and (-). are as for Fig. 7.2.

0.5×10^{-9} C cm^{-2} near the anode. In Pattern 7 (Fig. 7.4) the variation is from 1.9×10^{-9} C cm^{-2} near cathode to 1.2×10^{-9} C cm^{-2} near the anode. In patterns 8 and 9 (Fig. 7.4) the same linear dependence of surface charge distribution on the length of the solid dielectric as in P_6 and P_7, respectively is assumed except for the polarity of the charge where it is now negative.

7.5 Dependence of Electric Field on the Type of Charge Distribution, Charge Magnitude and Charge Polarity

The normalized components of the tangential field E'_{t_1} (Figs. 7.5 and 7.6) and the perpendicular field E'_{n_1} (Fig. 7.7) on the insulator surface at the interface boundary (on the vacuum side - region 1) due to the different patterns of surface charge distribution are presented. The applied electric field is 16 kV/cm. In Figs. 7.5, 7.6 and 7.7 the length of the solid insulator (L = 12.5 mm) and the material (glass-ceramic, $\varepsilon_2 = 5.8$) are kept constant. Only the type of charge distributions (P_1 to P_9), magnitude of charge density (-3.0×10^{-9} to $+3.9 \times 10^{-9}$ C cm^{-2}) and charge polarity (positive and negative) are investigated. The dependence of the enhancement of the electric field on insulator material at a fixed pattern will be further described in Section 7.7.2.

Figure 7.5 shows the normalized tangential field distribution along the solid insulator-vacuum boundary for patterns P_1 - P_5. The normalized E'_{t_1} at the triple cathode junction resulting from patterns P_1 to P_5, at 16 kV/cm applied field, are 1.275, 1.249, 1.156, 1.240 and 1.298, respectively. The corresponding E'_{t_1} at the anode triple junction are 1.146, 1.235, 1.10, 1.161 and 1.226, respectively. It will be observed that an enhancement in the electric field exists in both regions near the cathode and the anode. The enhancement in the field near the cathode is higher (about 10%) than the corresponding field near the anode. The higher electric field in the cathode region contributes to an increased emission of electrons according to the Fowler-Nordheim cold field emission [49]. The increased electron emission contributes to lowering of the withstand voltage of the solid insulator gaps as observed experimentally, compared to the same length of vacuum gaps without the presence of the solid insulator [12]. The higher current emission results in reaching a critical current leading to a catastrophic breakdown of the gap at a lower applied voltage than would be the case if there were no enhancements in the field in the cathode region. The value of the normalized tangential field E'_{t_1} resulting from patterns P_1 to P_5 decreases with increasing distance from the cathode junction until it reaches a minimum value between 0.82 to 0.92, depending on the specific distribution, around the mid region of the solid insulator. E'_{t_1} increases with further increasing distance away from the cathode and towards the anode triple junction (Fig. 7.5). It will be observed that when the assumed surface charge accumulation near the cathode has a positive polarity and near the anode is negative, there is

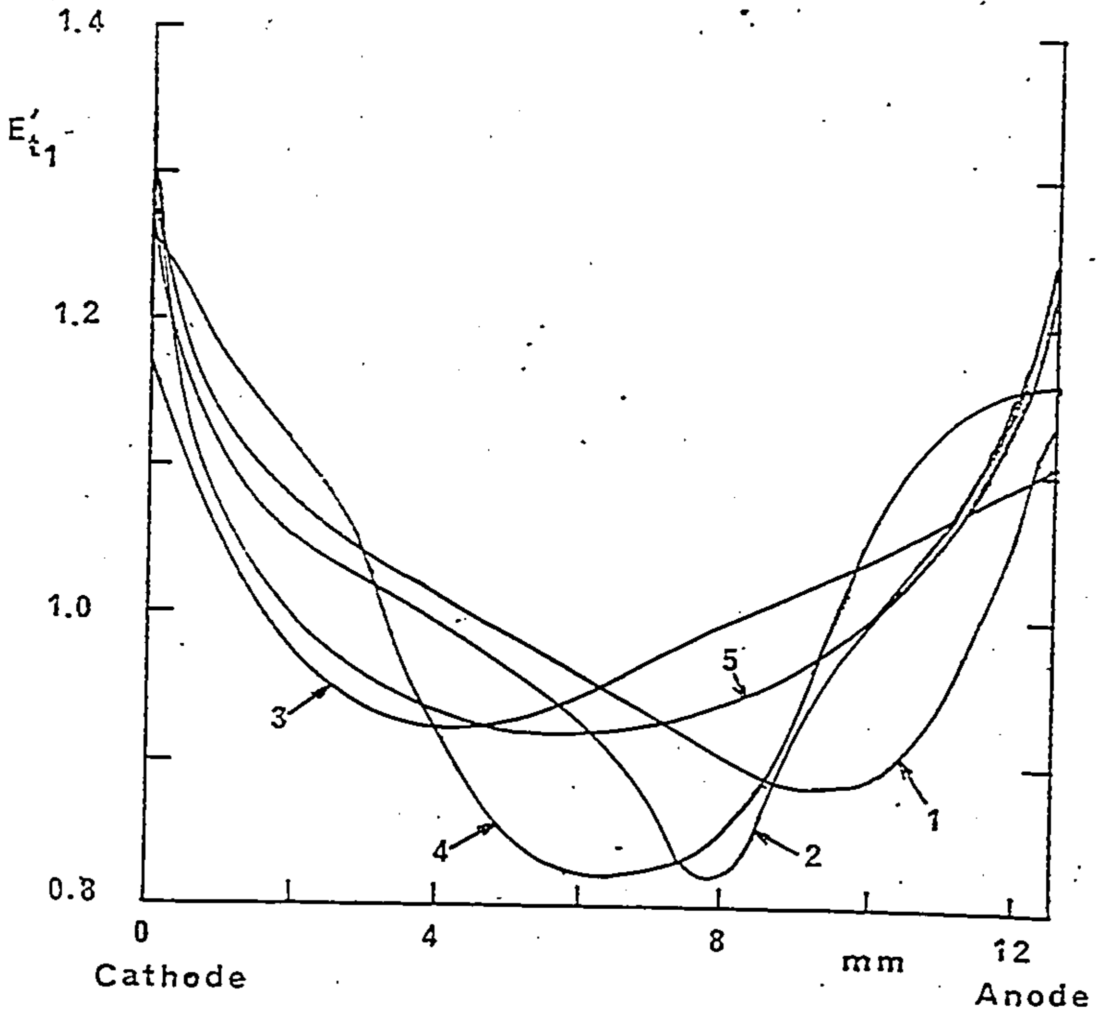

Fig. 7.5. Normalized tangential electric field E'_{t_1} along the solid dielectric insulator - vacuum boundary for the surface charge distribution Patterns P_1 to P_5 (defined in Figs. 7.2-7.3). Length of insulator L = 12.5 mm, $\varepsilon_2 = 5.8$ (glass-ceramic), Normalized field shown is on the vacuum side ($\varepsilon_1 = 1$) of the interface. Curve 1 corresponds to pattern P_1; curve 2, P_2; curve 3, P_3; curve 4, P_4; curve 5, P_5).

an enhancement in the field at both electrode junctions.

The variation of the tangential field along the length of the insulator obtained by using patterns P_6 to P_9 (defined in Fig. 7.4) is shown in Fig. 7.6. It will be seen that an entirely different electric field distribution is obtained along the surface of the insulator. An enhancement occurs near one electrode and a decrease in the field near the other electrode. The enhancement in the tangential field near the cathode junction is 1.24, and 1.27 for P_6 and P_7, respectively. Since the assumed peak value of σ_s is 1.9×10^{-9} C cm^{-2} the E'_{t_1} values are close to the values obtained for P_1 to P_5 (Fig. 7.5). However, the anode junction field is lower than the applied field. The E'_{t_1} values are 0.96 (Fig. 7.6, curve 6) and 0.84 (Fig. 7.6, curve 7) for P_6 and P_7, respectively. In the case of P_6, the assumed value of σ_s is 0.5×10^{-9} C cm^{-2} close to the anode but in the case of P_7 the value of σ_s is 1.2×10^{-9} C cm^{-2}. This is responsible for the lower value of anode field enhancemet in the case of P_7 compared to P_6. The values of E'_{t_1} near the cathode and anode are 0.71 and 1.185 respectively for pattern 8 and 0.66 and 1.280 for P_9. In the present case the enhancement in the field occurs near the anode (P_8 and P_9). In the case P_9 the value of E'_{t_1} is higher at the anode and lower at the cathode compared to P_8 because the assumed value of the surface charge density is -1.2×10^{-9} C cm^{-2} (P_9) when

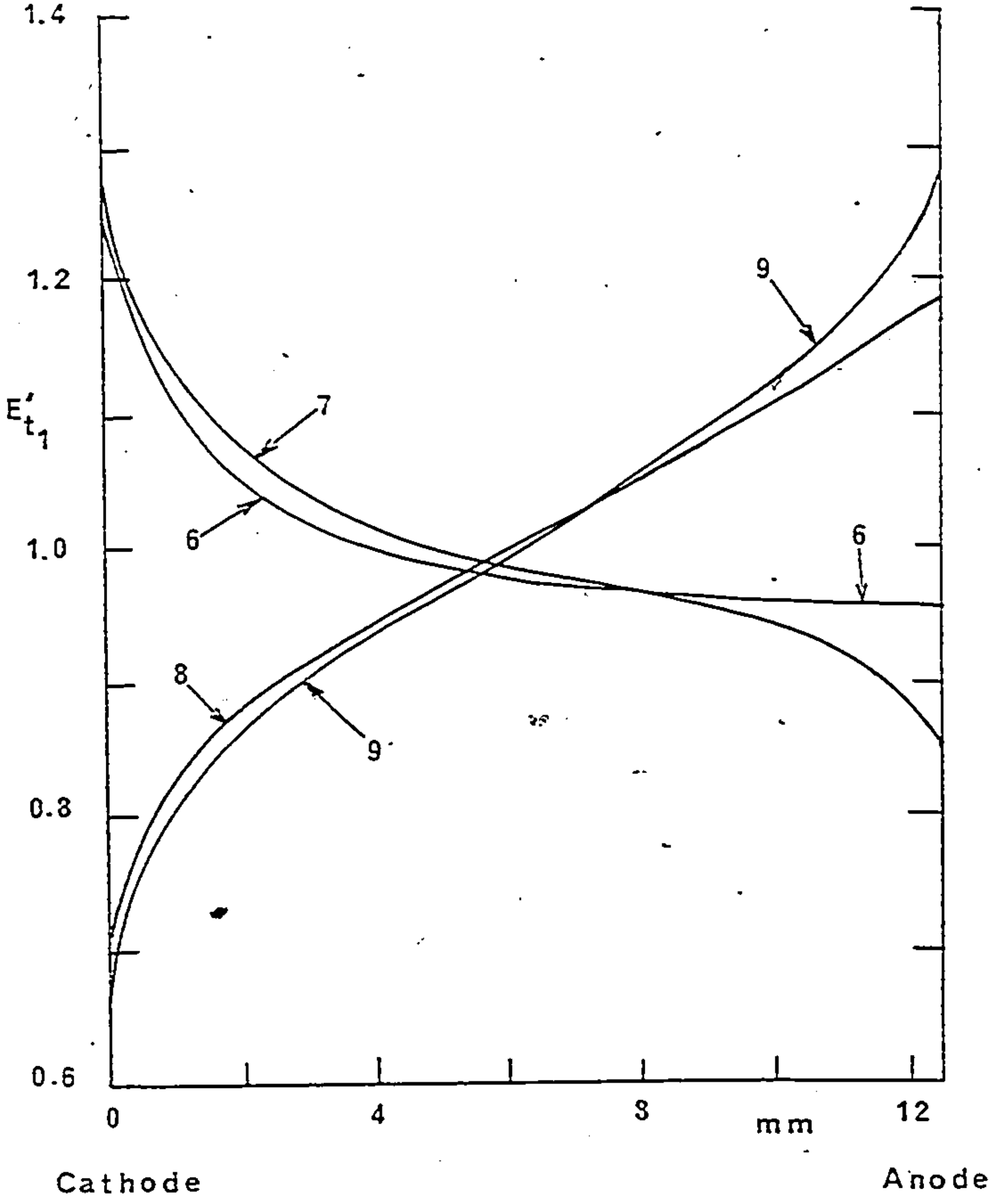

Fig. 7.6. E'_{t_1} along the solid insulator - vacuum interface using patterns P_6 to P_9 (defined in Fig. 7.4). Other conditions as for Fig. 7.5. Curve 6 corresponds to pattern P_6; curve 7, P_7; curve 8, P_8; curve 9, P_9.

compared to -0.5×10^{-9} C cm^{-2} used for P_8.

The normalized field components perpendicular to the insulator surface E'_{n_1} (at the solid insulator-vacuum interface) obtained by using patterns P_1 to P_6 and P_8 (defined in Figs. 7.2, 7.3 and 7.4) are shown in Fig. 7.7. The normalized value of E'_{n_1} is at a maximum value away from both electrodes and occurs near the mid gap of the solid dielectric. The value of E'_{n_1} changes towards slightly negative when reaching the anode region. The change in the sign of the field indicates that the field is directed inward towards the insulator. This is due to the assumed negative surface charge distribution towards the anode region. The change in the field direction has some significance, albeit small due to its low value. In practical systems where the presence of microparticles cannot be entirely avoided in the gap they are more likely to drift towards the surface of the insulator and be deposited in the favourable field. The normal field distribution for P_6 has also a maximum near the center, but no change occurs in the direction of the field (i.e., not becoming negative) near the anode. This is because the polarity of the charge is assumed to be positive throughout the surface length. In the case of pattern P_8 (Fig. 7.7, curve 8) the value of E'_{n_1} is negative close to the cathode and becoming positive around mid gap. E'_{n_1} becomes again negative close to the anode. This change in the direction of the field

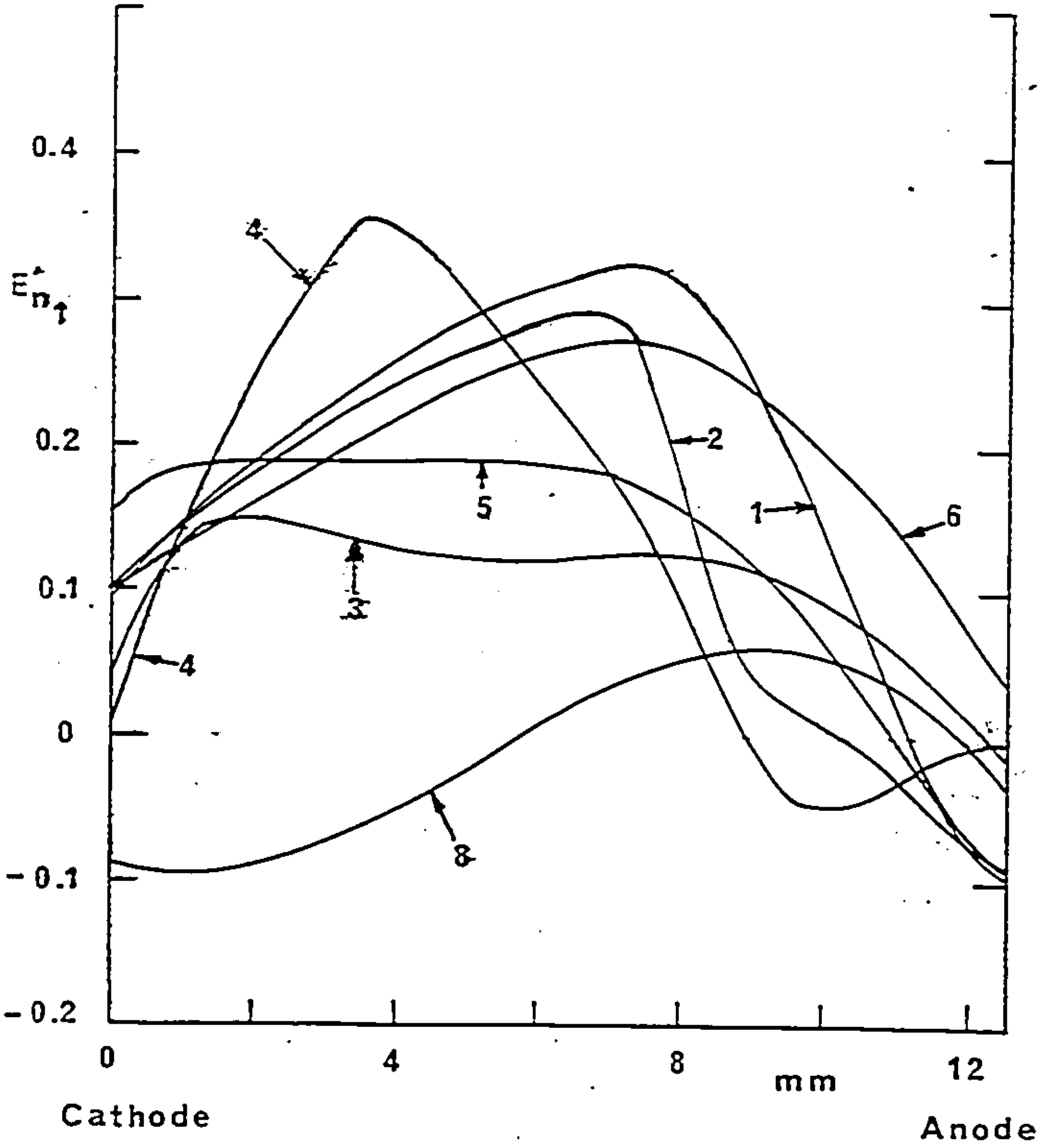

Fig. 7.7. Normalized normal field distribution E'_{n_1} along the solid insulator-vacuum interface for P_1 to P_6 and P_8. Curve 1 corresponds to P_1; curve 2, P_2; curve 3, P_3; curve 4, P_4; Curve 5, P_5; curve 6, P_6, curve 8, P_8. Other conditions as for Fig. 7.5.

from inward (negative) to outward (positive) of the surface of the solid insulator is due to the particular charge distribution pattern used. In general the contribution of E'_{n_1} to the total enhancement is not very large but at the same time it is not negligible. It reaches up to 33%, 29% and 36% of the average field for P_1, P_2 and P_4 respectively (Fig. 7.7). The development of E'_{n_1} due to the presence of surface charge enhances the radial diffusion loss of electrons from the main avalanche but E'_{t_1} is primarily responsible for the direct development of the discharge channel leading to breakdown.

It should be noted that some of the assumed patterns of surface charge density distributions along the length of the insulator are consistent with the distributions reported by Nakanishi et al. for epoxy spacers in SF_6 [71], Knecht [72] for bisphenolic epoxy resin spacers in SF_6 and N_2, Lee _et al_. [41] for plexiglass and Lucalox in vacuum and in N_2 gas. The assumed pattern P_3 is qualitatively similar to that simulated by Sudarshan et al. [23] and P_4 similar to that measured by Nakanishi et al. [71]. The assumed orders of magnitude for σ_s agree also with the simulated and measured values in the case of Al_2O_3 in vacuum by Brainard et al. [37], Teflon, Al_2O_3, plexiglass and nylon in vacuum by de Tourreil et al. [69,70]. The value of σ_s reported by Knecht [72] for epoxy insulators in high pressure gases is also of the same order of magnitude as that used here.

7.6 Potential Distribution Along the Surface of the Solid Insulator with Surface Charges

The potential distribution along the surface of the solid dielectric at the vacuum interface obtained using different patterns are shown in Fig. 7.8. The departure from linearity in the potential distribution is somewhat more distinct near the anode and the cathode regions. In general there is not much variation in the potential distributions amongst the different patterns. Therefore in Fig. 7.8 the potential distribution without surface charges and using only P_1 and P_2 are presented for clarity.

7.7 Dependence of the Electric Field on the Applied Voltage and Insulator Material with Hetero Charge Accumulation

The pattern P_1 (Fig. 7.2) is used here for further extensive calculations to investigate the dependence of the field on such parameters as the applied voltage, the magnitude of surface charge and the insulator length. P_1 is chosen as this distribution is thought to be realistic from practical consideration. The portion of the negative charge near the anode is assumed to be about 20% of the total accumulated surface charge. This consideration is reinforced by the fact that the differences among the computed fields at either the cathode or the anode for the different patterns P_1 to P_5

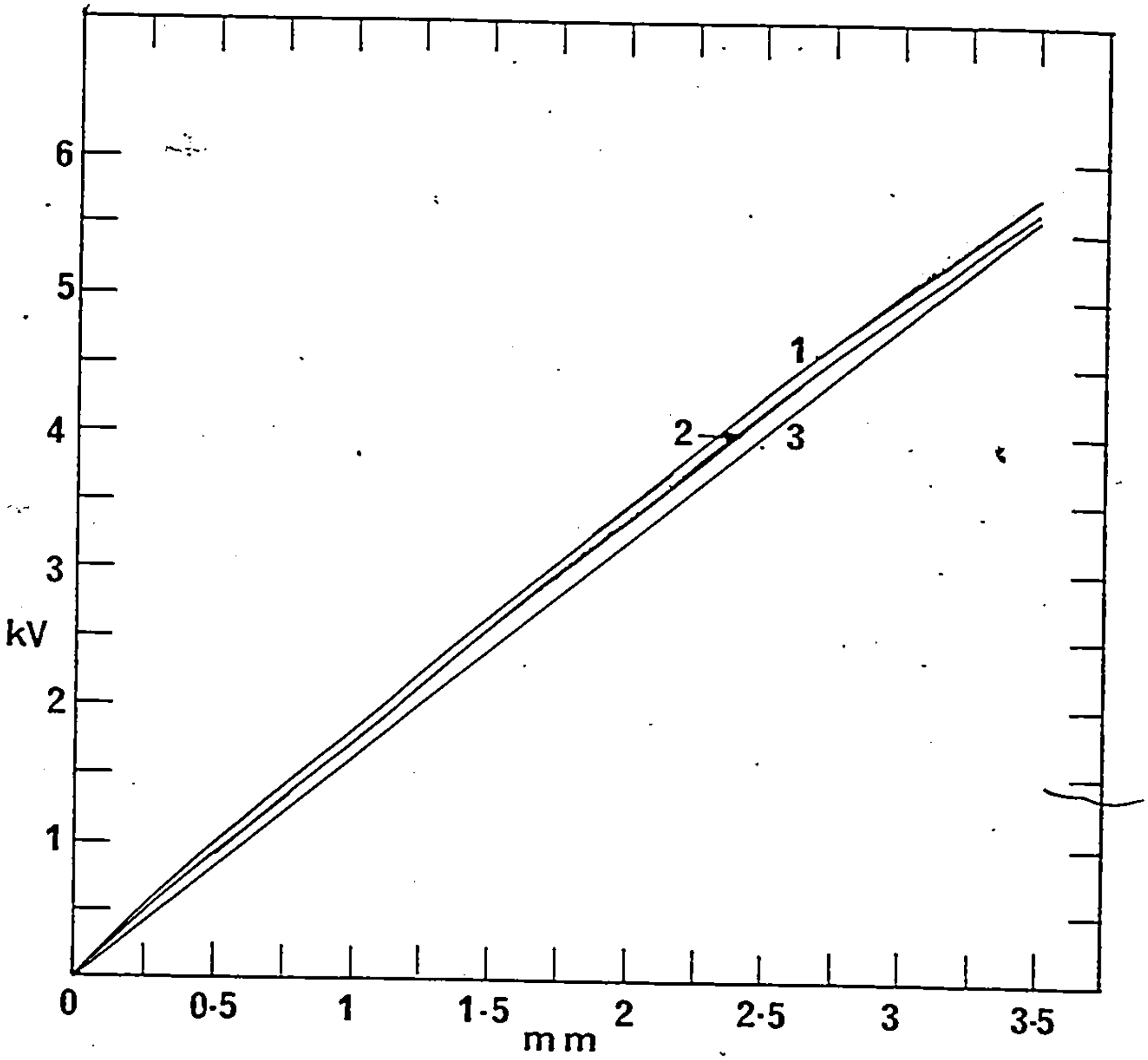

Fig. 7.8 Potential distribution along the surface of the solid insulator on the vacuum side for patterns P_1 to P_2. Curve 1 corresponds to P_1; curve 2, P_2; curve 3, without surface charge. Applied voltage 20 kV; Length of insulator = 12.5 mm; $\varepsilon_2 = 5.8$.

used are only within ± 5% in magnitude. (E'_{t_1} = 1.22 ± 0.06 at the cathode and 1.20 ± 0.05 at the anode, Fig. 7.5).

7.7.1 Dependence of the Electric Field at the Triple Junction on the Applied Field

The electric field at the triple junction of the solid insulator-electrode-vacuum is computed as a function of the DC applied field stress and taking into account the presence of surface charges on the solid insulator. The pattern of distribution assumed is that shown in Fig. 7.2 (P_1). It would be relevant to note that the surface charge measurements are still very scant at the present time despite the increasing importance of its role in the development of discharges in insulating systems. The reported measured surface charges suffers from considerable uncertainty arising among other things from the size of the probe used, capacitive coupling due to proximity objects, electrical interference and the inherent difficulty in the absolute calibration of the measuring system. In view of the marginal differences observed in the fields at the cathode and anode junctions with changing the charge patterns the present section though conducted for a particular pattern (P_1) it is not anticipated that the results will be seriously invalidated should a slightly different charge distribution be encountered by other researchers.

The tangential electric fields at the anode E_{ta_1} and the cathode E_{tc_1} junctions for alumina insulator of 12.7 mm in diameter and 12.7 mm in length is shown in Fig. 7.9 as a function of the applied DC field. The choice of a slightly different length of insulator (12.7 mm) in this case was done so that our calculations can be compared with the measurements reported by Sudarshan et al. [23]. The material is alumina ceramic having $\varepsilon_2 = 8.5$. The applied field is varied in the range 1.5 - 28 kV cm^{-1}. The values of the field at the elctrodes junctions are shown on the vacuum side of the solid dielectric - vacuum boundary. The surface charge density assumed for the different applied field is obtained from Fig. 7.1 curve 8 (Al_2O_3, Ref. 70). It will be observed from Fig. 7.9 that the junction fields are enhanced by the presence of charges on the surface of the solid insulator in general agreement with the reported measurement of the electric fields at both anode and cathode junctions using vibrating probes [23]. The junction field at the anode and the cathode is a linear function of the applied field and is larger than the applied field. The normal field at both the anode (E_{na_1}) and the cathode (E_{nc_1}) junctions is calculated for the same conditions of Fig. 7.9 ($\varepsilon_2 = 8.5$; Pattern P_1; Length of insulator 12.7 mm) and shown in Fig. 7.10. It should be mentioned that the direction of E_{na_1} is inward towards the insulator-anode junction while it is directed outward at the cathode-insulator junction. The values of the normal field E_{na_1} and E_{nc_1} increase linearly with increasing applied voltage as is the case with the tangential field (Fig. 7.9). However, the normal field components near the anode and cathode arising from surface charges are only about 10% of the applied field (Fig. 7.10). In general, the normal field reaches a maximum value in the mid region of the insulator and takes values ranging from 16% to 35% of the applied field (Fig. 7.7) depending on the surface charge distribution patterns. The higher value of tangential junction field is due to the accumulation of positive charge near the cathode and the negative charge near the anode. The additional enhancement obtained is about 20% of the applied field near the anode and 30% near the cathode junction respectively, at an applied field of 10 kV/cm (Fig. 7.9). This enhancement factor remains about the same for higher fields in the range up to 28 kV/cm. The enhancement in the electric field and as stated above contributes to the observed reduction in the withstand voltage of vacuum or gaseous gaps bridged by a solid insulator.

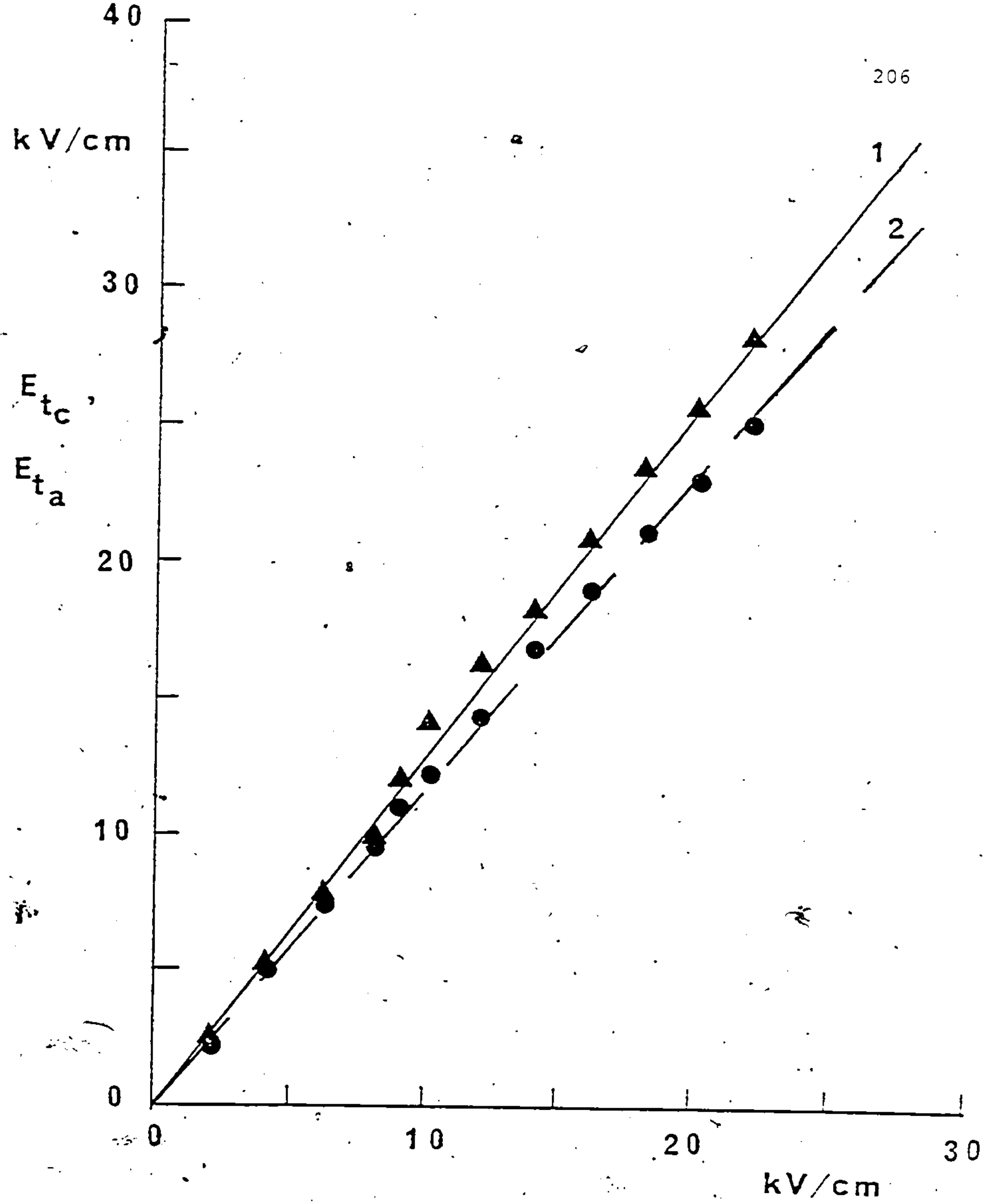

Fig. 7.9 Tangential field at the anode and cathode triple junction (calculated) as a function of applied field in alumina ceramic. Curve 1, field at the cathode; curve 2, field at the anode triple junction (calculated). ▲cathode junction field (measured) [23] ● anode junction field (measured) [23]; Pattern P_1 is used. $\varepsilon_2 = 8.5$; L = 12.7 mm.

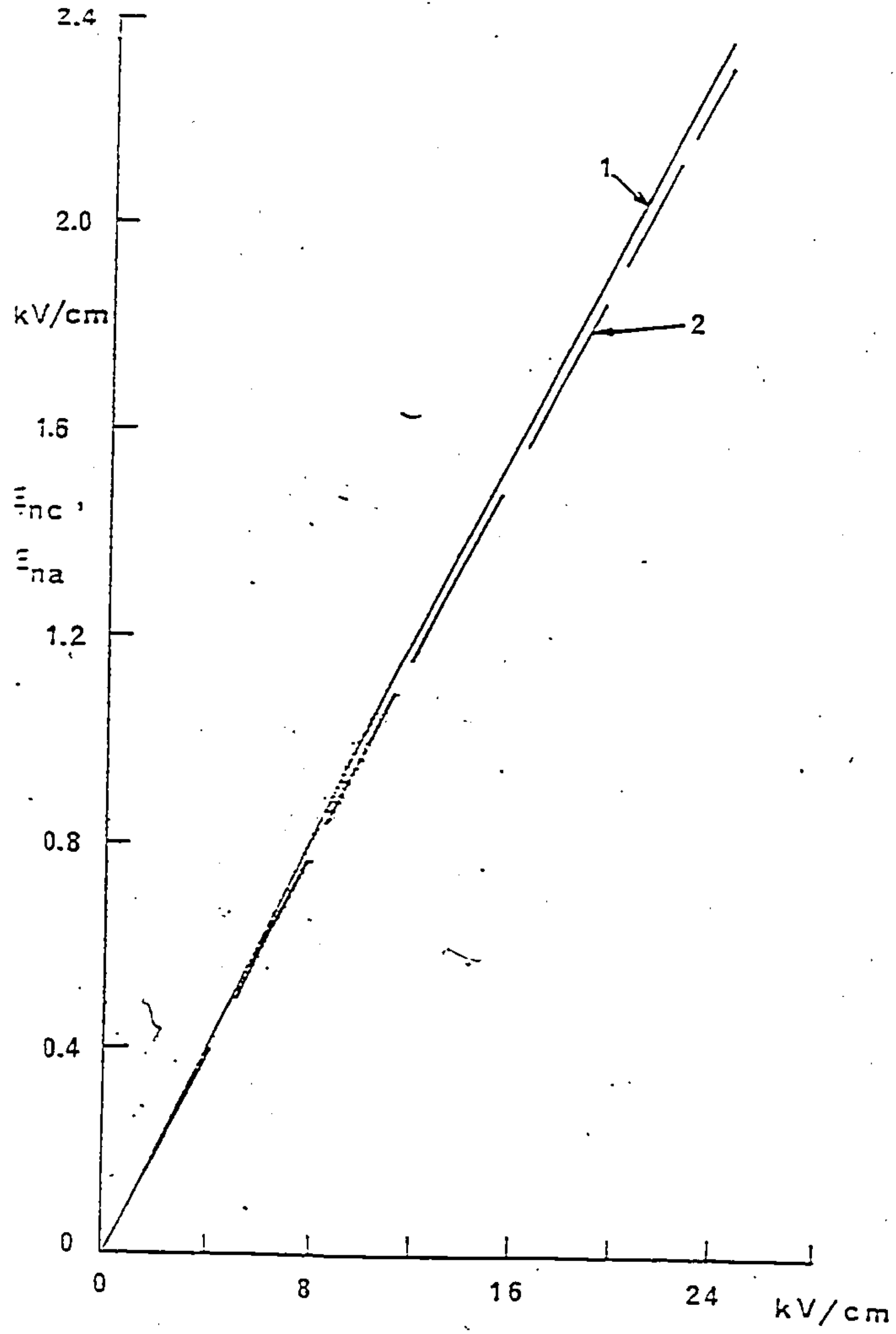

Fig. 7.10. Normal electric field at the anode and cathode triple junctions as a function of applied field in alumina ceramic. Curve 1, E_{nc}, normal field at the cathode curve 2, E_{na} normal field at the anode, $\varepsilon_2 = 8.5$; L = 12.7 mm; Pattern P_1; E_{na} is directed inward the junction; E_{nc} is directed outward the junction.

7.7.2 Dependence of Junction Field on Insulator Material

Measurements of the electric field at the triple junction at both the cathode and the anode indicate that the junction fields are different for different insulator materials of the same dimensions [22]. The values of the normalized tangential and normal fields for different insulating rod materials having the same dimensions ($2R_1$ = 1.25 cm, L = 1.25 cm) at 16 kV/cm applied field is presented in Table 7.1. Information on the impact energy (A_1) is obtained from Refs. 79 and 98 and on the relative dielectric constant (ε_2) from Refs. 34 and 103. Since the value of surface charge density depends on the impact energy of the material for the same applied field as can be seen from Eq. 7.8 the resultant junction field value at the electrodes also largely depends on the impact energy of the insulator. For example, in Quartz the value of the normalized tangential field at the cathode junction E'_{t_c} is 1.342 if the value of A_1 is assumed 30 eV. The value of E'_{t_c} becomes lower at 1.234 for an impact energy A_1 = 50 eV (Table 7.1). It has been found here that the higher the value of the electron impact energy, the lower the value of σ_s which lowers the enhancement of the field at the triple junction.

It will be observed from Table 7.1 that the normalized tangential and normal fields at both the anode and the

TABLE 7.1

Normalized tangential (E'_{t_1}) and normal (E'_{n_1}) field intensities near the anode (E'_{ta_1} and E'_{na_1}) and cathode (E'_{tc_1} and E'_{nc_1}) junctions, respectively for charge distribution P_1 and different solid insulator materials. Applied field E_{aV} = 16 kV/cm. σ_s obtained from Equation (7.8). L = 12.5 mm; $2R_1$ = 12.5 mm; $2R_2$ = 40 mm. A_o is assumed 5 eV.

Material	Dielectric Constant 34,103 ϵ_2	Impact Energy 79,98 A_1	Surface Charge Density σ_s in C cm^{-2}	E'_{ta_1} at Anode Junction On Vacuum Side	E'_{tc_1} at Cathode Junction On Vacuum Side	E'_{na_1} at anode Junction On Vacuum Side b	E'_{nc_1} at Cathode Junction On Vacuum Side c
Teflon	2.1	--	1.0×10^{-9} a	1.228	1.265	0.125	0.126
Plexiglass	3.4	30 eV	1.80×10^{-9}	1.227	1.371	0.160	0.163
Nylon	3.5	--	0.90×10^{-9} a	1.154	1.180	0.078	0.082
Quartz	3.8	30 eV	1.80×10^{-9}	1.208	1.342	0.147	0.150
		50 eV	1.33×10^{-9}	1.172	1.234	0.109	0.111
Pyrex glass	5.0	40 eV	1.52×10^{-9}	1.151	1.242	0.101	0.103
NaCl	5.6	20 eV	2.28×10^{-9}	1.178	1.349	0.138	0.141
Glass ceramic	5.8	20 eV	2.28×10^{-9}	1.171	1.342	0.134	0.137
		25 eV	2.00×10^{-9}	1.097	1.302	0.117	0.120
Mica	6.0	30 eV	1.80×10^{-9}	1.141	1.246	0.102	0.105
Alumina ceramic	8.5	20 eV	2.28×10^{-9}	1.140	1.262	0.101	0.104
Strontium oxide (SrO)	13.0	40 eV	1.52×10^{-9}	1.065	1.107	0.044	0.045
		60 eV	1.208×10^{-9}	1.057	1.082	0.035	0.036

[a] Measured Refs. 69 and 70; [b] E'_{na_1} is directed into the junction; [c] E'_{nc_1} is directed outward of the junction.

cathode junctions decrease slightly with increasing ε_2 of the solid insulator material for the same surface charge density. This might appear to be in conflict with the experimental observations which show that in most cases the withstand voltage decreases with increasing ε_2. However, very large enhancements in the field with increasing ε_2 have been found due to the unavoidable small geometrical curvature (edge effect) at the triple junctions [19]. The combined effects of the insulator geometry and that of the surface charges are discussed in Section 7.13.

In general, the surface charge density increases proportionately with increasing applied voltage. The junction field is therefore also enhanced if the applied field is increased. Since the relationship between the applied field and the charge density is linear, the normalized tangential field at the cathode junction are the same for different applied fields. Same applies to the normalized tangential fields at the anode. For a 12.5 mm length glass-ceramic insulator, the tangential field enhancements at the cathode E'_{t_c} and the anode E'_{t_a} are 1.30 and 1.09 respectively at an applied field of 40 kV/cm ($\sigma_s = 5 \times 10^{-9}$ cm^{-2}). The fields at the cathode and the anode triple junctions are 52 kV/cm and 43.6 kV/cm, respectively. When the applied field is 80 kV/cm the surface charge density becomes 10×10^{-9} C cm^{-2} for an assumed linear dependence of σ_s on the applied field (Eq. 7.8). The values of E'_{t_c} and E'_{t_a} are 1.30 and 1.09 respectivelv. The latter values of enhancements at an applied field of 80 kV/cm are identical as those obtained for an applied field of 40 kV/cm. To illustrate the influence of the surface charges, when the applied field = 80 kV/cm the cathode and the anode junction fields become 104 kV/cm and 87.2 kV/cm respectivelv for the same enhancement of 1.30 and 1.09. When the applied voltage is increased to that close to the flashover voltage of the insulator, the enhancement near the cathode junction is considerablv more because of the increased accumulation of surface charge with increasing pre-breakdown current conduction. This is expected to aid the flashover process causing it to occur at lower voltage when compared to an unbridged vacuum or gaseous gaps.

7.8 Effect of Hetero-Charge Accumulation on the Axial, Tangential and Normal Field Distribution

The electric field arising from a hetero-charge surface distribution as shown in Fig. 7.11,a is calculated at the solid insulator-vacuum interface, inside the solid insulator and in the vacuum (Fig. 7.11;b). The portion of the negative charge near the anode is assumed to be 20% of the total accumulated charge. A surface charge densitv having a maximum value of 5×10^{-9} C cm^{-2} near the cathode

(Fig. 7.11,a) is calculated from Eq. 7.8 at an applied field of 40 kV cm^{-1} in vacuum using an electron impact energy of 25 eV. This field value is just below the breakdown field.

The normalized tangential field E'_{t_1} is shown along the surface of the solid insulator on the vacuum side (region 1) of the solid insulator-vacuum interface in Fig. 7.11 (curve 1). The field is enhanced at the cathode and anode triple junctions by 32% and 9%, respectively. The enhanced field at the cathode, due to surface charges, contributes to the increased electron Fowler-Nordheim emission. Therefore, the higher electron current flowing in the gap leads ultimately to an instability occurring at a lower applied voltage than would be the case if the charges were absent from the solid insulator surface.

Inside the solid insulator the normalized field in the axial direction E'_{z_2} (region 2) at locations 4.6 mm (Fig. 7.11, curve 2) and 0.1 mm (Fig. 7.11, curve 3) away from the axis is shown along the gap length. It will be observed that the field at the cathode and anode triple junctions decreases with increasing distance from the surface of the solid insulator towards the central axis. Typically at the cathode junction E'_{z_2} = 1.16 and 1.10 at locations 4.6 mm and 0.1 mm, respectively distant away from the central axis. At the anode, the corresponding values are 0.941 and 0.920, respectively. The field

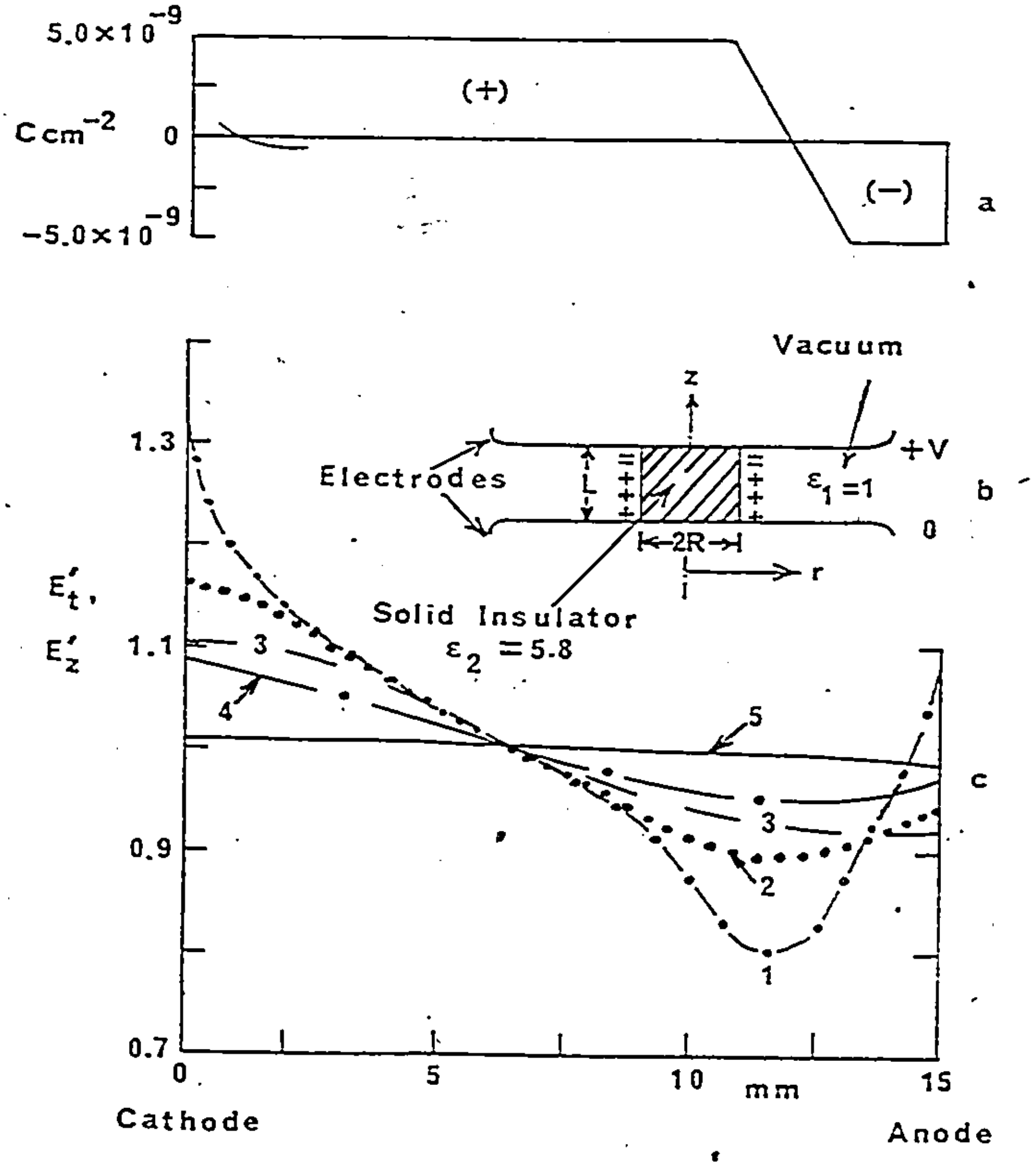

Fig. 7.11. (a) Surface charge distribution along the surface of the solid insulator; (b) Schematic arrangement of the solid insulator, electrodes, vacuum and surface charges. (c) Normalized tangential or axial electric field as a function of gap distance. Curve 1, E'_{t_1} along the solid dielectric-vacuum interface; curve 2, E'_{z_2} at the interior of the solid insulator in location r = 4.6 mm; curve 3 E'_{z_2} at the interior of the solid insulator at r = 0.1 mm; curve 4, E'_{z_1} in vacuum at r = 10.0 mm; curve 5 E'_{z_1} in vacuum at r = 15.0 mm; L = 15.0 mm; 2R = 13.5 mm; ε_2 = 5.8 (glass-ceramic).

enhancement inside the solid insulator is important when investigating volume breakdown of solid dielectrics.

In the vacuum (region 1) the normalized axial field is shown along the gap length at distances 10 mm (Fig. 7.11, curve 4) and 15 mm (Fig. 7.11, curve 5) distant away from the central axis. At the cathode $E'_{z_1} = 1.089$ and 1.013 at locations 10 mm and 15 mm, respectively. At the anode the corresponding values are 0.972 and 0.985, respectively. The effect of surface charges vanishes at large distances from the solid insulator surface (Fig. 7.11, curve 5). The value of E'_r is rather small both in the vacuum side and inside the solid insulator and is omitted here. However, the normal field E'_n on the solid dielectric and vacuum boundary is of considerable value.

7.9 Influence of Solid Insulator Length on Electric Field Distribution with Hetero Charge Accumulation

Figures 7.12 and 7.13 show the normalized tangential (E'_{t_1}) and normal (E'_{n_1}) fields, respectively at the solid insulator-vacuum interface for different lengths of the glass-ceramic insulator rod. The length is varied in the range 2-30 mm, and the applied field is kept constant at 40 kV/cm. The distribution of the charge along the length of the solid insulator is kept proportionately similar to that depicted in Fig. 7.11,a. It will be observed that both E'_{t_1} and E'_{n_1} increase with increasing length at both

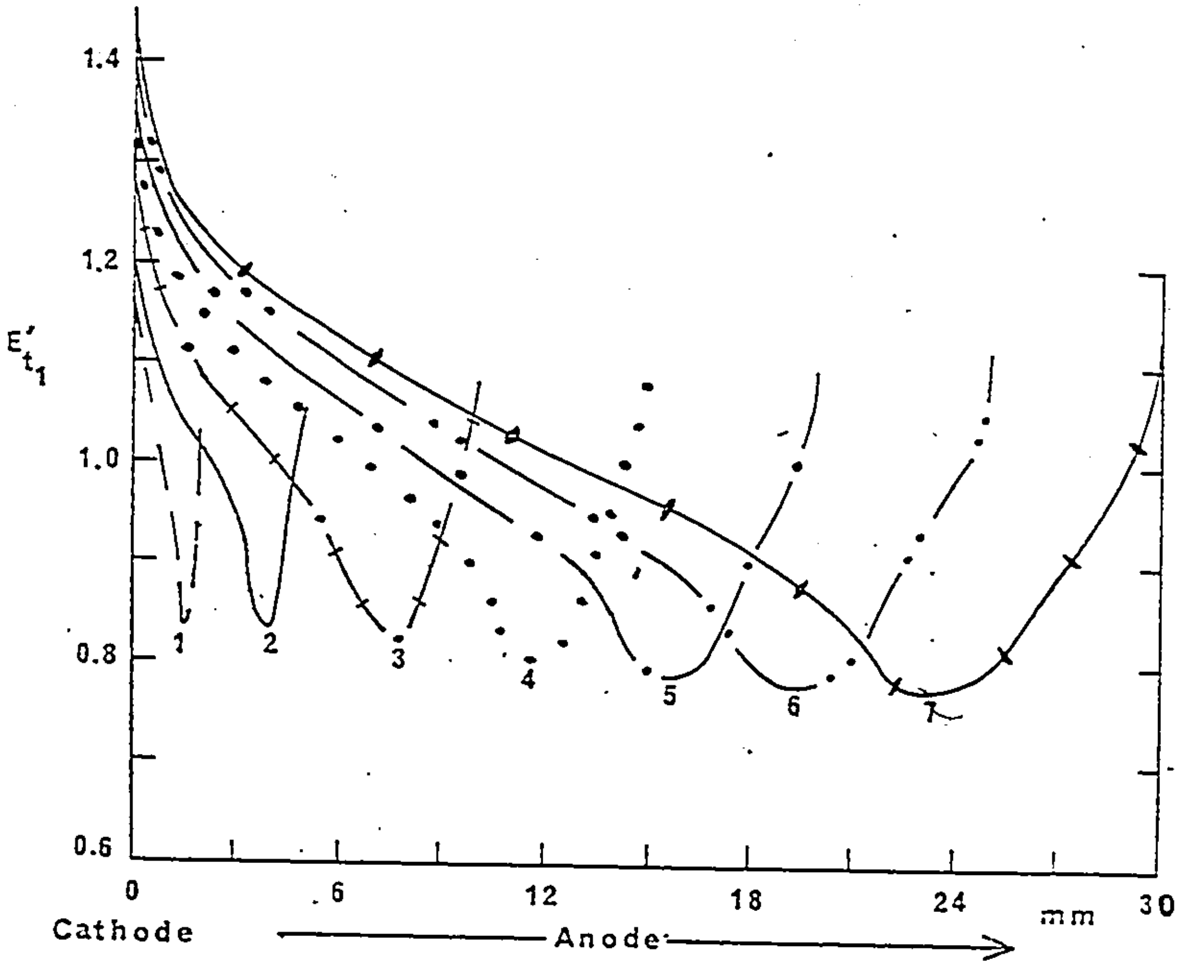

Fig. 7.12. Normalized tangential electric field E'_{t_1} along the solid dielectric-vacuum interface as a function of insulator length L in a glass-ceramic. Normalized field is shown on the vacuum side of the interface. Curve 1, corresponds to insulator length L = 2 mm; curve 2, 5 mm; curve 3, 10 mm; curve 4, 15 mm; curve 5, 20 mm; curve 6, 25 mm; curve 7, 30 mm.

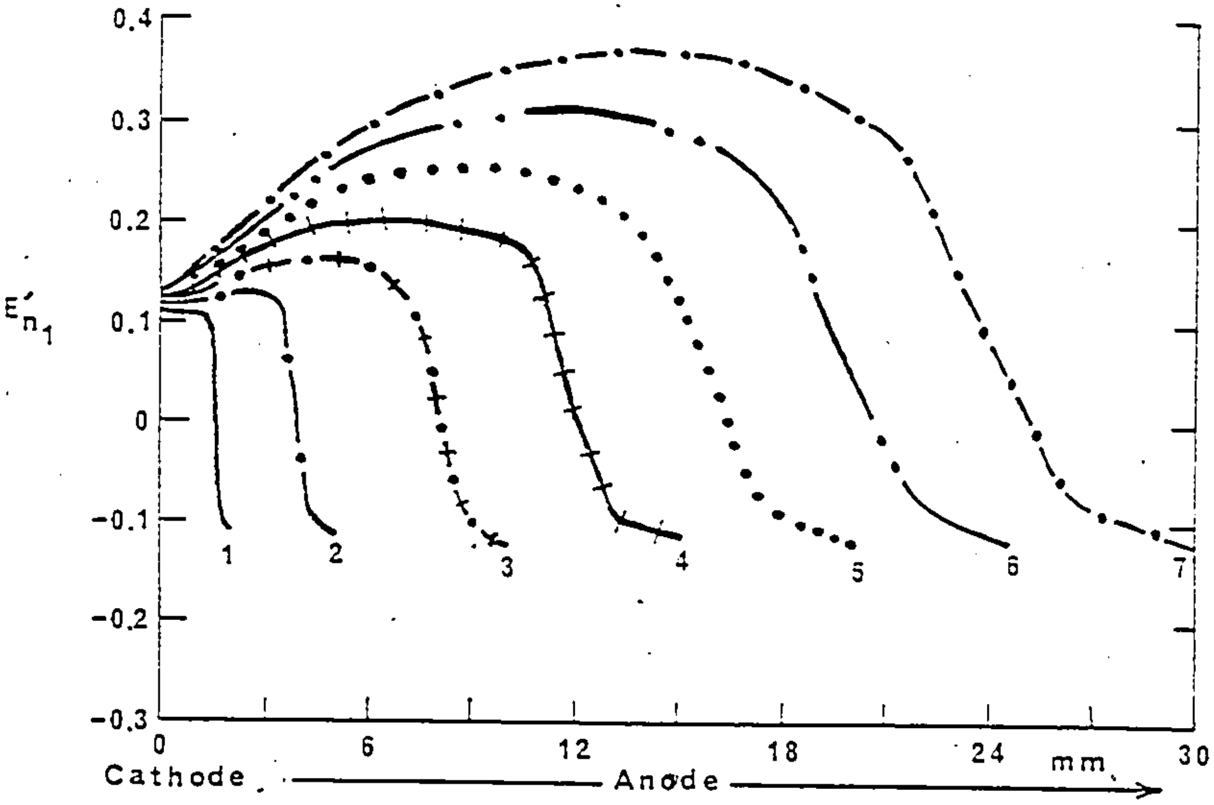

Fig. 7.13 Normalized normal field E'_{n_1} along the solid insulator-vacuum interface as a function of insulator length L in a glass-ceramic. Normalized field is shown on the vacuum side of the interface. Conditions and curves numbers are as shown for Fig. 7.12.

the cathode and the anode triple junctions. The maximum value of E'_{n_1} occurs near the mid gap and it increases with increasing length (Fig. 7.13). In Figs. 7.12 and 7.13 the cathode is fixed and the anode position is at the extreme right hand side of each curve from 1 to 7. The enhancements in the field at various locations are summarized in Table 7.2. The field enhancements at both electrode junctions is found to increase with insulation length leading to the non-linear dependence of the withstand voltage on insulator length.

7.10 Computation of Electric Field with Assumed Homocharge Distribution

Some of the reported surface charge measurements in vacuum and high pressure gases show that the insulator surface may be charged negatively near the cathode and positively near the anode. B. Cross [100] has reported that the permanent "homo" charge on electrets arose from a transfer of charge from electrode to dielectric surface often by discharges. The charge accumulation on the solid insulators used in DC compressed-gas-insulated equipment has been reported [101,102] by Cooke et al. Kerr electro-optic measurement by Lee et al. [41] indicated that when AC stress is applied to a glass insulator the surface is charged in both vacuum and in a high gaseous pressure.

Table 7.2

Normalized tangential (E'_{t_1}) and normal (E'_{n_1}) field intensities near the anode (E'_{ta_1} and E'_{na_1}), and the cathode (E'_{tc_1} and E'_{nc_1}) junctions and maximum normalized normal field intensity (E'_{n_1} maximum) at the solid insulator-vacuum interface as a function of insulator length. Normalized field is the ratio of local to average field. Region 1 indicates that the field value is given on the vacuum side of the interface. Average applied field E_{av} = 40 kV/cm. $\sigma_s = 5.0 \times 10^{-9}$ C cm^{-2}; $\epsilon_2 = 5.8$

Insulator Length (mm)	E'_{ta_1} at anode junction (on vacuum side)	E'_{tc_1} at cathode junction (on vacuum side)	E'_{na_1} at anode junction (on vacuum side)*	E'_{nc_1} at cathode junction (on vacuum side)**	E'_{n_1} maximum (on vacuum side)
2	1.034	1.160	0.109	0.115	0.116
5	1.057	1.216	0.116	0.118	0.127
10	1.082	1.273	0.117	0.120	0.160
15	1.093	1.321	0.118	0.121	0.202
20	1.099	1.363	0.119	0.122	0.253
25	1.117	1.396	0.120	0.123	0.307
30	1.136	1.414	0.121	0.124	0.366

* E'_{na_1} is directed into junction surface near the anode junction

** E'_{nc_1} is directed outward of the surface near the cathode junction

The interferogram analysis implied that the insulators were charged negatively near the cathode and positively near the anode with a transition occurring midway between the two electrodes. The measurement by Knecht [72] using a field-mill system of the accumulated charge on an epoxy resin spacer stressed with a DC voltage at a high pressure SF_6 gas showed that the polarity and distribution of the surface charge depends on the electric field configuration.

A homocharge distribution (Fig. 7.14,a) having positive surface charge (80% of the total charge) near the anode and 20% negative charge near the cathode is employed to compute the electric field. The electric field distribution at various locations within the insulating gap (Fig. 7.14,b) for quartz (ε_2 = 3.8) and pyrex glass (ε_2 = 5.0) having a fixed diameter 2R = 13.5 mm and varying lengths in the range L = 10 - 20 mm is computed. An enhancement in the field is observed at the surface of the insulator at locations away from the electrodes and a reduction near both electrode junctions.

7.11 Homocharge Accumulation Effect on the Axial, Tangential and Normal Field Distribution

The tangential electric field (E_t) and the normal electric field (E_n) on the surface of the solid insulator and at other locations are computed. The peak values of the surface charge density is calculated to be $\sigma_s = 4.5 \times 10^{-9}$ C cm^{-2} at an applied DC field of 40 kV cm^{-1} for the vacuum case for a Quartz insulator with an electron impact energy of $A_1 = 30$ eV [79]. For Pyrex glass $A_1 = 40$ eV [79] and the corresponding value is $\sigma_s = 3.8 \times 10^{-9}$ C cm^{-2} at the same applied field. An electron emission energy of $A_0 = 5$ eV is assumed for both materials. The electron energies are expected to be much lower in compressed gases. The mechanism of insulator surface charging may also be different in gas insulated systems. However, the assumption of a similar order of magnitude of charge density on the solid insulator in both vacuum and in high gaseous pressures appears to be reasonable on the basis of experimental observations [41,72].

The normalized tangential (or axial) field E'_{t_1} along the surface of a quartz solid insulator on the vacuum side (region 1) is shown in Fig. 7.14 c (curve 1). It will be observed that the maximum field occurs at a position away from the cathode where it is enhanced by up to 23.8 % over the average field. The increase in the field contributes to the observed reduction in the withstand voltage of the gap when bridged by a solid insulator. The breakdown field is expected to be higher if no charges on the surface of

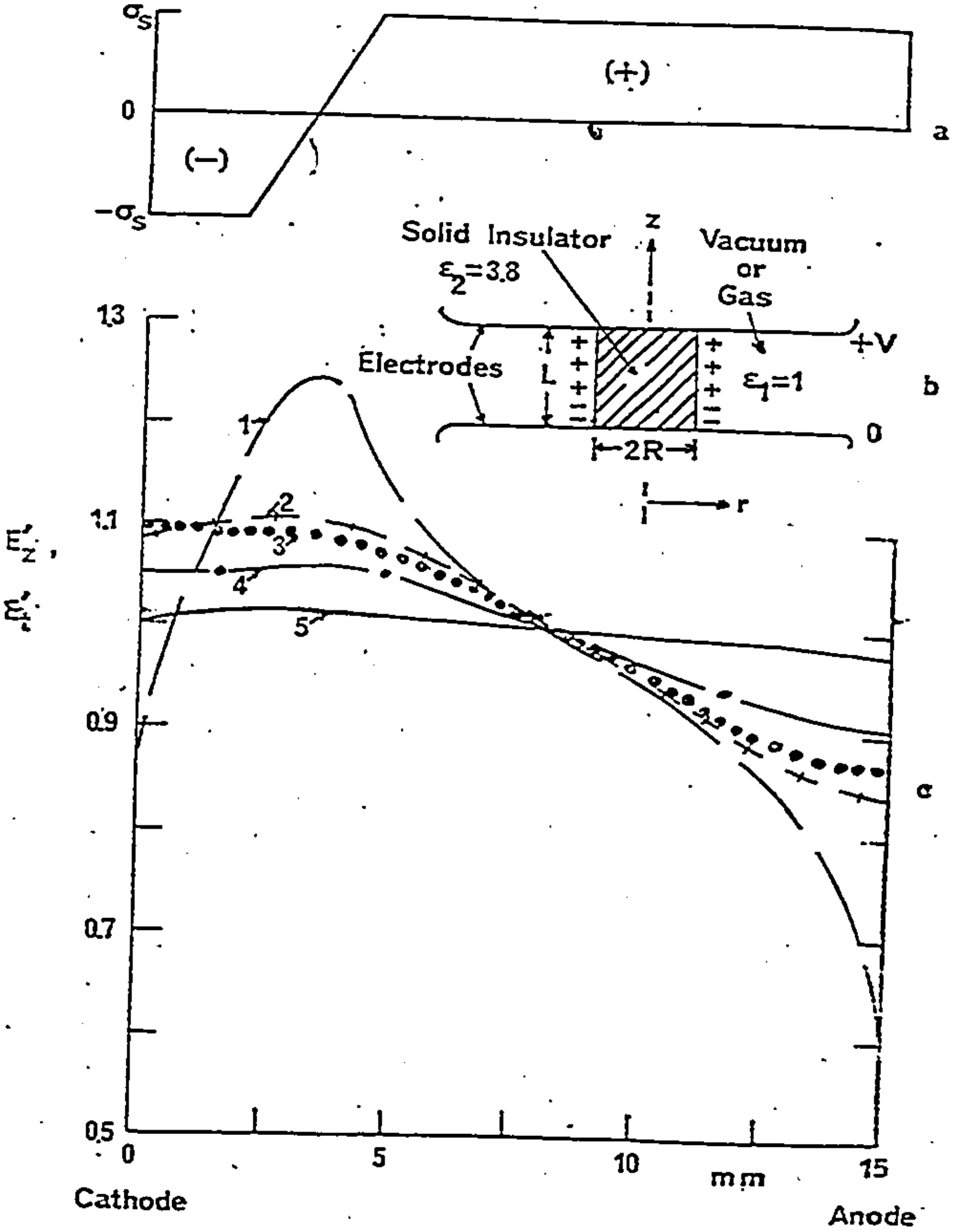

Fig. 7.14. (a) Surface charge distribution along the surface of the solid insulator; (b) schematic arrangement of the solid insulator, electrodes, gas (or vacuum) and surface charges; (c) normalized tangential or axial electric field as a function of gap distance. Curve 1: E'_{t_1} along the solid dielectric - gas interface; curve 2: E'_{z_2} at the interior of the solid insulator in location $r = 3.5$ mm; curve 3: E'_{z_2} at the interior of the solid insulator at $r = 0.5$ mm; curve 4: E'_{z_1} in gas at $r = 10$ mm; curve 5: E'_{z_1} in gas at $r = 15$ mm; $L = 15.0$ mm; $2R = 13.5$ mm; $\varepsilon_2 = 3.8$ (Quartz); $\sigma_s = 4.5\times10^{-9}$ C cm^{-2}; $E_{av} \doteq 40$ kV cm^{-1}; $A_1 = 30$ eV.

the solid insulator. The higher electric field at locations away from the electrodes may lead to the discharge starting at that location. Pfeiffer [104] has recently shown experimentally that the discharge started approximately at the mid-gap of a solid insulator in 2 bar of SF_6.

At the anode junction E'_{t_1} values are reduced to 0.61 and at the cathode to 0.87. This field distribution arises from the presence of charges near the electrodes of the same polarities as those of the electrodes. It is unlike the enhanced field found at the interface in the vicinity of both electrodes when the charges have opposite polarities to those of the adjacent electrodes (Section 7.9).

Inside the solid insulator (region 2) the normalized field in the axial direction E'_{z_2} at locations 3.5 mm (Fig. 7.14,c, curve 2) and 0.5 mm (Fig. 7.14,c, curve 3) away from the central axis is shown along the length of the solid insulator. The tangential field at the cathode end decreases and at the anode increases as the distance increases from the surface of the solid insulator towards the central axis.

In the vacuum (region 1) the effect on E'_{z_1} diminishes with increasing distance from the axis. E'_{z_1} is calculated at distances of 10 mm (Fig. 7.14,c, curve 4) and 15 mm (Fig. 7.14,c, curve 5) away from the central axis and as a function of distance from cathode to anode. For distances sufficiently long from the solid insulator surfaces ($>2R_1$) the field becomes almost uniform (within $<5\%$).

7.12 Dependence of the Field on Solid Insulator Material and Length with Homocharge Accumulation

Figure 7.15 shows the dependence of E'_{t_1} at the solid insulator-vacuum interface on distance from the cathode for Quartz (curves 1 and 2) and for Pyrex glass (curves 3 and 4). Two insulator lengths L = 10 mm (curves 2 and 4) and L = 20 mm (curves 1 and 3) are used. The surface charge distribution along the insulator surface is maintained proportionally similar to that depicted in Fig. 7.14 a, for both lengths. It will be observed that the maxima in E'_{t_1} occurs near the cathode and it is higher for Quartz than for Pyrex glass. Further, the maximum value of E'_{t_1} increases with increasing L (Fig. 7.15) which is consistent with the experimental observation that the dielectric strength decreases with increasing insulator length [30].

Calculations are made for the case of a homocharge distribution having an amplitude as that of Fig. 7.14,a but a change in the charge polarity occurring in the mid gap. E'_{t_1} at the cathode is found to be lower compared to the values shown in Fig. 7.15 for the charge distribution depicted in Fig. 7.14,a. The maxima in E'_{t_1} now occurs near

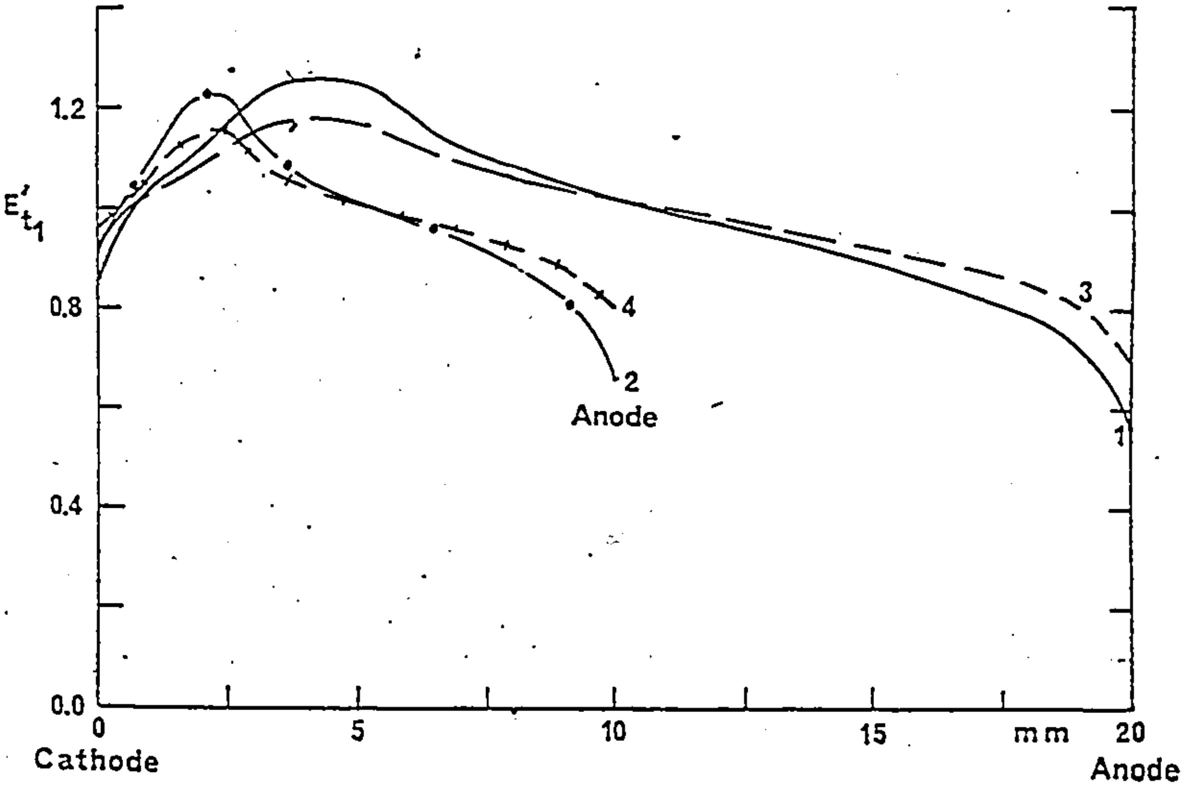

Fig. 7.15. Dependence of the normalized tangential electrical field E'_{t_1} at the solid dielectric-gas interface on the length (L) and the material (ε_2) of the solid insulator. Curve 1: $\varepsilon_2 = 3.8$ (Quartz), L = 20 mm; curve 2: $\varepsilon_2 = 3.8$, L = 10 mm; curve 3: $\varepsilon_2 = 5.0$ (Pyrex glass), L = 20 mm; curve 4: $\varepsilon_2 = 5.0$, L = 10 mm; $2R_1$ = 13.5 mm; A_1 (Quartz) = 30 eV; A_1 (Pyrex glass) = 40 eV; Applied field 40 kV cm^{-1}; σ_s (Quartz) = 4.5×10^{-9} C cm^{-2}; σ_s (Pyrex) = 3.8×10^{-9} C cm^{-2}.

the mid region. For a quartz insulator having a length of 20 mm the values of $E'_{t_{1m}}$, $E'_{t_{1a}}$ and $E'_{t_{1c}}$ are 1.23, 0.60 and 0.56 respectively. For Pyrex glass (L = 20 mm), the corresponding values for the same charge distributions are 1.16, 0.73 and 0.70 respectively. When these values are compared to Fig. 7.15 the effect of changing the charge distribution is seen to influence primarily the cathode junction but there is not much change in the maximum value.

The normalized normal field E'_{n_1} at the interface is shown in Fig. 7.16 for Quartz (curves 1 and 2) and Pyrex glass (curves 3 and 4) using two insulator lengths L = 10 mm (curves 2 and 4) and L = 20 mm (curves 1 and 3). The maxima in the curves of E'_{n_1} occur in mid-gap between the two electrodes. E'_{n_1} has a negative value near the cathode indicating that the field is directed towards the solid insulator. This is due to the presence of negative charges in the vicinity of the cathode and has influence on the deposition of micro particles which may be present near the solid insulator surface. The assumed charge distribution may have a practical significance for spacers used in high pressure electro-negative gases.

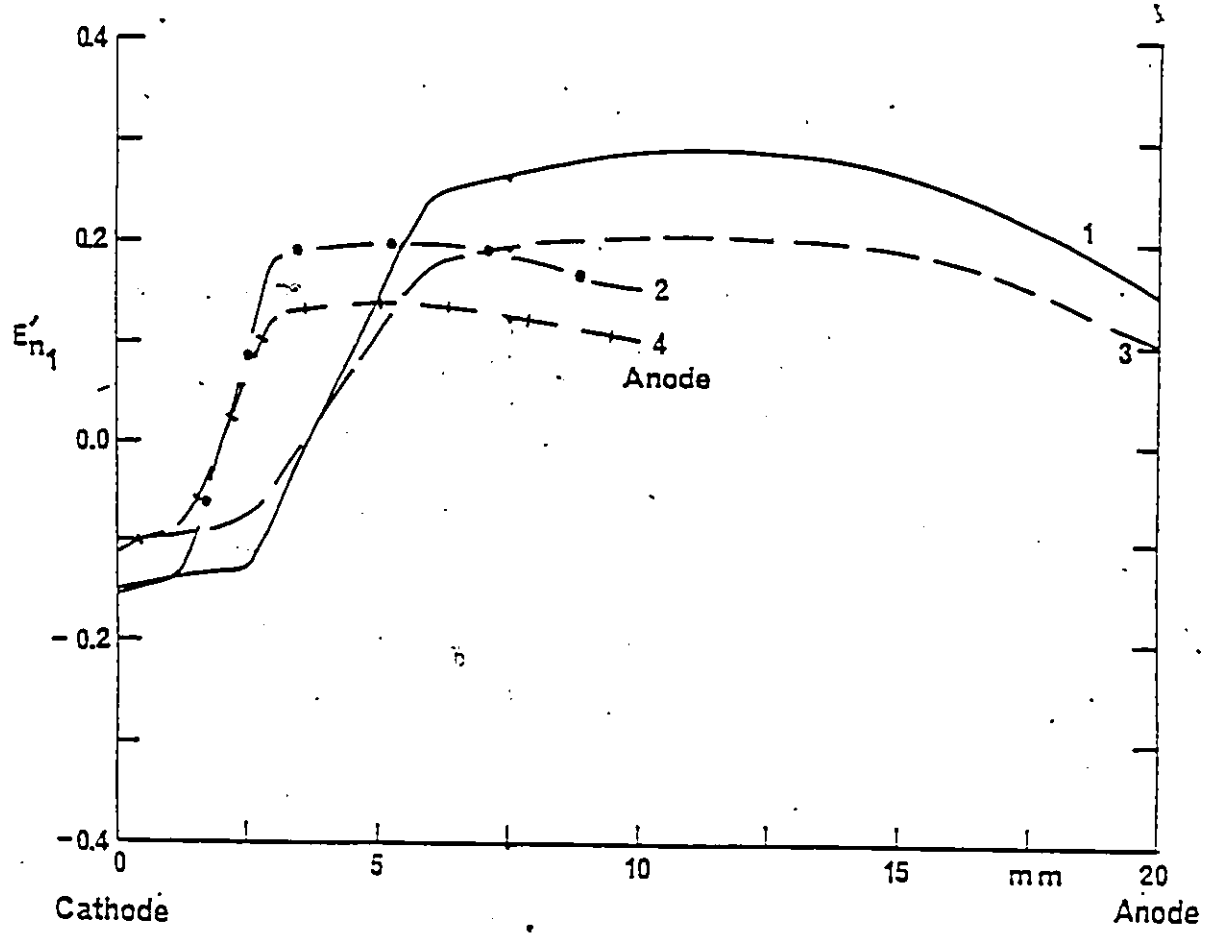

Fig. 7.16. Dependence of the normalized normal field E'_{n_1} at the solid dielectric-gas interface on the length and material of the solid insulator. Conditions and curve notations as for Fig. 7.15.

7.13 Combined Effect of Insulator Geometry and Surface Charge on Junction Field

The electric field distribution on the surface of the insulator is calculated by assuming a hetero surface charge distribution as shown in Fig. 7.17,a. This surface charge distribution is having 80% of the total charge positive and the remainder negative. This choice of surface charge distribution has not yet been confirmed experimentally but is consistent with the ratio of the hetro charge distribution reported using Monte Carlo simulation [23].

The toal junction field enhancement by taking into account the effect of the insulator geometry and the surface charge accumulation is calculated for Teflon, Quartz and Macor glass-ceramic. The obtained enhancement in the field is sufficiently close to the value considered necessary to initiate a breakdown in an equivalent planar vacuum gap.

7.13.1 Computation of Triple Junction Field

A maximum surface charge density of 14.5×10^{-5} C m^{-2} is calculated from Eq. 7.8 for Teflon when 40 kV is applied across a spacer length of 4 mm. This level of applied voltage is just below the conditioned DC flashover voltage of 43 kV (Chapter 3, Table 3.1). The electron impact energy from the surface of Teflon, which is required for calculation of the surface charge density, is not known but a value of 20 eV which corresponds to that of alumina-ceramic [79] may be reasonably assumed for Teflon. The latter assumption is justified by the reported measurements of the surface charge densities which are found to be very close to each other in both materials [69]. The value for the electron emission energy is low and assumed to be 5 eV [7].

It will be observed that the tangential field of the solid insulator (Fig. 7.17,b) is enhanced by 56% and 15%, respectively at the cathode and anode triple junctions. The enhancement in the field at the cathode of ξ_1 = 56% due to surface charges combined with that due to the unavoidable slight rounding of the solid insulator edges at the contact with the cathode of about ξ_2 = 10 to 20% (depending on the radius of curvature of the edge) [19] leads to an enhancement in the local field at the cathode by a factor of ξ = 66% to 76%. The large field intensification at the cathode results in an increased electron emission which ultimately leads to the observed reduction in the dielectric strength of vacuum gap when bridged by a solid insulator.

7.13.2 Comparison of the Cathode Surface Field in Vacuum with the Calculated Triple Junction Field

The following is an attempt to correlate the macroscopic breakdown field at the cathode surface in vacuum and the flashover field at the cathode triple junction for the same

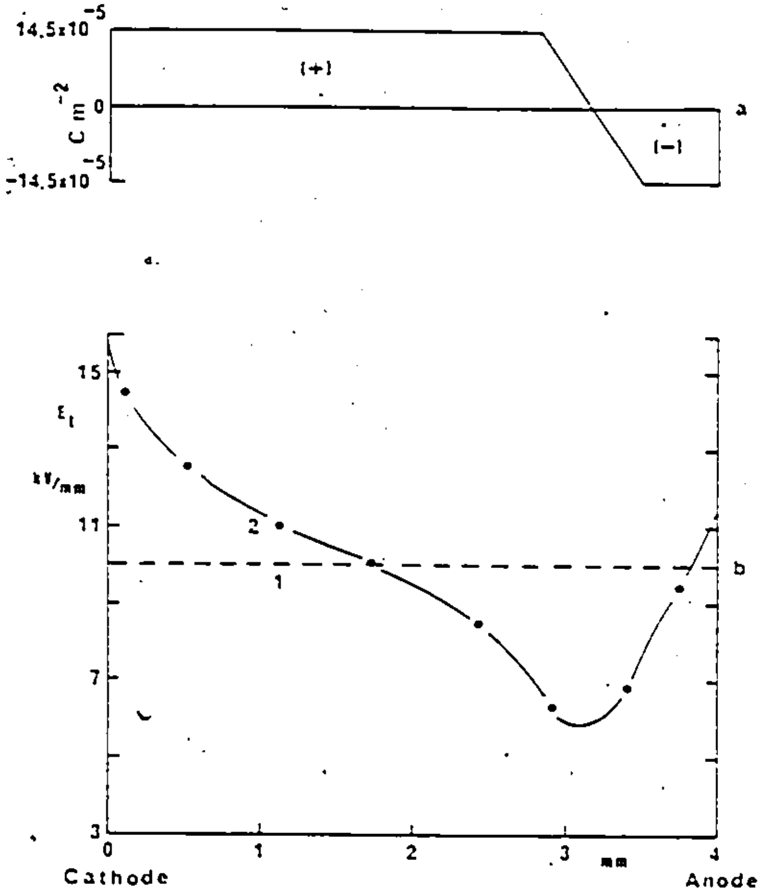

Fig. 7.17. (a) Assumed surface charge distribution along the surface of Teflon insulator. (+) indicates positive charge polarity; (-) negative charge polarity. (b) Tangential field along the length of the insulator. Applied voltage 40 kV.

gap length. A critical value of the electric field at the cathode junction leads to a sufficient electron emission which ultimately leads to gas desorption and vapour formation in which the arc is developed in the two cases of a pure vacuum gap and when the same gap is bridged by a solid insulator. Typical calculations are given for Teflon below and for the other materials summarized in Table 7.3. The breakdown voltage of a 4 mm gap in vacuum between stainless steel electrodes of the same type and surface finish (polished to a finish of 1 μm) to those used here but of slightly larger diameter was measured as 78.4 kV, giving an average field at the cathode of 19.6 kV/mm [38]. For the same vacuum gap bridged by a Teflon disc and considering the intensification in the field at the cathode triple junction due to surface charges of ($\xi_1 = 56\%$. Fig. 7.17,b) and due to slight curvature at the edge of the insulator at the contact with cathode of $\xi_2 = 10$ to 20% [19] the field at the cathode triple junction becomes,

$$E_c = E_{av} \cdot \xi \tag{7.9}$$

for $\xi_1 = 56\%$ and $\xi_2 = 10\%$

$$E_c = E_{av}\ \xi = \frac{43.5\ \text{kV}}{4\ \text{mm}} \times 1.66 = 18.1\ \text{kV/mm}$$

and for $\xi_1 = 56\%$ and $\xi_2 = 20\%$

$$E_c = 19.1\ \text{kV/mm}$$

where E_c is the macroscopic field at the cathode triple junction, E_{av} the average field equals to V/L and ξ the total macroscopic enhancement factor = $\xi_1 + \xi_2$. V = 43.5 kV is the flashover voltage (Chapter 3, Table 3.1) and L = 4 mm the length of the Teflon insulator disc. The calculated value of the field of between 18.1 to 19.1 kV/mm at the cathode triple junction compares well with the previously reported measurements of vacuum breakdown in stainless steel electrodes of 19.6 kV/mm in the same gap distance of 4 mm [38]. The calculations for all materials are shown in Table 7.3. A maximum surface charge density of 16×10^{-9} C/cm^2 is calculated for 3.5 mm quartz silica at the flashover voltage by assuming 30 eV [79] for the electron impact energy. For the glass ceramic, the electron impact energy is assumed to be 25 eV and the maximum value of surface charge density used is 27.5×10^{-9} C/cm^2. It will be observed that reasonable agreement is obtained between the macroscopic field at the cathode triple junction and the vacuum cathode surface for all materials (Table 7.3) when the enhancements due to surface charges and geometrical effects are taken into account. It is significant that the differences long reported between the vacuum breakdown voltage and the flashover voltage of solid insulator in vacuum can be quantitatively explained using the charge density equation originally reported by Boersch et al [7].

Table 7.3

Electrical field E_c at the cathode surface in vacuum [38] and at the cathode triple junction for different materials. ξ_1 enhancement at the cathode due to surface charges, ξ_2 enhancement at the cathode due to rounded edge [19]

Material	Gap (mm)	ξ_1 %	ξ_2 %	E_{av} (Table 3.1) kV/mm	E_c (Vacuum) [38] kV/mm	E_c (Triple Junction) Eq. (7.9) kV/mm
Teflon	4	56	10-20	10.9	19.6	18.1-19.1
Quartz	3.5	31	10-20	15.1	20.6	21.8-23.8
Glass-ceramic	1	12.2	10.20	22.5	38	27.8-30.3

However, many questions still remain to be illucidated including the magnitudes and the distribution of surface charges, charging mechanisms, times and decays under various applied voltages (Pulsed, DC and AC).

CHAPTER VIII

DESIGN OF OPTIMAL ELECTRODE - SOLID INSULATOR GEOMETRY

8.1 Introduction

Various methods of increasing the withstand voltage of solid insulators in vacuum and compressed gases, have been discussed here with specific emphasis on the elctrode junction. It has been shown that the electric field at the metal-solid dielectric junction can be reduced by suitable design of the junction [5,16,105] and thus a higher withstand voltage could be realized, Shaping the solid insulator say by zig-zagging [8] to increase the surface length was also attempted with substantial improvement in the dielectric strength particularly with a concave curvature [57]. The field computations obtained in the case of a solid insulator having metal inserts at both ends or when the solid insulator is placed in recessed electrodes, with and without the presence of surface charges show that the tangential field value decreases considerably at both electrode junctions. The field value was found to decrease with increasing penetration of the metal insert into the insulator and with increasing the recess depth of the electrodes. An added advantage for the latter two methods of reducing the electric field at the electrode junction is that the maximum value of the tangential field occurs on the insulator surface at a location away from the critical electrode junction. Higher flashover values have been reported when the solid insulator was placed in a recessed electrode at the cathode end in vacuum [5,22] and when the solid insulator had metal inserts at both ends in compressed gases [16,17].

The withstand voltage capability of a cylindrical solid insulator can also be improved considerably by incorporating a concave geometry in the insulator ends at the contact region with the conductors. It is found that the higher the value of the angle γ between the curved edge of the insulator and the ambient field the lower is the value of the tangential field at the triple junction. The influence of the relative dielectric constant of the material and the length of the insulator on the field at the triple junction is found to be negligibly small. Measurements of the flashover voltage in ultra high vacuum ($<10^{-8}$ Torr) are conducted for cylindrical rods made of glass-ceramic with concave curvature at both ends. γ is varied in the range 0 - 65°. The DC, AC and 1.2/50 μs lightning impulse flashover voltages are between 20 to 30% higher than the respective voltages of a straight cylindrical insulator of the same thickness. The DC pre-stress has negligible influence (<5%) on the subsequent combined DC + impulse and DC + AC flashover voltages, of a concave insulator made of Macor glass-ceramic.

8.2 Surface Charge Distributions

In the present study both hetero- and homo-surface charge distributions are considered. The surface charge density is distributed as a function of distance from the cathode in the format shown in Fig. 8.1. The shape of the distribution is arbitrarily chosen though it is qualitatively consistent with the recently reported measurements of surface charge distributions by Knecht [72], Lee et al [41] and the Monte Carlo simulation by Sudarshan et al [23].

For a plexiglass insulator in a vacuum environment A_o (electron emission energy in ev) and A_1 (electron impact energy in ev) are 4.7 and 30 ev respectively [7]. The surface charge density is calculated using equation 7.8 (Chapter 7).

The maximum value of surface charge density σ_s is equal to 4.3×10^{-9} C cm^{-2} which is appropriate to an applied field of 40 kV cm^{-1}. For the 40 mm gap considered in the present work, this level of the field is below that necessary to cause a breakdown of solid insulator in vacuum and at 1 bar SF_6 but well above the strength in atmospheric air.

Moreover, for compressed gas insulated systems (CGIS) also it was found that the surface charge density increases

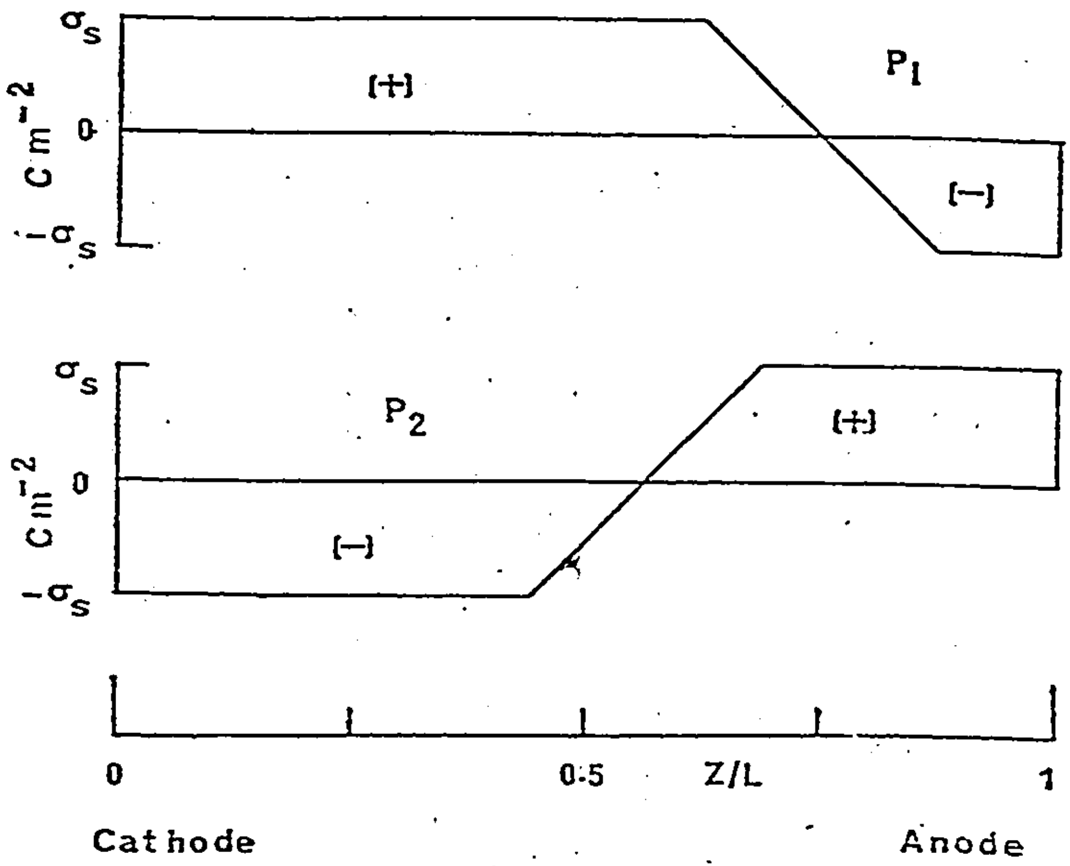

Fig. 8.1. Surface charge distributions along the surface of the solid insulator. P_1, heterocharge; P_2, homocharge; maximum value of surface charge density $\sigma_s = 4.3 \times 10^{-9}$ C cm^{-2}; (+ve) indicates positive charge polarity; (-ve) negative charge polarity. Insulator length = 4 cm; Insulator material: plexiglass ($\varepsilon_2 = 3.2$); Applied field E = 40 kV cm^{-1}; A_1 = 30 eV; A_o = 4.7 eV. (The above surface charge distribution patterns P_1 and P_2 are different from the charge distribution patterns discussed in Chapter VII).

linearly with increasing voltage stress [71] and is of the same order of magnitude used in the present study. In Fig. 8.1, pattern P_1 corresponds to the condition where a positive charge exists near the cathode and a negative charge near the anode (heterocharge). The portion of the charge near the anode is set at 21.4% of the total charge. P_2 (Fig. 8.1) shows a homocharge distribution giving a negative charge near the cathode and a positive charge near the anode. The portion of the charge near the anode is set at 42.8% of the total charges. A separate investigation by the author (Chapter 7) shows that the differences among the computed fields at either the cathode or at the anode for several different patterns of surface charge distributions resulted only in ± 5% difference in the values of the field enhancement provided the ratio of the positive to negative surface charges is kept constant (70-80% positive and 30-20% negative for a heterocharge distribution).

8.3 Electrodes, Insulator Material and Geometry

Figure 8.2 shows the cross section of plexiglass solid insulator having a relative dielectric constant $\varepsilon_2 = 3.2$ (region 2) sandwiched between two electrodes in vacuum (region 1, $\varepsilon_1 = 1$). The length of the solid insulator and the largest separation between the electrodes is 40 mm (L). The diameter of the cylindrical portion of the solid insulator is 40 mm (2R) and the applied voltage is 160 kV.

Figure 8.2a (System A) shows the insulator-electrode arrangement which is mainly used in high gas pressure applications to provide a physical support and to obtain a void-free contact with the electrode. The metal insert is used at both ends of the solid insulator. The depth of the metal insert is varied in the range 3-6 mm. Figure 8.2b (System B) shows a solid insulator placed in a recessed electrode at both ends. This arrangement is mainly used in vacuum devices. The depth of the elctrode-recess considered in the present study are 2 mm and 4 mm. Figure 8.2c (System C) shows the cylindrical solid insulator having a concave curvature at both electrode junctions. The concave rounded edge starting point is arbitrarily chosen to be 5 mm away from both electrodes. The concave edge is assumed to be part of a circle. The linear section on the cylindrical solid insulator is 3 cm and the total length of the gap between the electrodes is 4 cm. The linear section diameter is 4 cm. γ is the angle between the curved edges of the solid insulator contact point with the electrodes and the ambient electric field. For $\gamma = 0$, the solid insulator corresponds to a right cylindrical insulator without any curvature at the edges. The position of the contact point on the electrode varies according to the value of γ. Figure 8.2d (System D) shows a solid insulator having simultaneously metal insert at both ends and placed in recessed electrodes. The solid dielectric-electrode contact configura-

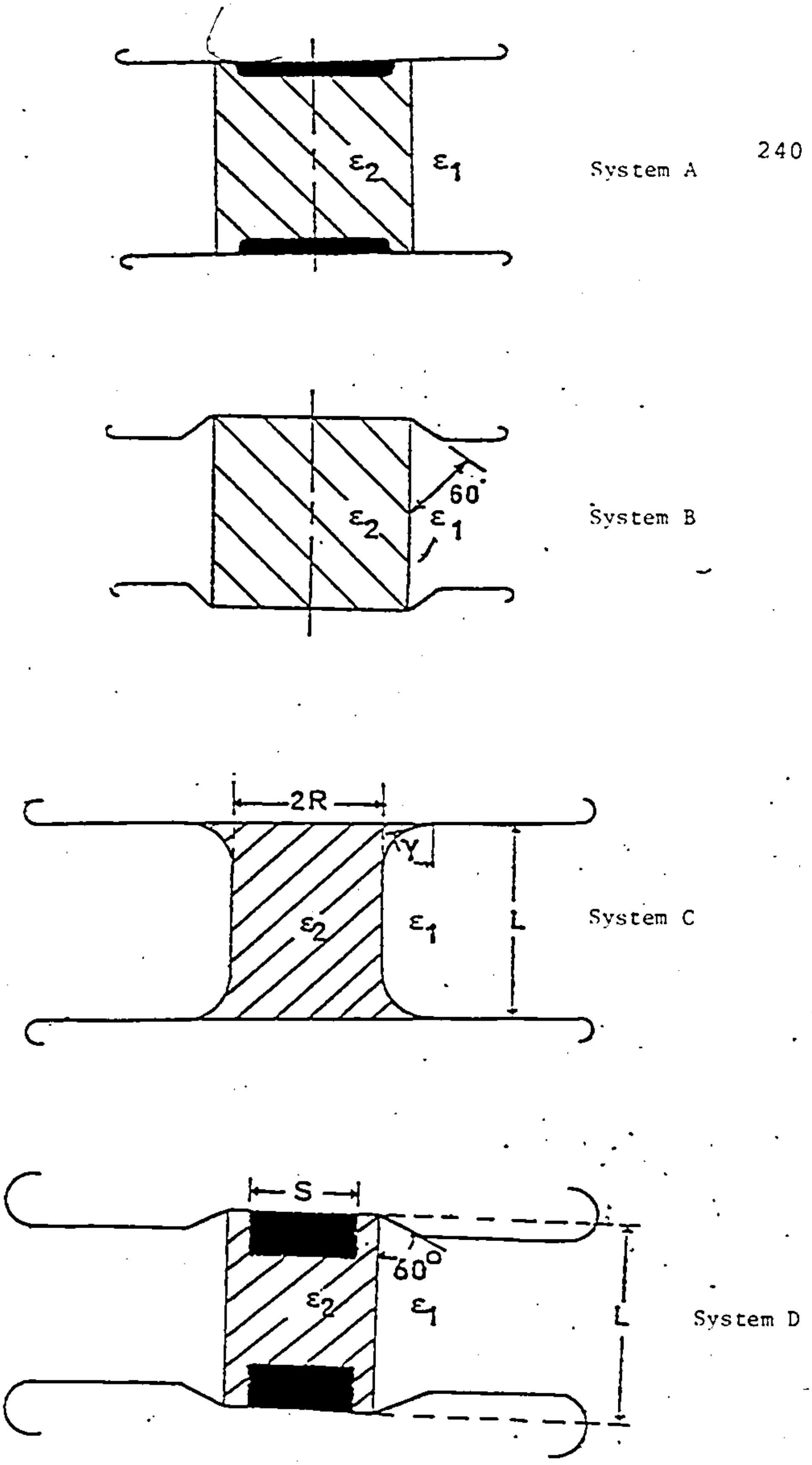

Fig. 8.2. Solid insulator-electrode arrangements. System A, cylinder solid insulator with metal inserts; System B, cylindrical solid insulator placed in recessed electrodes; System C, cylindrical solid insulator with concave curved edges; System D, cylindrical solid insulator with metal inserts. ε_2 = 3.2 (Plexiglass), L = 4 cm, 2R = 4 cm.

tions are referred to as system A, B, C and D, respectively in the following sections.

8.4 Method of Calculations

The electric field and the potential distributions along the solid insulator-vacuum interface are computed using the charge simulation technique [87] for the four different solid insulator-electrode configurations [Fig. 8.2]. Since the configuration considered has a rotational symmetry, the charge simulation is carried out by employing ring charges to model the electrodes and the solid dielectric boundaries. A typical number of ring charges used in the present work is 134. Further information on the simulation technique is discussed in Chapters 6 and 7. The computed tangential field intensity E_t and the normal field intensity E_n to the surface of the solid insulator are expressed in a normalized format,

$$E_t' = E_t/E_{av} \tag{8.1}$$

$$E_n' = E_n/E_{av} \tag{8.2}$$

$$E_{av} = V/L \tag{8.3}$$

where E_t' and E_n' are the normalized tangential and normal fields, respectively. V is the applied voltage at the top electrode with respect to the zero potential at the bottom electrode (Fig. 8.2) and L is the largest gap distance between the electrodes (Fig. 8.2). The normalized potential distribution ϕ' is similarly defined

$$\phi' = \phi/V \tag{8.4}$$

where ϕ is the computed potential.

The subscript 1 is used to represent the field in the vacuum region (region 1, Fig. 8.2) at the solid insulator-vacuum interface (E'_{t_1} and E'_{n_1}). The field in the solid dielectric E'_{t_2} and E'_{n_2} are similarly defined where the subscript 2 is used to refer to region (solid dielectric) (Fig. 8.2). The normalized tangential and the normalized normal field values at the cathode triple junction on the vacuum side are referred to as $E'_{t_{1c}}$ and $E'_{n_{1c}}$, respectively. At the anode junction $E'_{t_{1a}}$ and $E'_{n_{1a}}$ are similarly defined. The maximum of the normalized values of the tangential and the normal fields on the surface of the solid insulator on the vacuum side of the interface are referred to as $E'_{t_{1m}}$ and $E'_{n_{1m}}$, respectively.

The accuracy of the calculations are verified by calculating potential error, potential discrepancy and tangential field discrepancy (definition given in Chapter 6). For all the configurations studied the maximum potential error is about 0.49%. The maximum potential discrepancy and the tangential field discrepancy near the triple junctions are about 0.08% and 1.8%, respectively. The tangential field discrepancy is less than 0.01% at locations away from the triple junctions whereas the potential discrepancy is less than 0.001%. The assignment factor is kept between 0.9 to 1.8 throughout the computation [87,89].

8.5 Cylindrical Solid Insulator with Metal Inserts (System A).

The insulator-electrode arrangement termed System A (Fig. 8.2) is widely used in CGIS applications. Figures 8.3 and 8.4 show the normalized tangential field distribution along the surface of the solid insulator for 3 and 6 mm depths of a contacting insert into the solid insulator, respectively. It will be observed that the tangential fields at the cathode $E'_{t_{1c}}$ and at the anode $E'_{t_{1a}}$ decrease with increasing the depth of the metal insert into the solid insulator (Table 8.1). This dependence is observed for all the cases considered as can be seen by comparing Figs. 8.3 and 8.4 when the charge is absent (curve 1), a heterocharge (curve 2) and a homocharge (curve 3). Typically for $\sigma_s = 0$, $E'_{t_{1c}}$ (at the cathode) decreases from 0.77 (Fig. 8.3, curve 1) to 0.47 (Fig. 8.4, curve 1) with increasing depth of the metal insert from 3 to 6 mm. The normalized values of the tangential fields at the triple junctions and the maxima are summarized in Table 8.1. Figures 8.3 and 8.4 show that the maximum tangential field value occurs at a location on the surface of the insulator away from both electrode junctions. It is also observed that when using a metal insert, the peak value of

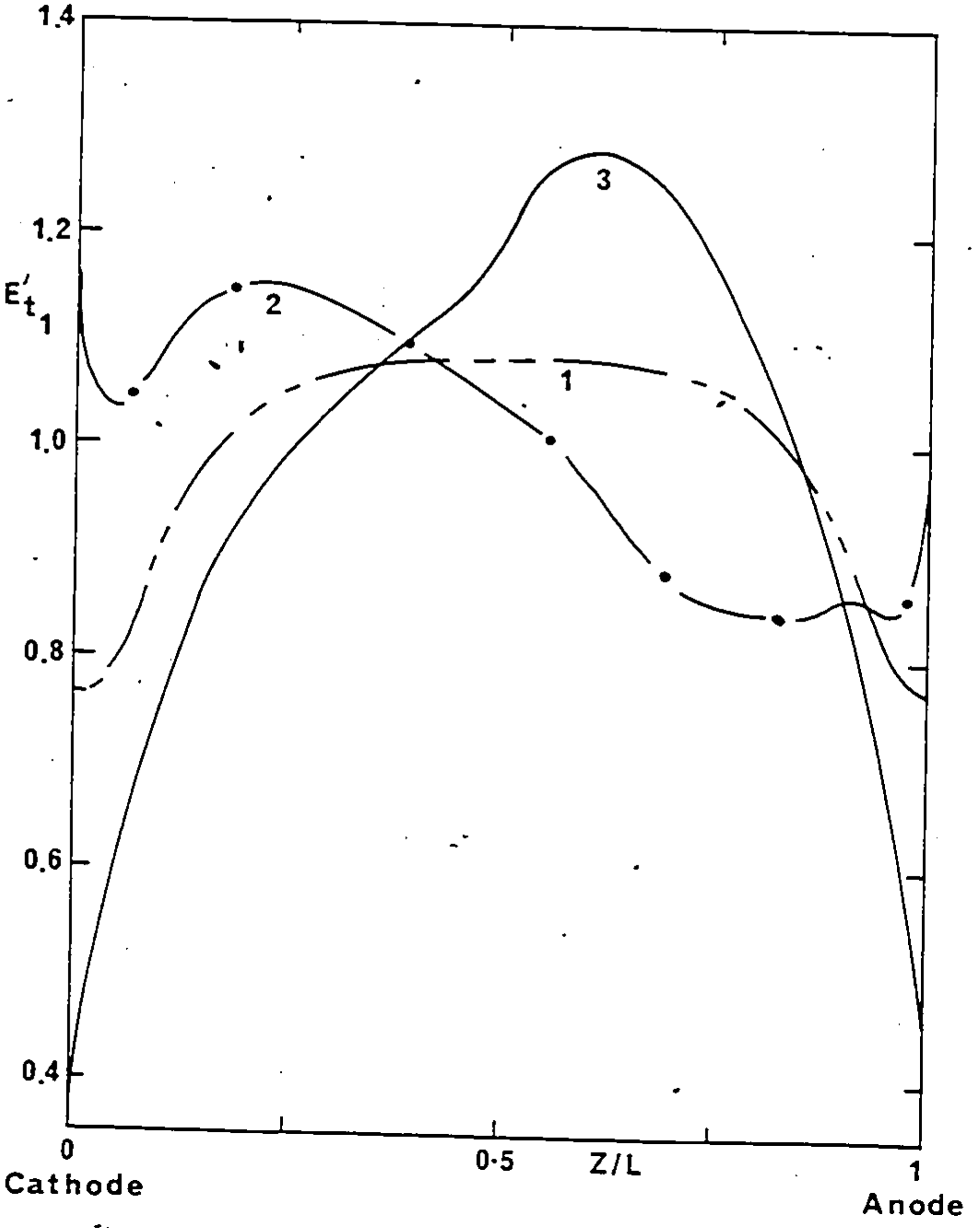

Fig. 8.3 Normalized tangential electric field E'_{t1} along the solid insulator-vacuum bondary for System A. Depth of metal insert = 3 mm. Normalized field is shown on the vacuum side ($\varepsilon_1 = 1$) of the interface. Curve 1 corresponds to surface charge $\sigma_s = 0$; curve 2, pattern P_1; curve 3, pattern P_2.

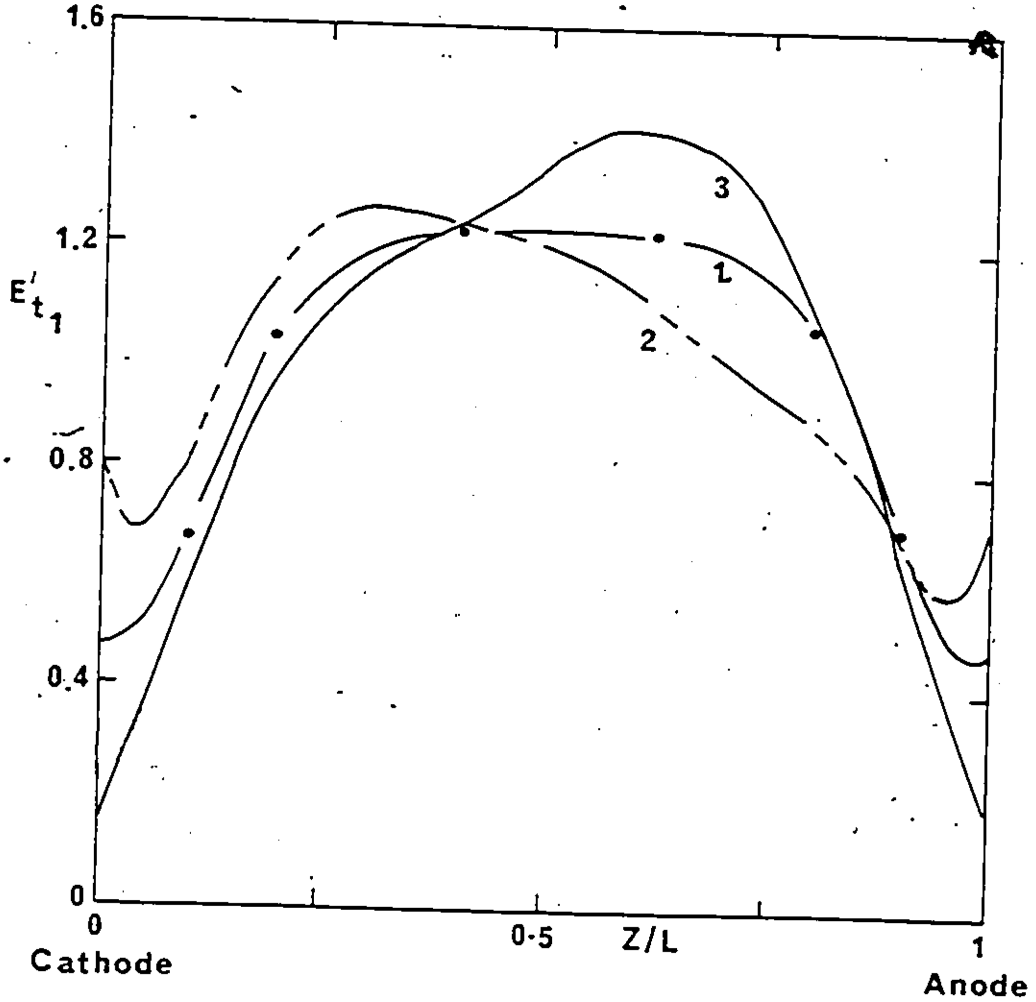

Fig. 8.4. E'_{t_1} for system A. Depth of metal insert = 6 mm. Other conditions are as for Fig. 8.3.

Table 8.1. Normalized Tangential Field E'_{t_1} Near the Cathode ($E'_{t_{1c}}$) and the Anode ($E'_{t_{1a}}$) Junctions and the Maximum Field $E'_{t_{1m}}$ for Different Solid Insulator-Electrode Arrangements.

Material: Plexiglass ($\varepsilon_2 = 3.2$); L = 4.0 cm; 2 R = 4.0 cm; Applied E = 40 kV cm^{-1}

Electrode and Insulator System (Shown in Fig. 8.2)	Cylindrical Insulator Electrode Geometry	Surface Charge $\sigma_s = 0$			Heterocharge P_1 (shown in Fig. 8.1)			Homocharge P_2 (shown in Fig. 8.1)		
		$E'_{t_{1c}}$	$E'_{t_{1a}}$	$E'_{t_{1m}}$	$E'_{t_{1c}}$	$E'_{t_{1a}}$	$E'_{t_{1m}}$	$E'_{t_{1c}}$	$E'_{t_{1a}}$	$E'_{t_{1m}}$
A	3 mm metal insert	0.76	0.76	1.08	1.16	0.98	1.16	0.38	0.47	1.28
A	4 mm metal insert	0.65	0.65	1.12	1.03	0.88	1.17	0.29	0.36	1.31
A	6 mm metal insert	0.47	0.47	1.23	0.81	0.71	1.26	0.14	0.19	1.41
B	2 mm recessed electrode	0.66	0.66	1.07	1.12	0.96	1.18	0.22	0.35	1.21
B	4 mm recessed electrode	0.62	0.62	1.07	1.08	0.92	1.14	0.19	0.25	1.24

$E'_{t_{1m}}$ increases with increasing the depth of the insert. Typically the value of $E'_{t_{1m}}$ without a surface charge for the case of a 3 mm insert depth is 1.08 (curve 1, Fig. 8.3) and increases to 1.23 at 6 mm depth (curve 1, Fig. 8.4). Both maxima occur away from the elctrodes. In the case of a heterocharge distribution (P_1) $E'_{t_{1m}}$ for a 3 mm insert is 1.16 and is located at the cathode triple junction. In the case of a 6 mm insert, $E'_{t_{1m}} \sim = 1.26$ and occurs at a location of 1.30 cm away from the cathode.

Although the maximum value of the tangential field is higher with increasing depth of the insert, it is still preferable to use a metal insert because the enhancement occurs at a location away from the cathode junction where it is less likely to be critical. The field at the cathode is reduced with increasing the depth of the metal insert. The present results are supported by the reported measurements of the flashover voltage which decreased with a large increase in the depth of the metal insert [17]. The reduction in the dielectric strength of the solid insulator with a large increase in the insert depth [17], is attributed to the increase of $E'_{t_{1m}}$ at the surface of the insulator despite the enhancement being a distance away from electrode junctions. For a homocharge distribution (P_2) the maximum values of the normalized tangential field $E'_{t_{1m}}$ are 1.28 (Fig. 8.3, curve 3) for 3 mm metal insert and 1.41 (Fig. 8.4, curve 3) for 6 mm metal insert, respectively. Both maxima occur at a location of 2.4 cm away from the cathode. This shows that a doubling of the depth of the metal penetration into the solid insulator causes only a slight increase in the maxima values of $E'_{t_{1m}}$ (typically 10% for P_2) but a much larger decrease (Table 8.1) for $E'_{t_{1c}}$ at the cathode (from 0.38 to 0.14 for P_1) and $E'_{t_{1a}}$ at the anode (from 0.47 to 0.19 for P_1).

Figures 8.5 and 8.6 show the normalized normal field distribution for 3 mm and 6 mm metal inserts respectively. It can be seen from Table 8.2 and Figs. 8.5 and 8.6 that the absolute value of E'_{n_1} increases with increasing depth of the metal insert. For both the hetero- and the homo-charge distributions, for System A, at both electrode junctions E'_{n_1} values are lower (Figs. 8.5 and 8.6) than without a metal insert [26]. For System A and when $\sigma_s = 0$ the normal field near the anode region is directed outward from the surface and near the cathode is directed inward. This helps to reduce both the normal and the tangential fields at the triple junctions when a heterocharge is present. The lower values of E'_{t_1} and E'_{n_1} contribute to the observed higher withstand voltage of solid insulator when using a contacting electrode with a metal insert.

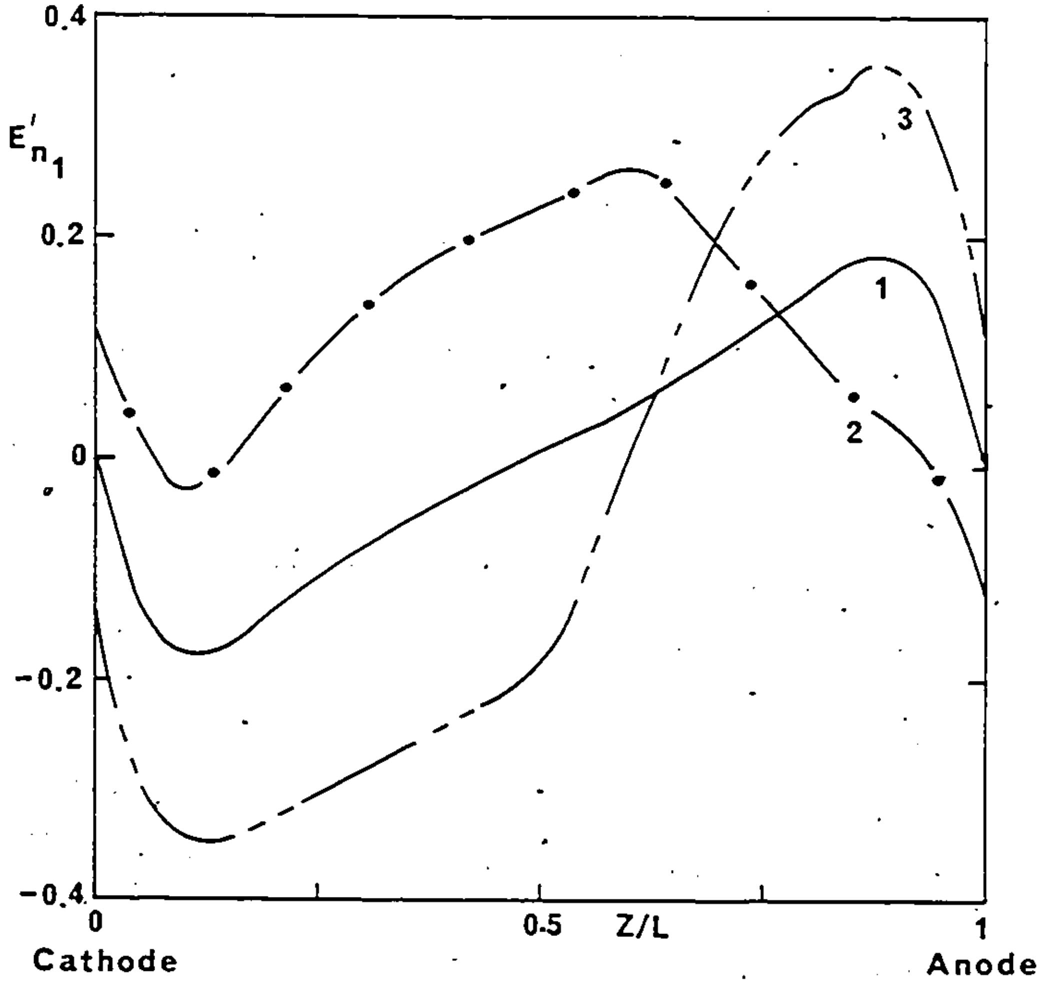

Fig. 8.5. Normalized normal field distribution E'_{n_1} along the solid insulator-vacuum interface for System A. Conditions and curve numbers are as for Fig. 8.3. Positive values: field vector directed away from surface; negative values: field directed into surface.

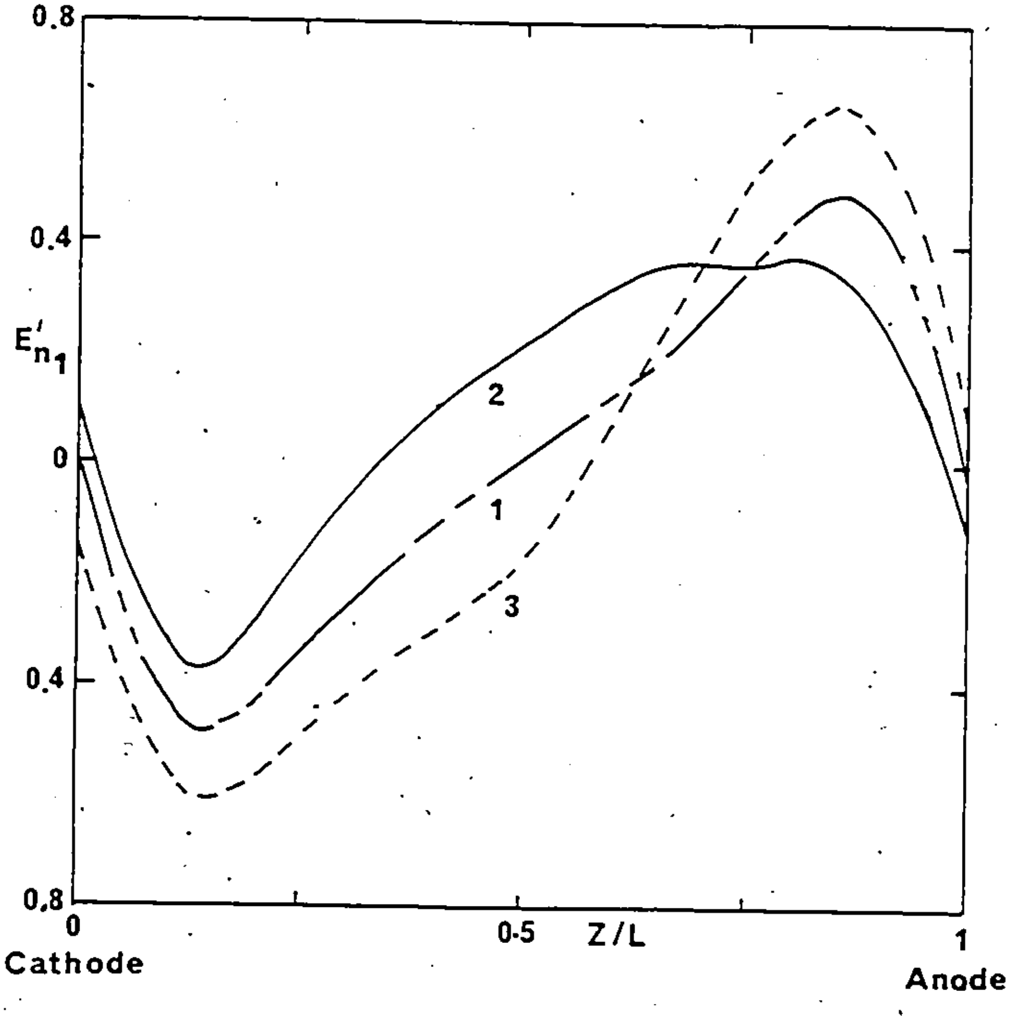

Fig. 8.6. E'_{n_1} for System A. Depth of metal insert = 6 mm. Other conditions are as for Fig. 8.5.

Table 8.2. Normalized Normal Field E'_{n_1} Near the Cathode ($E'_{n_{1c}}$) and the Anode ($E'_{n_{1a}}$) Junctions and the Maximum Field ($E'_{n_{1m}}$) for Different Solid Insulator-Electrode Arrangements. All Values are Given on the Vacuum Side of the Solid Insulator-vacuum Interface (region 1). Conditions are as for Table 8.1

Electrode and Insulator System (Shown in Fig. 8.2)	Cylindrical Insulator Electrode Geometry	Surface Charge $\sigma_s = 0$			Heterocharge P_1 (shown in Fig. 8.1)			Homocharge P_2 (shown in Fig. 8.1)		
		$E'_{t_{1c}}$	$E'_{t_{1a}}$	$E'_{t_{1m}}$	$E'_{t_{1c}}$	$E'_{t_{1a}}$	$E'_{t_{1m}}$	$E'_{t_{1c}}$	$E'_{t_{1a}}$	$E'_{t_{1m}}$
A	3 mm metal insert	-0.001	0.001	0.19	0.12	-0.12	0.27	-0.12	0.12	0.36
A	4 mm metal insert	-0.002	0.002	0.29	0.12	-0.12	0.29	-0.12	0.12	0.45
A	6 mm metal insert	-0.003	0.003	0.49	0.12	-0.12	0.38	-0.12	0.12	0.64
B	2 mm recessed electrode	0.39	-0.39	0.45	0.73	-0.63	0.75	0.06	-0.09	-0.21
B	4 mm recessed electrode	0.35	-0.35	0.45	0.70	-0.61	0.73	0.04	-0.06	-0.24

8.6 Cylindrical Solid Insulator Placed in a Recessed Electrodes (System B)

It has been suggested that the placing of the solid insulator in a recessed electrode would offer an advantage in reducing the field stress in the metal-electrode junction and thus leads to a higher withstand voltage of the insulating gap [5]. Measurements of the electric field at a recessed electrode junction also showed that the junction field enhancement was lower than that for an unrecessed electrode [22].

The tangential field E'_{t_1} for System B whereby a cylindrical insulator ends are placed within 2 mm and 4 mm recesses shown in Figs. 8.7 and 8.8 respectively. It will be observed that for $\sigma_s = 0$, the field at the electrode junction is reduced considerably (curve 1, Figs. 8.7 and 8.8) due to the effect of the recess. Increasing the recess depth from 2 to 4 mm results only in a small change in the values of $E'_{t_{1c}}$, $E'_{t_{1a}}$ and $E'_{t_{1m}}$ (for $\sigma_s = 0$. Figs. 8.7 and 8.8 and Table 8.1). For the cases of hetero- and homo-charges there is similarly a large reduction in E'_{t_1} at both electrode junctions when a recess is used in the electrodes (curves 2 and 3, Figs. 8.7 and 8.8).

The maxima of the normalized tangential field occur at locations away from the electrodes for the three situations considered ($\sigma_s = 0$, P_1 and P_2).

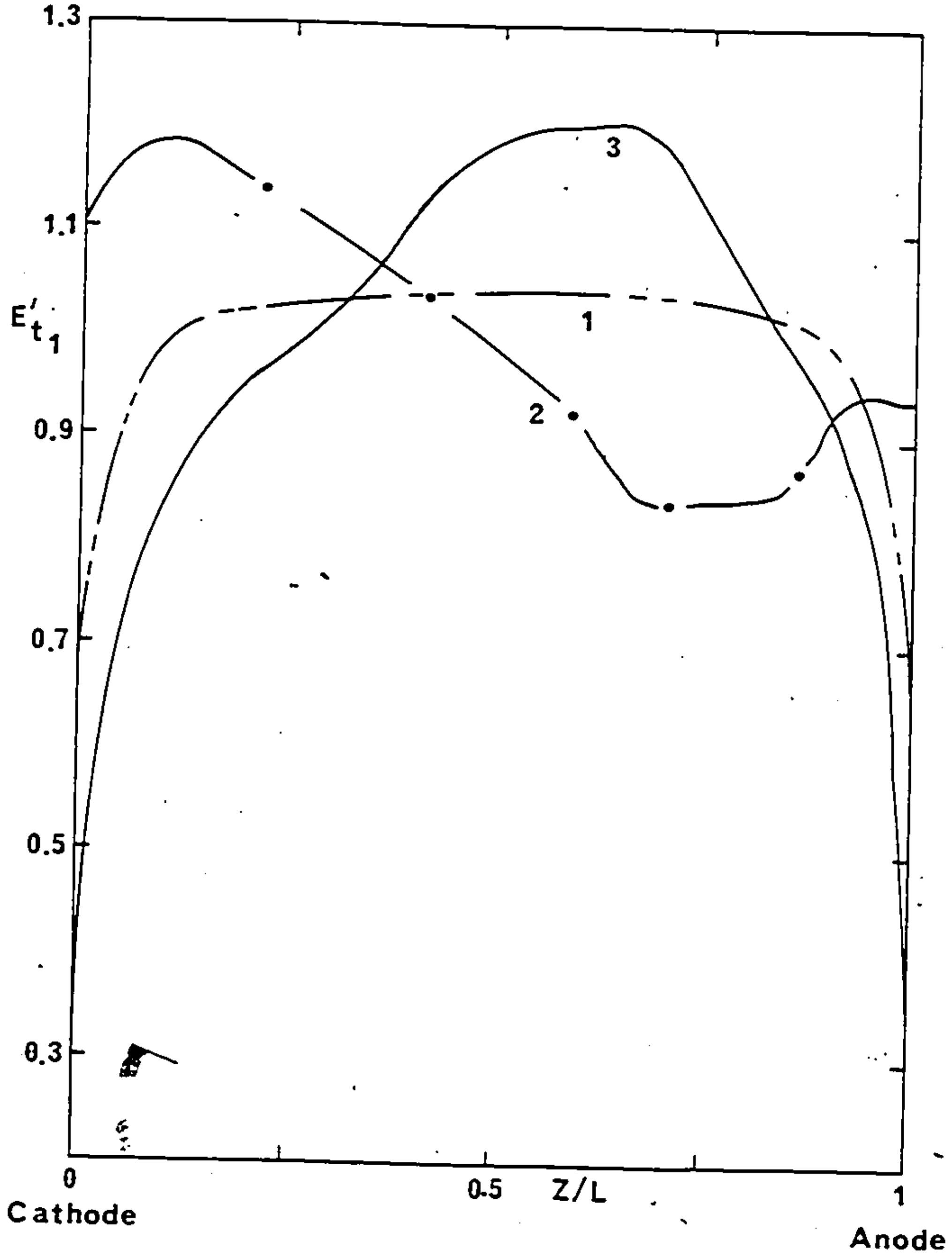

Fig. 8.7. E'_{t_1} for System B. Depth of electrode recess = 2 mm. Other conditions are as for Fig. 8.3.

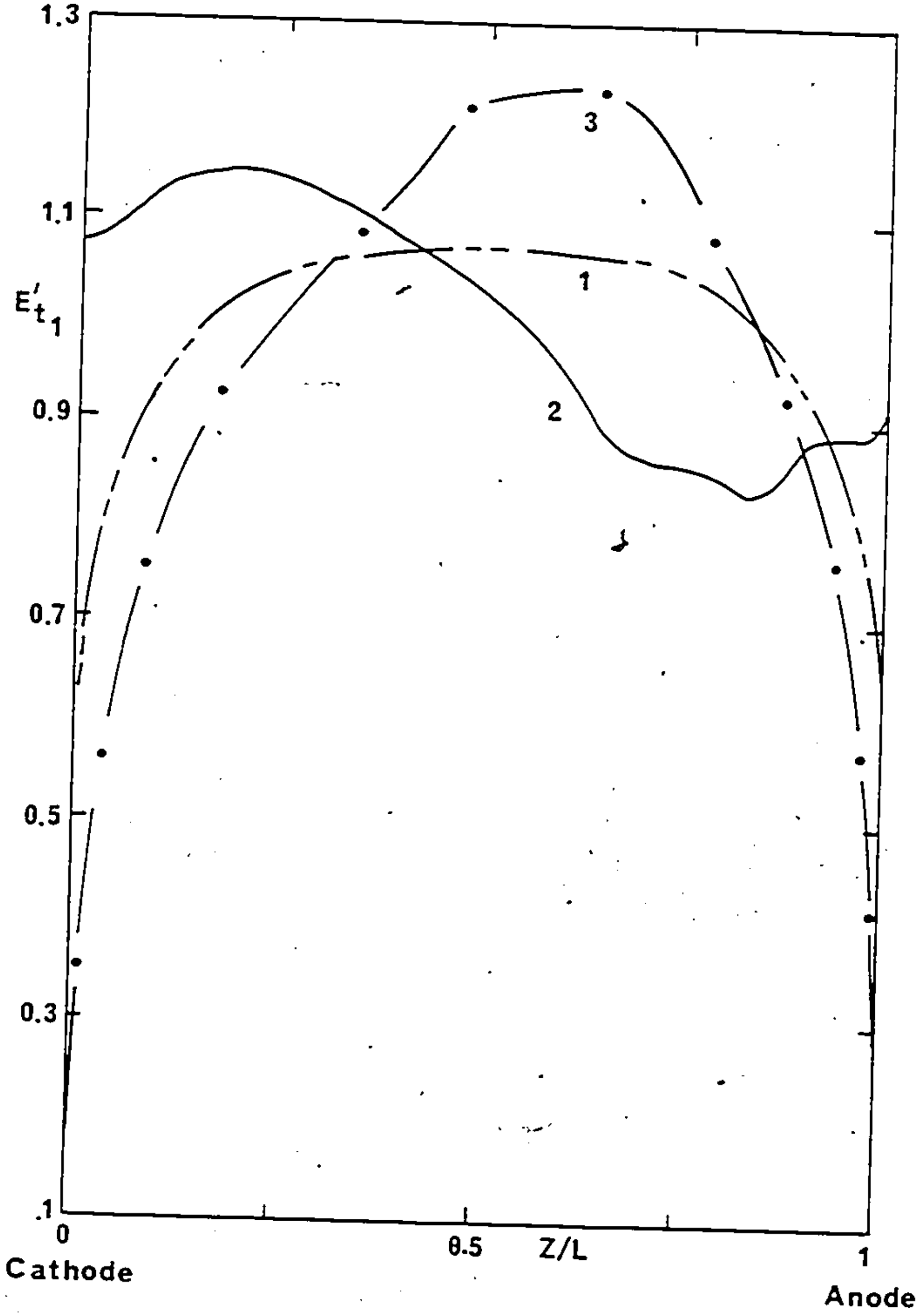

Fig. 8.8. E'_{t_1} for System B. Depth of electrode recess = 4 mm. Other conditions are as for Fig. 8.3.

Figures 8.9 and 8.10 show the E'_{n_1} for System B for 2 and 4 mm recess depths respectively. The normal field values are higher in the case of the recessed electrode (System B) compared to System A for $\sigma_s = 0$ (Table 8.2). The normal field is directed outward from the surface in the cathode region and inward in the anode region. These field directions helps to reduce $E'_{t_{1c}}$, $E'_{t_{1a}}$ and $E'_{t_{1m}}$ when a homocharge resides on the surface. It is also found that for the same depth of the recess (Table 8.1 , e.g., 4 mm) $E'_{t_{1m}}$ is lower than for the same penetration of the metal insert for the cases $\sigma_s = 0$, P_1 and P_2.

8.7 Cylindrical Solid Insulator with Concave Curved Edges (System C)

8.7.1 Effect of γ on the Tangential and the Normal Field Distributions

Figure 8.11 shows the normalized tangential field E'_{t_1} at the solid insulator surface (on the vacuum side) for γ = 5°, 15°, 30°, 45° and 65° as a function of Z/L in plexiglass. As can be seen from Fig. 8.11, the field at the electrodes junction decreases as γ increases. Moreover, the variation of the field is mainly in the ranges Z/L = 0 to Z/L = 0.2 and Z/L = 0.8 to 1 which is near to the concave portions of the cylinder. The normalized tangential field becomes unity towards the linear portion of the solid insulator.

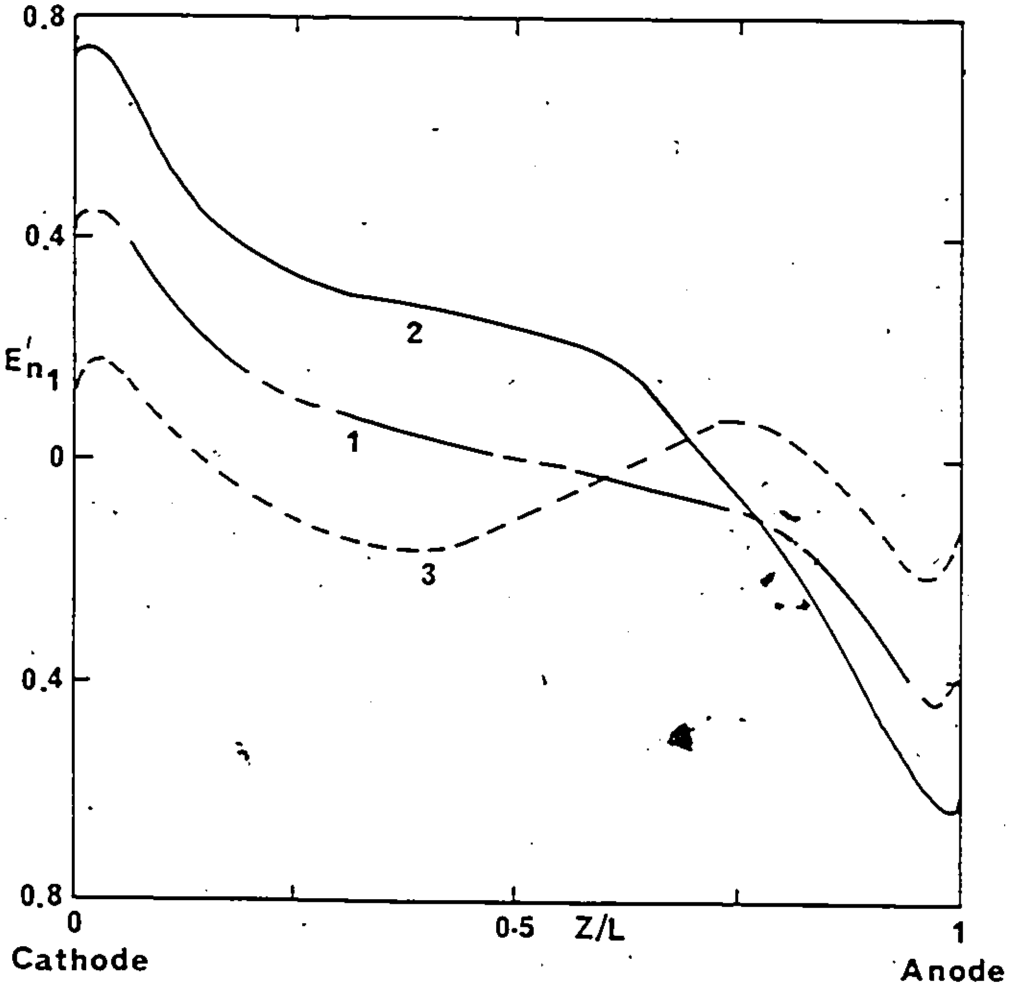

Fig. 8.9. E'_{n_1} for System B. Depth of electrode recess = 2 mm. Other conditions are as for Fig. 8.5.

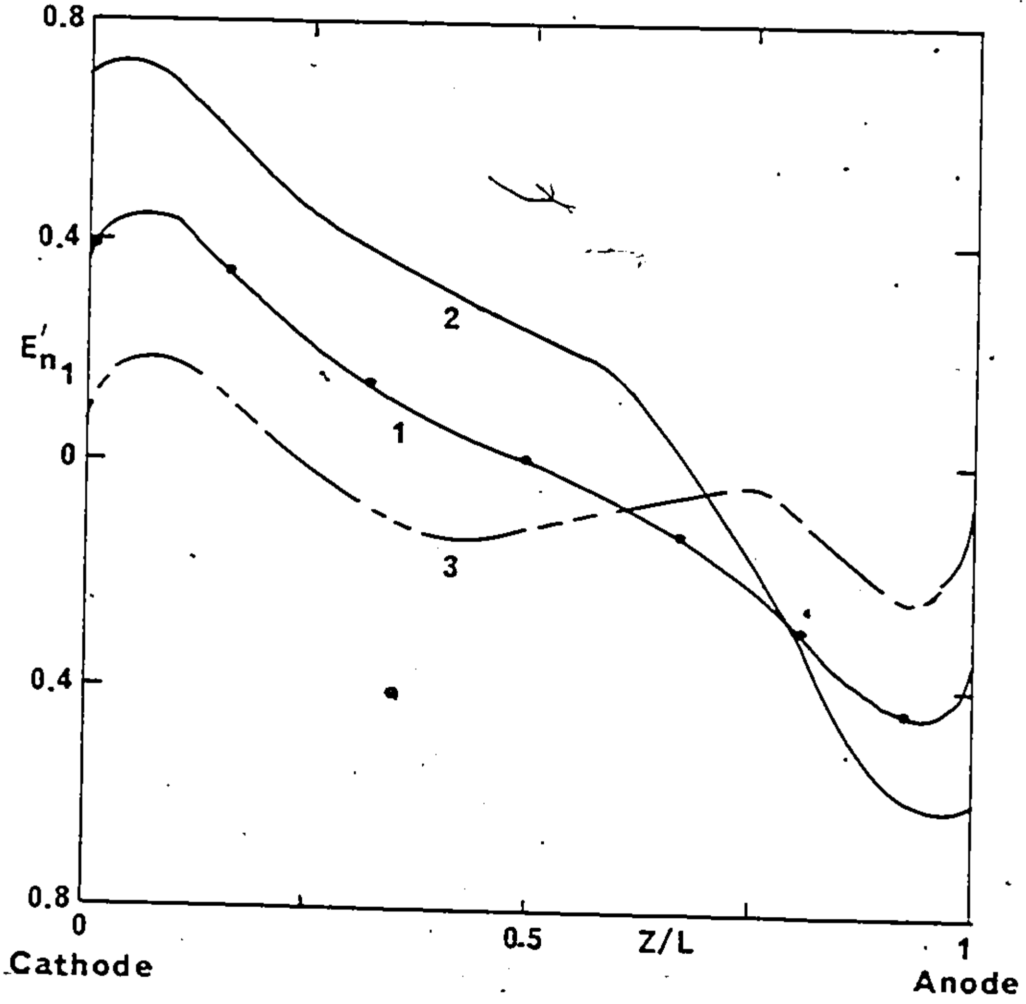

Fig. 8.10. E'_{n_1} for System B. Depth of electrode recess = 4 mm. Other conditions are as for Fig. 8.5.

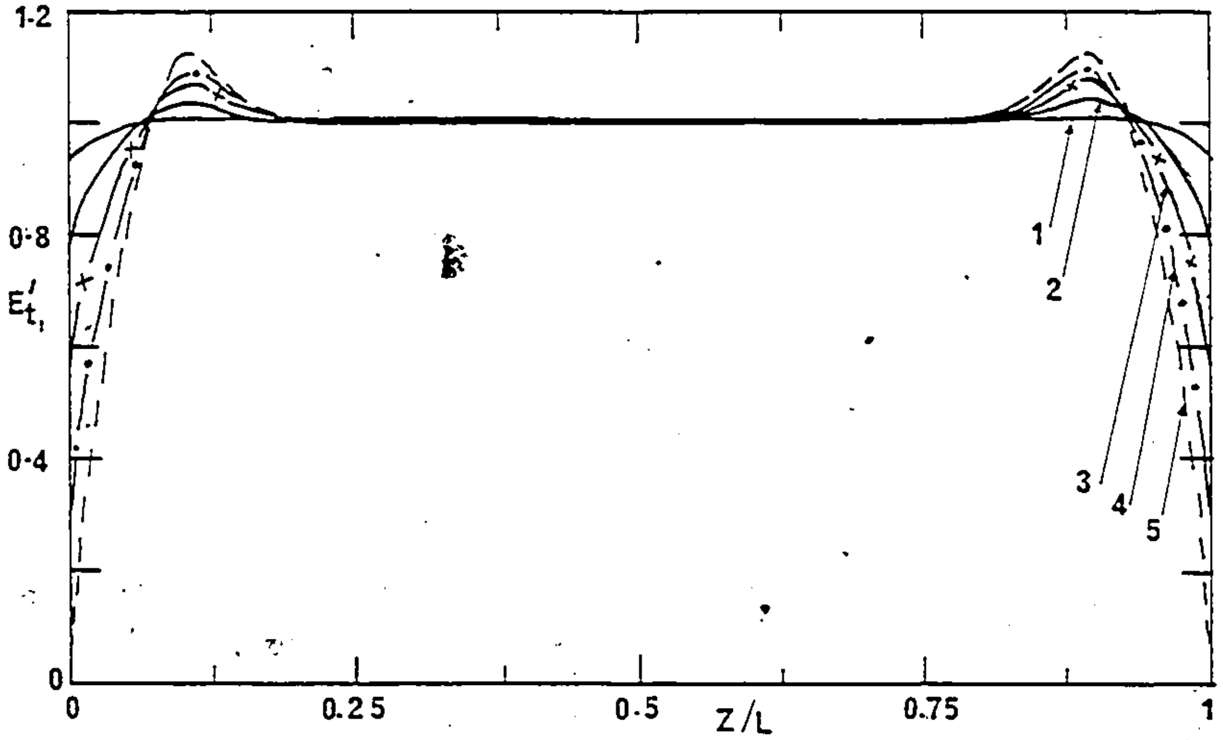

Fig. 8.11. Dependence of the normalized tangential electric field E'_{t_1} at the solid insulator-vacuum interface on the angle γ for System C. Solid insulator: plexiglass ($\varepsilon_2 = 3.2$) L = 4 cm, 2R = 4 cm. Curve 1 corresponds to γ = 5°; curve 2, γ = 15°; curve 3, γ = 30°; curve 4, γ = 45°; and curve 5, γ = 65°.

The normalized tangential and the normalized normal field values near the cathode and the anode triple junctions and the maxima in the field values are summarized in Table 8.3. Figures 8.12 and 8.13 show respectively the normalized tangential and the normalized normal fields, for $\gamma = 5°$, 30° and 60° in the regions of the electrodes. Since the change in the field value is mainly towards the electrode junction and is similar at both the electrode junctions, due to the symmetry of the solid dielectric considered here, the field values are plotted in Figs. 8.12 and 8.13 for Z/L values from 0 to 0.2 only. The linear portion of the insulator from the bottom electrode starts at Z/L = 0.125. It can be seen from Table 8.3 and Figs. 8.11, 8.12 and 8.13 that the higher the value of γ, the lower the value of $E'_{t_{1c}}$ (and $E'_{t_{1a}}$) and at the same time the higher the value of $E'_{n_{1c}}$ (and $E'_{n_{1a}}$).

For example, when $\gamma = 5°$, $E'_{t_{1c}}$ and $E'_{n_{1c}}$ values near the electrode junction (i.e., Z/L = 0), are 0.93 (Fig. 8.12, curve 2) and 0.13 (Fig. 8.13, curve 2), respectively. For a right angle cylindrical insulator (i.e., $\gamma = 0$) $E'_{t_{1c}} = 1.0$ (Fig. 8.12, curve 1), and $E'_{n_{1c}} = 0$ (Fig. 8.13, curve 1) near the electrode junctions. This shows that even a slight concave curvature (say $\gamma = 5°$) reduces the tangential field (Fig. 8.12). As the value of γ increases, the field value at the electrode junction E'_{t_1} starts to decrease and E'_{n_1} starts to increase. For example, at $\gamma = 30°$, $E'_{t_{1c}} = 0.56$ (Fig. 8.12, curve 3) and

Table 8.3. Normalized tangential (E'_t) and normalized normal (E'_n) fields for different values of γ (Fig: 8.2, System C). $E'_{t_{1a}}$ and $E'_{t_{1c}}$ refer to the field values near the cathode junction. $E'_{t_{1a}}$ and $E'_{n_{1a}}$ refer to the field values near the anode junction. $E'_{t_{1m}}$ and $E'_{n_{1m}}$ refer to the maxima in the field values on the solid insulation–vacuum interface. All field values are given on the vacuum side of the interface. E = 40 kV cm^{-1}, 2R = 4 cm; L = 4 cm; Material: Plexiglass (ϵ_2 = 3.2)

γ	$E'_{t_{1c}} = E'_{t_{1a}}$	$E'_{t_{1m}}$	$E'_{n_{1c}} = E'_{n_{1a}}$	$E'_{n_{1m}}$
0	1.00	1.00	0.00	0.00
5	0.93	1.01	0.13	0.13
15	0.78	1.04	0.34	0.34
30	0.56	1.07	0.60	0.60
45	0.31	1.10	0.77	0.78
65	0.07	1.12	0.90	0.92

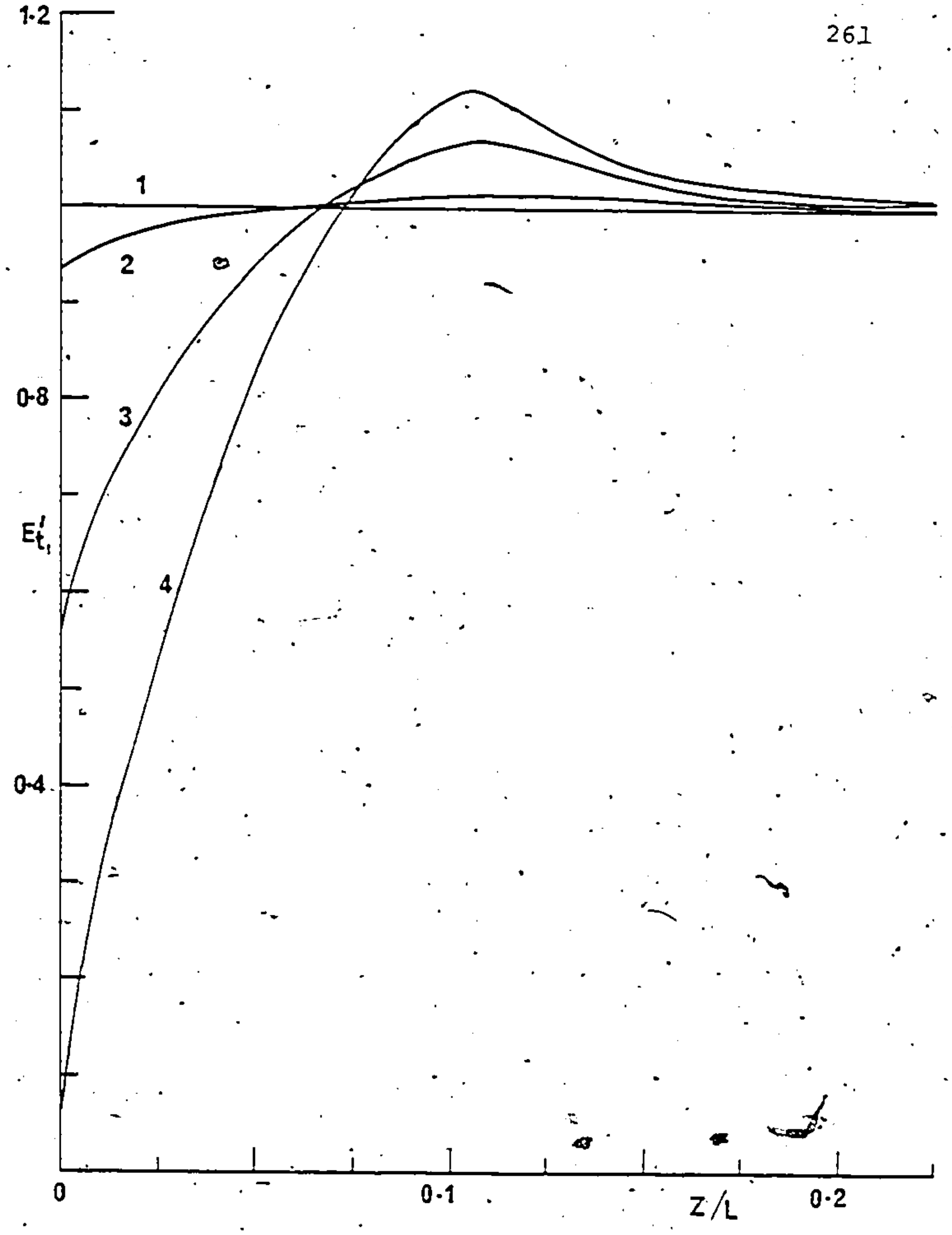

Fig. 8.12. Dependence of the normalized tangential field E'_{t_1} at the solid insulator-vacuum interface on γ near the electrodes regions for System C. Curve 1 corresponds to γ = 0; curve 2, γ = 5°; curve 3, γ = 30°; curve 4, γ = 65°.

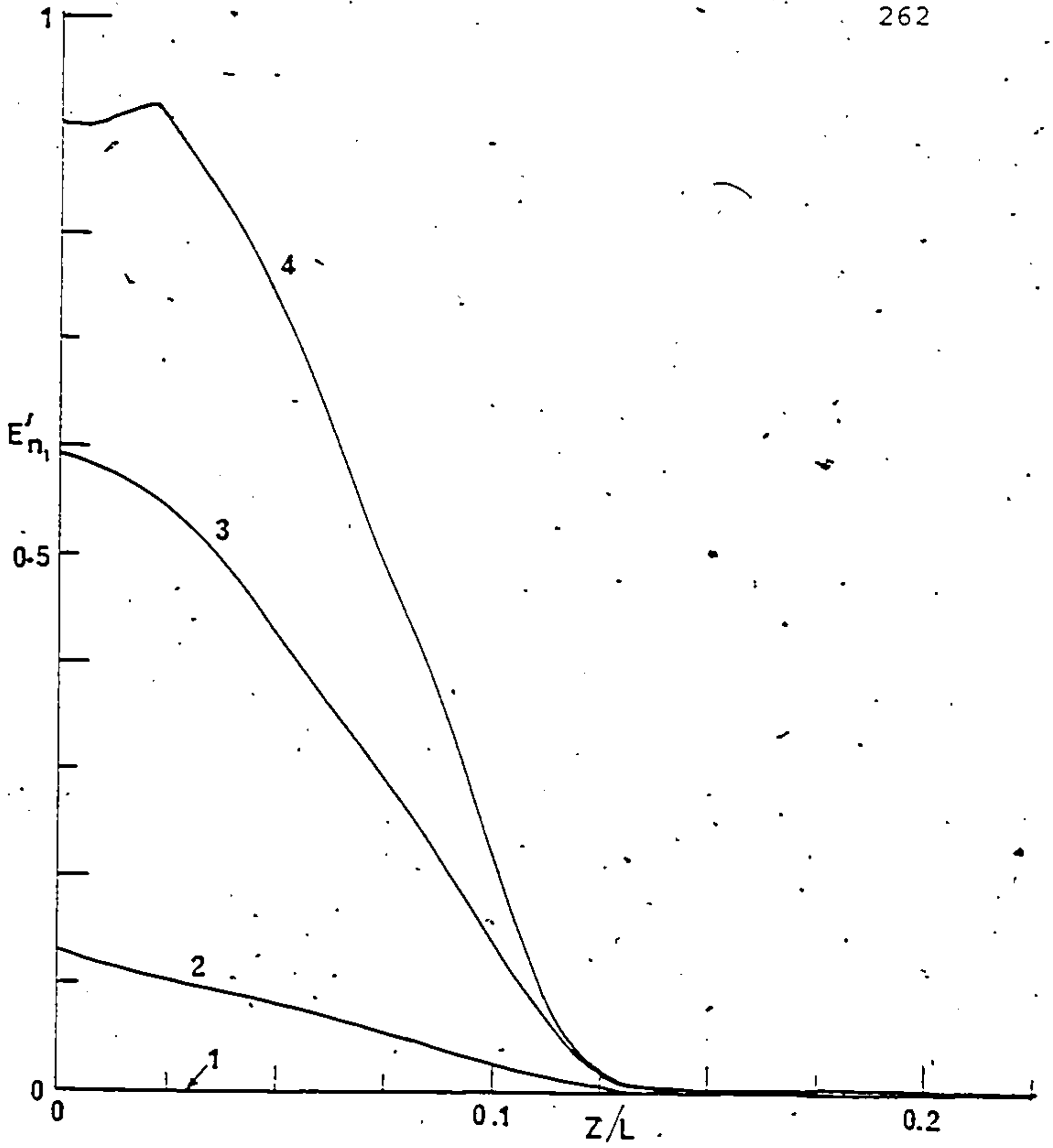

Fig. 8.13. Dependence of the normalized normal electric field E'_{n_1} at the solid insulator-vacuum interface on γ near the electrodes regions for System C. Curve numbers are as for Fig. 8.12.

$E'_{n_{1c}} = 0.60$ (Fig. 8.13, curve 3). When $\gamma = 65°$ $E'_{t_{1c}}$ value is much lower ($E'_{t_{1c}} = 0.07$) (Fig. 8.12, curve 4) and $E'_{n_{1c}}$ is higher at (Fig. 8.13, curve 4). The maximum value of tangential field $E'_{t_{1m}}$ for $\gamma = 30°$ and $65°$ are 1.07 and 1.12 respectively. The normalized normal field E'_{n_1} (Fig. 8.13) decreases rapidly with increasing Z/L from about Z/L = 0.025 to about Z/L = 0.125 and thereafter E'_{n_1} becomes negligibly small ($E'_n = 0$) in the linear portion of the solid insulator. Fig. 8.14 shows the normalized tangential and the normalized normal field values at the electrode triple junction as a function of γ. From Fig. 8.14, it can be seen that as the value of γ is increased the tangential field starts to decrease rapidly while the normal field increases. Both the normal and the tangential field values reach the same value when γ is about 28.5°. The magnitude of the normal field is important for the production of charges on the surface of the insulation either from the drift motion within the volume of the insulator towards the surface or via the deposition on the surface from charges present in the vacuum or in the gaseous region adjacent to the surface of the solid insulator.

Measurements of surface charges for solid insulators with concave curved edges have not yet been reported. Therefore, meaningful computations of the electric field distribution along the solid insulator-vacuum interface with the presence

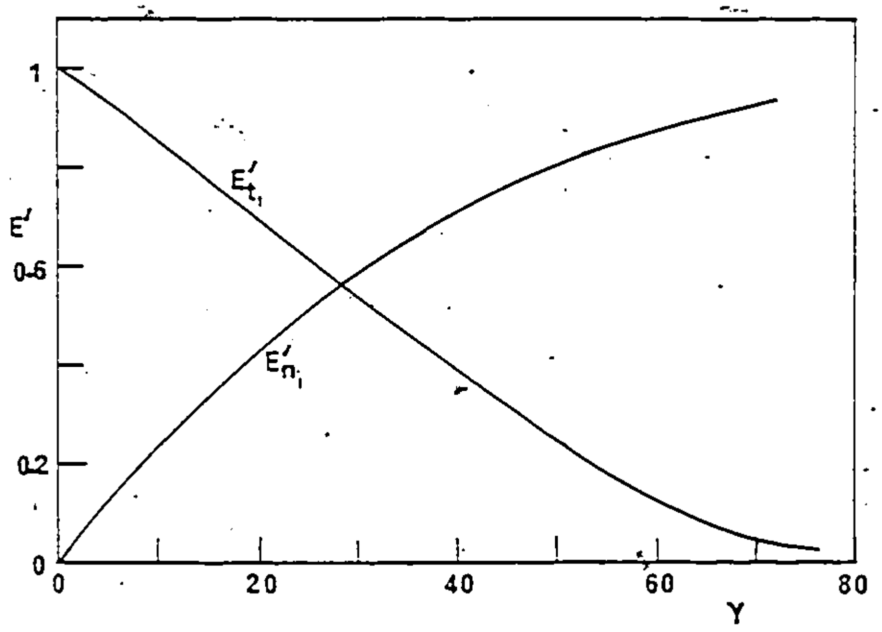

Fig. 8.14. Normalized tangential $E'_{n_{1c}}$ (=$E'_{t_{1a}}$) and normalized normal $E'_{n_{1c}}$ (=$E'_{n_{1a}}$) field at the electrodes contact region as a function of γ for System C. Field values are given on the vacuum side of the interface.

of surface charges await such measurements.

8.7.2 Potential Distribution Along the Solid Insulator-Vacuum Interface

The potential distribution along the surface of the solid dielectric-vacuum interface is shown in Fig. 8.15 for $\gamma = 0°$, 15°, 45° and 65°. Since the variation in the potential distribution is mainly in the curved portion of the solid insulator (Fig. 8.15) the distribution is shown in the range $Z/L = 0$ to 0.125. The departure from linearity occurs near the electrode region in curves 2 to 4 of Fig. 8.15. As γ increases, the change in the potential with increasing distance from the electrode decreases in the region near the contact region. The potential increases linearly with distance in the linear portion of the solid insulator as is to be expected. For example, when $Z/L = 0.125$, the normalized potential values for $\gamma = 0°$, 15°, 45° and 65° are 0.125, 0.01, 0.008, 0.005, respectively. This indicates that the higher the value of γ the lower the value of the potential change, thereby the lower becomes the field value towards the electrode junction.

8.7.3 Effect of Relative Dielectric Constant and Length of Solid Insulator on Field Enhancement

The normalized normal and the normalized tangential fields are computed for Teflon ($\varepsilon_2 = 2.1$), Plexiglass ($\varepsilon_2 = 3.2$),

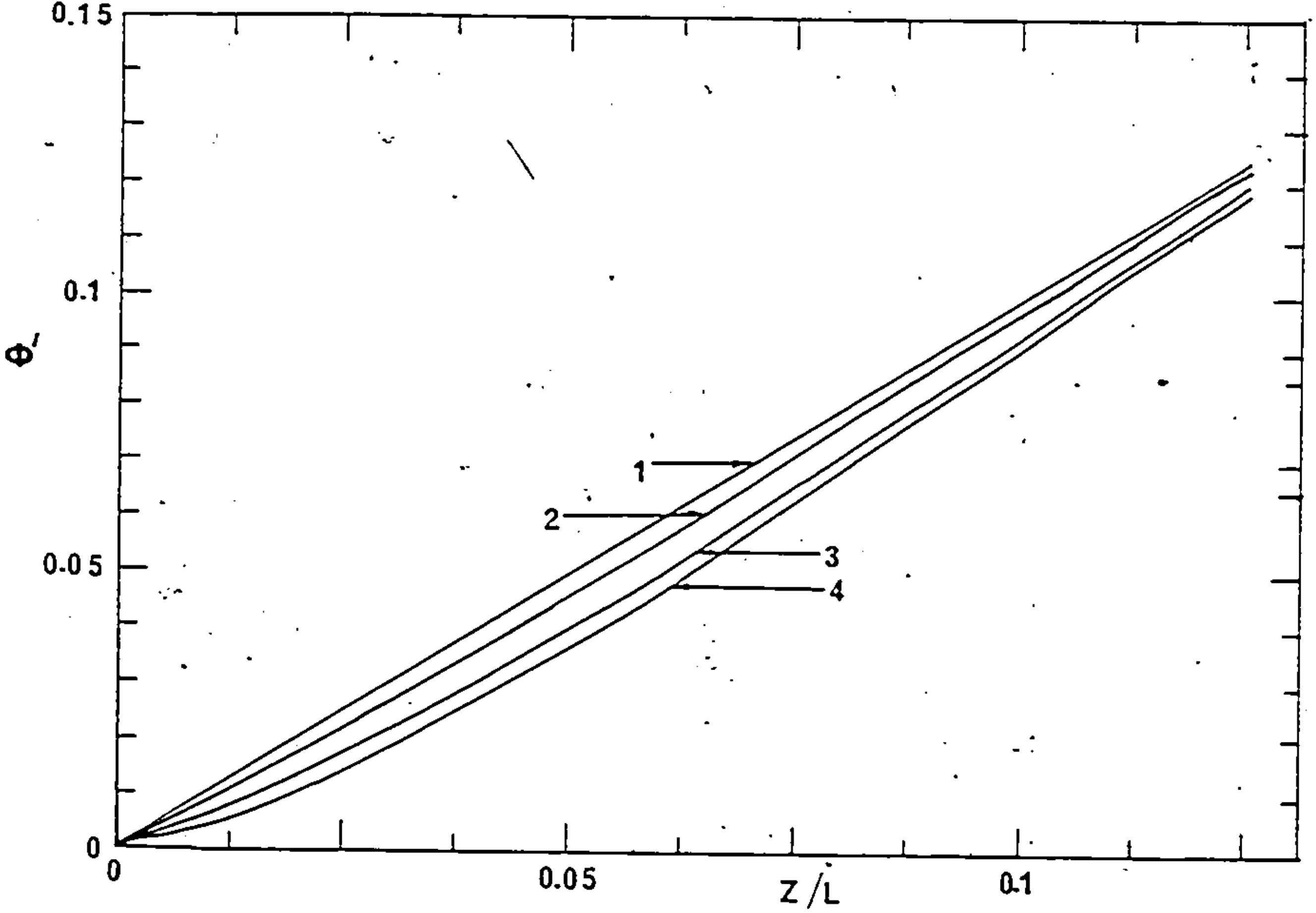

Fig. 8.15. Dependence of the normalized potential distribution Φ' at the solid insulator-vacuum interface on γ near the electrodes regions for System C. Curve 1, corresponds to $\gamma = 0$; curve 2, $\gamma = 15°$; curve 3, $\gamma = 45°$; curve 4, $\gamma = 65°$.

aluminium filled epoxy resin ($\varepsilon_2 = 4.7$), Macor-glass-ceramic ($\varepsilon_2 = 5.8$) and alumina-ceramic ($\varepsilon_2 = 9.0$) using $\gamma = 15°$ and $45°$. For purposes of clarity the fields are plotted as a function of Z/L only for alumina-ceramic, glass-ceramic and Teflon using $\gamma = 45°$ (Figs. 8.16 and 8.17). For $\gamma = 15°$ and also for plexiglass and aluminum-filled epoxy resin the results are summarized in Table 8.4. Figure 8.16 shows the normalized tangential field for $\gamma = 45°$ for Teflon (curve 1), Macor glass-ceramic (curve 2) and alumina-ceramic (curve 3) and Fig. 8.17 correspondingly for the normalized normal field. As can be seen from Fig. 8.16, the value of $E'_{t_{1c}}$ (at the cathode) [= $E'_{t_{1a}}$ (at anode)] decreases as the relative dielectric constant increases. However, the maximum value $E'_{t_{1m}}$ is higher for the materials having a higher dielectric constant. For the normal field, there is not much difference in the $E'_{n_{1a}}$ (=$E'_{n_{1c}}$) values while $E'_{n_{1m}}$ is higher for the materials having higher dielectric constants (Fig. 8.17). For (Fig. 8.17) example, when $\gamma = 45°$, the $E'_{t_{1c}}$ and $E'_{t_{1m}}$ values for $\varepsilon_2 = 2.1$ are 0.42 and 1.07 (Fig. 8.16, curve 1), respectively. The corresponding values when $\varepsilon_2 = 9.0$ at $E'_{t_{1c}} = 0.16$ and $E'_{t_{1m}} = 1.153$ (Fig. 8.16, curve 3). There is a reduction of 62% in $E'_{t_{1c}}$ and only an increase of 8% in $E'_{t_{1m}}$. This situation is opposite to that of a solid insulator with convex curvature at the edges (Chapter 6) where the junction field increases with increasing the dielectric constant of the solid insulator material. Since the junction field and the maximum field value is less affected by the dielectric constant, a concave

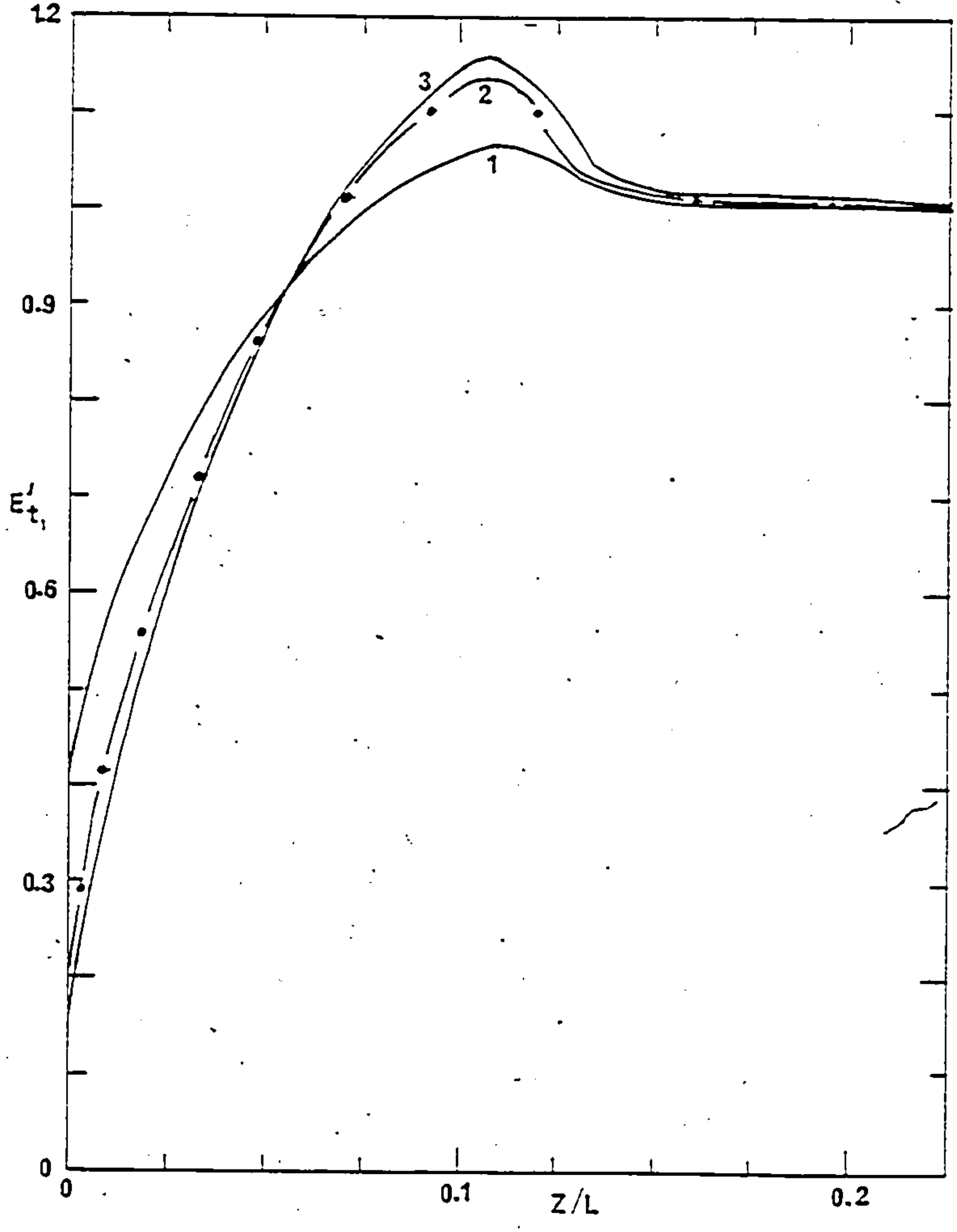

Fig. 8.16. Dependence of E'_{t_1} on Z/L for different solid insulator materials of System C. Curve 1, corresponds to $\varepsilon_2 = 2.1$ (Teflon); curve 2, $\varepsilon_2 = 5.8$ (Macor glass-ceramic); curve 3, $\varepsilon_2 = 9.0$ (alumina). $\gamma = 45°$, L = 4 cm. 2R = 4 cm.

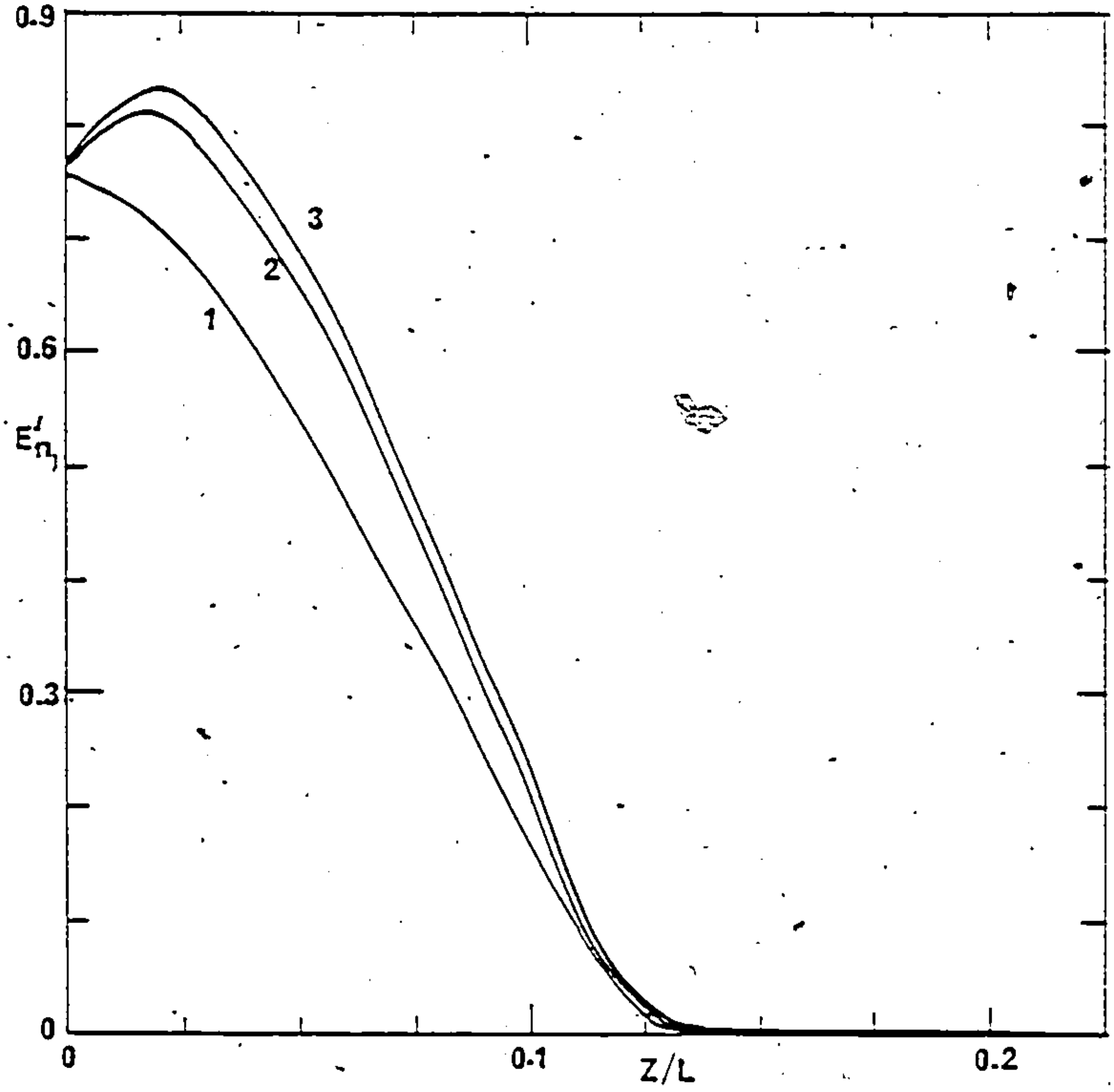

Fig. 8.17. Dependence of E'_{n_1} on Z/L for different solid insulator materials of System C. Curve numbers and other conditions are as for Fig. 8.16.

Table 8.4. Dependence of the normalized tangential and the normalized normal field values for different insulator materials for $\gamma = 15°$ and $\gamma = 45°$. Notations and conditions are as for Table 8.3

Material	ϵ_2	$\gamma=15°$				$\gamma=45°$			
		$E'_{t_{1c}} = E'_{t_{1a}}$	$E'_{t_{1m}}$	$E'_{n_{1c}} = E'_{n_{1a}}$	$E'_{n_{1m}}$	$E'_{t_{1c}} = E'_{t_{1a}}$	$E'_{t_{1m}}$	$E'_{n_{1c}} = E'_{n_{1a}}$	$E'_{n_{1m}}$
Teflon	2.1	0.83	1.029	0.32	0.32	0.42	1.070	0.756	0.754
Plexiglass	3.2	0.78	1.040	0.342	0.342	0.31	1.098	0.775	0.780
$A\ell$ filled epoxy	4.7	0.74	1.048	0.360	0.360	0.24	1.125	0.776	0.803
Glass-ceramic	5.8	0.72	1.052	0.368	0.368	0.21	1.135	0.776	0.813
Alumina	9.0	0.69	1.055	0.378	0.378	0.16	1.153	0.773	0.834

design might be more useful in cases which require a combination of a high dielectric constant and a low loss tangent [52].

It will be observed from Figs. 8.16 and 8.17 that for the materials used the change in the field value is only at the curved region and the E'_{t_1} value becomes unity at about Z/L = 0.2 and remains constant at this level up to Z/L = 0.8. Similarly the E'_{n_1} value declines towards zero and remains at this level from Z/L = 0.14 to 0.86. Since the field variation is mainly in the curved region, changing the length of the linear portion does not alter to a great extent the field value at the concave triple junction.

8.8 Cylindrical Solid Insulator with Metal Inserts and Placed in Recessed Electrodes (System D)

Figures 8.18 (curve 3) and 8.19 (curve 3) show the computed normalized tangential and normal fields, respectively along the solid insulator-vacuum interface for System D. The solid insulator has a 4 mm metal insert at both ends and placed in 2 mm recessed electrodes. As can be seen from Fig. 8.18 (curve 3), and Table 8.5, using the combination of metal inserts and recessed electrodes is better than using either a solid insulator with metal inserts or a solid insulator placed in recessed electrodes to reduce the tangential field component near the electrode triple junction. For System D, E'_{t_1} value near the electrode junction is 0.40. The E'_{t_1}

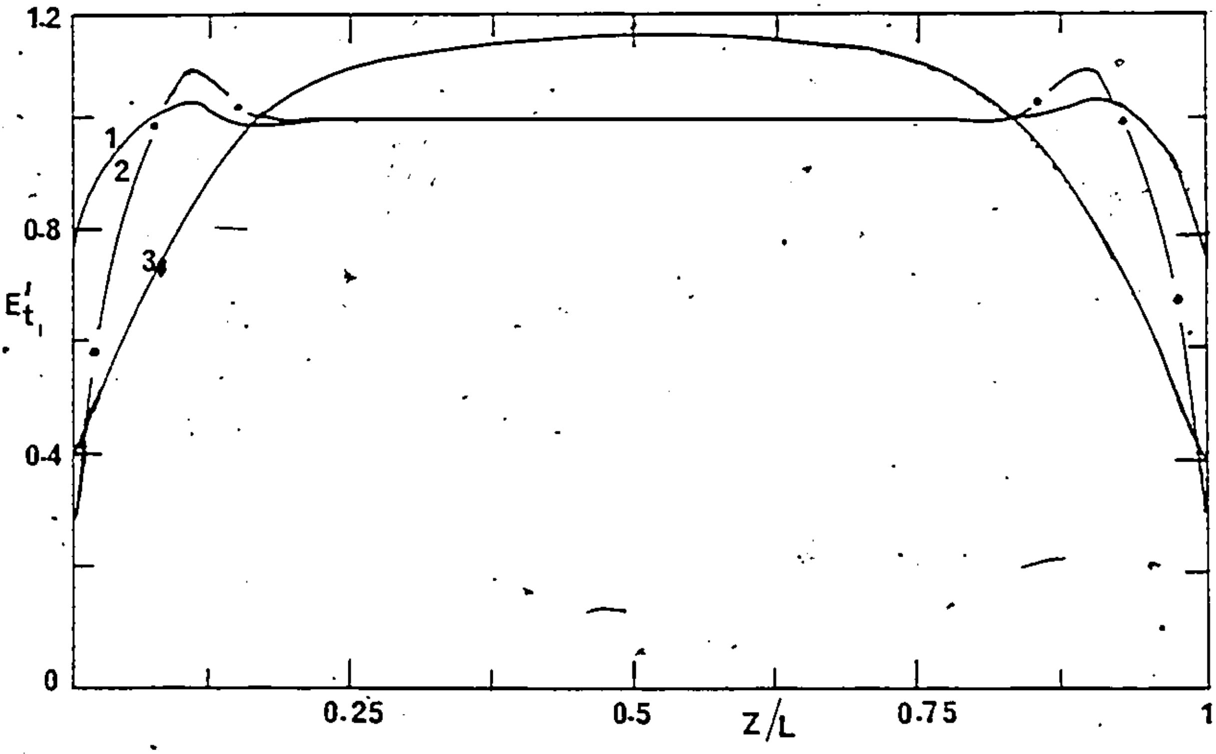

Fig. 8.18. Normalized tangential electric field E'_{t_1} along the solid insulator-vacuum boundary, (Systems C and D). Curve 1, corresponds to $\gamma = 15°$ (Fig. 8.2), System C; curve 2, $\gamma = 45°$ (Fig. 8.2) System C; curve 3, corresponds to Fig. 8.2, System D. Depth of metal insert = 4 mm, depth of electrode recess = 2 mm. Insulator thickness L = 4 cm; Insulator diameter 2R = 4 cm. Material: plexiglass ($\varepsilon_2 = 3.2$).

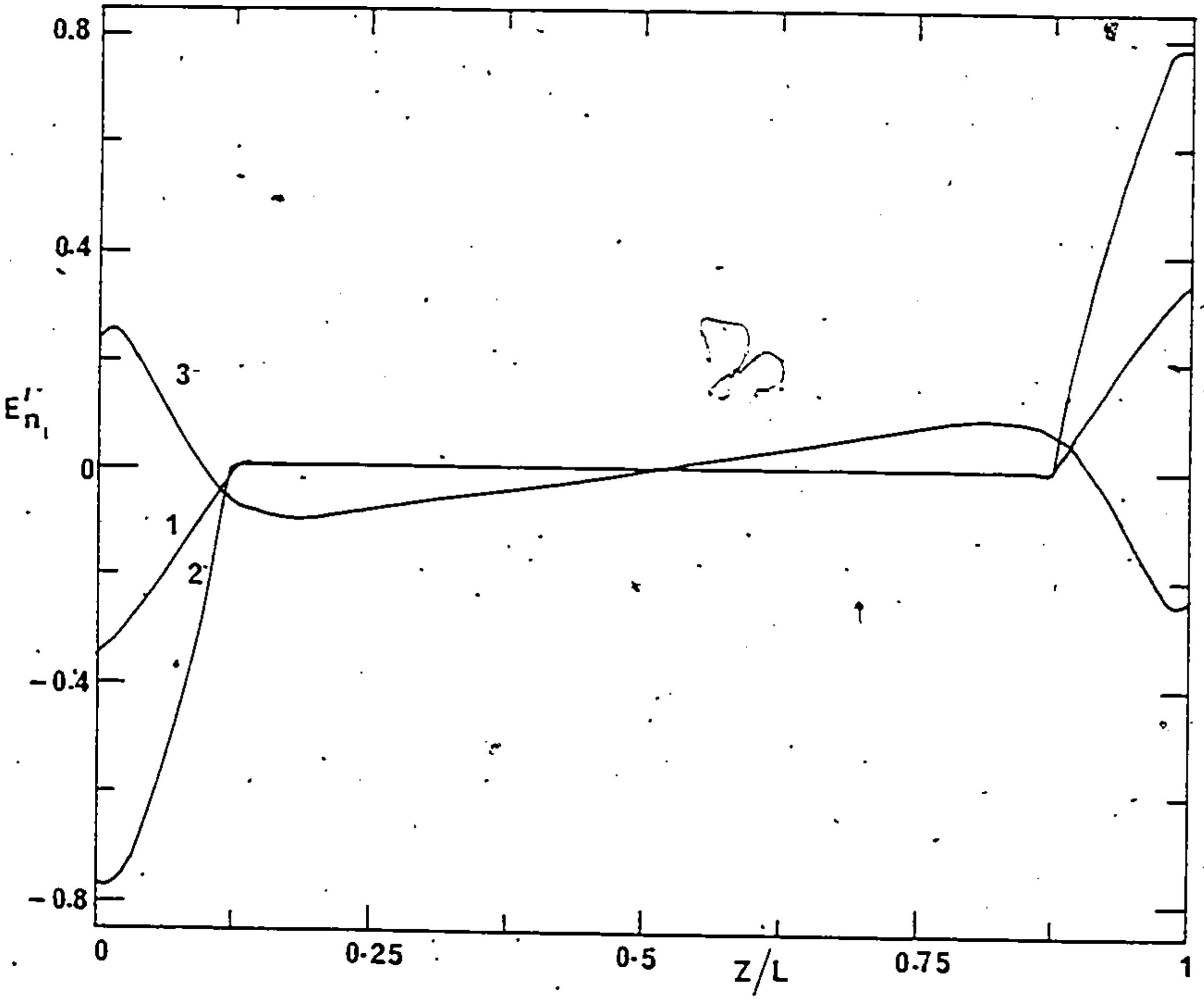

Fig. 8.19. Normalized normal electric field E'_{n_1} along the solid insulator-vacuum interface (Systems C and D). Curve numbers and conditions are as for Fig. 8.18.

value near the electrode junction is 0.65 for a solid insulator with 4 mm metal inserts and no recess. For a solid insulator placed in 2 mm recessed electrodes and no metal insert, the junction field value E'_t is 0.66. This shows that System D has the best field performance compared to System A and B. The maximum normal field value $E'_{n_{1m}}$ of System D is 0.25 which is lower when compared to System A ($E'_{n_{1m}}$ = 0.29) and System B ($E'_{n_{1m}}$ = 0.45).

8.9 Comparison of Computed Field Values Between Systems C and D (Fig. 8.2)

Table 8.5 gives the normalized tangential field $E'_{t_{1c}}$ (= $E'_{t_{1a}}$), the normalized normal field at the electrode junctions and the maximum field $E'_{t_{1m}}$ for (a) cylindrical insulator (4 cm thick and 4 cm in diameter) with concave edges using γ = 15° and 45° (Fig. 8.2, System C) and (b) a right angle cylindrical plexiglass insulator $\gamma = 0$, L = 4 cm and 2R = 4 cm having 4 mm depth of metal inserts at both ends and placed into a recessed electrodes to a depth of 2 mm [Fig. 8.2, System D]. When γ = 15°, System D is better than System C in that it has a lower tangential field at both triple junctions. Table 8.5 shows that the concave insulator at γ = 45° (Fig. 8.2, System C) has a lower tangential field than an insulator with either metal inserts or when placed in recessed electrodes or having a combination

Table 8.5. Normalized tangential (E'_t) and normalized normal field (E'_n) values near the cathode ($E'_{t_{1c}}$ and $E'_{n_{1c}}$) and anode ($E'_{t_{1a}}$ and $E'_{n_{1a}}$) triple junctions and the maximum field ($E'_{t_{1m}}$ and $E'_{n_{1m}}$) for Systems C, System D and comparison with system having metal inserts (System A), and recessed electrodes (System B). Solid insulator material: Plexiglass ($\varepsilon_2 = 3.2$); L = 4.0 cm; 2R = 4.0 cm. Field values are on the vacuum side of the solid insulator-varuum interface.

	$E'_{t_{1c}}$ $= E'_{t_{1a}}$	$E'_{t_{1m}}$	$E'_{n_{1c}}$	$E'_{n_{1a}}$	$E'_{n_{1m}}$
Solid insulator with curved edges (Fig. 8.2, System C)					
$\gamma = 15°$	0.78	1.04	-0.342	0.342	0.342
$\gamma = 45°$	0.31	1.10	-0.775	0.78	0.67
Solid insulator with 4 mm metal insert and placed in 2 mm recessed electrode (Fig. 8.2, System D)	0.40	1.15	0.24	-0.24	0.255
Solid insulator with 4 mm metal insert, no recess (Tables 8.1 and 8.2)	0.65	1.12	-0.002	+0.002	0.290
Solid insulator placed in 2 mm recessed electrode, no metal insert (Tables 8.1 and 8.2)	0.66	1.07	0.39	-0.39	0.45

of the latter two (Fig. 8.2, System D). The results obtained using an assumed heterocharge model on the surface of the solid insulator indicates that the cylindrical insulator with metal inserts might be better than an insulator placed in recessed electrodes (Sections 8.5 and 8.6). In the case of an insulator with metal inserts, the normal field towards the cathode junction is directed inward (negative) which helps to reduce the normal field due to a positive surface charge density which leads to a field directed outward from the surface (positive). In the case of System C (Fig. 8.2) the normal field towards the cathode is directed inward (negative). It is obvious that this geometry is also preferable when a heterocharge distribution is present on the surface of the solid insulator.

The tangential and the normal field distributions along the solid insulator-vacuum interface are shown respectively, in Figs. 8.18 and 8.19 in System C for $\gamma = 15°$ (curve 1) and $\gamma = 45°$ (curve 2) and for System D (curve 3). System C has $L = 4$ cm and $2R = 4$ cm and System D has an insert depth of 4 mm and a recess depth of 2 mm and the same thickness L and diameter 2R. By considering the field magnitudes at the triple junctions (shown in Fig. 8.18) it may be concluded that System C with $\gamma = 45°$ is electrically superior to System D. Furthermore, it is of course relatively easier to fabricate System C than System D. The conducting electrodes of System C are simpler in shape, the insulator format can be readily fabricated and therefore more economical than System D.

8.10 Surface Flashover of Cylindrical Solid Insulators with Concave Curved Edges

8.10.1 DC, AC and Impulse Flashover Voltages

Macor glass-ceramic ($\varepsilon_2 = 5.8$) is employed for flashover studies in the form of cylindrical spacers with concave curvature at the edges. The material thickness is 4 mm and the values of γ (Fig. 8.2,c) used are: 0 (right angle cylinder), 15°, 45° and 65°. For $\gamma = 0$, the diameter of the insulator is 4 mm. The surface flashover characteristics of the concave insulator using positive and negative polarities of DC, lightning impulse and AC are presented in Table 8.6. For all the γ used the AC (peak) flashover voltage is lower than the DC flashover voltage. The reason for this behaviour was recently explained in terms of the effect of the prestress caused by the opposing preceding half cycle [28]. The 1.2/50 μs impulse is at about the same level as that of the DC level. The DC, impulse and AC flashover voltage of the concave cylindrical insulator increases with increasing γ in the range from 0 to 45° and then starts to decrease with further increase in γ (Table 8.6). In all cases the flashover is higher than that of the right angle cylindrical

($\gamma = 0$) insulator. For example, when $\gamma = 45°$, the DC flashover voltage is 65 kV, which is about 30% higher than the right angle cylindrical insulator ($\gamma = 0$) of the same thickness. The AC and the impulse voltages, for $\gamma = 45°$ are also about 30-35% higher than for $\gamma = 0$. The DC, AC and impulse flashover voltages for $\gamma = 65°$ are lower when compared to $\gamma = 45°$ (Table 8.6) even though the calculated tangential field value at the cathode triple junction is lower when $\gamma = 65°$ (Table 8.3). This may be due to the effect of higher normal field value for $\gamma = 65°$. For Macor glass-ceramic, the tangential field decreases by 28% ($E'_{t_{1c}} = 0.72$) for 15° and by 79% ($E'_{t_{1c}} = 0.21$) for 45° (Table 8.4) when compared to a specimen having $\gamma = 0$. The corresponding increases in the DC breakdown are 18.7% and 30.8%, respectively for $\gamma = 15°$ and $\gamma = 45°$ (Table 8.6). The corresponding increases for the impulse flashover are 22.8% and 36.7% respectively for $\gamma = 15°$ and $\gamma = 45°$. For AC the increases in the flashover compared to the case of $\gamma = 0$ are 28.8% and 37.5% for $\gamma = 15°$ and $\gamma = 45°$, respectively (Table 8.6).

In the case of a plexiglass ($\varepsilon_2 = 3.2$) insulator having a thickness L = 4 mm, the DC, AC and 1.2/50 μs impulse flashover voltages for $\gamma = 0$ (right angle cylinder) are 48 kV, 39.5 kV and 49 kV respectively. For concave curvature at both ends (Fig. 8.2, System C) having $\gamma = 45°$ and the same thickness (L = 4 mm), the DC, AC and impulse flashover

Table 8.6. Surface flashover voltage of a solid insulator with a concave curvature (System C) for DC, AC and 1.2/50 μs impulse voltages and ~~different~~ γ. Material: Macor glass-ceramic (ε_2 = 5.8); Electrodes: Stainless steel (15 mm in diameter); Length of insulator = 4 mm; Diameter of insulator = 4 mm.

γ	DC (a) kV	DC (b) kV	AC (Peak) kV	1.2/50 μs (a) kV	1.2/50 μs (b) kV
0	49.7	50.0	40	49.0	48.5
15°	59.0	58.5	51.5	60.2	59.8
45°	65.0	65.5	55.0	67.2	66.9
65°	55.0	54.5	52.5	59.1	58.7

(a) Top insulator positive, bottom grounded
(b) Top insulator negative, bottom grounded

voltages are 59 kV, 52.5 kV and 63 kV respectively. The corresponding increases in the DC, AC and impulse flashover voltages when γ is changed from 0 to 45° are 20.8%, 32.9% and 28.6% respectively. Table 6.4 shows that the corresponding decreases in the field at the cathode triple junctions for plexiglass by 69% from $E'_{t_{1c}} = 1$ for $\gamma = 0°$ to $E'_{t_{1c}} = 0.31$ for $\gamma = 45°$. The DC, AC and impulse flashover voltages for a 4 mm thickness, 7 mm diameter plexiglass cylindrical insulator placed in 1.5 mm recessed electrodes are 23 kV, 20.8 kV and 24 kV respectively.

Clearly, the changes in the flashover voltage levels cannot be explained entirely by the changes in the electric field at the cathode due to the geometrical effects only. One must also consider the possible alteration in the surface charge patterns due to the changes ensued in the field arising from the concave geometry. The change in the charge distribution on the solid insulator surface would also modify the field at the cathode compared to the case of γ = 0 with a consequent further change in the flashover voltage.

8.10.2 Effect of DC Pre-stress on Flashover Voltage

Figure 8.20 shows the combined DC + 1.2/50 μs impulse (curve 1) and DC + AC (curve 2) flashover voltages of Macor glass-ceramic for γ = 45° as a function of the DC pre-stress. The impulse flashover voltage without any DC pre-stress is

67 kV. The combined DC and impulse voltage is increased by less than 5% when the DC pre-stress is increased from 0 to 30 kV. This has been found for an aiding DC pre-stress which has the same polarity as that of the lightning impulse and an opposite polarity to that of the lightning impulse. Similarly the combined DC + AC voltage is influenced by less than 10% (Fig. 8.20, curve 2). It has also been reported [68] that the combined DC± impulse flashover voltage is independent of the pre-stress when the solid insulator is placed in recessed electrodes.

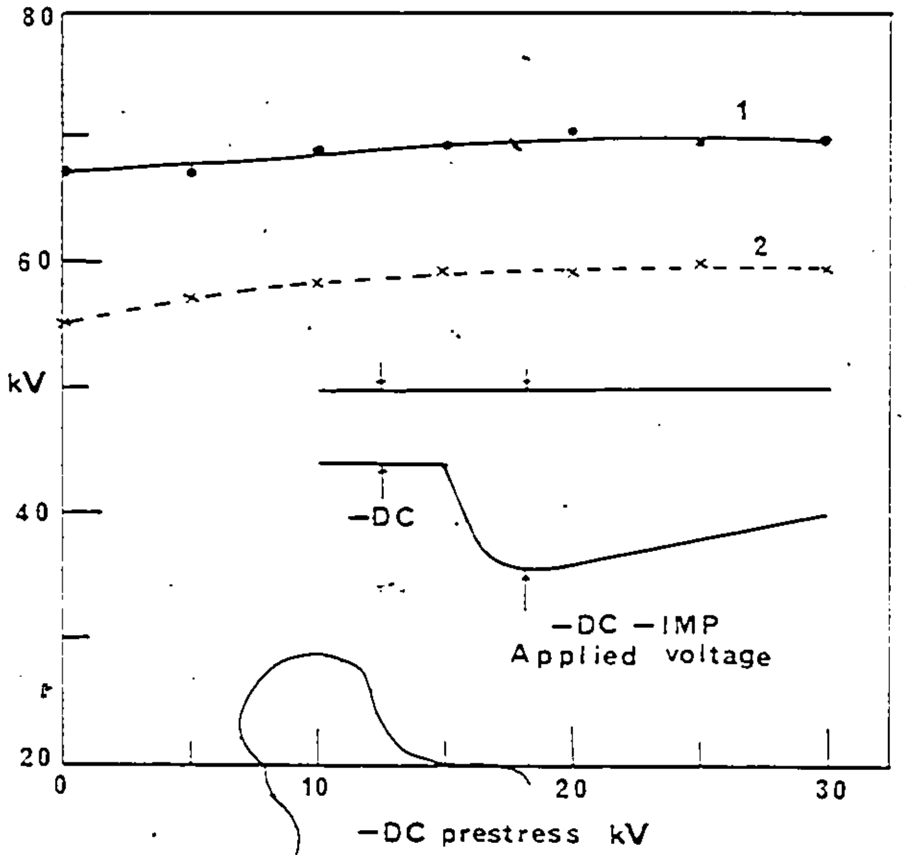

Fig. 8.20. Combined DC + 1.2/50 μs impulse and DC + AC flashover voltages for 4 mm thickness Macor glass-ceramic insulator. $\gamma = 45^\circ$ (System C). Curve 1, DC + 1.2/50 μs impulse; applied DC pre-stress polarity is as that of the impulse; curve 2, DC + AC.

CHAPTER IX

CONCLUSIONS

1. The surface flashover of Macor Glass-ceramic, Quartz, Teflon, Pyrex glass, Plexiglass and Sapphire cylindrical insulators have been investigated in ultra-high vacuum ($<10^{-8}$ Torr) using DC, AC (60 Hz) and 1.2/50 μs impulse voltages. The DC and impulse flashover voltages for a fixed length of the insulator are almost the same (within ± 5%) and AC flashover voltage is lower than the DC and the impulse. The flashover voltage depends on the material of the insulator and increases in a non-linear manner with increasing length of the insulator. In general the flashover voltages are independent of the pressure in the range 10^{-8} - 6×10^{-3} Torr for the insulators studied when stainless steel electrodes are used.

2. The DC and the impulse flashover voltage of conical insulators are higher for the positive values of θ than for the negative values of θ in glass-ceramic. The DC and the impulse flashover voltages are almost equal for θ in the range -55° to +55° and the AC flashover voltage is lower than that of the DC or impulse. The computed field and potential distributions also show that the cathode

junction field is lower for positive values of θ and higher for negative values of θ.

3. The DC, AC and lightning impulse flashover voltage of solid insulators are independent of electrode material.

4. The total area of the insulator affects the DC, AC and impulse flashover voltage of solid insulators in vacuum. Increasing the diameter of the glass-ceramic insulator for the same thickness reduces the flashover voltage.

5. The Ultra-Violet (UV) irradiation on the solid insulator-vacuum interface reduces the flashover voltage and the reduction in the flashover value depends on the insulator material. The flashover strength of the irradiated insulator sample recovers to the original strength of the sample before irradiation after 2-4 repeated flashovers.

6. The DC flashover voltage measured subsequent to applying a DC pre-stress with an opposite polarity is found to be considerably lower than the flashover voltage without a pre-stress. After 5 to 6 flashovers, the insulator recovers to its original flashover strength. A DC pre-stress of the same polarity has little effect on the subsequent DC flashover voltage.

7. For cylindrical insulators, an opposing DC pre-stress causes a reduction and an aiding DC pre-stress

causes an increase in the subsequent flashover voltage of the impulse superimposed on DC. However, the combined DC ± Impulse flashover voltages of conical glass-ceramic insulators are less influenced by the DC pre-stress than in the glass-ceramic cylindrical insulators. In general, a DC pre-stress causes an increase in the subsequent AC superimposed on DC flashover voltage.

8. A method has been proposed to calculate the DC surface flashover of cylindrical solid insulators in vacuum. This method is based on the assumption that the discharge occurs in a layer of desorbed gases from the insulator surface and also takes into account the secondary electron emission characteristics of the dielectric material. A dependence of the flashover voltage on the insulator length to a power law of 0.5 is theoretically predicted and verified experimentally.

9. The field enhancement at both electrode junctions increases with decreasing electron impact energy. A low electron impact energy causes an increased accumulation of surface charge and results in lowering the withstand voltage of solid insulators as has been observed and reported.

10. A heterocharge accumulation is expected to occur on the surface of a solid insulator subjected to electrical

stress in vacuum. The computed results with a heterocharge accumulation show that the electric field is enhanced at both the cathode and the anode junctions.

11. For a positive surface charge accumulation throughout the surface of the solid insulator, an enhancement in the field is found at the cathode junction and a reduction in the field value at the anode junction. In the case of a homocharge accumulation on the surface of a solid insulator, an enhancement in the field is observed at the surface of the solid insulator at locations away from the electrode junctions and a reduction near both the cathode and anode junctions.

12. For a cylindrical insulator with convex curved edges at both ends, large enhancements in the electric field at the triple junction formed by the solid insulator, electrode and vacuum are found. The electric field at the triple junction depends on the contact angle α between the solid insulator and the electrode and also the relative permittivity ε_2 of the dielectric. The higher the values of α the lower the value of the junction field.

13. A solid insulator with metal inserts at both ends, or placed in recessed electrodes, or a solid insulator using a combination of metal inserts and placed in recessed

electrodes has a lower tangential field component near the electrode junctions. The field value decreases with increasing depth of penetration of the metal insert or the depth of the recess. The maximum value of the tangential field occurs at a location away from the triple junction.

14. For a given solid insulator in an electrode system containing either a recess or a metal insert, the tangential field has approximately similar values at the same depth of penetration and recess. However, the system with a metal insert should have the best performance due to its normal field distribution, since a heterocharge is most likely to be present at the insulator surface.

15. For cylindrical insulators with concave curved edges at both ends, the tangential field value at the cathode and the anode junctions are lower than the average applied field. The reduction in the field value depends on the angle γ between the concave curvature of the insulator and the normal to the electrode at the contact point. As the value of γ increases, there is a reduction in the tangential field value and an increase in the normal field value at the triple junctions.

16. The DC, AC and impulse flashover strength of cylindrical insulators (glass-ceramic, plexiglass) with

concave curved edge at both ends are higher than that of a right angle cylindrical insulator of the same thickness. The DC pre-stress has relatively small influence (<10%) on the combined DC and impulse or DC and AC flashover level of the cylindrical insulator with concave curved edges.

APPENDIX I

Potentials (P_{ij}) and Field (F_{ij}) Coefficients of Ring Charges

$$P_{ij} = \frac{1}{4\pi\varepsilon_o\varepsilon_r} \cdot \frac{2}{\pi} \cdot \frac{K(k_1)}{\alpha_1}$$

$$F_{ijr}(\text{normal}) = -\frac{1}{4\pi\varepsilon_o\varepsilon_r}\,\frac{1}{\pi r_i}\left\{\left[\frac{r_j^{\,2} - r_i^{\,2} + (Z_i - Z_j)^2}{\alpha_1\,\beta_1^2}\right] \cdot E(k_1) - \frac{K(k_1)}{\alpha_1}\right\}$$

$$F_{ijz}(\text{tangential}) = \frac{1}{4\pi\varepsilon_o\varepsilon_r} \cdot \frac{2}{\pi} \cdot \frac{(Z_i - Z_j) \quad E\,(k_1)}{\alpha_1\,\beta_1^2}$$

where

$$\alpha_1 = \sqrt{(r_i + r_j)^2 + (Z_i - Z_j)^2}$$

$$\beta_1 = \sqrt{(r_i - r_j)^2 + (Z_i - Z_j)^2}$$

$$k_1 = 2\,\frac{\sqrt{r_i \cdot r_j}}{\alpha_1}$$

$K(k_1)$ Complete elliptic integral of the first kind

$$K\,(k_1) = \int_o^{\pi/2} \frac{d\,\theta}{\sqrt{1 - k_1^2\,\sin^2\theta}}$$

$E(k_1)$ Complete elliptic integral of the second kind.

$$E(k_1) = \int_0^{\pi/2} \sqrt{(1 - k_1^2 \sin^2 \theta)} \cdot d\theta$$

r_j - radius of the ring charge Q_j

Z_j - the Z co-ordinate of the ring charge Q_j

r_i - the radius of the contour point

Z_i - the Z co-ordinate of the contour point

ε_r - relative dielectric constant

ε_o - permitivity of free space

REFERENCES

1 P. H. Gleichauf, "Electrical breakdown over insulators in high vacuum," J. Appl. Phys., vol. 22, pp. 535-541, 1951.

2 P. H. Gleichauf, "Electrical breakdown over insulators in high vacuum," J. Appl. Phys., vol. 22, pp. 766-771, 1951.

3 E. S. Borovik and B. P. Batrakov, "Investigation of breakdown in vacuum," Sov. Phys. Tech. Phys., vol. 3, pp. 1811-1818, 1958.

4 M. J. Kofoid, "Phenomena at metal-dielectric junctions of high-voltage insulators in vacuum and magnetic field," AIEEE Trans. Part III, vol. 79, pp. 991-999, 1960.

5 M. J. Kofoid, "Effect of metal-dielectric junction phenomena on high-voltage breakdown over insulators in vacuum," AIEEE Trans. Part III, vol. 79, pp. 999-1004, 1960.

6 A. Fryszman, T. Strzyz and M. Wasinski, "On a mechanism of breakdown in high vacuum," Bull. Polonaise, vol. 8, p. 379, 1960.

7 H. Boersch, H. Hamisch and W. Ehrlich, "Surface discharges across insulators in vacuum," Z. Angew. Phys., vol. 15, pp. 518-525, 1963.

8 J. P. Shannon, S. F. Philip and J. G. Trump, "Insulation of high-voltage across solid insulators in vacuum," J. Vac. Sci. Tech., vol. 2, pp. 234-239, 1965.

9 A. Watson, "Pulsed flashover in vacuum," J. Appl . Phys., vol. 38, pp. 2019-2023, 1967.

10 I. D. Smith, "Pulse breakdown of Insulator surface in a poor vacuum," Proc. 1st Int. Symps. Insulation of High Voltages in Vacuum, Cambridge, U.S.A., pp. 261-280, 1964.

11 O. Milton, "Pulsed flashover of insulators in vacuum," IEEE Trans. Elect. Insul., vol. EI-7, pp. 9-15, 1972.

12 R. Hackam, IEE Invited Review for Colloquium, "Electrical phenomena on insulating surfaces in gases and in vacuum," IEE Digest No. 26, 1975.

13 R. Hawley, "Solid insulators in vacuum: A review," Vacuum, vol. 18, pp. 383-390, 1968.

14 S. Grzybowski and E. Kuffel, "Electric surface strength of high-voltage insulators in vacuum," IEEE Trans. PAS-99, pp. 1788-1794, 1980.

15 R. B. Britton, K. W. Arnold, and A. S. Denholm, "Ability of a voltage-graded surface to support a high-voltage in vacuum and in a pressurized gas," Rev. Sci. Instr., vol. 34, pp. 185-187, 1963.

16 C. M. Cooke and J. G. Trump, "Post-type support spacers for compressed gas-insulated cables," IEEE Trans. PAS-92, pp. 1441-1447, 1973.

17 T. Nitta, Y. Shibuya, F. Fujiwara, Y. Arahata, N. Takahashi and H. Kuwahara, "Factors controlling surface flashover of SF_6 gas insulated systems," IEEE Trans., PAS-97, pp. 959-965, 1978.

18 A. S. Pillai and R. Hackam, "Optimal electrode-solid insulator geometry with accumulated surface charges," IEEE. Trans. Elect. Insul. (To be published 1983).

19 A. S. Pillai, R. Hackam and P. H. Alexander, "Influence of radius of curvature, contact angle and material of the solid insulator on the electric field in vacuum (and gaseous) gas," IEEE Trans. on Elect. Insul., vol. EI-18, pp. 11-22, 1983.

20 R. Hackam, "Formation of microprotrusions on stainless steel cathodes in high vacuum," Materials Res. Bull., vol. 8, pp.868-870, 1973.

21 R. Hackam, "Determination of the electric field enhancement factor and crater dimensions in aluminium from scanning electron micrographs," J. Appl. Phys., vo. 34, pp. 114-118, 1974.

22 T. S. Sudarshan and J. D. Cross, "DC electric field modifications produced by solid insulators bridging a uniform-field vacuum gap," IEEE Trans. on Elect. Insul., Vol. EI-8, pp. 122-128, 1973.

23 T. S. Sudarshan, J. D. Cross and K. D. Srivastava, "Prebreakdown process associated with surface flashover of solid insulators in vacuum," IEEE Trans. on Elect. Insul., vol. EI-12, pp. 200-208, 1977.

24 R. A. Anderson and J.P. Brainard, "Mechanism of pulsed surface flashover involving electron-stimulated desorption," J. Appl. Phys., vol. 51, pp. 1414-1421, 1980.

25 J. P. Brainard, "Local fields at the cathode-insulator junction as a cause of breakdown of shaped insulators in vacuum," Proc. Conf. on Electrical Insulation and Dielectric Phenomena (CEIDP), Wahington, pp. 482-488, 1975.

26 A. S. Pillai and R. Hackam, "Modification of electric field at the solid insulator-vacuum interface arising from surface charges on the solid insulator," J. Appl. Phys., vol. 54, pp. 1302-1313, 1983.

27 J. H. Mason, "Discharges," IEEE Trans. Elect. Insul., vol. EI-13, pp. 211-238, 1978.

28 A. S. Pillai and R. Hackam, "Effect of DC Pre-stress on AC and DC surface flashover of solid insulators in vacuum," Proc. 10th Int. Symp. on Discharges and Electrical Insulation in Vacuum, Columbia, U.S., pp. 300-307, 1982.

29 A.S. Pillai and R. Hackam, "DC, AC and Lightning Impulse Surface Flashover of Conical Insulators in Vacuum", J. Appl. Phys. (to be published, 1983).

30 A. S. Pillai and R. Hackam, "Surface flashover of solid dielectric in vacuum," J. Appl. Phys., vol. 53, pp. 2983-2987, 1982.

31 A. S. Pillai and R. Hackam, "Electric field arising from a heterocharge accumulation on the surface of a solid insulator in vacuum," Proc. IEEE, vol. 71, pp. 268-269, 1983.

32 A. S. Pillai and R. Hackam, "Dependence of the electric field on accumulation of a homocharge on the surface of a solid insulator," Proce. IEEE, vol. 71, 1983.

33 A. S. Pillai and R. Hackam, "Improved performance of cylindrical solid insulators with concave curved edges in vacuum," IEEE Trans. on PAS. To be published, 1983.

34 F. M. Clark, Insulating materials for design and engineering practice, John Wiley & Sons, Inc., New York, 1962.

35 R. Hackam and S. K. Salman, "Novel design for accurate alignment of high voltage electrodes assembly," Vacuum, vol. 23, pp. 9-10, 1973.

36 R. Hackam and S. K. Salman, "Pre-breakdown currents in ultra high-vacuum gaps between aluminum electrodes," Proc. IEE, vol. 119, pp. 377-384, 1972.

37 J. P. Brainard and Dal Jensen, "Electron avalanche and surface charging on alumina insulators during pulsed high-voltage stress," J. Appl. Phys., vol. 45, pp. 3260-3265, 1974.

38 R. Hackam and S. K. Salman, "Effects of electrode curvature, distance from glass insulator, and addition of hydrogen on field-emission currents and breakdown voltage in vacuum," J. Appl. Phys., vol. 45, pp. 4384-4392, 1974.

39 Hanna, Moscicka and Grezesiak, "AC predischarges phenomena in vacuum for insulator-electrodes arrangement depending on insulator height," Proc. 7th Int. Symp. on Discharges and Electrical Insulation in Vacuum, Novosibirsk, USSR, pp. 278-281, 1976.

40 R. Lee, T. S. Sudarshan, J. E. Thompson and R. L. Boxman, "Predischarge current measurements in vacuum gaps bridged with plexiglass insulators," Proc. 10th Int. Symp. on Discharges and Electrical Insulation in vacuum, Columbia, USA, pp. 288-297, 1982.

41 R. Lee, R. Rhinehart, J. E. Thomson and T. S. Sudarshan, "Pre-discharge current measurements and optical surface field measurements associated with insulator flashover," Gaseous Dielectric III, L. G. Christophorou, editor, Pergamon Press, pp. 349-355, 1982.

42 A. A. Avdienko, "Surface breakdown of solid dielectrics in vacuum I, Characteristics for breakdown of insulators along the vacuum surface," Sov. Phys. Tech. Phys., vol. 22, pp. 986-991, 1977.

43 A. A. Avdienko and M. D. Malev, "Surface breakdown of solid dielectrics in vacuum II. Mechanism for surface breakdown," Sov. Phys. Tech. Phys., vol. 22, pp. 986-991, 1977.

44 A. A. Avdienko and M. D. Malev, "Surface breakdown of a solid dielectric in vacuum III. Quantitative model," Sov. Phys. Tech. Phys., vol. 24, pp. 581-587, 1979.

45 G. R. Govinda Raju, R. Hackam and F. A. Benson, "Breakdown mechanisms and electrical properties of a vacuum triggered gap," J. Appl. Phys., vol. 47, pp. 1310-1317, 1976.

46 K. D. Srivastava and C. De Tourreil, "Electrical breakdown across ceramic surfaces in high vacuum under DC and pulse voltages," Proc. 3rd Int. Symps. on Discharges and Electrical Insul. in Vacuum, Paris, pp. 243-247, 1968.

47 S. P. Bugaev, A. M. Iskoldski and G. A. Mesyats, "Investigation of the pulsed breakdown mechanism at the surface of a dielectric in vacuum I. Uniform field," Sov. Phys. Tech. Phys., vol. 12, pp. 1358-1362, 1968.

48 R. W. Sillars, Electrical insulating materials and their applications, Peter Peregrims Ltd., London, U.K., p. 59, 1973.

49 R. H. Fowler and L. N. Nordheim, " Electron emission in intense electric fields," Proc. R. Soc. A., vol. 119, pp. 173-181, 1928.

50 G. D. Theophilus, R. G. Van Heeswijk and K. D. Srivastava, "Problems of Pre-breakdown current measurement in 60 Hz vacuum breakdown studies in vacuum," Vacuum, Vol. 20 pp. 11-14, 1970.

51 R. Hawly and A. A. Zaky, "Conduction and Breakdown in High Vacuum," Progress in Dielectrics, vol. 7, pp. 115-215, 1967.

52 R. Hays and G. B. Walker, "Vacuum breakdown at a glazed ceramic surface," Proc. IEE, vol. 111, pp. 600-604, 1964.

53 R. A. Anderson, "Study of surface flashover of conical insulators using 3ns risetime pulses," Proc. 7th Int. Symps. on Discharges and Electrical Insulation in Vacuum, Novosibirsk, USSR, pp. 252-256, 1976.

54 M. Akahane, K. Kanda and K. Yahagi, "Effect of dielectric constant on surface discharge of polymer insulators in vacuum," J. Appl. Phys., vol. 44, p. 2972, 1973.

55 N. G. Trinh, F.A.M. Rizk and C. Vincent, "Electrostatic-field optimization of the profile of epoxy spacers for compressed SF_6-insulated cables," IEEE Trans. PAS-99, pp. 2164-2174, 1980.

56 T. Takuma and T. Watanaka, "Optimal profiles of disc-typ spacers for gas insulation," Proc. IEE, vol. 122, pp. 183-188, 1975.

57 D. A. Eastham, T. Joy and A. E. Groome, "High voltage breakdown of ceramic insulators bonded to titanium electrodes," Proc. 6th Int. Symps. on Discharges and Electrical Insulation in Vacuum, Swansea, U.K., pp. 190-194, 1974.

58 R. Hackam and L. Altcheh, "AC (50 Hz) and DC electrical breakdown of vacuum gaps and with variation of air pressure in the range 10^{-9} and 10^{-2} Torr using OFHC copper, nickel, aluminium, and niobium parallel planar electrodes," J. Appl. Phys., vol. 46, pp. 627-636, 1975.

59 B. A. Prichard, Jr., "Mechanism of electrical discharges in high vacuum at voltages up to 400 000 V," J. Appl. Phys., vol. 44, pp. 4548-4554, 1973.

60 C. A. Ramm, "Some features of beam handling equipment for the CERNPS," Int. Conf. on Instrumentation for High Energy Physics, Berkeley, 1960.

61 E. Kuffel, S. Grzybowski, and J. P. McMath, "Breakdown across insulation surface in vacuum under direct, alternating and surge voltages of various wave shape," Proc. 4th Int. Symps. on Discharges and Electrical Insulation in Vacuum, Waterloo, Canada, pp. 227-231, 1970.

62 A. S. Denholm, F. J. McCoy and C. N. Coenradds, Proc. of the Symposium on Electrostatic Energy Conversion, PIC-ELE 209, 1963.

63 J. Juchniewicz, B. Mazurek and A. Tyman, "The effect of number of spacer insulators on the breakdown voltage of vacuum insulation," IEEE Trans. Electr. Insul, vol. EI-14, pp. 107-110, 1979.

64 C. Enloe, R. Blaher, M. Coffing and R. E. Reinovsky, "Vacuum ultra-violet effects on power transport across a vacuum/solid dielectric interface," Proc. 10th Int. Symps. on Discharges and Electrical Insulation in Vacuum, Columbia, U.S.A., pp. 308-314, 1982.

65 O. I. Kondratov, V. H. Konchienko and I. P. Kuzekin, "Investigation of the influence of a charge accumulated on a surface on the electric strength of insulators in vacuum," Proc. 7th Int. Symps. on Discharges and Electrical Insulation in Vacuum, Novosibirsk, USSR, pp. 261-264, 1976.

66 G. L. Jackson, M. Kristiansen, J. Marx and A. Bowling, "Pulse flashover of solid dielectrics in vacuum," Proc. 10th Int. Symps. Discharges and Electrical Insulation in Vacuum, Columbia, USA, pp. 333-338, 1982.

67 A. Bradwell, R. Cooper and B. Varlow, "Conduction in polythene with strong electric fields and the effect of prestressing on the electric strength," Proc. IEE, vol. 118, pp. 247-254, 1971.

68 J. D. Cross and K. D. Srivastava, "The effect of DC pre-stress on impulse flashover of insulators in vacuum," IEEEE Trans. Elect. Insul., vol. EI-9, pp. 97-102, 1974.

69 C. H. de Tourreil, K. D. Srivastava and V. J. Woelke, "Experimental observation of surface charging of high voltage insulators for vacuum apparatus," IEEE Trans. Elect. Insul., vol. EI-7, pp. 176-179, 1972.

70 C. H. de Tourreil and K. D. Srivastava, "Mechanism of surface charging of high voltage insulators in vacuum," IEEE Trans. Elect. Insul., vol. EI-8, pp. 17-21, 1973.

71 K. Nakanishi, A. Yoshioka, Y. Shibuya and T. Nitta, "Charge accumulation on spacer surface at DC stress in compressed SF_6 gas," Gaseous Dielectrics III, L. G. Christophorou, Editor, Pergamon Press, pp. 365-373, 1982.

72 A. Knecht, "Development of surface charges on epoxy resin spacers stressed with direct applied voltages," Gaseous Dielectrics III, L. G. Christophorou, Editor, Pergamon Press, pp. 356-364, 1982.

73 I. Kitani and K. Arii, "Impulse breakdown of prestressed polyethylene films in the ns range," IEEE Trans. Electr. Insul., vol. EI-17, pp. 228-233, 1982.

74 S. Menju and T. Takahashi, "DC dielectric strength of a SF_6 gas insulated system," IEEE Trans. PAS-97, pp. 217-224, 1978.

75 R. A. Anderson, "Propagation velocity of cathode-initiated surface flashover," J. Appl. Phys., vol. 48, pp. 4210-4214, 1977.

76 R. A. Anderson, "Mechanism of fast surface flashover in vacuum," Appl. Phys. Lett., vol. 24, pp. 54-56, 1974.

77 J. D. Cross and K. D. Srivastawa, "High-speed photography of surface flashover of solid insulators under impulse voltages in vacuum," Appl. Phys. Lett., vol. 21, pp. 549-551, 1972.

78 P. A. Chatterton and D. K. Davies, "Secondary electron emission characteristics of insulator surfaces before and after impulse flashover," Proc. 8th Int. Symp. on Discharges and Electrical Insulation in Vacuum, Albuquerque, USA, D2-1, 1978.

79 S. C. Brown, Basic data of Plasma Physics, MIT Press, Cambrdige, 1959.

80 P. A. Redhead, J. P. Hobson and E. V. Kornelsen, The Physical Basis of Ultra High Vacuum, Chapman and Hall, London, 1968.

81 A. A. Avidenko and A. V. Kiselev, "Outgassing from insulator surfaces in a strong electric field in vacuum," Sov. Phys. Tech. Phys., vol. 12, pp. 381-384, 1967.

82 S. Dushman and J. M. Lafferty, Scientific Foundations of Vacuum Technique, Wiley, New York, 1962.

83 M. J. Drinkwine and D. Lichtman, "Electron stimulated desorption: a critical review," Progress in Surface Science, vol. 8, pp. 123-142, 1977.

84 J. H. Leck and B. P. Stimpson, "Desorption from gas covered surfaces by Electron Impact: A review of the subject," J. Vac. Sci. Technol., vol. 9, pp. 293-300, 1972.

85 R. Reather, Electron Avalanches and Breakdown in Gases, Butterworth, London, 1964.

86 O. I. Kondratov, "B. D. across insulators in vacuum in uniform electric field," Proc. 5th Int. Symp. on Discharges and Electrical Insulation in Vacuum, Poznan, Poland, pp. 289-294, 1972.

87 H. Singer; H. Steinbigler and P. Weiss, "A charge simulation method for the calculation of high voltage fields," IEEE Trans. PAS-95, pp. 1660-1668, 1974.

88 M. Akazaki, K. Mishijima and S. Sato, "Calculation of three-dimensional axisymmetric fields by charge simulation method," Elect. Engg. in Japan, vol. 98, pp. 1-7, 1978.

89 P. K. Mukerjee and C. K. Roy, "Computation of fields in and around insulators by fictitious point charges," IEEE Trans. Elect. Insul., vol. EI-13, pp. 300-307, 1978.

90 T. Takuma, T. Kouno and H. Matsuda, "Field behaviour near singular points in composite dielectric arrangement," IEEE Trans. Elect. Insul., vol. EI-13, pp. 426-435, 1978.

91 A. S. Pillai and R. Hackam, "Electric field and potential distributions for unequal spheres using symmetric and asymmetric applied voltages," IEEE Trans. Elect. Insul., In Press, 1983.

92 M. J. Khan and P. H. Alexander, "Charge simulation modelling of practical insulator geometries," IEEE Trans. Elect. Insul., vol. EI-17, pp. 325-332, 1982.

93 B. O. Popvic, Introductory Engineering Electro Magnetics, Addison-Wesley, Mas., 1971.

94 R. E. Bolz and G. L. Tuve, CRC Handbook of Tables for Applied Engineering Science, The Chemical Rubber Co., Ohio, p. 196, 1970.

95 G. R. Govinda Raju, R. Hackam and F. A. Benson, "Time delay to firing of a triggered vacuum gap with barium titanate in trigger gap," Proc. IEE, Vol. 124, pp. 828-832, 1977.

96 G. R. Govinda Raju, R. Hackam and F. A. Benson, "Probability of firing a triggered vacuum gap incorporating barium titanate," Int. J. Electronics, Vol. 42, pp. 185-191, 1977.

97 S. Menju, Y. Tsuchikawa and N. Kobayashi, "Electric potential and field of conical insulators for SF$_6$ metal clad switch gear," IEEE Trans. PAS-91, pp. 390-398, 1972.

98 P. H. Dawson, "Secondary electron emission yields of some ceramics," J. Appl. Phys., vol. 37, pp. 3644-3645, 1966.

99 S. S. Attwood, Electric and Magnetic Fields, John Wiley and Sons, New York, 1958.

100 B. Cross, "Static charges on dielectrics," British Journal of Applied Physics, vol. 1, pp. 259-267, 1950.

101 C. M. Cook, "Surface flashover of gas/solid interfaces," Gaseous Dielectrics III, L. G. Christophorou, Editor, Pergamon Press, pp. 337-348, 1982.

102 C. M. Cook, R. Nakata, M. Ouyang, S. J. Dale and T. F. Garrity, "Compressed gas insulation for advanced HVDC Transmission Equipment, CIGRE Report, 1982.

103 H. Forhlich, Theory of Dielectrics, Oxford University Press, London, 1958.

104 W. Pfeiffer, "Gas breakdown in case of steep-fronted pulses and insulator interfaces," IEEE Trans. Elect. Insul., vol. EI-17, pp. 505-511, 1982.

105 K. Itaka, T. Hara, T. Misaki and H. Tsuboi, "Improved structure avoiding local field intensifications on spacers in SF_6 Gas," IEEE Trans. PAS-102, pp. 250-255, 1983.

VITA AUCTORIS

May 1951	Born in Kallukatty, Kanyakumari District, Tamilnadu, India
March 1967	Completed Secondary School Leaving Certificate Examination through A.V.D. High School, Ganapathipuram, Tamilnadu
March 1968	Completed Pre-University Course through Scott Christian College, Nagercoil, Madurai University
April 1973	Graduated from the Annamalai University, Tamilnadu with a B.Eng. degree in Electrical and Electronics Engineering
July 1975	Graduated from the Indian Institute of Science, Bangalore with a M.Eng. Degree in Electrical Engineering
August 1975- July 1977	Electrical Engineer (Project), United Manufacturing Corporation, New Delhi, India
August 1977- July 1979	Associate Lecturer, Guindy Engineering College Madras University, India
August 1979- Sept. 1980	Scientist, High Voltage Laboratory, Central Power Research Institute, Bangalore, India
Sept. 1980	Joined the Electrical Engineering Department, University of Windsor, Windsor, Ontario, Canada for the degree of Doctor of Philosophy program
May 1983	Candidate for the Degree of Doctor of Philosophy

PUBLICATIONS

1. A. Sivathanu Pillai and R. Hackam, "Surface flashover of solid dielectric in vacuum." J. Appl. Phys. Vol. 53, pp. 2983-2987, 1982.
2. A.S. Pillai, R. Hackam and P.H. Alexander, "Influence of radius of curvature, contact angle and material of solid insulator on the electric field in vacuum (and gaseous) gaps." IEEE Trans. Elect. Insul., Vol. EI-18, pp. 11-22, 1983.
3. A.S. Pillai and R. Hackam, "Modification of electric field at the solid insulator-vacuum interface arising from surface charges on the solid insulator." J. Appl. Phys., Vol. 54, pp. 1302-1313, 1983.
4. A.S. Pillai and R. Hackam, "Electric field arising from a heterocharge accumulation on the surface of a solid insulator in vacuum." Proc. IEEE, Vol. 71, pp. 268-269, 1983.
5. A.S. Pillai and R. Hackam, "Dependence of the electric field on accumulation of a homocharge on the surface of a solid insulator." Proc. IEEE, Vol. 71, pp. 531-533, 1983.
6. A.S. Pillai and R. Hackam, "Effect of D.C. pre-stress on A.C. and D.C. surface flashover of solid insulators in vacuum." IEEE Trans. Elect. Insul., Vol. EI-18, pp. 292-300, 1983.
7. A.S. Pillai and R. Hackam, "Electric field and potential distributions for unequal spheres using symmetric and asymmetric applied voltages," IEEE. Trans. Elect. Insul. Accepted for publication, March, 1983.
8. A.S. Pillai and R. Hackam, "Optimal electrode-solid insulator geometry with accumulated surface charges," IEEE Trans. Elect. Insul. (to be published, 1983).
9. A.S. Pillai and R. Hackam, "Flashover of conical and cylindrical insulators in vacuum," J. Appl. Phys. (Submitted for publication, July, 1983).
10. A.S. Pillai and R. Hackam, "Improved performance of cylindrical solid insulators with concave curved edges in vacuum," IEEE Trans. on PAS (Submitted for publication, May, 1983).
11. A.S. Pillai and R. Hackam, "Analysis of Electric field of different geometries at interfaces of insulator-vacuum (or gaseous) triple junctions". Conference on Interfacial Phenomena in practical insulating systems, Maryland, U.S.A., September, 1983.
12. A.S. Pillai and R. Hackam, "Electrical breakdown of solid insulators in air and in vacuum", Fourth International Symposium on Gaseous Dielectrics, Knoxville, U.S.A., 1984.
13. A.S. Pillai, "Design of transient network analyzer to study switching overvoltages on EHV systems". Proceedings of International Symposium on EHV Engineering, Testing Equipments and Techniques. University of Roorkee, Roorkee, India, IV-4, pp. 21-26, September, 1980.
14. A.S. Pillai, "Sulphur-Hexafluoride (SF_6) Medium for insulation and interruption in HV and EHV applications." Electrical India, pp. 5-8, November, 1979.